Northumbria University
NEWCASTLE

HIGH DENSITY RATIO LATTICE BOLTZMANN SIMULATIONS FOR TERNARY SYSTEMS

NEERU BALA

PhD

2021

HIGH DENSITY RATIO LATTICE BOLTZMANN SIMULATIONS FOR TERNARY SYSTEMS

NEERU BALA

A thesis submitted in partial fulfilment of the requirements of the University of Northumbria at Newcastle for the degree of Doctor of Philosophy

Faculty of Engineering and Environment

September 2021

Abstract

Ternary fluid systems (and specifically the ones involving two liquids and a gas phase) are of special interest for a variety of practical applications, such as combustion engines, ink-jet printing, and oil recovery. The physics and dynamics of these systems involves a complex interplay of capillary, viscous and inertial forces. For such flows, some fundamental information such as the velocity field, strains, and stresses, usually cannot be observed in experiments. On the other hand, analytic descriptions struggle to account for complex boundary conditions at multiple interfaces. In this context, numerical approaches are able of revealing hidden details, and provide the missing link between experiments and theory. Additionally, numerical approaches allow to easily tune a variety of physical parameters over a broad range of values, usually difficult to access experimentally, allowing a broader and deeper understanding. In this thesis, I employ and further develop a ternary free energy lattice Boltzmann method (LBM) to investigate two fundamental problems involving ternary fluid systems.

The first problem focuses on the fluid flow and contact line dynamics of ternary fluids in presence of solid boundaries. To this aim, I propose three alternative schemes for solid boundaries for ternary fluids within the lattice Boltzmann framework. After benchmarking both static and dynamic properties, I focus on a system consisting of a train of two immiscible drops (bislug) confined within a long channel. By imposing a capillary force imbalance through the wetting boundaries for different phases, the bislug is self-propelled, and the steady velocity can be readily tuned by setting the bislug length. This will allow to extract simultaneous information on the contact line dynamics for all interfaces, evaluating the role of surface tension, density and viscosity contrast between phases.

The second and main problem focuses on the collision between immiscible drops surrounded by a low-density phase. Several experimental, and a few numerical studies have shown that, depending on the balance between viscous, inertial, and surface tension forces, different outcomes of collision are possible, such as Adhesion, Bouncing or Encapsulation. However, a detailed and systematic investigation is currently lacking. To cover this gap, I have performed systematic numerical simulations varying over a wide range of relevant dimensionless numbers tuning the relative surface tension of the fluid phases, the impact speed, the liquid viscosity, and the relative size of the drops. This allows to detect the transition boundaries between collision out-

comes within multi-dimensional parameter spaces. Furthermore, I focus on the details of collision dynamics, highlighting the link between physical parameters, collision mechanisms and final outcomes. While most previous studies consider a phase space consisting of Weber number (rescaled velocity) and impact parameter (drop alignment), to the best of my knowledge this is the first work including a systematic variation of the Ohnesorge number (rescaled viscosity) for such ternary system. Among the main results, I have identified a novel type of collision outcome named Delayed Adhesion, not reported previously. This novel outcome is specifically related to the presence of capillary forces acting between immiscible drops.

Contents

List of Figures

List of Tables

Acknowledgements

Firstly, I would like to express my sincere appreciation and thank to my primary supervisor Dr. Ciro Semprebon for his continuous support, motivation and guidance during my Ph.D journey.

I am also grateful to my co-supervisors Prof. Halim Kusumaatmaja in Durham University and Dr. Antonio Moro for always being supportive and willing to provide valuable suggestions. I want to thank Prof. Krishna Busawon and Dr. Rodrigo Ledesma Aguilar for serving on my thesis committee and their valuable comments throughout this project.

I would like to extend my gratitude to Northumbria University for providing me with the financial support via a Postgraduate Research Studentship. I also own my colleagues and friends for their support during last three years.

A special thank to my husband, parents, siblings, parents in-law for their unconditional love and support during my Ph.D journey.

Declaration

I declare that the work contained in this thesis has not been submitted for any other award and that it is all my own work. I also confirm that this work fully acknowledges opinions, ideas and contributions from the work of others.

Any ethical clearance for the research presented in this thesis has been approved. Approval has been sought and granted by the Faculty Ethics Committee on 10/10/2017.

I declare that the Word Count of this thesis is 39,172 words.

Name: Neeru Bala

Date: September 24, 2021

Chapter 1

Introduction

Ternary fluid system relevant for this work consists of one gas and two liquid components. These systems are of considerable scientific interest due to their broad range of applications. One of such applications is combustion engines, where it has been demonstrated that by adding a certain amount of water, the burning rate in the combustion chamber could be enhanced [130]. Here the ignition step following the collision between the fuel and water droplets can lead to micro-explosions if the fuel completely encapsulates the water drops. Another application is in oil recovery, especially in the immiscible water-alternating-gas (IWAG) displacement process. Here, the alternately displacement of oil by air and water shows improvement in the recovery of residual oil [43]. Furthermore, understanding of the dynamics of ternary fluids interactions is important for environmental problems. For example, if an oil spill occurs, raindrops dropping into the ocean slick oils can affect the environmental pollution. In particular, different behaviours are observed depending on oil layer fluid properties and its thickness, impacting droplet size and impact speed.[85].

The dynamics of ternary fluid systems is rich and complex with many technical and mathematical challenges that need to be addressed, in particular when one of the fluids is represented by a low density gas phase. On the one side, the experimental approaches are yet unable to provide in-depth information of the flow field, stresses and strains close to the interfaces for such a complex flows. On the other side analytic approaches are generally limited to relatively simple cases such as *Couette flow*, *Poiseuille flow* and *Jeffery-Hamel flow* [62] [8]. Therefore, numerical/computational methods represent a necessary step to bridge the two sides and gain further insight. The numerical

approaches allow a broad choice of simulation setups, in terms of initial and boundary conditions. They also provide substantial information on the flow field, stress, and dissipated energy. Numerical simulations when combined with theoretical analysis and experimental studies are powerful tools in studying the physics of ternary fluid systems.

Several computational approaches have been proposed in the literature to model fluid problems where interfaces play a significant role. At macroscopic scales these include, the conventional computational fluid dynamics (CFD) methods (for example Finite difference, Finite volume and Finite element methods) [1], [30]. These methods are usually efficient in describing mechanical properties of single phase flows, but require particular care in tracking multiple interfaces. For small space and time scales the molecular dynamics (MD) approach is often employed. Here the Newton's equations of motion are solved based on the microscopic scale by tracking the motion of individual molecules. This approach allows to account for intermolecular interactions directly, but the required computation power makes them unfit to simulate fluidic phenomena at the laboratory scale [126], [32].

Another promising approach is the lattice Boltzmann method (LBM), which is derived from kinetic equation [119], [87], [34], [143], [27]. The key idea of lattice Boltzmann method is to replace particles with fictitious cluster of particles on a fixed lattice, which do not follow Newtonian dynamics as in molecular dynamics (MD). This makes lattice Boltzmann approach computationally more affordable. The collective behavior of particles is represented by a probability distribution function. Therefore, instead of tracing the movement of particles, the evolution of the density distribution function, which depends on position and velocity, is traced. To incorporate multiphase fluid systems, the kinetic equation is coupled with phase field model which does not required to explicitly trace the interface. This makes LBM a mesoscopic approach that exists in between the micro and macro scale. The numerical scheme for the Boltzmann equation is easy to implement and is very amenable to high-performance computing on parallel architectures, including Graphics processing unit (GPUs). It can be shown that the lattice Boltzmann equation leads to the equations of fluid dynamics on the macroscale by performing Chapman-Enskog analysis [58].A more detailed discussion about differences between computational approaches, and specific lattice Boltzmann implementation will be discussed in Chapter 3.

1.1 Scope of this research

This thesis will report the studies carried out for liquid-liquid-gas systems at large density contrast (10^3). Common example of these systems are water-oil emulsions surrounded by a gas phase and slippery liquid-infused surfaces. This research is divided into two parts: the first part focuses on the development and benchmarking of a numerical scheme based on free energy lattice Boltzmann approach. This includes the development of three methods to simulate interaction with structured surfaces. The second part of the research involves numerical investigation of Immiscible drop collision. The emphasis is bouncing of droplets and complete encapsulation of one droplet by another.

1.2 Outline of the thesis

The thesis is outlined as below:

- Chapter 2 is devoted to the summary of necessary background to capillarity and wetting phenomenon. This summarises the fundamental concepts of thermodynamics and fluid dynamics which will be employed in the numerical study.
- Chapter 3 presents the basic concepts of lattice Boltzmann method (LBM). This includes the detailed background about the lattice Boltzmann equation and different approaches under LBM framework. In particular, in depth description of the *free-energy approach* is provided, which has been used to model ternary fluids with large density contrast between the liquids and gas phase.
- Chapter 4 is dedicated to the development and benchmark of the methods of wetting boundary conditions in a ternary free energy lattice Boltzmann model. These methods are optimised for ternary models (and with larger number of phases). This is relevant to simulate the ternary fluid systems in contact with structured surfaces such as Slippery Liquid Infused Porous Surfaces (SLIPS). The advantages and disadvantages of each method are addressed by performing both static and dynamic tests in this chapter.
- Chapter 5 discusses the fundamental background and relevant concepts specific to droplet collision phenomenon. The simulation setup and necessary benchmark tests before simu-

lating droplet collision problem are addressed in this chapter. These concepts are valid to discuss the results of chapter 6 and 7.

- Chapter 6 reports the systematic numerical study of the collision between two immiscible liquid droplets. The transition between the two collision outcomes, in particular *Adhesion* and *Bouncing* is the focus of study in this chapter. A detailed numerical investigation of *Bouncing* outcome as a function of collision parameters is discussed here.
- Chapter 7 is focused on the immiscible drop collision, in particular with one of the liquid close to spreading over the other liquid. The transition between the collision outcomes *Adhesion* and *Encapsulation* and role of surface tension which is one of the significant parameter for *Encapsulation* morphology is here studied in detail. The energy balance and its its dependency on other physical parameters has been investigated.
- Chapter 8 gives a summary of the dissertation together with recommendations for future research.

Chapter 2

Capillarity and Wetting Background

This chapter addresses the fundamental background to the phenomenon of capillarity and wetting. These concepts are required for discussing the dynamics of multiphase multicomponent fluid systems. The chapter begins with a basic thermodynamic background of binary fluid system (liquid-gas) and then extended to the ternary fluid system (liquid-liquid-gas). These concepts provide the basis for a wider variety of multiphase multicomponent systems. The fundamental equations of motion of fluid dynamics are discussed towards the end of the chapter.

2.1 Bulk and Interfacial Thermodynamics

2.1.1 Miscible and immiscible liquids

In general, the mixture of liquids can be categorised as *miscible* or *immiscible* in nature. In order to illustrate the difference between the two, assume the molecular representation of two liquid mixtures as shown in the Fig.1(a,b). The various types of molecules are depicted by different colours. In particular, the $liquid_1$ and $liquid_2$ in Fig.1(a) form a homogeneous mixture without an internal interface. This is the characteristic of a *miscible* liquid mixture. For example, the ideal gases are always miscible and for a range of concentrations, water and ethanol are also miscible. On the other hand the molecular representation of the *immiscible* liquids is shown by two liquids ($liquid_1$, $liquid_2$) in Fig.1(b). The inhomogeneity and the presence of internal interfaces are the attribute of immiscible liquids. The internal interfaces formed are characterised by surface tension and the fluid particles are divided into two regions (brown and blue). The typical example of an

immiscible mixture of liquids is oil and water.

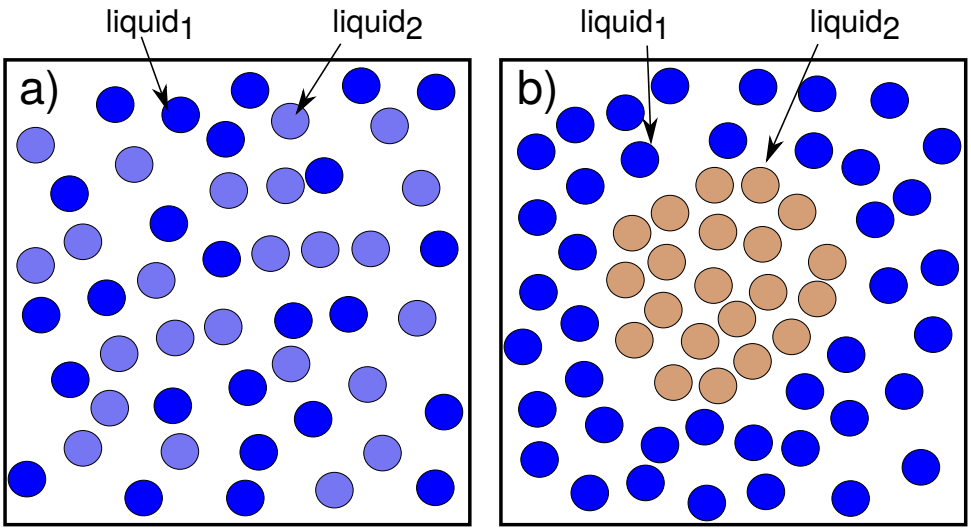

Figure 1: Illustrations of liquid mixtures which are (a) miscible and (b) immiscible.

2.1.2 Gibbs free energy

The physical state of equilibrium between multiphase multicomponent systems occurs when the pressure (P), temperature (T) and chemical potential (μ) of the two phases are identical. Equivalently, the state of equilibrium can be described on the basis of Gibbs free energy potential as shown in Eq.(2.1), which was formulated by *Josiah Willard Gibbs* in the *1870s*.

$$G(T, P, N_i) = H - TS \tag{2.1}$$

Where, H is the enthalpy defined as: $H = U + PV$. U, P and V denote internal energy, pressure and volume of the system, respectively. The differential of above equation is:

$$dG = -SdT + VdP + \sum_i \mu_i dN_i, \tag{2.2}$$

where the summation is over all components and phases in the system. The chemical potential of i^{th} component at constant T, P and μ of all the components/phases except for the i^{th}

$$\mu_i = (dG/dN_i)_{T,P,N_i'} \tag{2.3}$$

The key advantage of using Gibbs potential for the condition of equilibrium in the complex systems is that it depends only on the comprehensive variables N_i, which are the number of moles in each phase of each component. This means G is a homogeneous function of N_i of the order one as below:

$$G(T, P, qN_1, qN_2, qN_{3....}) = qG(T, P, N_1, N_2, N_3....) \tag{2.4}$$

Differentiation of Eq.((2.4)) w.r.t q and at q=1, we arrive at the below relation:

$$\sum_i N_i \left(\frac{dG}{dN_i}\right)_{T,P,N_i'} = G \tag{2.5}$$

Hence, $G = \sum_i N_i \mu_i (T, P)$. Combination of this expression with Eq.(2.2) leads to the *Gibbs-Duhem equation* as shown below:

$$SdT - VdP + \sum_i N_i d\mu_i = 0 \tag{2.6}$$

Above *Gibbs-Duhem equation*, implies the following equilibrium condition:

- Temperature is homogeneous through all phases and all components.
- Pressure is homogeneous through all phases and all components.
- Chemical potential is homogeneous through all phases and all components

2.1.3 Liquid-gas concurrence and Maxwell area construction rule

The theoretical interpretation of the general thermodynamic concepts includes the contribution of thermodynamic potential and its reliance on temperature, pressure and composition. This is often done in the form of a state equation that determines the dependence of the pressure on temperature and density. The simplest *ideal gas equation of state* is $P = \rho RT$, but any change in the phase is prohibited. *Van der Waals* provided the first state equation which could explain phase coexistence

[128] as stated below:

$$\left[P + a\rho^2\right]\left(\frac{1}{\rho} - b\right) = RT \tag{2.7}$$

Where P is the pressure of the fluid , T is the absolute temperature of the system, and ρ is the density. The constants a and b have positive values and are the attribute of the individual gas. After replacing the ρ with $\frac{N}{V}$, the following form of the EOS is extracted.

$$\left[P + a\left(\frac{n}{V}\right)^2\right]\left(\frac{V}{n} - b\right) = RT \tag{2.8}$$

where, V is the total volume of the fluid container and n is the number of particles. As the values of these constants *(a,b)* approach zero, the *van der Waals equation of state* approaches the ideal gas law $PV = nRT$. The constant *a* provides a correction for the intermolecular forces. Constant *b* is a correction for finite molecular size and its value is the volume of one mole of the atoms or molecules [128]. In the pressure-molar volume curve of *van der Waals equation* of state, there exists a minimum and a maximum in as shown in Fig.2.

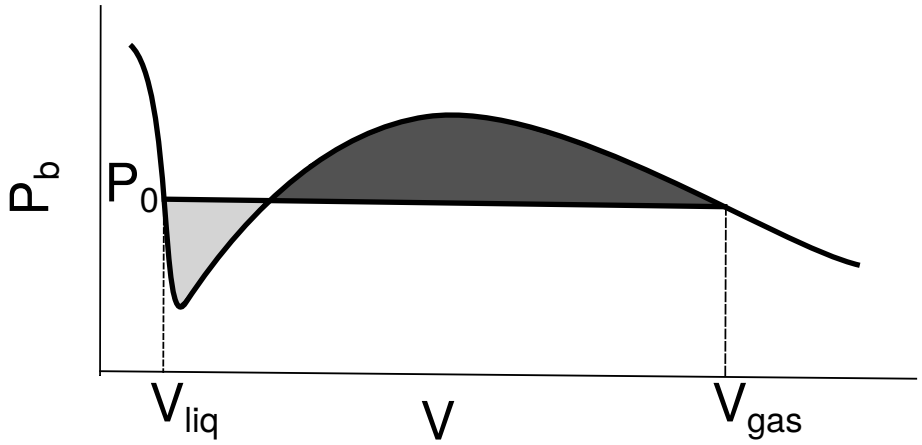

Figure 2: The Maxwell area construction rule at constant temperature (T) with the Van-der-Waals equation of state. The phase transition happens at P_0 such that the dark grey (above) and light grey area (below) are equal

Between these two extrema (minimum and maximum point), the thermodynamic states are unstable. If the system is prepared at any of these intermediate states, it will spontaneously phase separate into liquid and gas phase [58]. As seen from the Fig.2, there is a range of pressures for which two different molar volumes V can be incorporated at the same value of P_b. In order to de-

termine which P_0 the system will relax and, accordingly, which molar volume values (V_{liq}, V_{gas}) the liquid and gas phases will assume, we need to apply the *Maxwell area construction rule*. According to *Maxwell area construction law*, for a given temperature T, the phase transition occurs at a pressure P_0 such that both shaded areas (dark and light grey) in Fig.2 are equal.

$$\int_{V_{gas}}^{V_{liq}} (P_0 - P_b(V^{'}, T))dV^{'} = 0 \tag{2.9}$$

For both the gas and the liquid molar quantities satisfy:

$$P_0 = P_b(V_{gas}, T) = P_b(V_{liq}, T) \tag{2.10}$$

2.1.4 Advanced equations of states (EOS)

In the above section, we demonstrate the coexistence of liquid-gas using *van der Waals equation of state*. However, no single state equation continues to exist that correctly predicts the behaviors of all substances under all circumstances. In literature, there are several types of EOS with their acceptable spectrum of applicability. The Van-der-Waals equation of state is the simplest on but is not ideal for a liquid-gas system with a temperature much below the critical or higher liquid-gas density ratio. Nor is the van der Waals equation capable of correctly estimating phase equilibrium. In literature there are more realistic forms of equations of states such as Redlich-Kwong, Peng-Robinson and Carnahan-Starling equations of state [145]. A brief background about these advanced equation of states is given below as these will be employed in the later study.

Redlich-Kwong equation of state

The changes in the Van-der-Waals equation of state was conducted by finding the analytical temperature dependency of the attraction parameter *a* in Eq.(2.8). The first notable successful change to the attraction parameter was made in 1949 by Otto Redlich and Joseph Neng Shun Kwong by introducing the following expression:

$$\left[P + \frac{a}{\sqrt{T}V_m(V_m + b)}\right](V_m - b) = RT \tag{2.11}$$

where, V_m is the molar volume (V/n) and similar to Van-der-Waals EOS a is a constant that corrects for attractive potential of molecules, and *b* is a constant that corrects for volume. However, Redlich-Kwong equation of state is generally more accurate than the van der Waals equation and the ideal gas equation at temperatures above the critical temperature. And the important concept here is that the attraction parameter a of van der Waals needed to be made a function of temperature to do a better job of quantitatively matching experimental data. In Redlich-Kwong EOS, a and b are expressed as a function of critical temperature(T_c) and critical pressure (P_c) as below:

$$a = 0.42780\frac{R^2T_c^{2.5}}{P_c}, \quad b = 0.08664\frac{RT_c}{P_c} \tag{2.12}$$

The constant values 0.42780 and 0.08664 is derived from the critical conditions such that the first and second isothermal derivatives of pressure with respect to volume are set equal to zero at the critical point as shown below [21] [100].

$$P = 1, \quad \left(\frac{\partial P}{\partial V}\right)_T = 0, \quad \left(\frac{\partial^2 P}{\partial^2 V}\right)_T = 0$$

Peng-Robinson equation of state

The Peng-Robinson equation of state (PR-EOS) was developed in 1976. The major improvements in the PR-EOS as compared to van-der-Waals EOS was that the equation parameters are expressible in terms of the critical properties and as compared to Redlich-Kwong equation of state it is generally superior in predicting the liquid densities of many materials, especially nonpolar ones by expressing it as a function of the acentric factor as shown in Eq.(2.13). The PR-EOS also provide a reasonable accuracy near the critical point, particularly for calculations of the compressibility factor and liquid density. The PR-EOS state has following form in terms of density and volume

.

$$P = \frac{\rho RT}{1 - b\rho} - \frac{a\alpha\rho^2}{1 + 2b\rho - b^2\rho^2} \tag{2.13}$$

$$P = \frac{nRT}{1 - \frac{nb}{V}} - \frac{a\alpha n^2}{\left(1 + \frac{2bn}{V} - \frac{b^2n^2}{V^2}\right) V^2} \tag{2.14}$$

Where, $\alpha = \left[1 + (0.37464 + 1.54226\omega + 0.26992\omega^2)\left(1 - \sqrt{\frac{T}{T_c}}\right)\right]^2$ and $\omega = 0.344$, $a = 2/49$, $b = 2/21$, $R = 1$ corresponding to water. The choice of the parameters corresponds to the critical temperature $T_c = 0.0729$ [145] [79].

According to PR-EOS, the mixing rules should not employ more than a single binary interaction parameter, which should be independent of temperature, pressure, and composition. The equation should be applicable to all calculations of all fluid properties in natural gas processes.

Carnahan-Starling equation of state

Guggenheim (1965) and Carnahan and Starling (1969) modified the repulsive term of van der Waals equation of state and obtained more accurate expressions for hard sphere systems. This modified EOS is know as Carnahan-Starling equation of state (CS-EOS) which has the following form in terms of density and volume .

$$P = \frac{\rho RT\left(1 + \frac{b\rho}{4} + (\frac{b\rho}{4})^2 + (\frac{b\rho}{4})^3\right)}{\left(1 - \frac{b\rho}{4}\right)^3} - a\rho^2 \tag{2.15}$$

$$P = \frac{nRT\left(1 + \frac{nb}{4V} + (\frac{nb}{4V})^2 - (\frac{nb}{4V})^3\right)}{\left(1 - \frac{nb}{4V}\right)^3 V} - \frac{an^2}{V^2} \tag{2.16}$$

where the constant a and b in above equation is expressed as critical parameters as shown below:

$$a = \frac{0.4963R^2T_c^2}{P_c}, \quad b = \frac{0.18727RT_c}{P_c} \tag{2.17}$$

Where, T_c is the critical temperature and P_c is the critical pressure. The constants values in above equation are derived by satisfying the conditions at the critical point (at $V = 1$ and $T = 1$) shown in section.2.1.4 [59]. The CS-EOS is different from the above cubic EOS in that it modifies the hard sphere term of the vdW EOS, while all of the other cubic EOS modify the attraction term of

the vdW EOS.

By carefully selecting the EOS, one may explicitly introduce temperature while also obtaining a coexistence curve that is extremely near to the theoretical prediction and is thermodynamically well defined. P.Yuan and L.Schaefer (2006) compared numerical simulation results in terms of density ratios, spurious currents, and temperature ranges by including alternative equations of states into the lattice Boltzmann model [145]. In chapter 3 and 4, we employ Carnahan-Starling equation of state to study the dynamics of ternary fluid systems in contact with solid boundaries. For drop collision study, we derived a double well potential for computational optimisation.

2.1.5 Surface Tension

The collective intermolecular forces (also known as cohesive forces) such as hydrogen bonding and van der Waals forces between liquid molecules are responsible for the phenomenon known as surface tension. To illustrate this fact, consider water in a tank as shown in Fig.3.

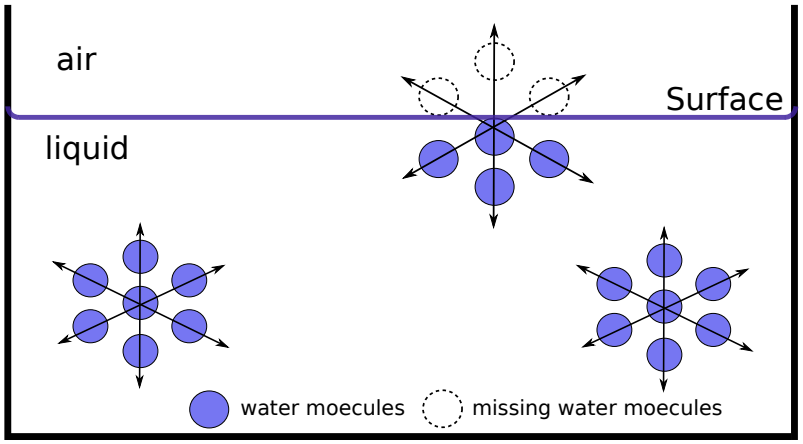

Figure 3: Representation of force balance between the water molecules in the bulk of the liquid with respect to at the surface, which gives rise to surface tension.

The molecules shown in the midst of the liquid benefits from the interaction with all the neighbours and experience zero net force. On the other hand, molecules that wander to the surface lose half of its cohesive interaction and experience an imbalance of collective intermolecular forces. If U is the coherent energy per molecule within the liquid, a molecule lying on the surface has less than about half of that energy (U/2). Surface tension is a direct measure of this energy deficit per unit area.

Surface tension in terms of Gibbs energy:

Gibbs free energy defined in Eq.(2.2) in the presence of flat interfaces can be written as:

$$dG = -SdT + VdP + \sum_i \mu_i dN_i + \gamma dA \tag{2.18}$$

With the help of above equation it is also possible to give a definition of the surface tension. It can be expressed as the increase in Gibbs free energy (G) that accompanies an increase in the surface area at constant total volume (V), temperature (T) and number of molecules (n).

$$\gamma = \left[\frac{dG}{dA}\right]_{T,V,n} \tag{2.19}$$

Surface tension in terms of mechanical energy:

Surface tension can also be looked as a mechanical quantity, to demonstrate that consider we want to distort a liquid to increase its surface area by an amount ΔA. The work required is proportional to the number of molecules that must be bought up to the surface such that:

$$dW = \gamma.dA \tag{2.20}$$

where, γ is the surface tension and can described as the energy that must be supplied to increase the surface tension by one unit. Dimensionally γ is expressed as mJ/m^2 or dyne/cm.

2.1.6 Laplace Law

Consider a single spherical liquid droplet of radius r is surrounding by air. The surface tension of the liquid-gas interface is represented by γ. From the principle of surface tension acting as a contractile membrane, it follows automatically that there must be a difference in pressure $\Delta P = P_{in} - P_{out}$ between the liquid contained in a droplet and the ambient material. In Fig.4, the distribution of surface tension along a meridian circle of a spherical droplet is shown.

For mechanical equilibrium the force resulting from the surface tension should be equivalent to

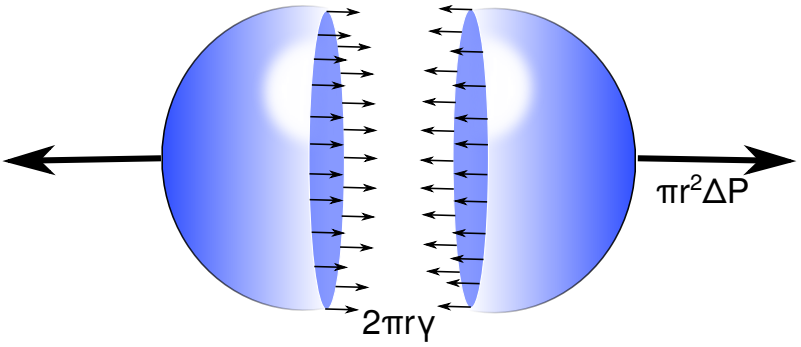

Figure 4: The force balance resulting from the surface tension ($2\pi r\gamma$) along a meridian circle of the droplet and the one from the pressure difference ($\pi r^2 \Delta P$) between the liquid and surrounding gas.

the one from the pressure difference between the liquid and the surrounding vapor. So

$$2\pi r\gamma = \pi r^2 \Delta P, \quad or \quad \Delta P = \frac{2\gamma}{r} \tag{2.21}$$

This relation is a special case of the well-known fundamental equation called *Young and Laplace* as shown below:

$$\Delta P = \gamma \left(\frac{1}{r_1} + \frac{1}{r_2} \right) \tag{2.22}$$

where the expression in parenthesis is a geometry factor representing the two principal radii of curvature (r_1, r_2). For an arbitrary, smooth surfaces and curves, the curvature at any point may be defined by assigning two radii of curvature, (r_1 and r_2 here), in two normal planes that cut the interface along two principal curvature sections. These two normal planes are also normal to each other and their line of intersection is the surface normal at the chosen point [113].

2.1.7 Ternary fluid system

So far, we have discussed the basics of liquid/gas (binary) system which makes the fundamental of multiphase multicomponent fluid systems. In this section emphasis is given on liquid-liquid-gas (ternary) fluid systems. The most common morphologies of ternary fluid systems are *"Double emulsion"* and *"Liquid lens"*. One of these two is the equilibrium form obtained by ternary fluid systems , which relies on the properties of the fluids. The key features of these two morphologies are discussed below:

Double emulsion

Double emulsion also know as "compound droplets" is a special type of mixture made by combining two liquids that normally don't mix. Few examples of double emulsion morphologies are shown in Fig.5 to Fig.7. These morphologies depends upon the combination of the surface tensions between each interface. As sketched in Fig.5, consider three fluids ($fluid_1$, $fluid_2$, $fluid_3$). The fluids are formulated in such as way that there exists three interfaces. The surface tension representing the interface between $fluid_1$ and $fluid_2$ is γ_{12}, between $fluid_1$ and $fluid_3$ is γ_{13} and $fluid_2$ and $fluid_3$ is γ_{23}.

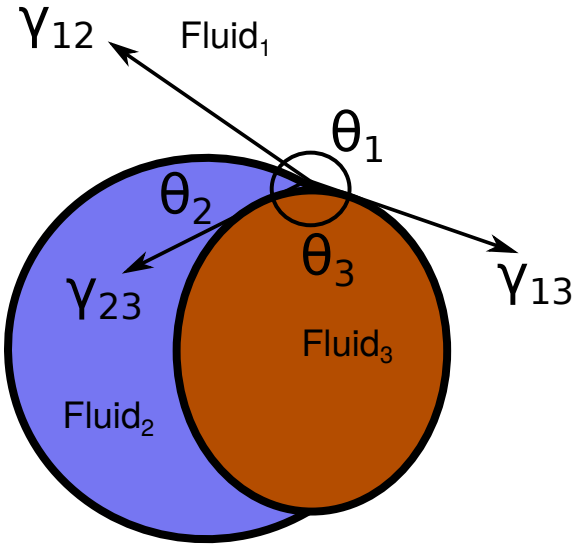

Figure 5: Representation of non symmetric double emulsion and corresponding three interfacial tensions, Neumann angles at the triple point.

The point of contact at which the three interfaces meet is called triple point. The balance of forces acting on the three-phase contact line can be expressed in the form of relations (also known as the Neumann triangle) between the contact angles and the interfacial tensions [37], [144], [6] :

$$\gamma_{23}\cos\theta_3 + \gamma_{13} + \gamma_{12}\cos(\theta_2+\theta_3) = 0 \tag{2.23}$$

$$\gamma_{23}\cos\theta_2 + \gamma_{12} + \gamma_{13}\cos(\theta_2+\theta_3) = 0 \tag{2.24}$$

In the double emulsion configuration one can solve Eq.(2.23) and Eq.(2.24) with respect to $\cos\theta_1$,

$\cos\theta_2$, $\cos\theta_3$ as expressed below with the constrain θ_1 + θ_2 + θ_3 =360°

$$Fluid_1 \quad \cos\theta_1 = \frac{\gamma_{23}^2 - \gamma_{12}^2 - \gamma_{13}^2}{2\gamma_{12}\gamma_{13}}, \tag{2.25}$$

$$Fluid_2 \quad \cos\theta_2 = \frac{\gamma_{13}^2 - \gamma_{12}^2 - \gamma_{23}^2}{2\gamma_{12}\gamma_{13}}, \tag{2.26}$$

$$Fluid_3 \quad \cos\theta_3 = \frac{\gamma_{12}^2 - \gamma_{13}^2 - \gamma_{23}^2}{2\gamma_{12}\gamma_{13}}, \tag{2.27}$$

One can also define the spreading parameter of each fluid as a function of surface tension combination as below:

$$Fluid_1 \quad S_1 = \gamma_{23} - \gamma_{12} - \gamma_{13}, \tag{2.28}$$

$$Fluid_2 \quad S_2 = \gamma_{13} - \gamma_{12} - \gamma_{23}, \tag{2.29}$$

$$Fluid_3 \quad S_3 = \gamma_{12} - \gamma_{13} - \gamma_{23}, \tag{2.30}$$

A special case of the above scenario is when the tension between $fluid_1/fluid_2$ and $fluid_1/fluid_3$ is identical such that γ_{12}=γ_{23} , θ_2=θ_3 and S_2=S_3 as shown in Fig.6.

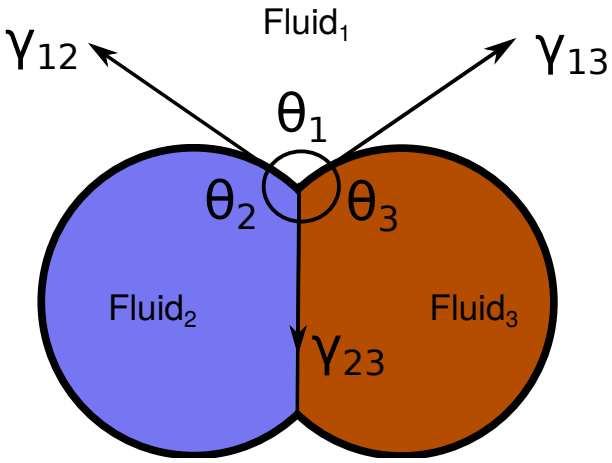

Figure 6: Representation of symmetric double emulsion and corresponding three interfacial tensions, Neumann angles at the triple point.

Another example of double emulsion morphology shown in Fig.7, is when $Fluid_3$ is entirely encapsulated by $Fluid_2$. The surface tension combination in this case is such that the spreading parameter of $fluid_2$ is of interest. The spreading parameter compares the energy cost per unit area for the formation of an interface between $Fluid_2$ and $Fluid_1$ or having a layer of $Fluid_2$ in between. If the spreading parameter S_2 is positive, then $Fluid_2$ spontaneously spreads and encapsulates the drop of $Fluid_3$. Liquids can be found in an encapsulated morphology also when $S_2 < 0$, but if the interfaces come close, the system gains energy by forming three finite angles called Neumann angles, univocally determined by the combination of surface tensions. The specific values of Neumann angles satisfy the balance between surface forces, corresponding to a state of local minimum of the free energy. A temporarily out of equilibrium system dynamically converges to a local equilibrium, and the excess of free energy is dissipated according to the second law of thermodynamics.

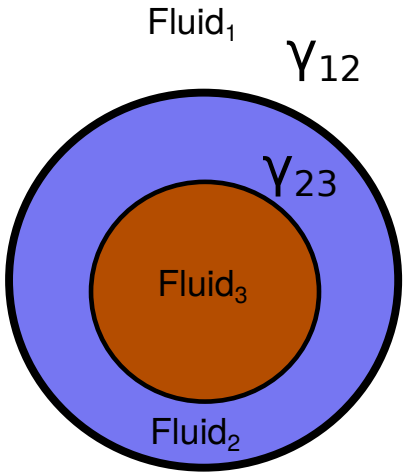

Figure 7: Representation of non-symmetric double emulsion when one fluid encapsulate the another one.

Liquid lens

The spreading of liquids on other immiscible liquids bath is another example of ternary fluid systems. For the same ternary fluid system defined above that is $Fluid_1$, $Fluid_2$, $Fluid_3$, spontaneous spreading is expected for $S_2 > 0$ and for $S_2 < 0$, one expects the formation of a stable lens-shaped drop of $Fluid_2$ on the surface of $Fluid_3$ as sketched in Fig.8.

The forces resulting from the surface tension and acting per unit length along the three-phase line. The mechanical equilibrium between these forces occurs which is represented by the three

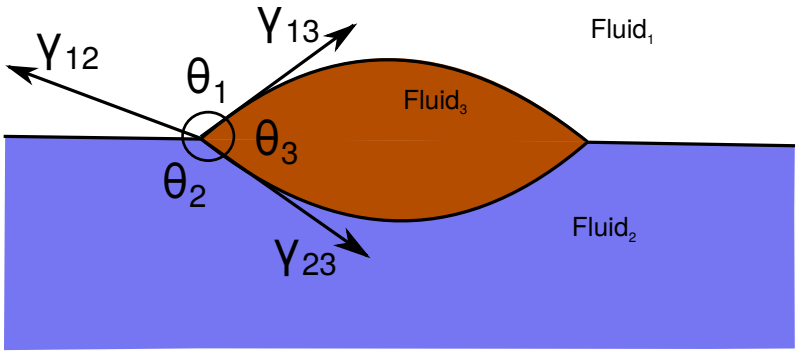

Figure 8: Representation of liquid lens morphology and corresponding three interfacial tensions, Neumann angles at the triple point.

Neumann angles formed at the triple point made by three interfaces [24], [37], [109].

2.2 Interaction with surfaces

2.2.1 Spreading on solid substrate

In Fig.9, consider a liquid is in contact with solid surface and is surrounded by gas. The interfacial tension between the solid-gas, liquid-solid and liquid-gas is represented by γ_{sg}, γ_{ls} and γ_{lg} respectively. In order for the liquid droplet to completely spread over the solid surface as shown in Fig.9, the interfacial tension between the solid and gas γ_{sg} must be greater than the sum of other two i.e γ_{sl} + γ_{lg}. This leads to the *spreading coefficient* as defined below:

$$S = \gamma_{sg} - \gamma_{lg} - \gamma_{ls} \tag{2.31}$$

The spreading of the liquid is preferred at positive spreading parameter $(S \geq 0)$. In this case, the system is solely guided by the surface or interfacial forces and presumed to be ideal, i.e completely smooth.

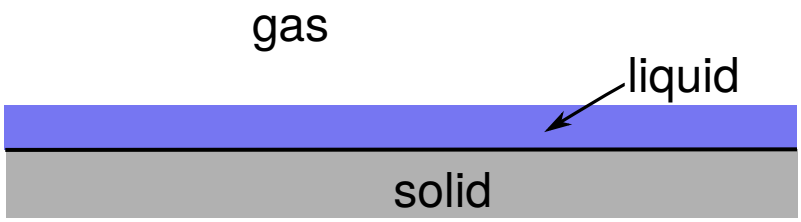

Figure 9: An ideal surfaces covered by a liquid layer.

2.2.2 Young's Angle

If a drop is placed on a solid surface, such that the spreading coefficient of the droplet is negative and droplet forms a wedge like shape (partial wetting). At the common point of contact, the interaction between all three interfacial tensions creates a characteristic equilibrium contact angle θ_e shown in Fig10.

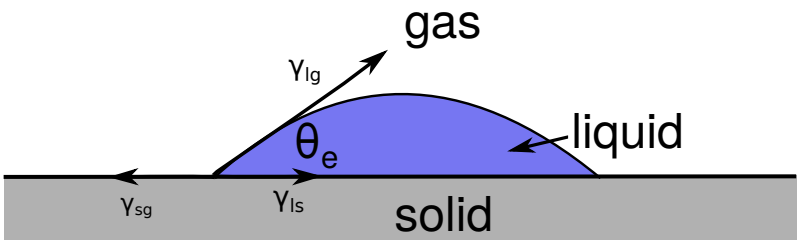

Figure 10: Liquid droplet on solid surface with equilibrium contact angle θ_e.

This contact angles that exist at the boundary between the three phases vapour, liquid and solid depend on the physical and chemical properties of each of them. For the setup above, by making a balance between the horizontal components of the force acting per unit length along the three phase line, the Young's equation is derived as shown in Eq.(2.33).

$$\gamma_{sg} = \gamma_{ls} + \gamma_{lg} \cos\theta_e \tag{2.32}$$

$$\cos\theta_e = \frac{\gamma_{sg} - \gamma_{ls}}{\gamma_{lg}} \tag{2.33}$$

combining the Eq.(2.31) and Eq.(2.33), *Young-Dupre Law* is deduced which has the following form:

$$S = \gamma_{lg}(\cos\theta_e - 1) \tag{2.34}$$

Eq.(2.34) shows that the equilibrium contact angle θ_e and the interfacial tension between liquid and gas can determine the degree of spread of liquid on top of solid surface. Which is broadly classified into four sets: *Perfect wetting* ($\theta_e = 0°$), *High wettability* ($0° < \theta_e < 90°$), *Low wettability* ($90° \leq \theta_e < 180°$), *Non-wetting*($\theta_e = 180°$) .

2.2.3 Contact Angle Hysteresis

The equilibrium contact angle θ_e defined by Young's Law in Eq.(2.33) describes the force balance on clean, homogeneous solid surfaces. But in reality most of the surfaces exhibit chemical or geometrical heterogeneity. Observed contact angle on such non ideal surfaces is not a unique value but varies within two limits $\theta_R < \theta < \theta_A$, where (θ_A) is *Advancing contact angle* and (θ_R) is *Receding contact angle*. Let us imagine an experiment where liquid can be added or withdrawn from a drop at rest and a non ideal flat substrate. This could be obtained by operating on the drop with a needle, or through condensation/evaporation of a volatile liquid. The angle θ_A (advancing contact angle) is measured when the liquid/solid contact area increases as shown in Fig.11(a), while θ_R (receding contact angle) is measured when the contact area shrinks as in Fig.11(b).

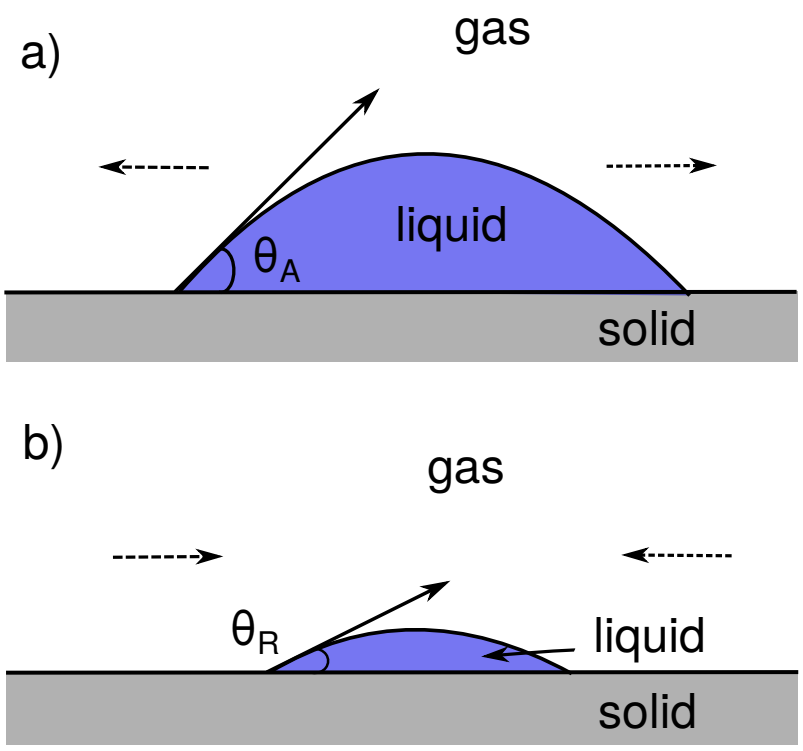

Figure 11: a) advancing contact angle when droplet and solid surface area increases b) the receding contact angle when the droplet and solid surface area decreases.

The contact angle hysteresis (CAH), is then defined in Eq.(2.35) as the difference between these limiting angles [24]. In literature, there are many techniques to measure the CAH and measurement methods can be divided into optical (needle and tilting methods) [115] [93] and force (Wil-

helmy method) [124] depending on the measurement principle used.

$$CAH = \theta_A - \theta_R \tag{2.35}$$

Contact angle hysteresis arises when several different thermodynamically stable contact angles are identified on a non-ideal surface. These changing thermodynamically stable contact angles defined as metastable states for liquid morphologies. This emphasizes that the contact angle is selected at the molecular scale, and it therefore acts as a boundary condition for the macroscopic interface [116] [117]. The motion of this phase boundary, involving advancing and receding contact angles, is known as dynamic wetting. The difference between dynamic and static wetting angles is proportional to the capillary number (Ca), which describe the relative importance of viscous drag forces versus surface tension forces at the interface between a liquid and a gas.

A consequence of Young's equilibrium is that a drop on a solid surface, or a column of liquid in a thin capillary, should move even with the slightest external force. However, a contact line is pinned, so when one tries to move a drop or a liquid column, Eq.(2.32) is violated. In 1984, Joanny and de Gennes [50] observed that apart from the surface heterogeneities that could cause contact angle hysteresis, its fundamental origin is embedded in the most basic definition of the Gibbsian surface thermodynamics: *Work must be spent when creating new surface*

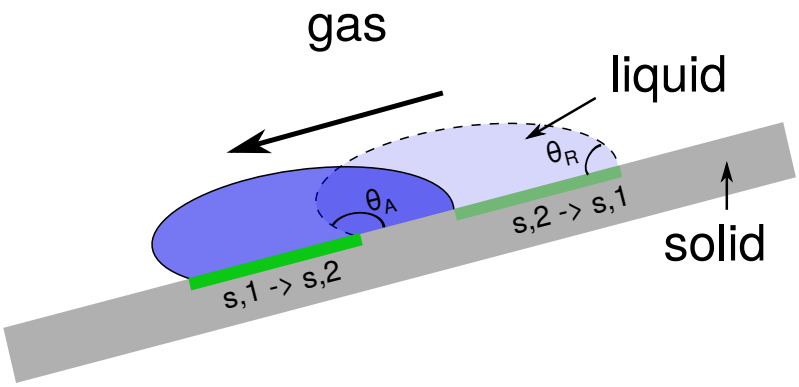

Figure 12: Sliding of a drop which creates a new interface, the solid-gas(S,1) interface disappears and a solid-water(S,2) interface forms at the advancing contact line. Correspondingly, the solid-water(S,2) interface disappears and a solid-gas(S,1) is formed at the receding contact line.

In Fig.12, it is shown that when a three-phase contact recedes along the solid surface, a new solid surface is created behind the contact line. Correspondingly, when a contact line advances, a new solid-water interface is created behind it [75]. The work done (dW) to create a new surface,

following the force (F) definition has the following form:

$$F = \frac{dW}{dx} = \gamma \frac{dA}{dx} = \gamma w \tag{2.36}$$

When the contact line on the left side of Fig.12 is forced to advance to the left, thus creating a new solid-liquid interface, the frictional tension that resists the motion equals γ_{S2}. At advancing and receding, when applying the force balance including the frictional tension in addition to the tensions that exist already in the static equilibrium, following expression are deduced:

$$\begin{aligned} Advancing \quad & \gamma_{s2} = \gamma_{s1} \left(\cos\theta_e - \cos\theta_A\right) \\ Receding \quad & \gamma_{s2} = \gamma_{s1} \left(\cos\theta_R - \cos\theta_e\right) \end{aligned} \tag{2.37}$$

In the above equation, the frictional terms on the left side of both advancing and receding angles can be interpreted by the conventional concept of the work of wetting.

2.2.4 Wetting on non-ideal textured surfaces

A well known deviation from ideal smooth surface is where the surface of interest has a rough texture. In general there are two type of surface roughness: *homogeneous* and *heterogeneous*. The *homogeneous* wetting regime occurs when only topographic structures are present, but the solid is chemically homogeneous. The *heterogeneous* occurs when the chemical properties of the surface differ from place to place. These can arise naturally as for the topographic roughness, or can be produced by coating a surface with specifically designed patterns. An significant example of such a hybrid surface is one made up of both air and strong patches. Two main models that attempt to describe the wetting of textured surfaces are *Wenzel model* and *Cassie–Baxter model*. However, these models only apply when the drop size is sufficiently large compared with the surface roughness scale [76].

Wenzel Model:

The most common model that describes the homogeneous wetting regime was developed in 1936 by Robert N. Wenzel. Now it is universally known as *Wenzel model*, according to which when the liquid is in intimate contact with a microstructured homogeneous surface and is fully wet and penetrate the structure, contacting the pillar bases as shown in Fig.13. The equilibrium contact angle (θ_e) determined by Young's equation will change to θ_W as below:

$$\cos\theta_W = r\cos\theta_e \tag{2.38}$$

where θ_e is the equilibrium contact angle on ideal surface. The roughness ratio, r, is a measure of how surface roughness affects a homogeneous surface. The roughness ratio is defined as the ratio of true area of the solid surface to the apparent area.

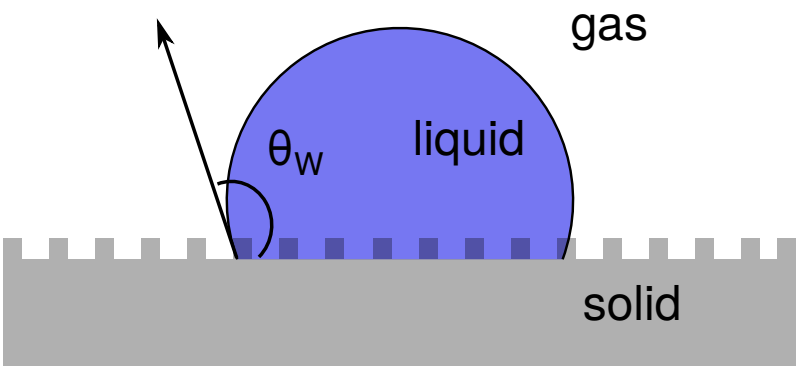

Figure 13: Contact angle on rough surface a) Wenzel state b) Cassie - Baxter state.

Cassie-Baxter Model:

The apparent contact angle on the heterogeneous surfaces can be described in 1940's by the *The Cassie–Baxter model*. In the example shown in Fig.14, where the liquid is suspended over the surface topography, leaving an air cushion underneath. The combination of liquid-gas and liquid solid portions of interface is therefore interpreted as a heterogeneous substrate formed by solid patches on a continuous matrix.

The apparent contact angle is described by Cassie-Baxter Model has the following form:

$$\cos\theta_{CB} = r_f f\cos\theta_e + f - 1 \tag{2.39}$$

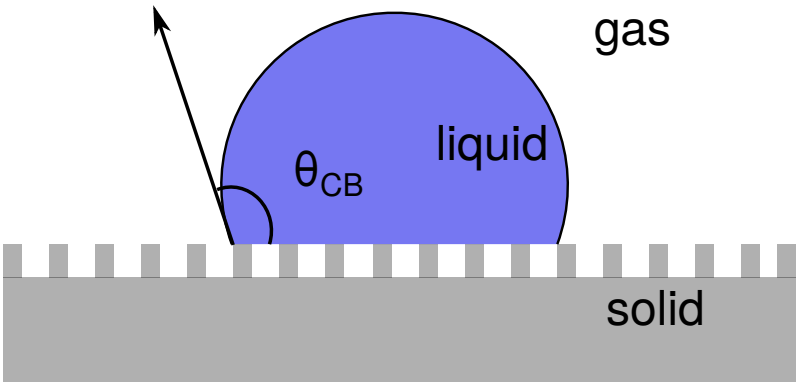

Figure 14: Contact angle on rough surface a) Wenzel state b) Cassie - Baxter state.

Here the r_f is the roughness ratio of the wet surface area and f is the fraction of solid surface area wet by the liquid. It is important to realize that when $f = 1$ and r_f = r, the Cassie–Baxter equations becomes the Wenzel equation.

Although both Wenzel's and Cassie-Baxter equations demonstrates the contact angle of a rough surface is different from the intrinsic contact angle, they do not account for contact angle hysteresis. This is due to implicit assumption that the surface fractions parameters entering the equations represent a global thermodynamic minimum. In reality the contact line can be pinned at the patch edges trapping the system in one of the possible metastable state.

2.2.5 Dynamic wetting

When a liquid drop comes in contact with a solid, it directly start spreading unless it is on hydrophobic surface. Consider Fig.15(a), where a droplet of initial radius R that is placed on a flat solid surface. The liquid has a surface tension γ, dynamic viscosity μ and density ρ. The contact line moves radially outward from the contact point during the spread and the drop wets a circular area of radius r(t). For the late times of spreading, the drop assumes the shape of a spherical cap Fig.15(b) [28]. The dynamics is regulated by viscous effects near the contact line and characterized an apparent (dynamic) contact angle. When the substrate is fully wet, the so-called *Tanner's law* [123] describes this phenomenon such that:

$$\frac{r}{R} = \left(\frac{\gamma t}{\mu R}\right)^{1/10} \tag{2.40}$$

The *Tanner's law* describe the late-time actions of spreading viscous drops, it does not apply in

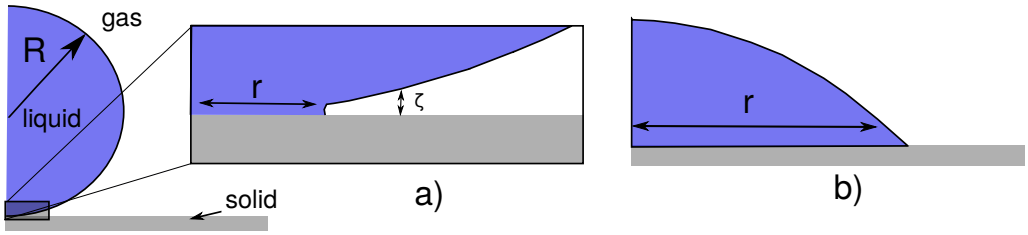

Figure 15: Representation of the geometry of the drop during spreading at a) early stage (b) late stages (*Tanner's law*)

short periods of time. During the short time period the geometry of the drop is entirely different Fig.15(a). Right after touching, the drop shape is strongly curved near to the contact point, with a meniscus characterised by a short thickness ζ as indicated in Fig.15(a). This strongly curved meniscus produces a fast flow within the drop. The size of the meniscus decrease as r decrease ($\zeta \sim 0$ as r ~ 0) inducing diverging capillary stresses [11].

If we use the problem formulation presented by *Tanner law*, the relationship for a complete spreading case can be easily derived based on a force balance between the capillary and the viscous force. On the other hand, If we consider a droplet which has a shape of wedge as shown in Fig.16 at the contact line. Two representations of the contact point is shown in the sketch where Fig.16(a) shows the microscopic scale (θ_m) and the apparent dynamic (θ) contact angle and Fig.16(b) shows the molecular motion at the contact line. where k_0 is the characteristic jump frequency, λ the length between adsorption sites and θ the dynamic contact angle.

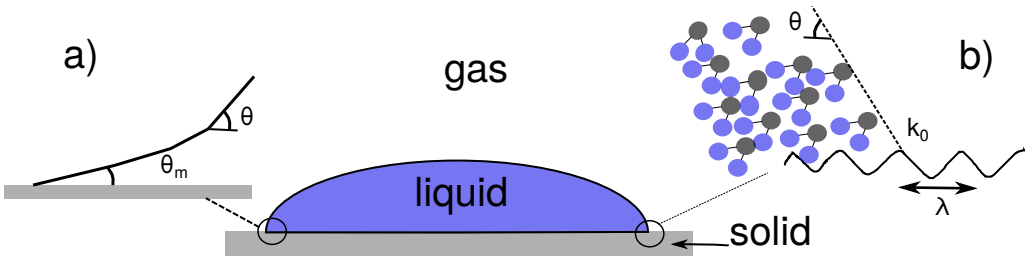

Figure 16: Spreading of droplet on solid substrate shows the interpretation of a) microscopic (θ_m) and the apparent dynamic (θ) contact angle b) molecular motion at the contact line

At the contact line in Fig.16, the viscous dissipation can be equated and balanced by capillarity [16] such that:

$$\theta = \left[log\left(\frac{L}{L_m}\right) \frac{\mu U}{\gamma} \right]^{1/3} \tag{2.41}$$

In Eq.(2.41), θ is the apparent contact angle and U the spreading speed. L and L_m are length scales for the macroscopic and microscopic length, respectively. The microscopic length L_m is assumed to be the height of the precursor film (a thin film of macroscopic lateral extent) ahead of the drop [95]. While this length is frequently found to be much greater than what can be physically argued, it can be interpreted as the slip length at the contact line. For a spherical cap shaped drop with $\theta << 1$, the apparent contact angle relates to the spreading radius, r, in the manner $\theta \sim 4V/r^3$. After placing this relationship into Eq.(2.41) at U = dr/dt and integrating, one arrive at the Eq.(2.40).

2.3 Fluid dynamics

Fluid dynamics describes the motion of fluids and how external forces affect them. At mesoscopic and macroscopic scales, the fluids are conveniently described by continuous fields such as density, concentration and flow field. The motion of fluid substances are describe by these set of equations describing the *conservation of mass conservation of momentum* and *conservation of energy*. In the following sections a brief overview these fundamental equations are discussed.

2.3.1 Continuity equation

Consider a fluid element wit density ρ and has a some fixed volume V_0. The total mass of the fluid element will be $\int_{V_0} \rho dV$. Any change of the mass per unit time due to fluid flow into or out of the volume element will be :

$$\frac{\partial}{\partial t}\int_{V_0} \rho dV = -\oint_{\partial V_0} \rho \mathbf{u} \cdot d\mathbf{A} \tag{2.42}$$

where the closed area integral is taken over the boundary ∂V_0 of the volume element V_0, $\mathbf{u}$ is the fluid velocity, and we take the outward normal as the direction of dA. The surface integral on the right-hand side of Eq.(2.42) can be transformed into a volume integral using the divergence theorem to give:

$$\int_{V_0} \frac{\partial \rho}{\partial t} dV = -\int_{V_0} \nabla \cdot (\rho \mathbf{u}) dV \tag{2.43}$$

which leads to the below continuity equation in fluid dynamics. The continuity equation is a partial differential equation (PDE) reflecting the conservation of mass [58] [1].

$$\frac{\partial \rho}{\partial t} + \nabla \cdot (\rho \mathbf{u}) = 0 \tag{2.44}$$

2.3.2 Navier-Stokes equation

The change of momentum of a fluid element with density ρ and velocity u, occupying a small volume V_0. For a simple ideal fluid, the change of net momentum can be due to (i) flow of momentum into or out of the fluid element, (ii) differences in pressure p and (iii) external body forces F. Each of these contributions is written respectively on the right-hand side of the following momentum balance equation

$$\frac{d}{dt}\int_{V_0} \rho \mathbf{u} dV = -\oint_{\partial V_0} \rho \mathbf{u} \otimes \mathbf{u} \cdot d\mathbf{A} - \oint_{\partial V_0} P d\mathbf{A} + \int_{V_0} \mathbf{F} dV \tag{2.45}$$

Here, $\mathbf{u} \otimes \mathbf{u}$ is a dyad, a special case of tensor product, which results in a second rank tensor; the divergence of a second rank tensor is again a vector (a first-rank tensor) [65]. Transforming the surface integrals into volume integrals using the divergence theorem, the above equation can be rewritten as

$$\int_{V_0} \frac{\partial(\rho \mathbf{u})}{\partial t} dV = -\int_{V_0} \nabla \cdot (\rho \mathbf{u} \otimes \mathbf{u}) dV - \int_{V_0} \nabla P dV + \int_{V_0} \mathbf{F} dV \tag{2.46}$$

Above equation leads to Euler equation which conservation of momentum for an ideal fluid.

$$\frac{\partial(\rho \mathbf{u})}{\partial t} + \nabla \cdot (\rho \mathbf{u} \otimes \mathbf{u}) = -\nabla P + \mathbf{F} \tag{2.47}$$

or

$$\mathbf{u}\frac{\partial \rho}{\partial t} + \rho \frac{\partial \mathbf{u}}{\partial t} + \mathbf{u} \otimes \mathbf{u} \cdot \nabla \rho + \rho \nabla \cdot (\mathbf{u} \otimes \mathbf{u}) = -\nabla P + \mathbf{F}$$

After placing $\nabla \cdot (\mathbf{u} \otimes \mathbf{u}) = (\nabla \cdot \mathbf{u})\mathbf{u} + \mathbf{u} \cdot \nabla \mathbf{u}$, we get the following form of the equation

[58]:

$$\mathbf{u}\frac{\partial \rho}{\partial t} + \rho\frac{\partial \mathbf{u}}{\partial t} + \mathbf{u} \otimes \mathbf{u} \cdot \nabla\rho + \rho\mathbf{u} \cdot \nabla\mathbf{u} + \rho\mathbf{u}\nabla \cdot \mathbf{u} = -\nabla P + \mathbf{F} \tag{2.48}$$

The dyadic product of two vectors such as $\mathbf{u} \otimes \mathbf{u}$ is also denoted by $\mathbf{uu}$, which leads to following form of equation [65]:

$$\mathbf{u}\left(\frac{\partial \rho}{\partial t} + \mathbf{u} \cdot \nabla\rho + \rho\nabla \cdot \mathbf{u}\right) + \rho\left(\frac{\partial \mathbf{u}}{\partial t} + \mathbf{u} \cdot \nabla\mathbf{u}\right) = -\nabla P + \mathbf{F} \tag{2.49}$$

$$\mathbf{u}\left(\frac{\partial \rho}{\partial t} + \nabla \cdot (\rho\mathbf{u})\right) + \rho\left(\frac{\partial \mathbf{u}}{\partial t} + \mathbf{u} \cdot \nabla\mathbf{u}\right) = -\nabla P + \mathbf{F} \tag{2.50}$$

The leftmost expression enclosed in parentheses is, by mass continuity (shown in Eq.(3.40)), equal to zero. Noting that what remains on the left side of the equation is the material derivative of flow velocity:

$$\rho\frac{D\mathbf{u}}{Dt} = -\nabla P + \mathbf{F} \tag{2.51}$$

This appears to simply be an expression of Newton's second law ($F = ma$) in terms of body forces instead of point forces. A shorter though less rigorous way to arrive at this result would be the application of the chain rule to acceleration:

$$\begin{aligned}\rho\frac{d}{dt}\left(\mathbf{u}(\mathbf{x}, \mathbf{y}, \mathbf{z}, \mathbf{t})\right) = \rho\left(\frac{\partial \mathbf{u}}{\partial t} + \frac{\partial \mathbf{u}}{\partial x}\frac{dx}{dt} + \frac{\partial \mathbf{u}}{\partial y}\frac{dy}{dt} + \frac{\partial \mathbf{u}}{\partial z}\frac{dz}{dt}\right) &= \rho\left(\frac{\partial \mathbf{u}}{\partial t} + u\frac{\partial \mathbf{u}}{\partial x} + v\frac{\partial \mathbf{u}}{\partial y} + w\frac{\partial \mathbf{u}}{\partial z}\right) \\ &= \rho\left(\frac{\partial \mathbf{u}}{\partial t} + \mathbf{u} \cdot \nabla\mathbf{u}\right) = -\nabla P + \mathbf{F}\end{aligned}$$

where $\mathbf{u} = (u, v, w)$.

2.3.3 Energy Dissipation

Fluid flow and its shape deformation requires energy. This energy is dissipated during the flow and converted into its internal energy. In the viscous fluid flow the viscosity of the fluid will take energy from the motion of the fluid (kinetic energy) and transform it into heat. Viscous dissipation for fluid with suspended particles and in pure Newtonian flows are equivalent [140]. To deform a shape and to change the volume of a element of fluid, the rate of work done is defined as:

$$\sigma : \nabla V = \underbrace{-p\nabla.v}_{\text{rate of work for volume change}} + \overbrace{\underbrace{\tau : \nabla v}_{\text{rate of work for shape change}}}^{\text{Dissipation function}} \tag{2.52}$$

Where the first term on the right hand side of the Eq.(2.52) corresponds to the rate of work done to change the volume of the fluid at keeping the shape fixed. The second term on the right hand side is the rate of work for shape change at constant volume and is called *Dissipation function*.

$$\phi = \tau : \nabla v \tag{2.53}$$

The component form of the *Dissipation function* in the Cartesian ordinates looks like below:

$$\begin{aligned} \tau : \nabla V = 2\mu \left[\left(\frac{\partial v_x}{\partial x} \right)^2 + \left(\frac{\partial v_y}{\partial y} \right)^2 + \left(\frac{\partial v_z}{\partial z} \right)^2 - \frac{1}{3} (\nabla . v)^2 \right] \\ + \mu \left[\frac{\partial v_y}{\partial x} + \frac{\partial v_x}{\partial y} \right]^2 + \mu \left[\frac{\partial v_z}{\partial y} + \frac{\partial v_y}{\partial z} \right]^2 + \mu \left[\frac{\partial v_x}{\partial z} + \frac{\partial v_z}{\partial x} \right]^2 \end{aligned} \tag{2.54}$$

where, $\nabla \cdot \mathbf{V} = \frac{\partial v_x}{\partial x} + \frac{\partial v_y}{\partial y} + \frac{\partial v_z}{\partial z}$. In left hand side of Eq.(2.52),, the σ denotes the stress which is the combination of pressure p, and extra stress τ as shown in Eq.(2.55) and $\nabla \cdot \mathbf{V}$ and $\nabla \mathbf{V}$ are the divergence of velocity vector and gradient of velocity.

$$\sigma = -pI + \tau \tag{2.55}$$

Eq.(2.54) provides evidence that viscous heating can be considered as the sum of two terms:

- The rate of viscous dissipation due to the contribution of the density variation.

- The rate of viscous dissipation for an incompressible fluid.

2.3.4 Dimensionless numbers

The dimensionless numbers more commonly used in flow assurance as in multiphase flow and fluid interfaces. Dimensionless numbers reduce the number of variables that describe a system, thereby reducing the amount of experimental data required to make correlations of physical phenomena to scalable systems. The dimensionless numbers are very useful. Specially the fact that the fluid flows which share the same dimensionless numbers provide the same physics upon a simple scaling by the typical length and velocity scales in the problem. This important statement is called the *law of similarity*. The most useful dimensionless number in the context of this work are listed below:

- **Reynolds number:** It describes the predominance of inertial forces to viscous forces occurring in the fluid flow.

$$Re = \frac{\rho u L}{\mu} = \frac{vL}{\nu} = \frac{\text{Inertial forces}}{\text{Viscous forces}} \tag{2.56}$$

  ρ is the density of the fluid (SI units: kg/m^3), u is the flow speed (m/s), L is a characteristic linear dimension (m), μ is the dynamic viscosity of the fluid (Pas or Ns/m^2 or $kg/(ms)$), ν is the kinematic viscosity of the fluid (m^2/s). Re number has applications in predicting the incompressible flow of fluid in pipe lines, motion of submarine completely under water.

- **Weber number:** It shows the importance of inertial forces to surface tension forces.

$$We = \frac{\rho u^2 L}{\gamma} = \frac{\text{Inertial forces}}{\text{Surface tension}} \tag{2.57}$$

  where, γ is the surface tension and when $We < 1$, the surface tension is predominant. This happens when the curvature of the liquid droplet is smaller compared to its depth. We number is significant in many of applications such as blood flow in veins and arteries, liquid amortisation, capillary flow of water in soil and thin layer of fluid on surface.

- **Ohnesorge number:** Oh is a dimensionless number that relates the viscous forces to inertial

and surface tension forces.

$$Oh = \frac{\sqrt{We}}{Re} = \frac{\mu}{\sqrt{\rho\gamma L}} = \frac{\text{Viscous forces}}{\sqrt{\text{(Inertial forces) (Surface tension)}}} \tag{2.58}$$

This is often used to relate to free surface fluid dynamics such as dispersion of liquids in gases and in spray technology and inkjet printing.

- **Mach number:** is a dimensionless quantity in fluid dynamics representing the ratio of flow velocity past a boundary to the local speed of sound

$$Ma = \frac{u}{c} = \frac{\text{Compressible fluid velocity}}{\text{Speed of sound in compressible fluid}} \tag{2.59}$$

where, u is fluid velocity and c is speed of sound. At Mach 1, the local flow velocity u is equal to the speed of sound. Pilots of high-altitude aerospace vehicles use flight Mach number to express a vehicle's true airspeed

- **Knudsen number:** it defines the ratio between the mean free path and the representative physical length scale

$$Kn = \frac{l_{mfp}}{l} = \frac{\text{Mean free path}}{\text{Physical length scale}} = \alpha\frac{Ma}{Re} \tag{2.60}$$

where α is a numerical constant. At $\mathsf{Kn} << 1$, the hydrodynamic picture (Navier-Stokes) is valid, whereas for $\mathsf{Kn} >> 1$, kinetic theory is applicable.

- **Capillary number:** it is a dimensionless quantity representing the relative effect of viscous drag forces versus surface tension forces acting across an interface between a liquid and a gas, or between two immiscible liquids. The capillary number plays a role in the dynamics of capillary flow; in particular, it governs the dynamic contact angle of a flowing droplet at an interface and has the following form:

$$Ca = \frac{\text{Viscous drag force}}{\text{Surface tension forces}} = \frac{\mu V}{\gamma} \tag{2.61}$$

where μ is the dynamic viscosity of the liquid, V is a characteristic velocity and γ is the

surface tension or interfacial tension between the two fluid phases. For low capillary numbers (less than 10^{-5}), flow in porous media is dominated by capillary forces, whereas for high capillary numbers the capillary forces are negligible compared to the viscous forces. Flow through the pores in an oil field reservoir have capillary number on the order of 10^{-6} whereas flow of oil through an oil well drill pipe has a capillary number on the order of 1.

- **Froude number:** is a dimensionless number defined as the ratio of the flow inertia to the external field (the latter in many applications simply due to gravity). Named after *William Froude*, the Froude number is based on the speed–length ratio which he defined as:

$$Fr = \frac{\text{Flow inertia}}{\text{External field}} = \frac{u}{\sqrt{gL}} \tag{2.62}$$

where u is the local flow velocity, g is the local external field, and L is a characteristic length. The Froude Number is relevant in fluid dynamic problems where the weight (gravitational force) of the fluid is an important force. In general this is the situation for free surfaces like cold windows and hot radiators - or flow in open conduits like water channels, sewer pipes . It is used when calculating momentum transfer in general and open channel flow and wave and surface behavior in particular. The Froude Number is important when analyzing flow in spillways, weirs, channel flows, rivers and in ship design.

2.4 Conclusions

This chapter illustrated the necessary theoretical and conceptual principles needed to understand the dynamics of multi-phase multi component systems. A brief background about the thermodynamics of bulk and interfaces in binary and ternary fluid systems has been described followed by wetting principles on solid surfaces. Basic set of equations describing the dynamics of fluid are shown here. The solution of these set of equations using lattice Boltzmann method will be shown in the later chapters. The essential context required for the interpretation of the numerical results of each chapter will be defined at the beginning of the chapters.

Chapter 3

Lattice Boltzmann method

A general background, necessary to understand computational fluid dynamics and common approaches to solve a fluid dynamics problem using computational fluid dynamics is discussed in this chapter. More emphasis is given to the fundamentals of the lattice Boltzmann method which includes an introduction to the lattice Boltzmann equation (LBE), general framework for its solution and various LB approaches used to solve multi-phase multi-component fluid systems. A thorough review on the *Free energy approach* unique to *Ternary fluid systems* will be explained in detail, as this approach is employed in the later study. The guidelines to select the free energy parameters for obtaining a wide range of surface tension combinations are discussed which has been published in Physical Review E journal [7].

3.1 Computational fluid dynamics

Until 1960, the fluid dynamics problem were operated in *"two-approach world"* which is experimental and theoretical. The development of accurate numerical algorithm along with advent in high speed digital computer has introduced another approach to solve the physical problems in fluid dynamics, called *"Computational fluid dynamics (CFD)"*. As sketched in Fig.17, CFD nowadays is an equal participant in the study and solution of fluid-dynamic problems with pure theory and pure experimentation making it as *"three-approach world"* [1].

The subject matter of *Computational Fluid Dynamics (CFD)* is to obtain approximate computer-based solutions to the governing equations of fluid dynamics (Section.2.3). These equations form

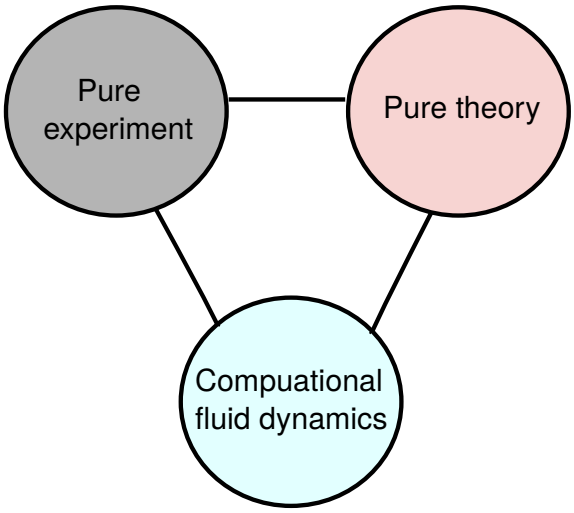

Figure 17: Three dimensions of fluid dynamics.

a set of coupled, non-linear partial differential equation are not possible to solve analytically and needs Computational fluid dynamics for most of the fluid dynamic problems. Computational fluid dynamics has application in the field of Aerodynamics, Industrial Fluid Dynamics, Fluid Structure Interaction, Heat Transfer, Hydrodynamics and Multi-phase Flows [1] [58].

3.2 Computational approaches

Computational fluid dynamics (CFD) is a fluid mechanical branch that uses numerical models to analyse and address fluid flow problems by solving Navier–Stokes(N-S) equations in discrete space and time. The solution of Navier–Stokes equations (N-S) and the way they are discretized can depend significantly on the problem. In the last 50 years, fluid flow analysis has dominated the solution of the Navier-Stokes(N-S) equation using conventional fluid dynamic (CFD) methods (for example finite volumes and finite difference). However, new techniques have appeared in the past two decades and continue to hold strong because of their capacity to handle more complicated fluid flow problems. In the context of different computational approaches, they are often categorises based on length scale (*microscopic, mesoscopic, and macroscopic*) of the fluid dynamics problem and based on the depth of the details required, different simulation techniques are suitable. A brief overview on the various computational methods covered by each approach (macro, micro and meso) is given in the following sections.

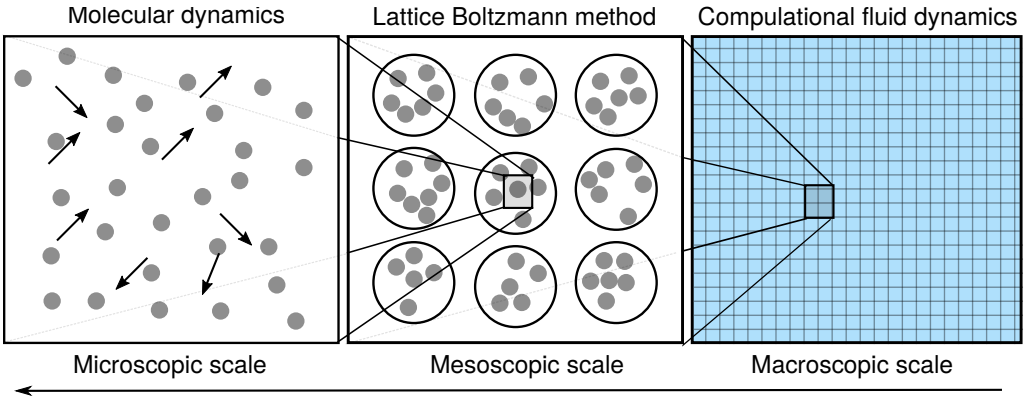

Figure 18: Different computational approaches in a typical fluid dynamics problem based on the hierarchy of length scale

3.2.1 Macroscopic approaches

In macroscopic scale one directly deals with the variation in the properties of fluid such as density, velocity and pressure. The state of the fluid is predicted in terms of these observable quantities.The discretiztion of the Navier-Stokes equations(N-S) in space and time and solving them numerically yields the flow properties at each node of the grid without giving any consideration to the molecular behaviour of the fluid. In both fundamental and industrial driven research the capabilities of many computational fluid dynamics techniques has been proven. Highly accurate and efficient systems are now capable of solving a number of problems, but certain mechanisms, such as turbulent flows and multi-phase flows, are still subject to extensive study. Since no attention is given to molecular activity in the macroscopic N-S equations, the simulation of multiple phases must be modelled explicitly for these approaches. The modelling of multi phase flows using this approach broadly falls into two categories: *front tracking method and front capturing* methods.

In *front tracking method*, the location of the interface is tracked explicitly using irregular moving mesh [127] [125]. Due to the moving nature of the mesh, in this method a frequent rearrangement of the mesh is needed which affects the conservation of fluid volume. Also, the parallelization of this scheme is very challenging. On the other hand in *Front capturing methods*, the movement of the fluid is captured first and then the location of the two-phase interface is established. The two fluids are modelled as one continuum in such a way that the interface has discontinuous properties. Generally, the front capture approaches have a weaker representation of the interface compared to front tracking methods but it is convenient to implement and efficient to compute. The most commonly used front capturing methods are Volume-of-Fluid method [42] and Level-set method

[96].

3.2.2 Microscopic approaches

Unlike macroscopic methods, in microscopic approaches explains the fluid dynamics at the molecular level to describe the behaviour of the fluid. Microscopic approaches are based on kinetic theory which describes the behaviour of fluids using the concept that the fluids are composed of large number of molecules [41]. The most simple and accurate representation of fluid flow is using *molecular dynamics(MD)* approaches, in which the Newtonian movement of all particles of the system is tracked in time. Very specific information on the state of a system can be obtained using molecular dynamics(MD)-type approaches. In these approaches the interactions between the particles are performed by prescribing the potential functions of the inter-particle force. The time required for the analysis in MD approaches is a small time-step and the number of atoms or molecules required for a statistically stable ensemble is extremely large, this makes these approaches time consuming and computationally expensive. Therefore, only very small systems with limited molecules can be modelled on current computing resources and this is the reason why it is not practical to use MD for problems of a macro-scale

3.2.3 Mesoscopic approaches

One has to coarsen the real particles in order to simulate fluid flow on higher scales. In such a modelling system, a pack of real particles called pseudo-particles are considered and they can be put either on the fixed lattice or off-lattice. *Dissipative particle dynamics* and *Direct Simulation Monte Carlo (DSMC)* are off-lattice pseudo-particle methods in which pseudo-particles move continuously in space. The *lattice Boltzmann method (LBM)* is one of the pseudoparticles approaches in which movements of fictitious particle clusters on the fixed grid do not follow the Newtonian dynamics as in MD, and are therefore computationally more susceptible. In LBM, a single particle probability distribution function (usually density distribution function) which is function of space and velocity is tracked. The LBM seems promising because coding, implementing and parallelizing is easy. Moreover, LBM can easily include interfacial phenomena as a particle method [119]. Under LBM framework, there are many approaches in literature to model fluid flow problems especially multiphase flows. There are four main LBM approaches to treat two phase flows: *Color-Fluid model* [36] [105], *Interparticle-Potential model* [111] [112], *Free-Energy model* [121]

and *Mean-Field theory model* [40]. General background about these models will be discussed in the later sections.

3.3 Lattice Boltzmann method (LBM) vs other solvers

Overall, different solvers have different benefits and drawbacks, and various forms of fluid simulation have different demands on the solver. The LBM derives a substantial benefit from being centred on the Boltzmann equation rather than the fluid dynamics equations (Navier-Stokes equation). Although LBM describes the dynamics of fluid at a mesoscopic scale as shown in Fig.(18), one can easily lead to the equations of fluid dynamics on the macroscale though the *Chapman-Enskog analysis*. Many of the difficulties of traditional methods lie in evaluating and discretising the non-linear *convection* term $(u \cdot \nabla)u$ of Navier-Stokes equation Eq.(**??**). In LBM, on the other hand , the non-linearity resides locally, which makes it ideal for high-performance parallel architecture computing including GPUs. The LBM is well adapted for the simulation of mass-conserving flows in complex geometries such as porous media and moving boundaries because unlike conventional numerical schemes, LBM has the advantage of not having to track the interface explicitly.

3.3.1 Sharp and diffuse interface

In general, to model multiphase and multicomponent flows where inerface plays a significant role, two different approaches are usually used which are *Sharp interface model* and *Diffuse interface model*. In the *Sharp interface models*, the interface is a two dimensional boundary as shown in Fig.19(a). The interface motion needs to be tracked explicitly by distinct computational mesh. Furthermore, the fluid flow velocity at the boundary must be continuous, and there is a stress jump normal to the interface corresponding to the Laplace pressure in Eq (2.22). In the literature there are many approaches to implement *Sharpe interface model*, such as: volume-of-fluid [135], front-tracking [125], and immersed boundary methods [92].

A schematic of a typical $1D$ order parameter (density in multi-phase fluid flows) in the diffuse interface model is shown in the Fig.19(b). When the order parameter is far from the interface, it approaches the bulk values and has smooth variation between the two bulk values across the interface. The *interface width* is the interface length scale which characterises the variance in the density profile. This is typically the order of nanometres for a real physical system. The interface

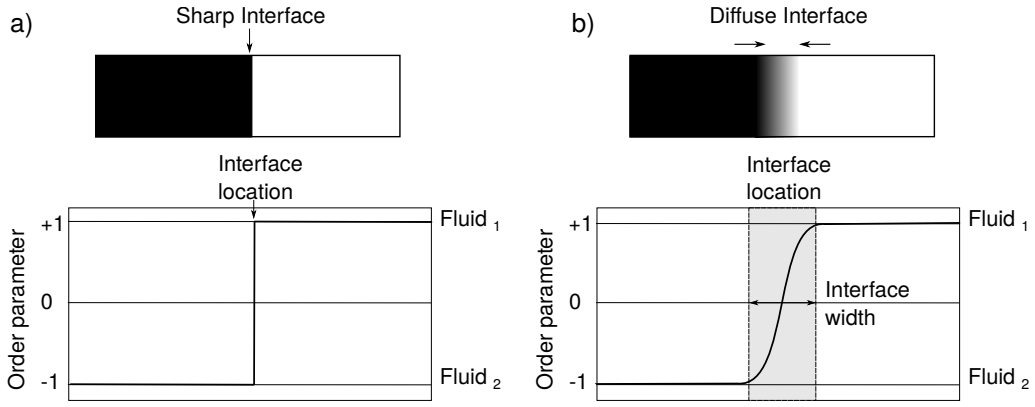

Figure 19: A typical interface profile in the diffuse interface model.

width in the computational domain is selected to be many lattice spacing for stable simulations. The models under lattice Boltzmann framework are diffuse interface models. The main advantage of *diffuse interface models* is that, in these models there is no need to introduce any additional mesh for the interface hence no need to track interface motion explicitly. All fluid nodes, whether in the bulk of the fluid or at the interface, should be handled equally. For the analysis of complex surface geometries, this makes *diffuse interface models* easy to use.

The LBM technique offers numerous benefits over traditional numerical methods: it is flexible because the numerical methodology can be easily implemented with complicated solid or free boundaries for multicomponent/multiphase systems. LBM is a Navier-Stokes solver in the bulk fluid; however, at the fluid-solid interface, where boundary conditions are imposed on particle distributions rather than directly on fluid variables such as velocity [147]. For these reasons, the LBM has been widely utilized in interfacial fluid problems. Furthermore, fluids in complex environments such as porous media and moving boundaries can be easily simulated, whereas other CFD methods might be difficult to work with when dealing with complex boundaries. LBM can also handle complicated, coupled flow with heat transfer and chemical interactions [20] [79]

However, despite the many advantages and simplicity, lattice Boltzmann method have few limitations. In many LBM methods, below a certain velocity there is existence of microcurrents at the fluid-fluid interface. These microcurrents also known as spurious or parasitic currents and are unphysical. Spurious currents are caused by numerical approximations of the surface tension force and set a lower bound in terms of Ohnesorge number and upper bound in terms of Reynolds number. Hence, large Reynolds numbers in the standard LBM simulation can be achieved by ex-

tensive grid refinement which become computationally demanding. Few LB formulations for the multiphase flows have restriction in terms of low density ratio between the liquid and vapor phases and interface thickness. When compared to actual fluids, the interface thickness is generally large in LB methods [137] [147] [111] [15],[64]

In many LB and non-LB methods, the existence of microcurrents at the fluid-fluid interface are observed which is caused by numerical approximations of the surface tension force. This microcurrent also known as spurious or parasitic currents are unphysical and therefore undesirable effect in computational fluid dynamics. LBM, being lattice based model, also experience existence of these spurious currents near fluid-fluid interfaces. The magnitude of the spurious currents varies in different models under LB framework. The specific feature of each LB models are discussed in the below section.

3.4 Multiphase multicomonent LB models

Multiphase and multicomponent flows refer to flows comprising two (or more) different fluids which differ by their physical properties, such as density, viscosity, conductivity etc. In literature, there are several approaches under lattice Boltzmann framework and are suitable for simulating multiphase multicomonent fluid systems The most common ones are Color-Fluid model, Shan-Chen model, mean-field theory model and Free-energy model. A quick overview of these strategies is presented below.

3.4.1 Color-Fluid model

One of the first models for two-phase simulations implemented for the LBM, was inherited from the lattice gas automata color model [36], [105]. The model uses the concept of two distribution functions representing two different fluids. Each distribution function is calculate using lattice Boltzmann general framework, followed by the calculation of interface at each time step. The surface tension acts as a external force which is applied to the fluid. An additional collision step is applied to the nodes at the interface between the fluids. This collision step redistributes the fluid densities among the discrete directions so that they move towards regions with the same composition. But the interfacial interaction are treated non-thermodynamically. At large fluid density ratios, the model is unstable due to the presence of large spurious currents around interface

[55]. Recently the original color fluid model was modified to improve the magnitude of spurious currents and to account for large density contrast fluids [101], [69]. However, these changes are also only applicable for static situations and still can not be used to resolve the complex dynamical effects of multi-phase phenomena.

3.4.2 Pseudopotential model

The Pseudopotential model also known as "Shan-Chen" model is based on microscopic interaction between fluid elements [111] [112]. This could be in the form of interaction potentials that eventually lead to the macroscopic separation of phases and introduces surface tension effects. Because of its versatility, the Shan and Chen models is the most common multi-phase solution with LBM. However, there are issues related to the original Shan and Chen models, such as lack of thermodynamic accuracy, additional spurious currents across the droplet that ultimately disrupt equilibrium, low density ratio of liquid to vapour, and dependency of the state equation on the parameters added by the model. To choose the surface tension independently from the equation of state, a modified multi-range pseudo-potential method was developed [108]. In multi-range pseudo-potential, the interaction is not limited to the nearest neighbors but to the next nearest neighbors. In the literature, improvements have been done to the original Shan-Chen method to incorporate different suitable equations of states and large density contrast between the two fluids. [108], [145], [98]. However, there is lack in the thermodynamics consistency of the model [39].

3.4.3 Mean-Field theory model

The mean-field theory model is valid in the nearly incompressible limits and applies to non ideal gases [40]. In this method, two distribution functions are used. The calculation of the pressure and velocity fields of an incompressible liquid is done via first distribution function and the second is used to locate the interface. Interfacial phenomena is modelled by the application of molecular interaction forces, which are estimated by the mean-field theory. This model will reliably predict the Rayleigh-Taylor instability and Kelvin-Helmholtz instability, even with non-ideal and dense fluids and improvement of the model is stable for high density ratios [38],[67]. However, in general, the mean-field theory model and its modifications are close to conventional computational fluid dynamics approaches for interface capture and are equivalent to the LBM level set and volume of fluid approaches.

3.4.4 Free-energy model

The free-energy model is a top-down approach which start with a free energy functional and ensures the thermodynamic consistency[121]. This energy functional contains the thermodynamics of the intended systems, and then other relevant physical quantities can be derived from its. To introduce the non-ideal interaction into the LB framework, the free energy model either uses a pressure term [121] or a forcing term [129]. Analytically the two forms are equivalent and they give very similar simulation results but show a difference in the stability of the algorithms. The original free-energy model has significant lack of Galilean invariance, inability to handle large density contrast fluids, numerical instability and thus its applications are limited to model either stationary or quasi-dynamical problems. Improvements have been done in the free-energy approach by introducing two sets of populations, one for capturing interface and the other for computing velocity field. However, with these improvements, the most fundamental advantage of multiphase LB formulation, which eliminates the requirement for interface capture, is no longer valid [148], [46].

In this study, we will take this direction in order to establish an efficient and robust free energy solution specific to *Ternary fluid systems* that can be further generalized to multi-phase multi-component systems and used to model droplet dynamics for realistic applications.

3.5 Lattice Boltzmann equation

The basic quantity of LBM is discrete-velocity distribution function $f_i(x,t)$, also known as particle population. It represents the density of particles with velocity c_i = (c_{ix}, c_{iy}, c_{iz}) at position x and time t. The Lattice Boltzmann equation is derived from Boltzmann equation. After discretising the Boltzmann equation in velocity space, physical space, and time the Lattice Boltzmann equation takes the below.

$$\underbrace{f_i(x + c_i\Delta t, t + \Delta t)}_{\text{Steaming}} = \underbrace{f_i(x,t) + \Omega_i(x,t)}_{\text{Collision}} \tag{3.1}$$

This expresses that particles $f_i(x,t)$ move with velocity c_i to a neighbouring point $x + c_i\Delta t$ at the next time step $t + \Delta t$. At the same time, particles are affected by a collision operator Ω_i .

This operator models particle collisions by redistributing particles among the populations $f_i(x,t)$ at each site. There are many forms of collision operators Ω_i available in the literature. The most popular and simper one is Bhatnagar–Gross–Krook (BGK) (Bhatnagar et al.) as shown in Eq.(3.2). However in literature, there are many types collision operators to solve lattice Boltzmann equation for example, multi relaxation time (MRT), single relaxation time (SRT), entropic collision operator.

$$\Omega_i(f) = -\frac{f_i - f_i^{eq}}{\tau}\Delta t \tag{3.2}$$

It relaxes the populations towards an equilibrium f_i^{eq} at a rate determined by the relaxation time τ. Where the f_i^{eq} is defined as:

$$f_i^{eq}(x,t) = w_i\rho\left(1 + \frac{u_i}{c_s^2} + \frac{(u\cdot c_i)^2}{2c_s^4} - \frac{u\cdot u}{2c_s^2}\right) \tag{3.3}$$

Where, with the weights w_i specific to the chosen velocity set. The representation of velocity sets in LBM is D_mQ_n. Where m represents the dimension and n shows the no of velocity vectors. The most common velocity sets to solve the Navier-Stokes equation are D_1Q_3 (1 dimensional and contains 3 velocities), D_2Q_9, D_3Q_{15}, D_3Q_{19}, D_3Q_{27}. Different velocity sets are used for different purposes. Typically, employing small number of velocities allow to minimise memory and computing requirements. However, larger velocity set (e.g. D_3Q_{27}), compared to smaller velocity sets (e.g. D_3Q_{15}) is more isotropic, which helps minimising spurious currents and provide better stability. In $3D$, the most widely used velocity set is D_3Q_{19}, which provides the optimum balance of computation requirements and accuracy [58] [120]. In Eq.(3.3), c_s shows the model's speed of sound at constant temperature such that $c_s = (1/3)\Delta x^2/\Delta t^2$, Δx and Δt are the lattice spacing and difference in the time step and are usually equal to unity.

$$\rho(x,t) = \sum f_i(x,t) \quad , \quad \rho u = \sum c f_i(x,t)) \tag{3.4}$$

In general the lattice Boltzmann equation Eq.((3.1)) can be split into two two distinct parts:

- Collision step $f^\star(x,t) = f_i(x,t) + \Omega_i(x,t)$

- Streaming step $f_1(x + c_i\Delta t, t + \Delta t) = f^{\star}(x, t)$

Where $f^{*}(x, t)$ represents the distribution function after collisions. As shown in Fig.20(a), in *Collision* step, the particles represented by black arrows are colliding at the central node. Collision is simply an algebraic local operation. First, one calculates from Eq.(3.4), the density ρ and the macroscopic velocity u then equilibrium distributions function as shown by (3.3) and finally compute collision operator as in (3.2). Plugging in all these eventually helps to compute $f^{\star}(x, t)$ as described in collision step equation above. In the second step, *Streaming*, Fig.20(b), the resulting distribution $f^{\star}(x, t)$ is streamed back to the neighbouring nodes. When these two operations are complete, one time step has elapsed, and the operations are repeated. During the collision, no communication is required: the communication to only adjacent nodes is needed while performing the streaming/propagation. This feature of two step process makes LBM approach easy to implement and parallelize.

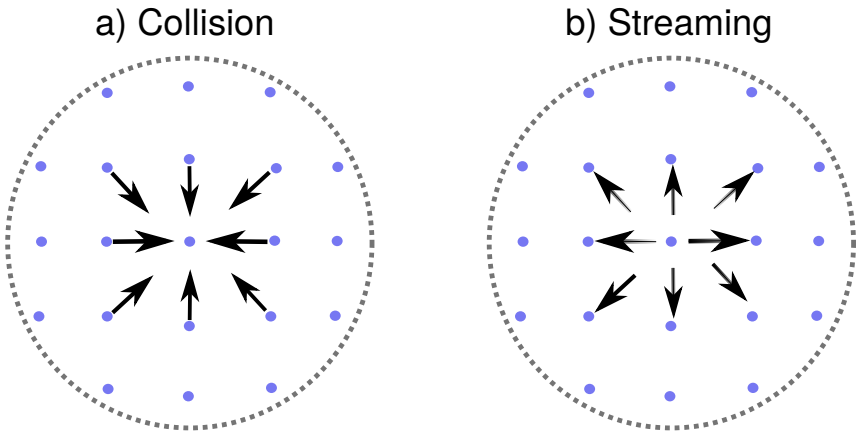

Figure 20: Representation of two step process of lattice Boltzmann equation (a) Collision (b) Streaming

3.6 Entropic Lattice Boltzmann equation

The most restrictive drawback of original lattice Boltzmann equation with BGK approximation is numerical instability. The second thermodynamic rule (Boltzmann's H-theorem) was reduced to restore this problem through the latest theoretical invention of the entropic lattice Boltzmann method [52] [53] [54] [2] [3] [52]. According to entropic scheme the lattice Boltzmann equation

reads below:

$$f_i(\mathbf{x} + \mathbf{c}_i\Delta t, t + \Delta t) = f_i(\mathbf{x}, t) + \alpha\beta\left[f_i^{eq}(\rho, \mathbf{u}) - f_i(\mathbf{x}, t)\right] \tag{3.5}$$

where,

- β corresponds to the kinematic viscosity (ν) (Eq.(3.6)) and is a fixed parameter in the range from 0 to 1 ($0 < \beta < 1$). By performing Chapman-Enskog expansion on lattice Boltzmann equation, it is possible to identify the relation between β and viscosity μ as shown below [79], [53], [54], [3].

$$\nu = \mu/\rho = c_s^2\left(\frac{1}{2\beta} - \frac{1}{2}\right) \tag{3.6}$$

  where $c_s = \frac{1}{\sqrt{3}}$ is the lattice speed of sound. Eq.(3.6) has below form after placing value of c_s.

$$\nu = \mu/\rho = (\beta^{-1} - 1)/6$$

- α parameter is the non-trivial root of the entropy estimate as below:

$$H\left(f_i' + \alpha\left[f_i^{eq}(\rho, \mathbf{u} + \delta\mathbf{u}) - f_i'\right]\right) = H\left(f_i'\right). \tag{3.7}$$

  where, in above Eqn, f_i' represents the mirror state (Eq.(3.8)) and is equal to the entropy in the initial state. H(f) is the entropy (Eq.(3.9)) .

$$f_i' = f_i + [f_i^{eq}(\rho, \mathbf{u} + \delta\mathbf{u}) - f_i^{eq}(\rho, \mathbf{u})] \tag{3.8}$$

$$H(f) = \sum_i f_i \ln(f_i/w_i), \tag{3.9}$$

Overall, α determines the maximally possible change of populations in the relaxation step with

$\beta > 0$ being responsible for the production of entropy. The combination $\alpha\beta$ is the effective relaxation parameter in the fully discrete kinetic picture. At α=2, standard lattice Boltzmann equation is recovered.

3.7 Framework of Lattice Boltzmann algorithm

The framework to implement Lattice Boltzmann algorithm can be explained in the following sequence of steps:

1. Initialisation: Compute the macroscopic moments $\rho(x,t)$ and $u(x,t)$ from $f_i(x,t)$ (Eq.(3.4))
2. Equilibrium distribution: Compute the equilibrium distribution function f^{eq} using (Eq.(3.3))
3. Collision: Perform the collision step ($f^{\star}(x,t)$) by applying the relevant collision operator.
4. Streaming: Perform the streaming step by which calculate the post-collision distribution functions and propagate it to the neighbouring sites, i.e $f_1(x + c_i\Delta t, t + \Delta t) = f^{\star}(x,t)$
5. Increase the time step, setting t to $t + \Delta t$, and go back to step 1 until the last time step or convergence has been reached.

In one of the approach called *"push algorithm"*, where collision and streaming steps is merged together is implemented in this study (Fig.(22)).

3.8 Binary free energy model

We will begin by introducing the free energy approach specific to *Binary fluid systems* (liquid-gas). This will help to explain the more complex formulation of free energy for *ternary fluid systems* (liquid-liquid-gas).

The free energy model is based on the top down approach which starts with an energy functional and from it we derive the other relevant quantities such as chemical potential, pressure tensor, which eventually goes into the equation of motion and has all the information about the thermodynamics of the system. The Free-energy formulation usually consists of three terms as shown

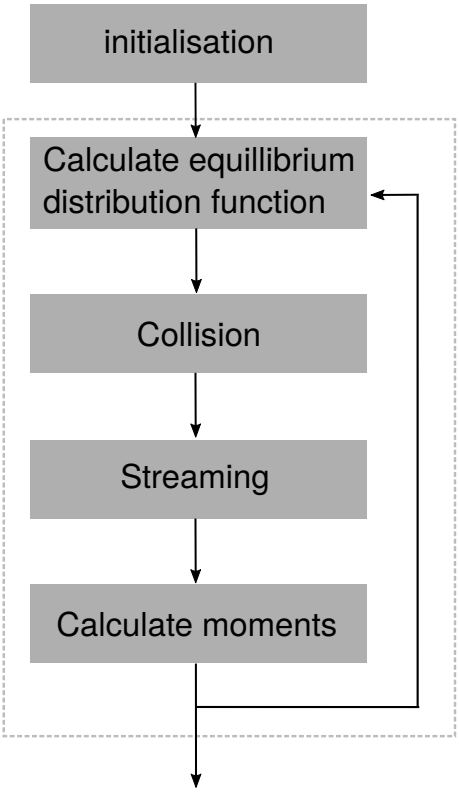

Figure 21: Flow chart of the framework of lattice-Boltzmann algorithm.

below:

$$F = \int [f_{Bulk} + f_{Inter}]\, dV \tag{3.10}$$

where f_{Bulk} and f_{inter} are the functions of space and time. Where, the first term in Eqn. (3.10) represents the free energy of bulk and contributes to equation of state that allows the coexistence of liquid-gas. The second term f_{Inter} in Eq.(3.10) indicates the interface's excess free energy, for managing surface tension and/or bending energy of the interface, its shape can be modified. Typically, for binary fluid systems it is a gradient term that penalises any difference in the density between the two phases. In Eq.(3.10), after placing the Bulk and interfacial part the free energy functional has the following form [142] :

$$F = \int \left[\Psi_{eos}(\rho, T) + \frac{\kappa}{2}(\nabla\rho)^2\right] dV \tag{3.11}$$

where, κ is the surface tension coefficient and ρ is the local density. The term $\Psi_{eos}(\rho, T)$ is derived

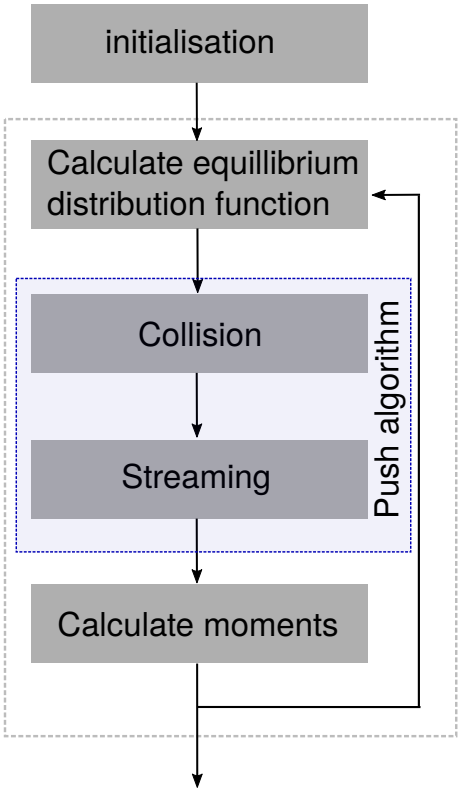

Figure 22: Flow chart of the framework of push algorithm in lattice-Boltzmann framework.

by integrating any suitable non ideal equation of state such that:

$$p_{eos} = \rho \left(\frac{\partial \Psi_{eos}}{\partial \rho} \right) - \Psi_{eos} \tag{3.12}$$

In order to derive the pressure tensor for a liquid-vapor system, for simplicity consider equilibrium in the presence of a flat interface which is defined as:

$$\frac{\partial \Psi_{eos}}{\partial \rho} - \kappa \frac{d^2 \rho}{dz^2} = \mu \tag{3.13}$$

By multiplying Eq.(3.13), with $\frac{d\rho}{dz}$, we get:

$$P = -\Psi_{eos} + \mu\rho + \frac{\kappa}{2} \left(\frac{d\rho}{dz} \right)^2 = constant \tag{3.14}$$

Combining Eq.(3.12), Eq.(3.13) and Eq.(3.14), we get a closed-form equation for the stress (or

total pressure, since it includes both the thermodynamic pressure and the effect of the flat interface):

$$P = p_{eos} - \kappa\rho\frac{d^2\rho}{dz^2} + \frac{\kappa}{2}\left(\frac{d\rho}{dz}\right)^2 \tag{3.15}$$

Above is the zz component of Korteweg's stress. Generalization to three dimensions of the pressure tensor P for a liquid- vapor system was found by Korteweg known as Korteweg's stress which is defined by: [57], [79], [84], [142]:

$$\mathbf{P} = \left(p_{eos} - k\rho\nabla^2\rho - \frac{k}{2}(\nabla\rho)^2\right) I + k(\nabla\rho)\cdot(\nabla\rho) \tag{3.16}$$

where, p_{eos} is the equation of state Eq.(3.12), I is the unit tensor. This defines the term $\mathbf{F_f}$, related to pressure tensor (Korteweg's stress) as below:

$$\mathbf{F_f} = \nabla\cdot(\rho c_s^2\mathbf{I} - \mathbf{P}). \tag{3.17}$$

Where, $c_s^2 = 1/3$ is the speed of sound in the lattice Boltzmann scheme. This force is plugged into the lattice Boltzmann equation along with other forces if present such as gravity, wetting force in the presence of solid boundary. To demonstrated how is this implemented into lattice Boltzmann equation, consider the entropic lattice Boltzmann equation Eq.(3.5), augmented with a forcing term, is written as:

$$f_i(\mathbf{x} + \mathbf{c}_i\Delta t, t + \Delta t) = f_i(\mathbf{x}, t) + \alpha\beta\left[f_i^{eq}(\rho, \mathbf{u}) - f_i(\mathbf{x}, t)\right] + F_i. \tag{3.18}$$

where, F_i decodes of the thermodynamics of the systems and is implemented via the Exact Differences scheme[82] as below:

$$F_i = \left[f_i^{eq}(\rho, \mathbf{u} + \delta\mathbf{u}) - f_i^{eq}(\rho, \mathbf{u})\right], \tag{3.19}$$

where $\delta\mathbf{u} = (\mathbf{F}/\rho)\Delta t$ is the correction to the fluid velocity arising from the force. where Δt = 1

is the lattice time step and F_i is the force composed of three contributions as below:

$$F = F_f + F_s + F_g \tag{3.20}$$

where F_f, F_s, F_g correspond to the implementation of Korteweg's stresses for a two-phase fluid, the fluid-solid interaction, and gravity, respectively. For simplicity consider at the moment there is no solid boundary and gravity in the system ($F_s = 0$,$F_g = 0$) and F_f is computed from Eq.(3.17).

3.9 Extension of non ideal EOS model to Ternary fluids

The model presented here is an extension of the previous model, which is now specific to ternary fluid system (liquid-liquid-gas) at high density contrast between liquid and gas phase [141]. However this model can be easily extended to more than three liquid components. Following the same concept of total free energy as in the Eq.((3.10)) and in the absence of wetting boundary conditions, the ternary free energy model's f_{Bulk} and f_{Inter} is often expressed as below:

$$f_{Bulk} = \underbrace{\frac{\lambda_1}{2}(\Psi_{\text{eos}}(\rho) - \Psi_0)}_{\text{Coexistence of liquid and gas}} + \overbrace{\underbrace{\frac{\lambda_2}{2}C_2^2(1-C_2)^2 + \frac{\lambda_3}{2}C_3^2(1-C_3)^2}_{\text{Coexistence of liquid-liquid}}}^{Double-well potential} \tag{3.21}$$

$$f_{Inter} = \frac{\kappa_1}{2}(\nabla\rho)^2 + \frac{\kappa_2}{2}(\nabla C_2)^2 + \frac{\kappa_3}{2}(\nabla C_3)^2. \tag{3.22}$$

The first term in Eqn. (3.21) tunes the coexistence of high density (ρ_l) liquid with a low density (ρ_g) gas. The term $\Psi_{eos}(\rho)$ is derived by integrating any suitable non ideal equation of state Fig.((3.12)) . Here we employ the Carnahan-Starling equation of state:

$$\Psi_{eos} = \rho\left(C - a\rho - \frac{8RT(-6+b\rho)}{(-4+b\rho)^2} + RT\log(\rho)\right), \tag{3.23}$$

where the constants C and Ψ_0 enforce $\Psi_{eos}(\rho_g) = \Psi_{eos}(\rho_l) = \Psi_0$. This condition ensures that the common tangent construction is valid for all coexisting phases. The values of a, b, R and T_c as described in section.2.1.4 and the relative concentration of the gas phase is as below:

$$C_1 = \frac{\rho - \rho_l}{\rho_g - \rho_l}, \tag{3.24}$$

for which $C_1 = 0$ when $\rho = \rho_l$ and $C_1 = 1$ when $\rho = \rho_g$. The second and third terms in Eqn. (3.21) represent a double well potential, as function of the relative liquid concentrations: C_2 and C_3. Each concentration has two minima at $C_{2,3} = 0$ and $C_{2,3} = 1$ corresponding to the presence or absence of the liquid. For convenience we introduce the phase field $\phi = \chi(C_2 - C_3)$ which, together with the density ρ, describes the system state. The parameter χ usually takes the value $\chi = 5$ in our model, and is employed to rescale the field ϕ such as the distance between minima is similar in both the ρ and ϕ fields. The variable transformations

$$C_2 = \frac{1}{2}\left[1 + \frac{\phi}{\chi} - \frac{\rho - \rho_l}{\rho_g - \rho_l}\right], \tag{3.25}$$

and

$$C_3 = \frac{1}{2}\left[1 - \frac{\phi}{\chi} - \frac{\rho - \rho_l}{\rho_g - \rho_l}\right], \tag{3.26}$$

enforce the constraint

$$C_1 + C_2 + C_3 = 1 \tag{3.27}$$

and allow us to map the density and phase field to the concentration fields. The bulk free energy density in Eqn. (3.21) describes three distinct energy minima in the (ρ, ϕ) space, corresponding to $(\rho, \phi) = (\rho_g, 0)$ (gas phase), and $(\rho_l, +\chi)$, $(\rho_l, -\chi)$ (liquid phases) as illustrated in Fig.(23). The set of lambdas (λ_1, λ_2 and λ_3) tunes the magnitude of the energy barriers between each pair of phases. In Fig.23, the top two energy minima, corresponds to the liquid components ($liquid_1$ and $liquid_2$) and have same density. The lower minima represents the gas component at lower density value. The dashed lines connecting the three energy minima represent the path in case the interfacial profile of different phases perfectly overlapping (ideal interface). Numerically computed path of the interface profiles in mechanical equilibrium are shown by data points. Deviations of numerically computed path from the dashed lines reveal the interface path is away from the ideal

profile. This is a typical issue related to the stiffness of density gradient, which does not appear in equal density model.

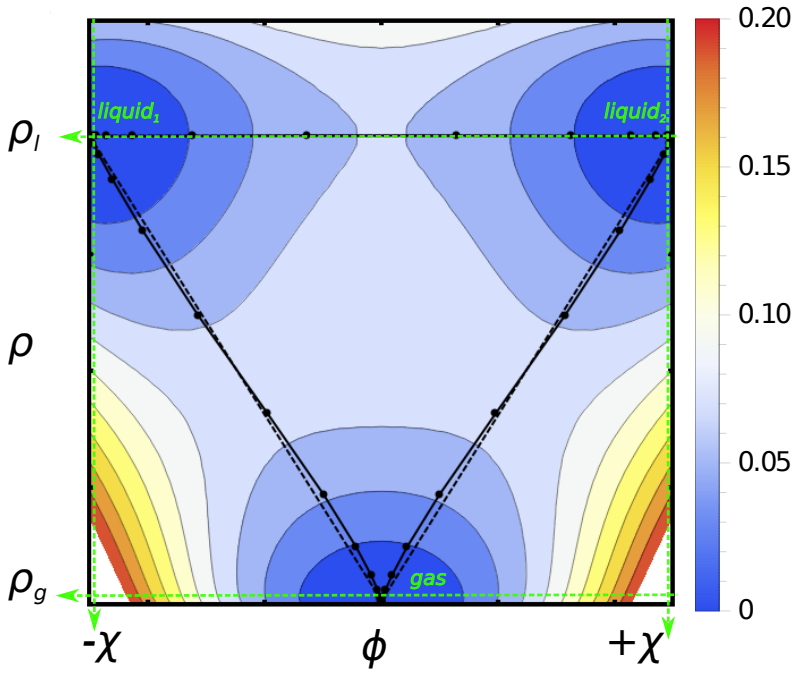

Figure 23: Contour plot of the bulk free energy density f_{Bulk} as a function of two order parameters, ρ and ϕ. Three distinct minima exist, corresponding to a gas component at ρ_g,0, and two liquid components at $\rho_l, +\chi$ and $\rho_l, -\chi$

Eq.(3.22) contains gradient terms of the density field and the concentration of the two liquid components, describing the energy penalty in the formation of the interfaces, tuned by the set of kappas (κ_1, κ_2 and κ_3). Summarising, this free energy model depends on six independent parameters, to fully determine the thermodynamic properties of the system.

3.9.1 Derivation of the pressure tensor

The chemical potentials μ_ρ and μ_ϕ are obtained directly from the free energy

$$\mu_\rho(\mathbf{r}) = \frac{\delta F}{\delta \rho(\mathbf{r})} = \mu_\rho^{Bulk} + \mu_\rho^{Inter} \tag{3.28}$$

$$\mu_\phi(\mathbf{r}) = \frac{\delta F}{\delta \phi(\mathbf{r})} = \mu_\phi^{Bulk} + \mu_\phi^{Inter}. \tag{3.29}$$

For convenience we express the chemical potentials in terms of the relative concentrations and, to simplify the notation, we define the auxiliary function $g(x) = x(x-1/2)(x-1)$:

$$\mu_\rho^{Bulk} = \frac{\lambda_1}{2}\frac{d\Psi_{eos}}{d\rho} - \frac{\lambda_2}{\Delta\rho}g(C_2) + \frac{\lambda_3}{\Delta\rho}g(C_3), \tag{3.30}$$

$$\mu_\phi^{Bulk} = \frac{\lambda_2}{\chi}g(C_2) - \frac{\lambda_3}{\chi}g(C_3), \tag{3.31}$$

$$\mu_\rho^{Inter} = -\kappa_{\rho\rho}\nabla^2\rho - \kappa_{\rho\phi}\nabla^2\phi, \tag{3.32}$$

$$\mu_\phi^{Inter} = \kappa_{\rho\phi}\nabla^2\rho - \kappa_{\phi\phi}\nabla^2\phi. \tag{3.33}$$

In Eqn. (3.62) $d\Psi_{eos}/d\rho$ is the first derivative by the density of the non ideal equation of state, and $\Delta\rho = \rho_l - \rho_g$. For the Carnahan-Starling EOS the first derivative of Eqn. (3.23) is

$$\frac{d\Psi_{eos}}{d\rho} = C - 2a\rho + RT(1+\log\rho) + \frac{16RT(b\rho-12)}{(-4+b\rho)^3}. \tag{3.34}$$

Furthermore, in Eqns. (3.32) and (3.33) the mixing coefficients for the gradient terms are

$$\kappa_{\rho\rho} = \left[\kappa_1 + \frac{\kappa_2+\kappa_3}{4(\rho_g-\rho_l)^2}\right], \tag{3.35}$$

$$\kappa_{\phi\phi} = \frac{\kappa_2+\kappa_3}{4\chi^2}, \tag{3.36}$$

$$\kappa_{\rho\phi} = -\frac{\kappa_3-\kappa_2}{4\chi(\rho_g-\rho_l)}. \tag{3.37}$$

The pressure tensor can be inferred from the relation $\nabla\cdot\mathbf{P} = \rho\nabla\mu_\rho + \phi\nabla\mu_\phi$ and takes the form

$$\begin{aligned} P_{\alpha\beta} &= p_0\delta_{\alpha\beta} \\ &+ \kappa_{\rho\rho}\left[(\partial_\alpha\rho)(\partial_\beta\rho) - \left(\rho(\partial_{\gamma\gamma}\rho) + \frac{1}{2}(\partial_\gamma\rho)^2\right)\delta_{\alpha\beta}\right] \\ &+ \kappa_{\phi\phi}\left[(\partial_\alpha\phi)(\partial_\beta\phi) - \left(\phi(\partial_{\gamma\gamma}\phi) + \frac{1}{2}(\partial_\gamma\phi)^2\right)\delta_{\alpha\beta}\right] \\ &+ \kappa_{\rho\phi}\left[(\partial_\alpha\rho)(\partial_\beta\phi) + (\partial_\alpha\phi)(\partial_\beta\rho)\right. \\ &\quad \left. - \left(\rho(\partial_{\gamma\gamma}\phi) + \phi(\partial_{\gamma\gamma}\rho) + (\partial_\gamma\rho)(\partial_\gamma\phi)\right)\delta_{\alpha\beta}\right], \end{aligned} \tag{3.38}$$

where p_0 is the pressure in the fluid bulk

$$p_0 = \rho\mu_\rho^{Bulk} + \phi\mu_\phi^{Bulk} - f_{Bulk}. \tag{3.39}$$

3.9.2 Entropic Lattice Boltzmann Implementation

The dynamic evolution of the isothermic ternary system follows the continuity, Navier-Stokes, and Cahn-Hilliard equations:

$$\partial_t\rho + \nabla\cdot(\rho\mathbf{v}) = 0, \tag{3.40}$$

$$\begin{aligned}\partial_t(\rho\mathbf{v}) + \nabla\cdot(\rho\mathbf{v}\otimes\mathbf{v}) = \\ -\nabla\cdot\mathbf{P} + \nabla\cdot[\mu(\nabla\mathbf{v} + \nabla\mathbf{v}^{\mathbf{T}})],\end{aligned} \tag{3.41}$$

$$\partial_t\phi + \underbrace{\nabla\cdot(\phi\mathbf{v})}_{\text{Advection}} = \underbrace{M\nabla^2\mu_\phi}_{\text{Diffusion}} \tag{3.42}$$

where $\mathbf{v}$ is the fluid velocity, μ is the dynamic viscosity, and M represents the mobility in the Cahn-Hilliard model for the order parameter ϕ. To solve the equations of motion we introduce two sets of distribution functions, evolving the density ρ and the order parameter ϕ.

- *Evolution of density ρ:* For the density ρ, we employ the entropic lattice Boltzmann method (ELBM) Eq.((3.18),(3.19) (3.20))[80, 81]. Where F=F_f and is the sum of Eq.((3.21),(3.22))
- *Evolution of order parameter ϕ:* To evolve the order parameter ϕ, a standard LBGK scheme is employed Eq.((3.2)).

A schematic of sequence of steps for this approach is show in Fig.24.

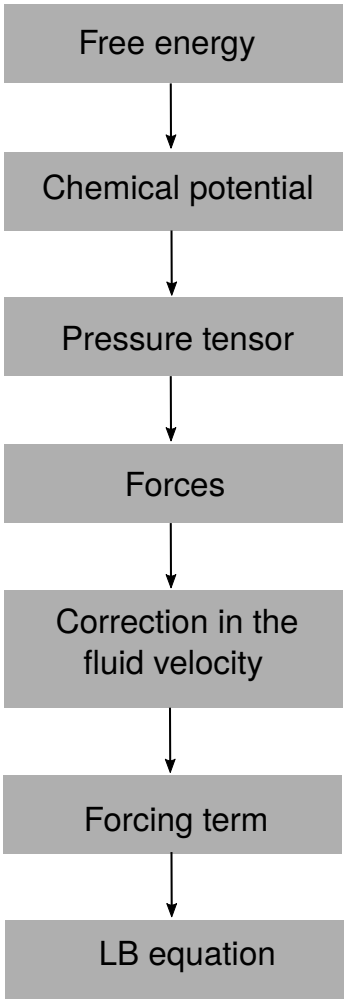

Figure 24: Flow chart of the ternary free energy lattice-Boltzmann algorithm.

3.9.3 Surface tensions in Ternary free energy model

In free energy models based on double well potentials [14, 13], the shape of the concentration profile against the spatial coordinates takes the form of a hyperbolic tangent. This feature is inherited in our ternary model, but only for the liquid-liquid interface between phases C_2 and C_3, which is characterised by the parameter

$$\alpha_{23} = \sqrt{\frac{\kappa_2 + \kappa_3}{\lambda_2 + \lambda_3}}. \tag{3.43}$$

We can assume that the density does not vary at the interface between C_2 and C_3, and set $C_1 = 0$ along the interface. Following Ref. [110], if the coordinate x measures the distance from the interface along its normal direction, the concentration profiles of the components C_2 and C_3 vary

according to

$$C_{2,3}(x) = \frac{1 \pm \tanh \frac{x}{2\alpha_{23}}}{2}. \tag{3.44}$$

Integrating of the concentration profiles along x we derive a simple expression for the surface tension [110]

$$\gamma_{23} = \frac{\alpha_{23}}{6}(\lambda_2 + \lambda_3). \tag{3.45}$$

For the liquid-gas interfaces, it is not possible to assume a priori that the ρ and ϕ fields vary in the same way. Indeed, the minimization of the free energy seeks for a path which cannot be described analytically. To illustrate this aspect, we study in detail four cases, represented by the parameter sets reported in table 1. For each set we independently compute for all interfaces the surface tension $\gamma = \Delta P R$ by measuring the pressure jump ΔP across the interface of 2D drop of radius R (bubble test).

set	**1**	**2**	**3**	**4**
λ_1	0.6	0.6	0.01	0.1
κ_1	0.01	0.01	0.01	0.01
λ_2	1.0	1.1	1.5	1.0
κ_2	1.0	1.1	1.5	1.6
λ_3	1.0	0.5	1.5	0.2
κ_3	1.0	0.5	1.5	-0.4
γ_{12}	0.414	0.431	0.333	0.321
γ_{13}	0.414	0.334	0.333	0.120
γ_{23}	0.323	0.259	0.485	0.180
θ_1	134.1	143.1	86.3	–
θ_2	112.9	129.2	136.8	–
θ_3	112.9	87.6	136.8	–
				

Table 1: Parameters of four selected sets, and the relative surface tensions and Neumann angles. The last row reports the global energy minimum configuration of a double emulsion. The white region corresponds to the gas phase (C_1), while the blue and red regions correspond to the liquids C_2 and C_3.

The 4 sets are listed in order of increasing mismatch between the interfacial profiles. The first set represents two liquids with symmetric properties, where the liquid-liquid surface tension is slightly lower than both the liquid-gas ones. The second set describes three fluids with different properties. The third set also describes two equal liquids but λ_1 is much smaller than in the first set, leading to a liquid-liquid surface tension significantly larger than the liquid-gas ones. The

fourth set describes also three fluids, but in this case the parameter κ_3 is negative, leading to a spontaneous encapsulation of liquid C_2 by liquid C_3. Negative values of lambdas or kappas are generally allowed in the ternary model, as long as the three minima in the $[\rho, \phi]$ space are well defined.

In Fig. 25 we inspect the properties of the diffuse interfaces for the parameter sets described in table 1. The color maps illustrate the contours of the bulk free energy in the $[\phi, \rho]$ space. As expected, the bulk free energy is symmetric in ϕ for sets 1 and 3, and non-symmetric for sets 2 and 4. Introducing the variable transformation Eqns. (3.56), (3.57) and (3.58) into Eqn. (3.27) we can easily see that the absence of the third component at any interface leads to a linear relation between ρ and ϕ connecting the corresponding minima, represented by straight lines in the $[\rho, \phi]$ space in Fig. 25. However, the minimisation of the free energy does lead to different paths, depicted by connected dots. As Eqn. (3.27) must be satisfied, the inverse variable transformation will produce a certain fraction of the minor component at the interface.

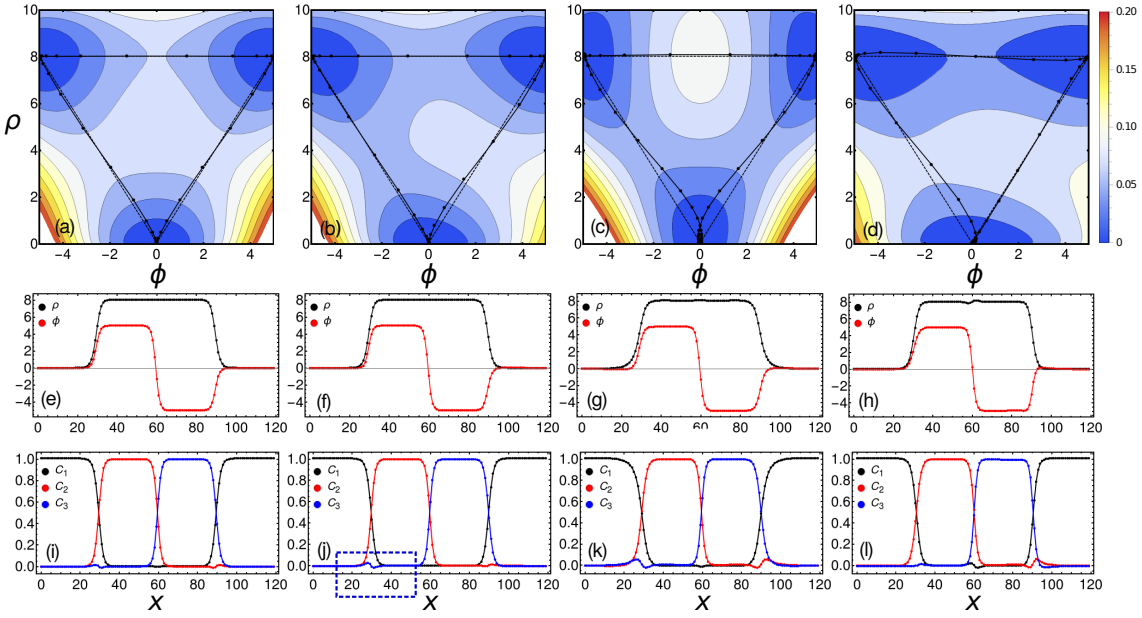

Figure 25: Upper row: color maps of the bulk free energy for the parameter sets 1,2,3 and 4 (panels a,b,c and d). The dashed lines connecting the three energy minima represent the path in the of $[\phi, \rho]$ space of an ideal interface, where the third components is completely absent. Data points represent the path of the numerically computed interface profiles in mechanical equilibrium. Deviations from the dashed lines reveal the creation of a fraction of concentration the third component. Middle row (panels e,f,g and h): Profiles of ρ and ϕ along interfaces between fluids, placed in the sequence $1, 2, 3, 1$. Bottom row (panels i,j,k and l): Profiles of C_1, C_2 and C_3 along interfaces between fluids in the corresponding sequence $1, 2, 3, 1$.

For set 1 the interface path is close to the $ideal$ profile. The deviations in the remaining sets increase with the increasing mismatch between the profiles of ρ and ϕ. For the set of parameters defined in table 1, In Fig.25 (e, f, g, h), the profile of ρ and ϕ along the interfaces between the fluids placed in the sequence $gas(1), liquid_1(2), liquid_2(3), gas(1)$ are shown. Similarly, though variable transformation, we show the concentration profile (C_1, C_2 and C_3) for all three components in Fig.25 (i, j, k, l). The mismatch between the profiles of ρ and ϕ is reflected in these plots as highlighted by a dashed box in Fig.25 (j). To quantify these mismatches we define the $Deformation\ coefficient\ D$ as the difference between the maximum and minimum values of the minority phase in a region Ω near the interface between the two majority phases as shown in Fig.26 (magnified boxed region of panel (j) of Fig.25) For example, at the interface between C_1 and C_2, the Deformation coefficient D_3 is defined as

$$D_3 = \max_{\mathbf{x}\in\Omega}(C_3) - \min_{\mathbf{x}\in\Omega}(C_3) \tag{3.46}$$

and similarly for the other interfaces. Based on our free energy formation for ternary systems, it is challenging to completely eliminate the existence of $Deformation\ coefficient$; nonetheless, we aim to minimize its value. The magnitude of $Deformation\ coefficient$ highly depends on the choice of free energy parameters and affect the interfacial properties of ternary fluid systems.

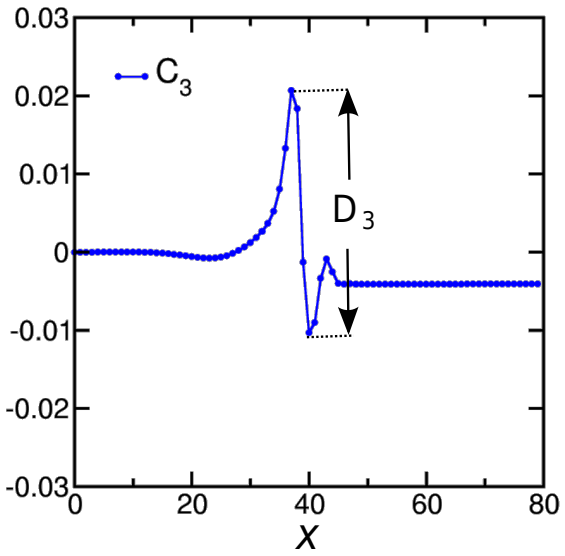

Figure 26: (Color online) Example of profile of the concentration C_3 at the interface between C_1 and C_2 illustrating the definition of the Deformation Coefficient (D_3).

3.9.4 Parameter scan for Ternary free energy model

To quantify the interfacial properties arising in the ternary model, we have carried out a systematic analysis for a wide range of parameters. Because a complete scan of the six-dimensional parameter space formed by $\lambda = (\lambda_1, \lambda_2, \lambda_3)$ and $\kappa = (\kappa_1, \kappa_2, \kappa_3)$ is too demanding, we have identified eight subspaces. The criterion for the choice of the subspaces is to facilitate simulations of systems with similar surface tensions (within a subspace), and capture the effect of systematic variations of the surface tension in the fluid response. Consequently, the same parameter sets might be included in different subspaces, but will differ in the local variation of some parameters.

subspace	λ_1	λ_2	λ_3	κ_1	κ_2	κ_3
1	Y	X	X	0.01	X	X
2	Y	X	X	0.01	$0.5X$	$0.5X$
3	Y	X	0.5	0.01	X	0.5
4	0.01	X	Y	0.01	X	Y
5	0.5	X	Y	0.01	X	Y
6	1.0	X	Y	0.01	X	Y
7	Y	X	0.5	0.01	$2X - 0.5$	$1 - X$
8	0.1	X	1.0	0.01	Y	$1 + X - Y$

Table 2: Summary of surface tension tests. Details for each case in AppendixA.

The maps $\lambda(X, Y)$ and $\kappa(X, Y)$ are summarised in table 2. In Subspace 1 we consider immiscible liquids with identical properties $\lambda_2 = \lambda_3 = \kappa_2 = \kappa_3 = X$ and explore the relative effect of the variation of the liquid-gas component $\lambda_1 = Y$. Subspace 2 is similar, but the choice of $\lambda_2 = \lambda_3 = \kappa_2 = \kappa_3$ produces a larger width of liquid-liquid interface, resulting in lower Neumann angles for the gas pahse θ_1 (more repelling liquids). In Subspace 3 we fix $\lambda_3 = \kappa_3 = 0.5$, and explore the interplay between the gas phase and the first liquid. This set is useful to explore system with non symmetric interfacial properties of the liquids. In Subspace 4, 5 and 6 we fix the the values of the bulk term for the equation of state to three values $\lambda_1 = 0.01, 0.6, 1.0$, leading respectively to a small, medium and large contribution to the surface tension from the liquid-gas component. In all three subspaces we systematically explore all combinations of the two liquids $\lambda_2 = \kappa_2 = X$ and $\lambda_3 = \kappa_3 = Y$, allowing to tests systems with enhanced asymmetry in the surface tension properties of the liquids. In Subspace 7 and 8 we consider combinations with negative values of κ_2, necessary to achieve spontaneous encapsulation of liquid 3 by liquid 2. The parameters can be tuned in order to compare systems where the spreading parameters S_2 continuously shifts from positive to negative. The same subspaces can describe the opposite

situation by swapping phases 2 and 3.

Below, we will discuss the details about inerfacial properties from one of the subset (subspace 4) while the analysis from the rest of the subspace will be provided in the AppendixA.

Simulation setup

Each Subspace is described by two coordinates, X and Y and is mapped by a $20 \times 20 = 400$ points grid, where each point represents a given parameter set. For each parameter set we have performed three independent measures (drop/bubble test) of the surface tensions using Laplace relation (in two dimensions) $\Delta P = \gamma/R$. This is done for each interface such that γ_{12} represents the surface tension between gas and liquid component 1 (Fig.27(a)), γ_{13} shows the surface tension between gas and liquid component 2 (Fig.27(b)) and the surface tension between liquid component 1 and liquid component 2 is denoted by γ_{23} (Fig.27(c)). We have chosen a drop of radius $R = 80$ lattice units for all tests, contained in a simulation domain of 320×320 lattice units. The surface tension is consequently computed as $\gamma = R\Delta P$ where the pressure jump ΔP at the fluid interface is obtained from the differences of the bulk pressures p_b in the centre of the drop/bubble and far in the surrounding fluid. The shape of the diffuse interface for the various components is measured along the radial direction from the centre of the drop/bubble to the boundary of the simulation domain.

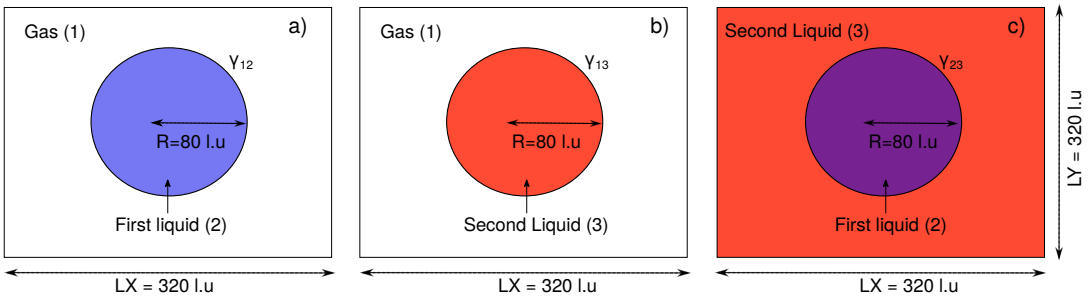

Figure 27: Simulation set up for Laplace test for each interface.

Analysis of the subspace 4

In Fig. 28 we report, as an example, our analysis of the subspace 4. The first row of panels depicts the surface tensions γ_{12}, γ_{13} and γ_{23} respectively. As expected, γ_{12} and γ_{13} mainly depend on the variation of $X = \lambda_2$ and $Y = \lambda_3$ respectively, while γ_{23} is function of $X + Y = \lambda_2 + \lambda_3$.

The non perfect alignment of the contour lines with the main axes for γ_{12} and γ_{13} suggests that the contribution of the liquid-gas component varies, even if λ_1 is fixed throughout the subspace. The variation of γ_{23} instead is more regular, because no variation of the density field occurs at this interface, and closely follows the values of surface tension predicted by Eqn. (3.45) (comparison not shown). The second row of panels in Fig. 28 reports the Neumann angles θ_1, θ_2 and θ_3 computed as functions of the surface tensions:

For the full range of parameters explored in this subspace, the Neumann angles are always well defined by Eq.(2.25) to Eq.(2.27), indicating that the spreading parameter is in the negative range for all the components as shown by the third row and represented by Eq.(2.28) to Eq.(2.30) The fourth row of panels in Fig.28 reports the *Deformation coefficient* D, measured for each interface such that:

$$D_1 = \max_{\mathbf{x}\in\Omega}(C_1) - \min_{\mathbf{x}\in\Omega}(C_1), \tag{3.47}$$

$$D_2 = \max_{\mathbf{x}\in\Omega}(C_2) - \min_{\mathbf{x}\in\Omega}(C_2), \tag{3.48}$$

$$D_3 = \max_{\mathbf{x}\in\Omega}(C_3) - \min_{\mathbf{x}\in\Omega}(C_3). \tag{3.49}$$

As expected, $D_1 \simeq 0$ throughout the whole map. In contrast, D_2 and D_3 vary up to 25% of the concentration interval ($[0, 1]$). While the color maps provide a visual and intuitive summary of the properties, to automatize the parameter selection based on the desired combination of tensions, for each subspace we have fitted the surface tensions with a high order polynomials, of the form below.

$$\gamma = A(x) + B(x)y + C(x)y^2 \tag{3.50}$$

$$A(x) = a_1 + a_2x + a_3x^2 + ...$$
$$B(x) = b_1 + b_2x + b_3x^2 + ...$$
$$C(x) = c_1 + c_2x + c_3x^2 + ...$$

In AppendixA, We report a detailed description, including fitting functions for the surface tensions, of each subspace. This database can provide guidance to select the free energy parameters and

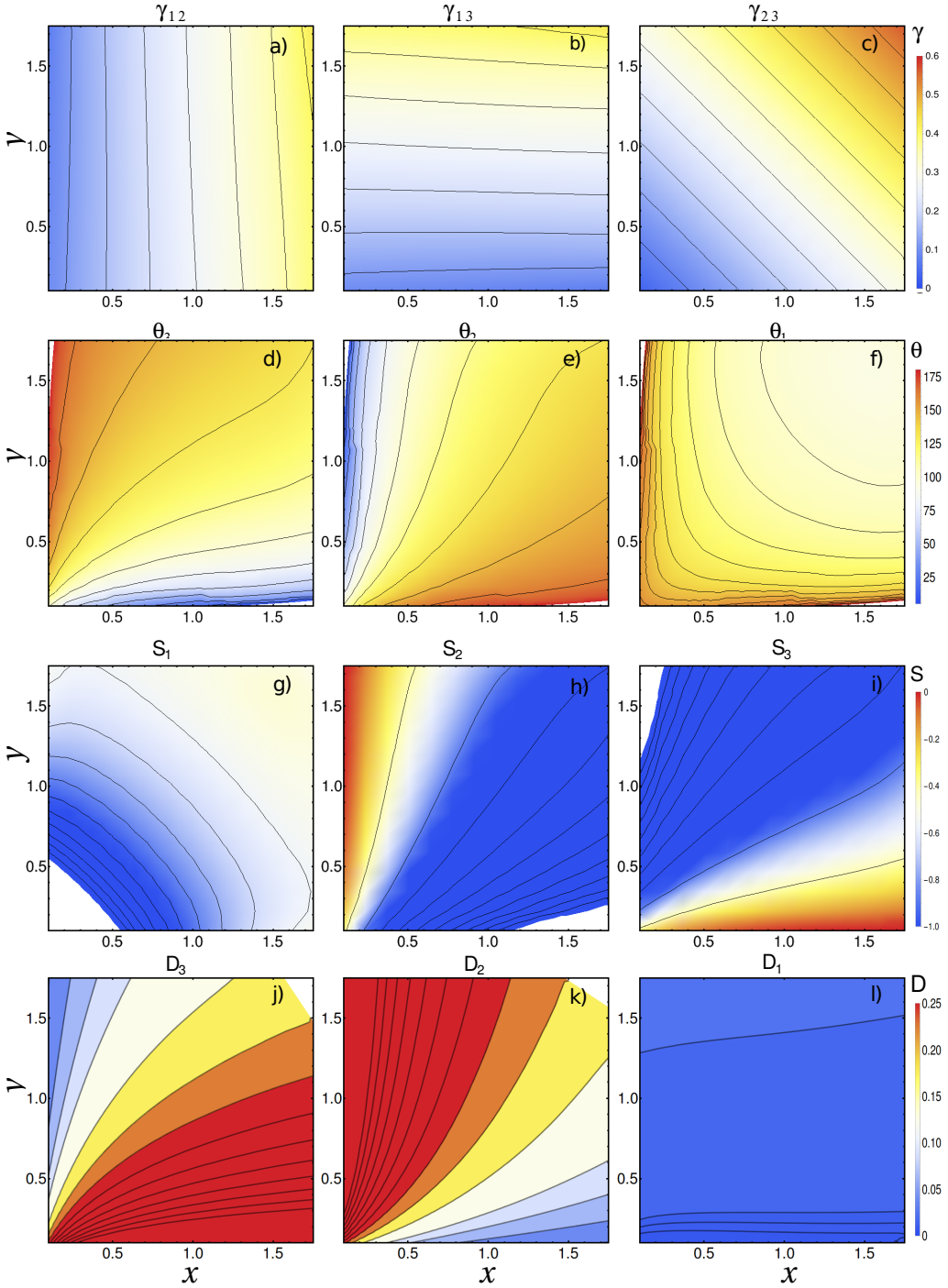

Figure 28: Colour maps of relevant quantities as function of the coordinate $X = \lambda_2$ and $X = \lambda_3$ Upper row (a,b,c): surface tensions (λ_{12}, λ_{13} and λ_{23}); Middle row (d,e,f): Neumann angles (θ_3, θ_2 and θ_1); Lower row (g,h,i): Deformation coefficient (D_3, D_2 and D_1).

reproduce target combinations of surface tensions.

3.9.5 Guidelines to choose the parameters

Typically, to choose the parameter sets for our simulations, we perform the following steps:

1 Identify a suitable subset, considering whether symmetric ($liquid_1$ and $Liquid_2$ are identical) or non-symmetric surface liquid properties are required, whether liquid-liquid surface tensions should be larger or lower than liquid-gas tensions, or whether a positive spreading parameter (spontaneous encapsulation) is necessary.

2 Visually identify a region in term of the coordinates X and Y approximately matching the required properties. A compromise might be necessary to minimise the interface deformation.

3 Employ the fitting functions to precisely determine a set of coordinates X and Y, the corresponding surface tension combinations, and the required combinations of free energy parameters $\lambda = (\lambda_1, \lambda_2, \lambda_3)$ and $\kappa = (\kappa_1, \kappa_2, \kappa_3)$.

3.10 Improved Ternary free energy model

The free energy model described above has been employed in the next chapter in developing three methods for wetting boundaries and work well in the regime where spreading parameter are negative, but suffer of stability issues when spreading parameters approach zero. As this condition is systematically required in our study of bouncing droplets, we have developed an improved free energy model, discarding the use of non-ideal equations of states in favor of more regular double well potentials. Unlike the previous model (Eq.(3.21)), in the improved version the bulk free energy is further split in three terms as below:

$$F_{Bulk} = F^{in}_{Bulk} + F^{out}_{Bulk} + F^{gas}_{Bulk}. \tag{3.51}$$

The first term F^{in}_{Bulk} is expressed by

$$F^{in}_{Bulk} = \int \left[\sum_{i=1,2,3} \left(\frac{\lambda_i}{2} f(C_i) \right) \right] dV. \tag{3.52}$$

where C_1, C_2, C_3 are the concentrations of the three phases, having minima in $C_i = 0$ and $C_i = 1$ determined by the double well potential $f(x) = x^2(x-1)^2$. The energy barrier between minima are tuned by the parameters $\lambda_1, \lambda_2, \lambda_3$. The second term F_{Bulk}^{out} is a correction applied for $C_i < 0$ and $C_i > 1$ to ensure a better numerical stability,

$$F_{Bulk}^{in} = \int \left[\sum_{i=1,2,3} \left(\frac{\lambda_0}{2} g(C_i) \right) \right] dV. \tag{3.53}$$

In this case we set $g(x) = 0$ if $x \in [0, 1]$ and $g(x) = f(x)$ otherwise. As this correction term does not affect the energy barriers between minima, we employ a single parameter $\lambda_0 > 0$ for all concentrations, chosen such that $\lambda_0 + \lambda_i > 0$ for any λ_i, to ensure that the sum of the contributions remains positive in the outer region. This allows to extend the range of λ_i parameters to negative values, resulting in a wider control of surface tensions of the fluid interfaces. The last term F_{Bulk}^{gas} will be discussed later. Typical profiles of the free energy as function of the concentration C_i are shown in Fig.29

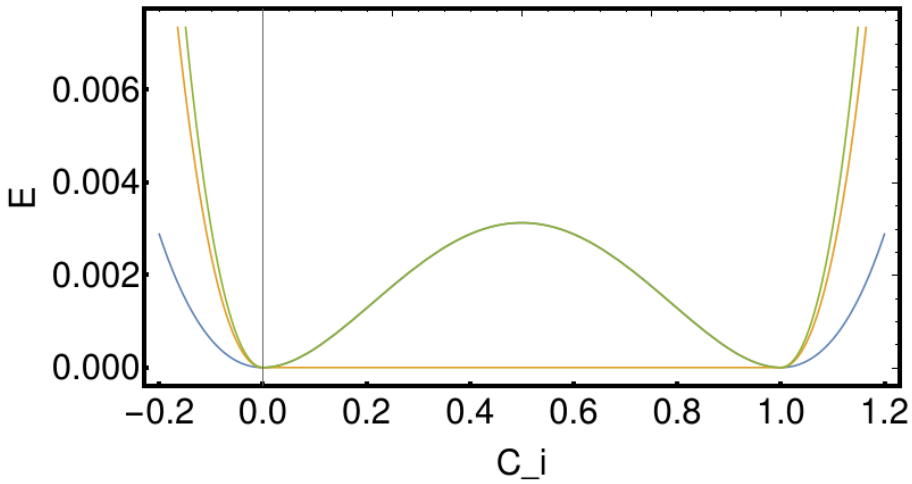

Figure 29: Shape of the patched double well potential ($\lambda_i/2 f(C_i)$, $\lambda_0/2 g(C_i)$ and $\lambda_i/2 f(C_i) + \lambda_0/2 g(C_i)$) for $\lambda_i = 0.05$ and $\lambda_0 = 0.2$

Having defined the properties of three independent concentration field, we are now seeking for a variable transformation allowing for three independent densities ρ_1, ρ_2 and ρ_3. The natural choice is defining the local density of the ternary fluid as function of all concentrations reads

$$\rho = \rho_1 C_1 + \rho_2 C_2 + \rho_3 C_3, \tag{3.54}$$

completed by the auxiliary variable transformations

$$\phi = C_2 - C_3, \quad \&\&1 = C_1 + C_2 + C_3, \tag{3.55}$$

where the latter relation also imposes the conservation of the sum of concentrations. The inverse variable transformations are

$$C_1 = \frac{2\rho + \phi(\rho_3 - \rho_2) - (\rho_2 + \rho_3)}{2\rho_1 - \rho_2 - \rho_3}, \tag{3.56}$$

$$C_2 = \frac{-\rho + \phi(\rho_1 - \rho_3) + \rho_1}{2\rho_1 - \rho_2 - \rho_3}, \tag{3.57}$$

and

$$C_3 = \frac{-\rho + \phi(\rho_2 - \rho_1) + \rho_1}{2\rho_1 - \rho_2 - \rho_3}, \tag{3.58}$$

which substituted in Eqns.(3.52) and (3.53) allow to express the double well contribution to bulk free energy as function of only two fields ρ and ϕ. An example of landscape of the free energy is reported in Fig.30. Where all the three components (gas, $liquid_1$, $liquid_2$) are at three different densities. In all panels, the top two energy minima, corresponds to the liquid components ($liquid_1$ and $liquid_2$). Unlike previous version of the model, now the two liquids are also at different density values. The lower minima represents the gas component at lower density value than both liquid components.

For this variable transformation, the choice $\rho_1 < \rho_2$ and $\rho_1 < \rho_3$ (i.e. the concentration C_1 is assigned to the low-density, gas phase) ensures the best numerical stability. This formulation of the free energy is suitable for ternary fluid system having density of similar order of magnitude. If one of the fluid represents a low density gas phase, with density ratio of order 10^3 or above, this form of the free energy is not sufficient to ensure that the density remains positively defined. To prevent negative values of the density, therefore, we included the third term in Eqn.(3.51).

$$F_{Bulk}^{gas} = \int [f_{gas}(\rho)]\, dV. \tag{3.59}$$

The functional form of this term is deduced observing the shape of free energy derived from any

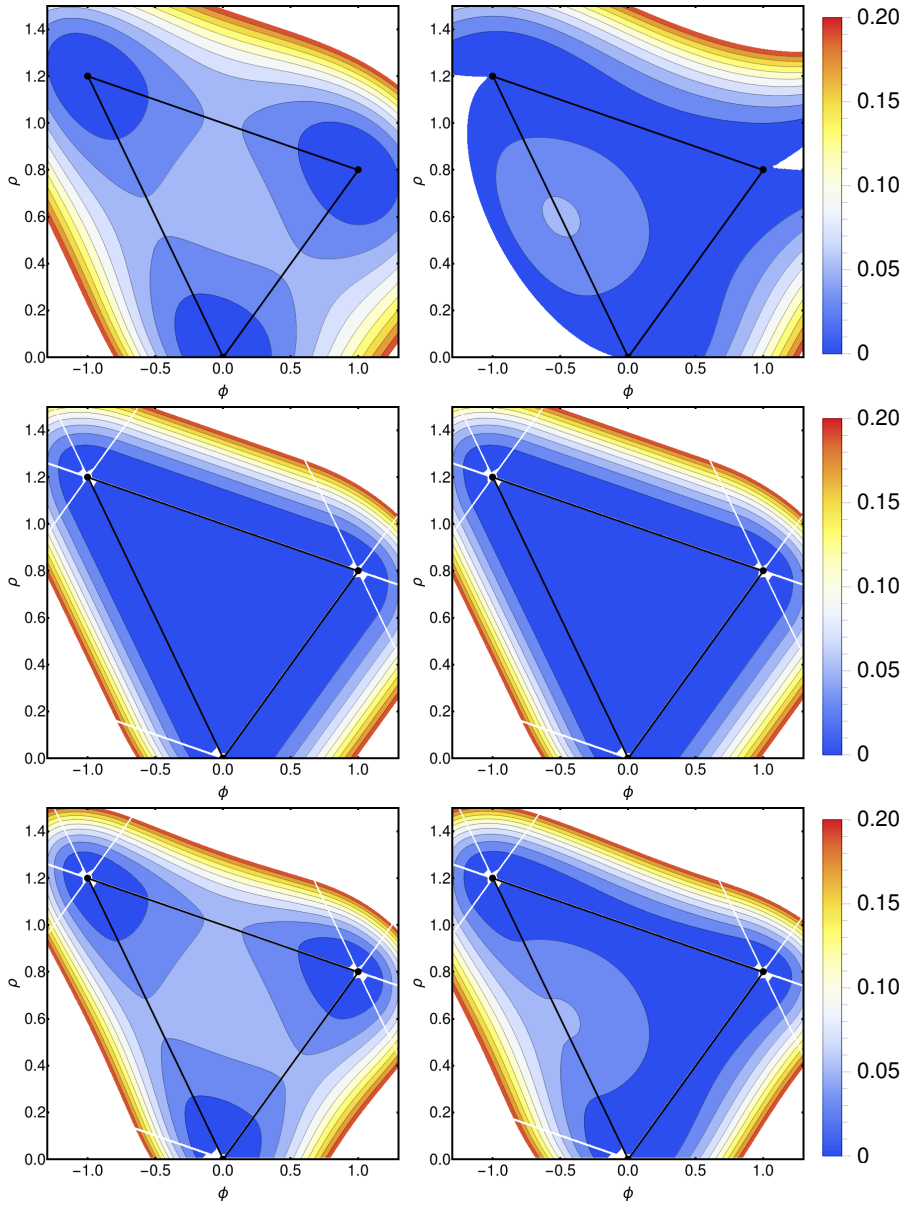

Figure 30: Left: energy landscape for all $\lambda_i > 0$; Right: energy landscape for $\lambda_1 > 0$, $\lambda_2 < 0$ and $\lambda_3 > 0$. Top: Bulk free energy of $\sum_{i=1,2,3}\left(\frac{\lambda_i}{2}f(C_i)\right)$ Middle: Bulk free energy of $\sum_{i=1,2,3}\left(\frac{\lambda_i}{2}g(C_i)\right)$ Bottom: Sum of the previous terms. Parameters: $\lambda_0 = 0.2$, $\lambda_1 = 0.1$, $\lambda_2 = 0.1$ (left), $\lambda_2 = -0.05$ (right), $\lambda_3 = 0.1$, $\rho_1 = 0.001$, $\rho_2 = 0.8$, $\rho_3 = 1.2$.

non ideal equation of state. The key feature is a steep potential with a vertical asymptote $(\partial E/\partial\rho)$ but a finite energy $E = E_0 < \infty$ in the limit $\rho \to 0$. To mimic this feature we choose an elliptical shape

$$f_{gas}(\rho) = \left(\rho_1 - \sqrt{\rho_1^2 - (\rho - \rho_1)^2}\right) E_0/\rho_1 \tag{3.60}$$

where the value E_0 is a free parameter.An example of free energy near the minimum corresponding

to the gas phase, highlighting the steep contribution of the term F_{Bulk}^{gas} is reported in Fig. 31.

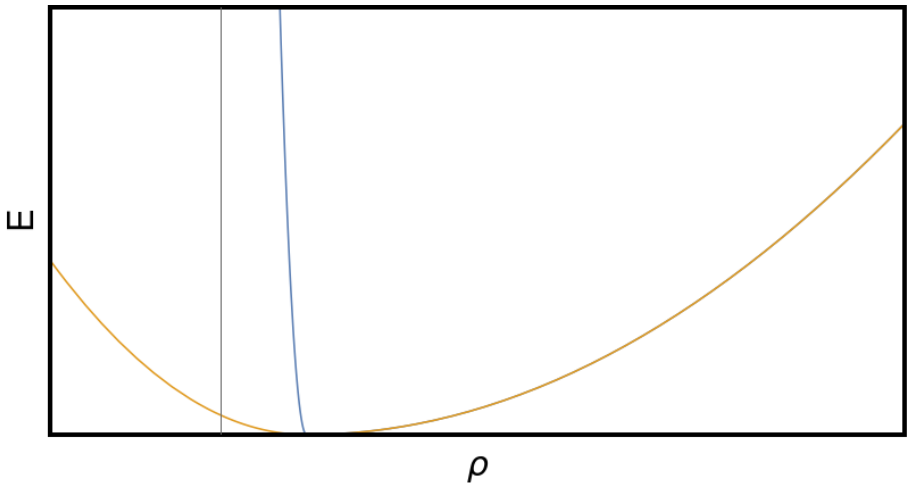

Figure 31: Free energy near the gas minimum as function of the density ρ for $\phi = 0$. The blue curve shows the steep profile when including the gas free energy patch. Parameters: $\lambda_0 = 0.2$, $\lambda_1 = 0.1$, $\lambda_2 = 0.1$, $\lambda_3 = 0.1$, $\rho_1 = 0.001$, $\rho_2 = 0.8$, $\rho_3 = 1.2$, $E_0 = 0.0001$.

Similar to Eqn.(3.22), to accounts for the energy penalty in creating the interfaces below form of inerfacial energy is used. For convenience we employ the squared gradient of each concentration,

$$f_{Inter} = \sum_{i=1,2,3} \left(\frac{\kappa_i}{2} (\nabla C_i)^2 \right), \tag{3.61}$$

where the parameters $\kappa_1, \kappa_2, \kappa_3$ allow to tune the width of the diffuse interfaces and the three surface tensions.

3.10.1 Derivation of the pressure tensor

The chemical potentials μ_ρ and μ_ϕ are obtained directly by placing the improved free energy in Eq.(3.28), (3.29) and has the following form:

$$\mu_\rho^{Bulk} = \sum_{i=1,2,3} \left(\frac{\delta F_{Bulk}^{in}}{\delta C_i} \frac{dC_i}{d\rho} \right) + \sum_{i=1,2,3} \left(\frac{\delta F_{Bulk}^{out}}{\delta C_i} \frac{dC_i}{d\rho} \right) + \frac{\delta F_{Bulk}^{gas}}{\delta \rho} \tag{3.62}$$

and

$$\mu_{\phi}^{Bulk} = \sum_{i=1,2,3}\left(\frac{\delta F_{Bulk}^{in}}{\delta C_i}\frac{dC_i}{d\phi}\right) + \sum_{i=1,2,3}\left(\frac{\delta F_{Bulk}^{out}}{\delta C_i}\frac{dC_i}{d\phi}\right) \tag{3.63}$$

where

$$\frac{\delta F_{Bulk}^{in}}{\delta C_i} = \lambda_i C_i(1 - 3C_i + 2C_i^2), \tag{3.64}$$

$$\frac{\delta F_{Bulk}^{out}}{\delta C_i} = \begin{cases} \lambda_0 C_i(1 - 3C_i + 2C_i^2) & \text{if } C_i < 0 \text{ and } C_i > 1 \\ 0 & \text{otherwise} \end{cases} \tag{3.65}$$

and

$$\frac{\delta F_{Bulk}^{gas}}{\delta \rho} = \begin{cases} \frac{\rho-\rho_1}{\sqrt{\rho(2\rho_1-\rho)}}\frac{E_0}{\rho_1} & \text{if } \rho < \rho_1 \\ 0 & \text{otherwise} \end{cases} \tag{3.66}$$

The differentials of the concentrations C_1, C_2 and C_3 by the fields ρ and ϕ are constant terms, given by:

$$(dC_1)/(d\rho) = 2/\Delta \tag{3.67}$$

$$(dC_2)/(d\rho) = -1/\Delta \tag{3.68}$$

$$(dC_3)/(d\rho) = -1/\Delta \tag{3.69}$$

$$(dC_1)/(d\phi) = (\rho_3 - \rho_2)/\Delta \tag{3.70}$$

$$(dC_2)/(d\phi) = (\rho_1 - \rho_3)/\Delta \tag{3.71}$$

$$(dC_3)/(d\phi) = (\rho_2 - \rho_1)/\Delta \tag{3.72}$$

$$\tag{3.73}$$

where

$$\Delta = 2\rho_1 - \rho_2 - \rho_3. \tag{3.74}$$

For the gradient terms we apply fist the variable transformation again to define

$$\nabla C_1 = \frac{2\nabla\rho + (\rho_3 - \rho_2)\nabla\phi}{2\rho_1 - \rho_2 - \rho_3}, \tag{3.75}$$

$$\nabla C_2 = \frac{-\nabla\rho + (\rho_1 - \rho_3)\nabla\phi}{2\rho_1 - \rho_2 - \rho_3}, \tag{3.76}$$

$$\nabla C_3 = \frac{-\nabla\rho + (\rho_2 - \rho_1)\nabla\phi}{2\rho_1 - \rho_2 - \rho_3}, \tag{3.77}$$

Collecting the gradient terms we obtain the following expression for the interface part of the chemical potential

$$\mu_\rho^{Inter} = -\kappa_{\rho\rho}\nabla^2\rho - \kappa_{\rho\phi}\nabla^2\phi \tag{3.78}$$

and

$$\mu_\phi^{Inter} = -\kappa_{\rho\phi}\nabla^2\rho - \kappa_{\phi\phi}\nabla^2\phi \tag{3.79}$$

where the mixing coefficients are defined by

$$k_{\rho\rho} = \frac{4k_1 + k_2 + k_3}{(2\rho_1 - \rho_2 - \rho_3)^2}, \tag{3.80}$$

$$k_{\phi\phi} = \frac{k_1(\rho_3 - \rho_2)^2 + k_2(\rho_1 - \rho_3)^2 + k_3(\rho_2 - \rho_1)^2}{(2\rho_1 - \rho_2 - \rho_3)^2}, \tag{3.81}$$

$$k_{\rho\phi} = \frac{2k_1(\rho_3 - \rho_2) + k_2(\rho_3 - \rho_1) + k_3(\rho_1 - \rho_2)}{(2\rho_1 - \rho_2 - \rho_3)^2}, \tag{3.82}$$

The mixing coefficients are also employed in the definition of the pressure tensor, that can be

inferred from the relation $\nabla \cdot \mathbf{P} = \rho \nabla \mu_\rho + \phi \nabla \mu_\phi$ and takes the form

$$\begin{aligned} P_{\alpha\beta} &= p_0 \delta_{\alpha\beta} \\ &+ \kappa_{\rho\rho} \left[(\partial_\alpha \rho)(\partial_\beta \rho) - \left(\rho(\partial_{\gamma\gamma}\rho) + \frac{1}{2}(\partial_\gamma \rho)^2 \right) \delta_{\alpha\beta} \right] \\ &+ \kappa_{\phi\phi} \left[(\partial_\alpha \phi)(\partial_\beta \phi) - \left(\phi(\partial_{\gamma\gamma}\phi) + \frac{1}{2}(\partial_\gamma \phi)^2 \right) \delta_{\alpha\beta} \right] \\ &+ \kappa_{\rho\phi} \left[(\partial_\alpha \rho)(\partial_\beta \phi) + (\partial_\alpha \phi)(\partial_\beta \rho) \right. \\ &\quad \left. - \left(\rho(\partial_{\gamma\gamma}\phi) + \phi(\partial_{\gamma\gamma}\rho) + (\partial_\gamma \rho)(\partial_\gamma \phi) \right) \delta_{\alpha\beta} \right], \end{aligned} \tag{3.83}$$

where p_0 is the pressure in the fluid bulk

$$p_0 = \rho \mu_\rho^{Bulk} + \phi \mu_\phi^{Bulk} - f_{Bulk}. \tag{3.84}$$

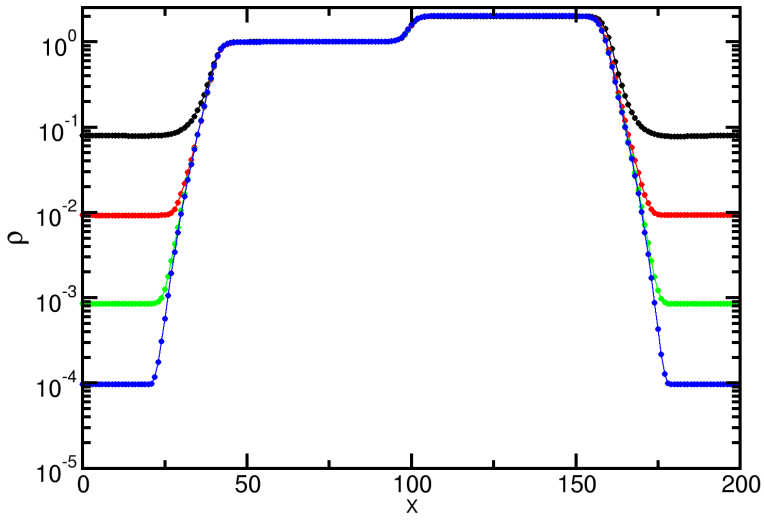

Figure 32: Density profiles for ternary system, with density ratio up to $\simeq 10^4$.

Apart from the better stability of the improved ternary free energy model, we can also have ever larger density contrast between liquid and gas phase ($\simeq 10^4$). Also the two liquids an be simulated at different densities, in all the three components (including all phases) can be at three different densities in the improved version of free energy model as shown in Fig.32. In the figure, the profiles of ρ along interfaces between fluids, placed in the sequence $gas(1)$, $liquid_1(2)$, $liquid_2(3)$,

$gas(1)$ are shown. Here, all four cases where the density of all three components is different and the ratio of density between two phase is up to $\simeq 10^4$.

3.11 Conclusion

A basic background to the computational approach has been introduced in this chapter. A general framework of the *lattice Boltzmann method (LBM)* along with different approaches to solve multiphase multicompoenent systems under LBM framework is discussed . The emphasis is given on the free energy method to solve *Ternary fluid systems*. We have thoroughly benchmarked our ternary high density ratio free energy model, and provided guidelines to select the free energy parameters for obtaining a wide range of surface tension combinations. We have quantified the deviations of the interface profile by measuring the *Deformation coefficient*, and systematically investigated 8 subspaces, covering relevant combinations of parameters. All data are reported in the AppendixA, including fitting functions to estimate the surface tensions. We also showed an improvement in the existing ternary free energy model. This improved model is more stable and can handle the fluid components at three different densities with larger density contrast between liquid and gas phase ($\simeq 10^4$) in the region of interest will be used later to study the drop collision study in chapter 6 and 7.

Chapter 4

Wetting boundaries for ternary lattice Boltzmann method

In this chapter we extend a recently proposed ternary free energy lattice Boltzmann model with high density contrast [141], by incorporating wetting boundaries at solid walls. The approaches are based on forcing and geometric schemes, with implementations optimised for ternary (and more generally higher order multicomponent) models. Advantages and disadvantages of each method are addressed by performing both static and dynamic tests, including the capillary filling dynamics of a liquid displacing the gas phase, and the self-propelled motion of a train of drops. Furthermore, we measure dynamic angles and show that the slip length critically depends on the equilibrium value of the contact angles, and whether it belongs to liquid-liquid or liquid-gas interfaces. These results validate the model capabilities of simulating complex ternary fluid dynamic problems near solid boundaries, for example drop impact solid substrates covered by a lubricant layer. The work presented here has recently been published in Physical Review E journal [7].

4.1 Introduction

Understanding the wetting and spreading properties of fluids on a solid boundary is key in many natural phenomena and technological applications such as, advanced oil recovery, the Water-Alternate-Gas (WAG) techniques are frequently employed to enhance the recovery [17]. The spilling of an oil layer at the surface of sea water strongly affects the production of marine aerosol

when rain drops impact on the oil layer [85]. In contrast, placing a lubricant layer on a rough solid is the key idea behind the recent development of Slippery Lubricant Impregnated Surfaces (SLIPS), allowing to virtually eliminate contact line [56] [114] pinning with applications in coatings and packaging.

In the past, work has been done using different approaches under lattice Boltzmann framework to simulate the wetting properties and contact line motion. For example, using the free-energy approach, in 2004 Briant et al investigated the applicability of lattice Boltzmann simulations to the problem of contact line motion in one and two component two phase flows [15] [121]. Latva-Kokko and Rothman in 2005 derived an estimate of the contact angle as a function of a wetting tendency of the wall using color-gradient-based LBM [64]. Based on a meanfield free-energy lattice Boltzmann method, the moving contact line problem of liquid-vapor interfaces was studied by Zhang and Kwok [147]. Furthermore, the multicomponent multiphase LBM proposed by Shan and Chen [111] was used in many studies of the contact line problems [89] [77] [51].

Although LBM has been successfully used in interface studies, existing LB methods are still subject to considerable disadvantages, such as restrictions. Thermodynamic stability, kinematic viscosity, density ratio between liquid and vapour phases, interface thickness and, in particular, low impact velocity for impinging on a solid surface. Consequently , the current LB formulations for multi-phase or multi-component multi-phase streams are not capable of resolving complex dynamics for wetting and spreading processes in a quantitative manner, and thus their implementations are primarily limited to the simulation of droplets sitting on the surface or displacing droplets due to external forces.

In this regard, we describe the implementation of three approaches adapted to ternary fluid systems. The approaches are: *Force method*, *Geometric extrapolation* and *Geometric interpolation*. For simplicity we consider boundaries aligned with the domain axis and located at half distance between lattice nodes, but all methods can be extended to solid structures with corners and wedges. In all methods we treat the first layer of solid nodes as ghost nodes, to store values of ρ and ϕ. These values are employed in the finite difference stencils to compute $\nabla\rho$, $\nabla\phi$, $\nabla^2\rho$ $\nabla^2\phi$, in order to evaluate the chemical potentials and the pressure tensor (Eqns. (3.32), (3.33), (3.38)) of the fluid near the solid boundaries, as illustrated in Fig.33(a).

Throughout the whole fluid domain, the forces are computed by numerically differentiating the pressure tensor in Eq.(3.17). As $\mathbf{P}$ is not defined on the solid nodes, its partial derivatives in the first fluid layer are computed differently. Specifically, near the solid boundaries we impose $\nabla \mathbf{P}_{\perp} = 0$ (perpendicular to the solid), while a one-sided biased gradient [68] is employed for the gradient $\nabla \mathbf{P}_{\parallel}$ (parallel to the solid), as illustrated in Fig.33(a). After the collision and streaming steps, standard bounce-back rules are applied [61].

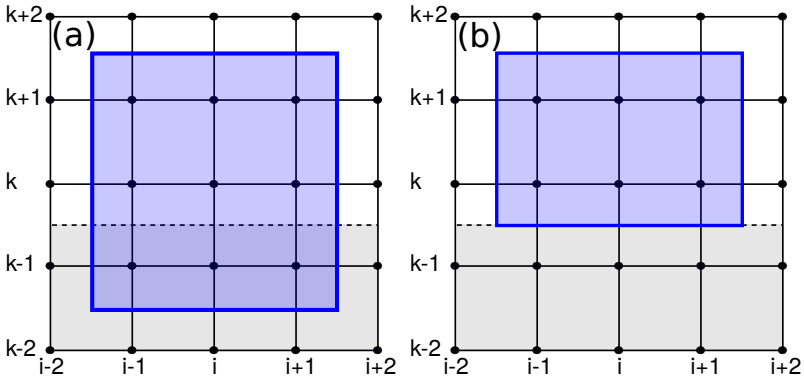

Figure 33: Sketch in 2D of the stencils employed for the computation of gradients. (a) The stencil for $\nabla\rho$, $\nabla\phi$, $\nabla^2\rho$ and $\nabla^2\phi$ is the same as in the fluid bulk, and relies on the quantities stored in the ghost nodes in the solid layer. (b) The stencil for $\nabla \mathbf{P}_{\parallel}$ excludes solid nodes, where $\mathbf{P}$ is not defined.

4.2 Forcing approach (Method 1)

The forcing method [44, 81] is inspired by pseudo-potential models for multicomponent fluids, where the liquid-solid interaction is introduced through a forcing term. In our implementation, the values of ρ and ϕ in the ghost nodes at the solid layer are constantly updated by copying the values in the first fluid layer. This procedure alone gives to the solid neutral wetting properties. In this method, higher or lower affinity of the fluid phases to the solid are obtained by adding a local force term:

$$\mathbf{F}_s(\mathbf{x},t) = \rho^{rel}(\mathbf{x}) \left(\kappa_\rho^w + \phi^{rel}(\mathbf{x})\kappa_\phi^w\right) \sum_i w_i s(\mathbf{x}+\mathbf{c}_i\delta t)\mathbf{c}_i. \tag{4.1}$$

where s is a function that takes a value of 1 on fluid nodes connected two lattice vectors away from solid nodes. In practice, for a flat substrate as in the sketch in Fig. 34, s takes value 1 on the second layer of fluid nodes only. We apply the force to the second fluid layer instead of the first one (as proposed in other works [81]), to improve the stability of the algorithm. One can easily

verify that force terms of smaller magnitude are necessary at the second fluid layer to obtain the same target contact angle.

The pre-factor $\rho^{rel}(\mathbf{x})\left(\kappa_\rho^w + \phi^{rel}(\mathbf{x})\kappa_\phi^w\right)$ accounts for the variation of the interaction strength as function of the fields ρ and ϕ, tuned by the parameters κ_ρ^w and κ_ϕ^w. We employ the rescaled fields $\rho^{rel}(\mathbf{x}) = (\rho(\mathbf{x}) - \rho_g)/(\rho_l - \rho_g)$ and $\phi^{rel}(\mathbf{x}) = \phi(\mathbf{x})/\chi$, which vary in the interval $[0, 1]$ and $[-1.1]$ respectively.

Furthermore, for the stability of the algorithm it is essential that no large forcing terms are applied in the gas phase ($[\rho, \phi] = [\rho_g, 0]$), which is achieved by multiplying both κ_ρ^w and κ_ϕ^w by $\rho^{rel}(\mathbf{x})$ in our approach. In absence of this precaution, large forcing terms would cause strong deviations of the gas density from the equilibrium thermodynamic value.

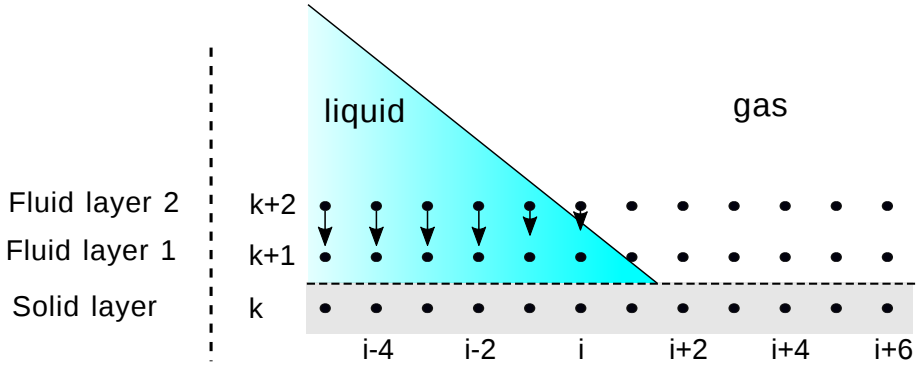

Figure 34: Sketch of the forcing terms acting near the liquid-liquid interface in contact to a solid boundary. The arrows represent the direction and magnitude of the local force Eqn. (4.1).

When defining a contact angle between two phases we indicate with the first index the phase in which a contact angle is measured, and with the second index the other phase. In our work we adopt the convention of measuring the angles in the liquid phase at liquid-gas interfaces, while at the liquid-liquid interface we measure the angle in the liquid with index 2. The following relations are implied: $\theta_{12} = \pi - \theta_{21}$, $\theta_{13} = \pi - \theta_{31}$ and $\theta_{32} = \pi - \theta_{23}$.

A typical dependence of θ_{21}, θ_{31} and θ_{23} from the parameters κ_ρ^w and κ_ϕ^w is reported in Fig. 35 (panels a-c), for the parameter set 1 in table 1. Contact angles are measured after equilibrating 2D sessile drops for each interface and fitting the drop interfaces with circular profiles. To keep the accuracy of the contact angle, across the whole parameter range, the drop area is fixed to $\simeq 100^2$l.u.^{2} while the size and aspect ratio of the simulation domain is adjusted to accommodate drops of different shapes.

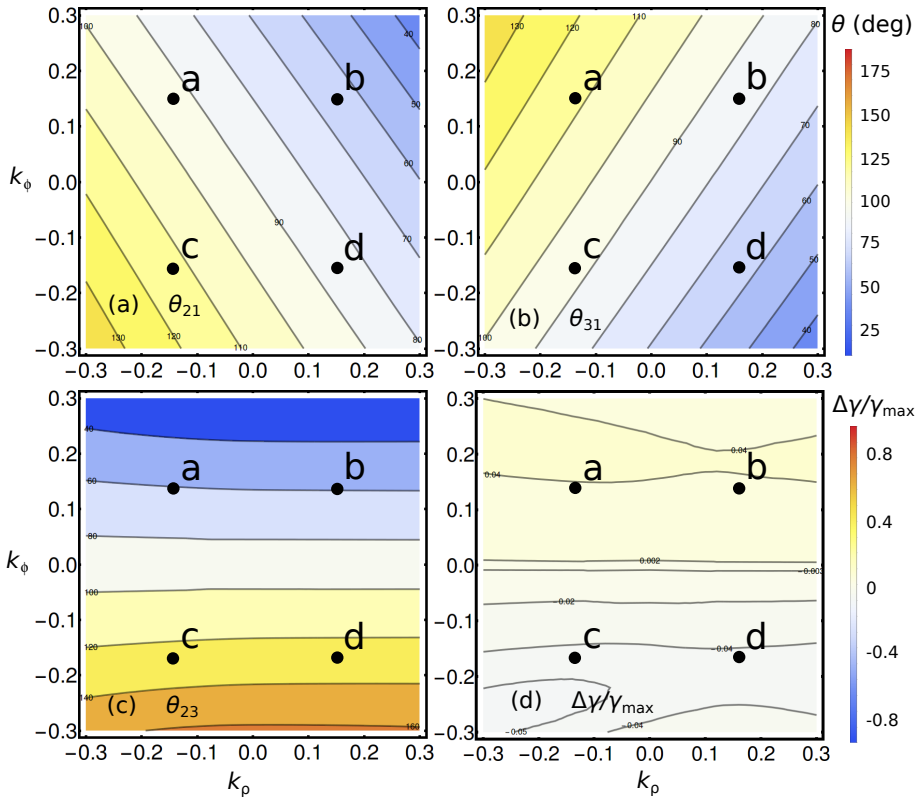

Figure 35: Colour maps of equilibrium contact angles measured from sessile drops, as function of κ_ρ^w and κ_ϕ^w. Panels a-c) refer to the interfaces $[1,2]$, $[1,3]$ and $[2,3]$ respectively. Panel d) reports the quantity $\Delta\gamma$, (Eqn. 4.2). The combinations of surface tensions are given by the first set in table 1. Black dots denoted by letters refer the the double emulsions depicted in Fig. 36.

The maps, as shown in Fig. 35, are specific for each set of free energy parameters. For example the inclination of the diagonal contour lines of θ_{21}, θ_{31} depends on the value of the surface tension for each interface. θ_{23} instead is predominantly a function of κ_ϕ^w, with only a residual dependence on κ_ρ^w in the region of small κ_ϕ^w.

On ideal surfaces the combinations of contact angles are not independent, but obey the Girifalco-Good relation [35], which according to our convention reads

$$0 = \Delta\gamma = \gamma_{23}\cos\theta_{23} - \gamma_{13}\cos\theta_{31} + \gamma_{12}\cos\theta_{21} \tag{4.2}$$

This condition is automatically satisfied by the force method, as can be deduced from panel d) in Fig. 35, which reports the variation of $\Delta\gamma$ on a scale set by the largest value surface tension in the system ($\gamma_{\max} \simeq 0.5$). Small deviations identified by the contour lines can be attributed to the uncertainties in the measurement of the contact angles. Figure 36 reports 4 examples of

double liquid emulsions in contact with a solid substrate were the wetting properties are given by $\kappa_\rho^w = \pm 0.15$, $\kappa_\phi^w = \pm 0.15$.

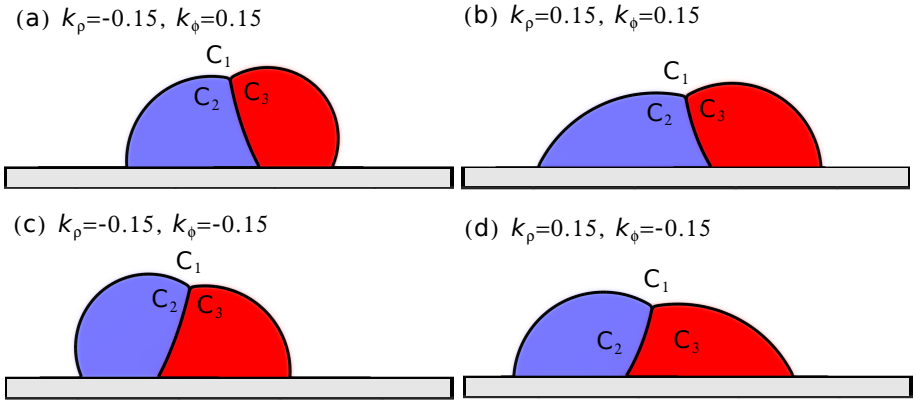

Figure 36: Double emulsions in contact to a solid surface in mechanical equilibrium. The combination of surface tensions are given by the first set in table 1, while the wetting properties are introduced with the force method, by setting: a) $\kappa_\rho^w = -0.15$, $\kappa_\phi^w = 0.15$, $\theta_{12} = 94.35$, $\theta_{13} = 113.19$, $\theta_{23} = 57.89$; b) $\kappa_\rho^w = 0.15$, $\kappa_\phi^w = 0.15$, $\theta_{12} = 64.96$, $\theta_{13} = 85.26$, $\theta_{23} = 56.15$; c) $\kappa_\rho^w = -0.15$, $\kappa_\phi^w = -0.15$, $\theta_{12} = 113.19$, $\theta_{13} = 94.35$, $\theta_{23} = 122.34$; d) $\kappa_\rho^w = 0.15$, $\kappa_\phi^w = -0.15$, $\theta_{12} = 85.26$, $\theta_{13} = 64.96$, $\theta_{23} = 124.15$;

4.3 Geometric approaches (Method 2 and 3)

We now introduce the two geometric approaches employed in our model. The key idea in both models is to manipulate the values of the fields in the ghost nodes at the solid boundaries according to a geometrical criterion, in order to reproduce a prescribed contact angle. In both cases, the ternary implementation requires us to identify in advance the correct interface, in order to select the correct target contact angle. This step is performed by implementing a set of rules that combine the local value of ρ and ϕ and of their gradients parallel to the solid $\nabla_\parallel \rho$ and $\nabla_\parallel \phi$:

$$\begin{cases} \text{if } |\nabla_\parallel \rho|/|\nabla_\parallel \phi| < 0.01(\rho_l - \rho_g)/\chi & \text{set interface 2-3} \\ \text{if } \nabla_\parallel \rho \cdot \nabla_\parallel \phi < 0 & \text{set interface 1-3} \\ \text{if } \nabla_\parallel \rho \cdot \nabla_\parallel \phi > 0 & \text{set interface 1-2} \\ \text{if } \rho > \rho_l/2 \text{ and } \phi < -0.95\chi & \text{set interface 1-3} \\ \text{if } \rho > \rho_l/2 \text{ and } \phi > 0.95\chi & \text{set interface 1-2} \end{cases}$$

This set of rules proves to be accurate in all our tests, even if the variation of ρ and ϕ is not strictly monotonous near the interface. An alternative approach consists in weighting the contact angles based on the local concentration fields [146].

4.3.1 Geometric extrapolation

We now introduce our ternary implementation of the method proposed by Ding and Spelt [25]. The key idea is to compute the normal vector of a fluid interface in contact with the solid surface from the gradient of a field: $\mathbf{n}_s = \nabla c/|\nabla c|$. We employ $c = \rho$ at any liquid-gas interface, and $c = \phi$ for the liquid-liquid interface. Referring to the sketch of the contact line geometry in Fig. 37, $\mathbf{n}$ defines the vector normal to a plane solid surface, while the perpendicular and parallel components of a field gradient can be expressed as $\nabla c_\perp = \mathbf{n} \cdot \nabla c$ and $\nabla c_\parallel = |\nabla c - (\mathbf{n} \cdot \nabla c)\mathbf{n}|$.

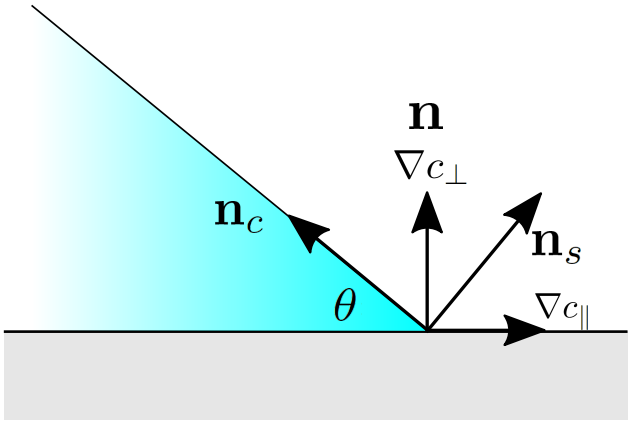

Figure 37: Sketch of the main vectors defined by fluid interface near the contact line.

In the algorithm, first the parallel component of the gradient $\nabla c_\parallel$ is measured along the surface, and then it is employed to reconstruct the perpendicular component of the gradient $\nabla c_\perp$. For a diffuse interface forming an angle θ with the solid surface, the relation between components of the field gradients is

$$\nabla c_\perp = \tan\left(\frac{\pi}{2} - \theta\right) \nabla c_\parallel. \tag{4.3}$$

For example, in a 2D lattice addressed by the indices i, k, let us assume the layer k represents a solid surface for any i, while the layer $k+1$ represents the first fluid layer. The values of the field $c_{i,k}$ are computed by extrapolating the from the field value in the above layer

$$c_{i,k} = c_{i,k+1} + \nabla c_\perp, \tag{4.4}$$

where c represents either ρ or ϕ. For this reason, we denote this method as *geometric extrapolation*.

The 3D implementation differs from the 2D case only by replacing the component parallel to the surface of the concentration gradients with the norm of the two components in the plane. For example, if x and y define the coordinates in the plane, we have $|\nabla_{\parallel} c| = \sqrt{(\nabla_x c)^2 + (\nabla_y c)^2}$ for a solid plane at $z = \text{const}$. The correction applies both in the determination of the interface, and in the reconstruction of the perpendicular component $\nabla_{\perp} c$.

In contrast to the force approach, there is no limitation in choosing any combination of contact angles, keeping in mind that a physically consistent set of contact angles needs to fulfil the Girifalco-Good relation in Eqn. (4.2). We will take advantage of combinations of angles not fulfilling Eqn. (4.2) to simulate self propelled bi-slugs in a channel in Sec. 4.5.

4.3.2 Geometric interpolation

This third method is inspired by the algorithm proposed by Lee and Kim [66]. Here the key idea is to interpolate the field values from the upper layer, where the interpolating point is shifted according to the slope of the liquid interface. For a few special values of contact angles the slope of the interface connects to lattice nodes, and the required values of the field correspond exactly to the values already stored. Let us consider a 2D example: for the three nearest lattice nodes along the direction i of the solid surface we can simply assign

$$
\begin{aligned}
c_{i,k}|_{\theta \simeq 18.43^\circ} &= c_{i-3,k+1} \\
c_{i,k}|_{\theta \simeq 26.56^\circ} &= c_{i-2,k+1} \\
c_{i,k}|_{\theta = 45^\circ} &= c_{i-1,k+1} \\
c_{i,k}|_{\theta = 90^\circ} &= c_{i,k+1} \\
c_{i,k}|_{\theta = 45^\circ} &= c_{i+1,k+1} \\
c_{i,k}|_{\theta \simeq 153.43^\circ} &= c_{i+2,k+1} \\
c_{i,k}|_{\theta \simeq 161.56^\circ} &= c_{i+3,k+1}.
\end{aligned}
\tag{4.5}
$$

For any other slope instead we linearly interpolate the values of the two closest nodes. For this reason we denote this method as *geometric interpolation*. As shown in Fig.38 (a), in the 2D implementation we compute the distance of the interpolating point from the node i as $l_{\|} = \tan(\theta - \pi/2)$. In a local coordinate system centred in the node (i, k), the interpolating points are located at $l_0 = \text{floor}(l_{\|})$ and $l_1 = \text{floor}(l_{\|}) + 1$, and their lattice indices are $i_0 = i + l_0$ and $i_1 = i + l_1$. Considering that $l_1 - l_0 = 1$, the linear interpolation scheme is:

$$c_{i,k} = (c_{i_1,k+1} - c_{i_0,k+1})l_{\|} + (l_1 c_{i_0,k+1} - l_0 c_{i_1,k+1}). \tag{4.6}$$

The 3D implementation requires the selection of an appropriate support for the interpolation in the plane. As in the previous case, let us assume a solid surface defined by the plane plane $z = \text{const}$, where solid nodes have constant index k and the first fluid layer is at $k + 1$. Also, the lattice nodes in the planes parallel to the solid surface are addressed by the indices i and j. The location of the interpolating points is determined by the gradients of the concentration field in the plane $l_x = l_{\|}\nabla_x c/|\nabla c_{\|}|$ and $l_y = l_{\|}\nabla_y c/|\nabla c_{\|}|$. The simplest interpolation scheme for a plane in 3D requires three points. In our implementation we select the three furthest points (out of four) from the location (i, j) in a planar square lattice (Fig.38(b)).

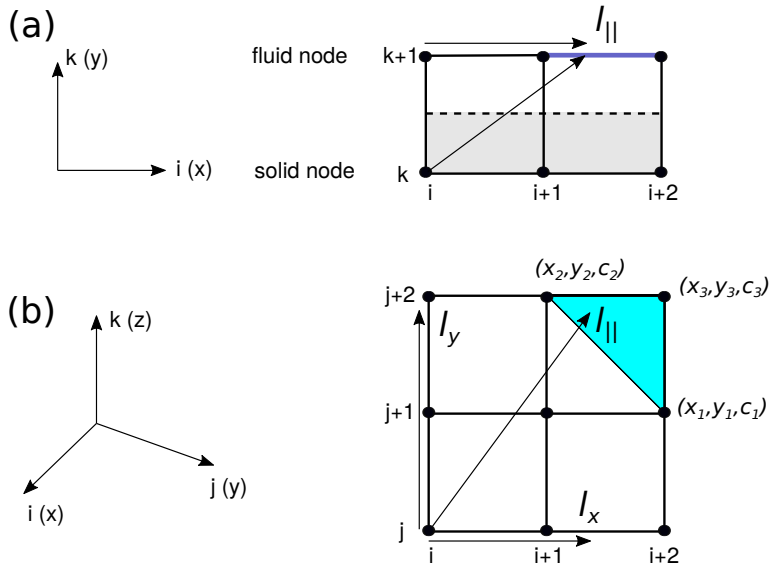

Figure 38: Sketch of the *geometry interpolation* boundaries: a)2D implementation: the selected interval for the linear interpolation is highlighted. b)3D implementation: the selected triangle for the planar interpolation is highlighted.

Once the three points are selected, we consider the three triplets (x_1, y_1, c_1), (x_2, y_2, c_2) and (x_3, y_3, c_3), describing a plane, where the third coordinate represents the value of the concentration c in each point. The following interpolation scheme is employed to compute the field values in the ghost node located in (i, j, k):

$$c_{i,j,k} = \frac{Al_x + Bl_y + C}{D}, \tag{4.7}$$

where A, B, C, D are the polynomials

$$\begin{aligned}
A =& y_2c_1 - y_3c_1 - y_1c_2 + y_3c_2 + y_1c_3 - y_2c_3 \\
B =& -x_2c_1 + x_3c_1 + x_1c_2 - x_3c_2 - x_1c_3 + x_2c_3 \\
C =& -x_3y_2c_1 + x_2y_3c_1 + x_3y_1c_2 \\
& - x_1y_3c_2 - x_2y_1c_3 + x_1y_2c_3 \\
D =& -x_2y_1 + x_3y_1 + x_1y_2 - x_3y_2 - x_1y_3 + x_2y_3.
\end{aligned} \tag{4.8}$$

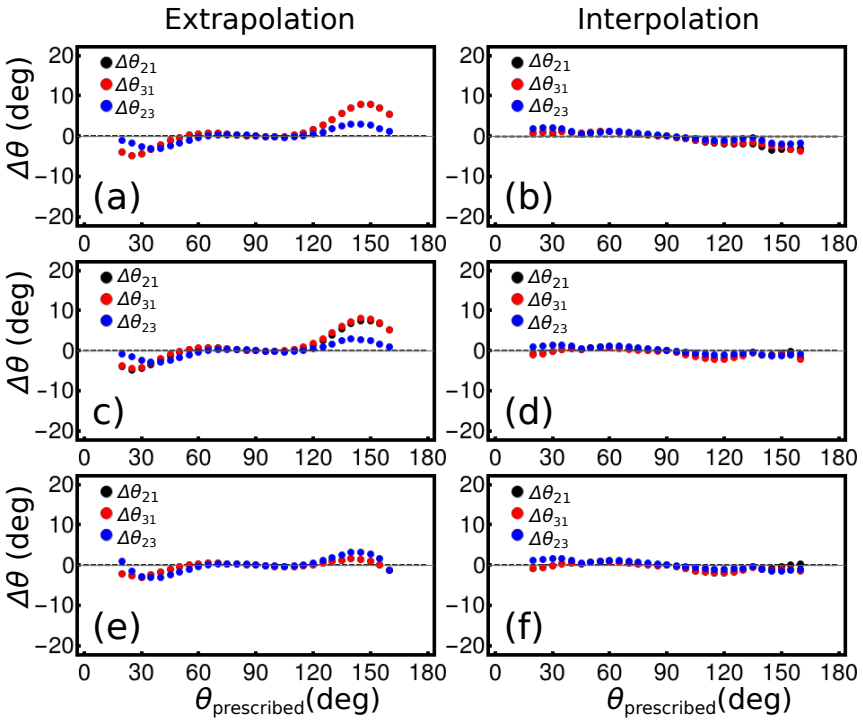

Figure 39: Deviation of contact angles θ_{21}, θ_{31} and θ_{23}, measured on sessile drops in mechanical equilibrium from the prescribed values. Results for the *geometric extrapolation* method (left column) and the *geometric interpolation* method (right column). The interfacial properties correspond to set 1 (first row); set 2 (second row); and set 3 (first row) listed in table 1.

In Fig.39, we have assessed the accuracy of both geometric methods by simulating sessile drops in mechanical equilibrium for each fluid-fluid interface and comparing the parameter sets 1, 2 and 3 in table 1. The simulation setup and analysis are the same as previously employed to validate the force method. In the intermediate range of angles $[60°, 120°]$ both methods show good agreement, with deviations below $1°$, while for larger and smaller angles the *geometry interpolation* method is to be preferred. In view of this result, we discard the *extrapolation* in favour of the *interpolation* method for the remaining tests.

4.4 Capillary filling

To assess the dynamic properties of fluid interfaces, we simulate the capillary filling of a channel by a liquid. The problem was studied independently by Richard Lucas [72] and Edward Washburn [136]. It represents a classical benchmark for wetting boundary conditions in lattice Boltzmann implementations [138, 70, 71], as it provides analytical or semi-analytical expressions to compare. Let us now consider the system sketched in Fig.40, consisting of a $2D$ channel of height H, initially containing a gas phase only, and filled by liquid. The liquid-gas surface tension is denoted by γ, while the liquid forms a contact angle θ with the solid.

In a 2D geometry, the resulting capillary force at the two contact points of the liquid interface with the channel walls is:

$$F^{\text{cap}} = 2\gamma \cos\theta. \tag{4.9}$$

Except for the initial transient time, the resisting force is mainly provided by viscous dissipation. In virtue of the high density ratio in our model, we neglect the dissipation in the gas phase [26]. For a liquid of viscosity $\mu = \rho_l \nu$ forming a column of length x, and assuming a fully developed Poiseuille velocity profile, we have a resisting force

$$F^{\text{visc}} = -\frac{12\rho_l \nu x \dot{x}}{H}, \tag{4.10}$$

where $\dot{x}$ is the mean velocity of the fluid column, corresponding to the velocity of the liquid-gas

interface. Combining Eqns. (4.9) and (4.10) lead to the so-called Washburn law

$$x(t) = K\sqrt{(t - t_0)}, \tag{4.11}$$

where t_0 is a time constant. The pre-factor

$$K = \sqrt{\frac{\gamma \cos\theta H}{3\nu\rho_l}}, \tag{4.12}$$

is a function of material and geometric parameters only: the surface tension γ, the equilibrium contact angle θ, the kinematic viscosity ν of the liquid and channel height H.

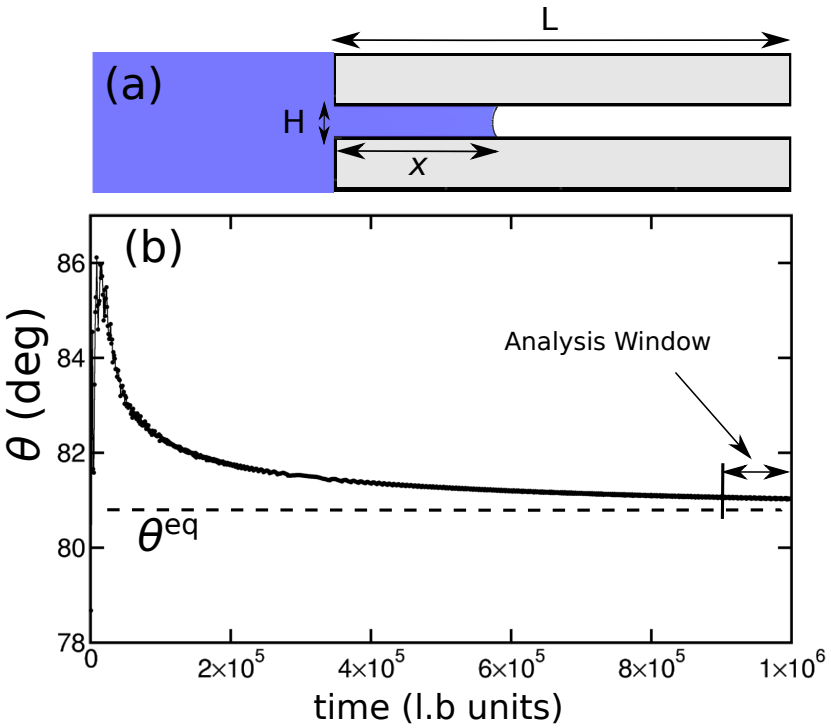

Figure 40: Capillary filling: (a) Sketch of the simulation setup; (b) Dynamic contact angle vs simulation time for the *Geometric Interpolation* method and $\theta_{21} = 80°$. The analysis window consists of the last 10% of the simulation time, over which the dynamic contact angle is averaged.

In our simulations the channel length is $L = 2000$ l.u. and the height $H = 70$l.u. The channel is preceded and followed by reservoirs filled with liquid and gas respectively. This geometry has been previously employed [26] to minimise the viscous drag of the fluid outside the channel. Throughout all simulations we employ the first parameter set in table 1, for which $\gamma = 0.414$ in both liquid-gas interfaces, and set $\beta = 0.5$, giving a kinematic viscosity $\nu = 1/6 = 0.16667$.

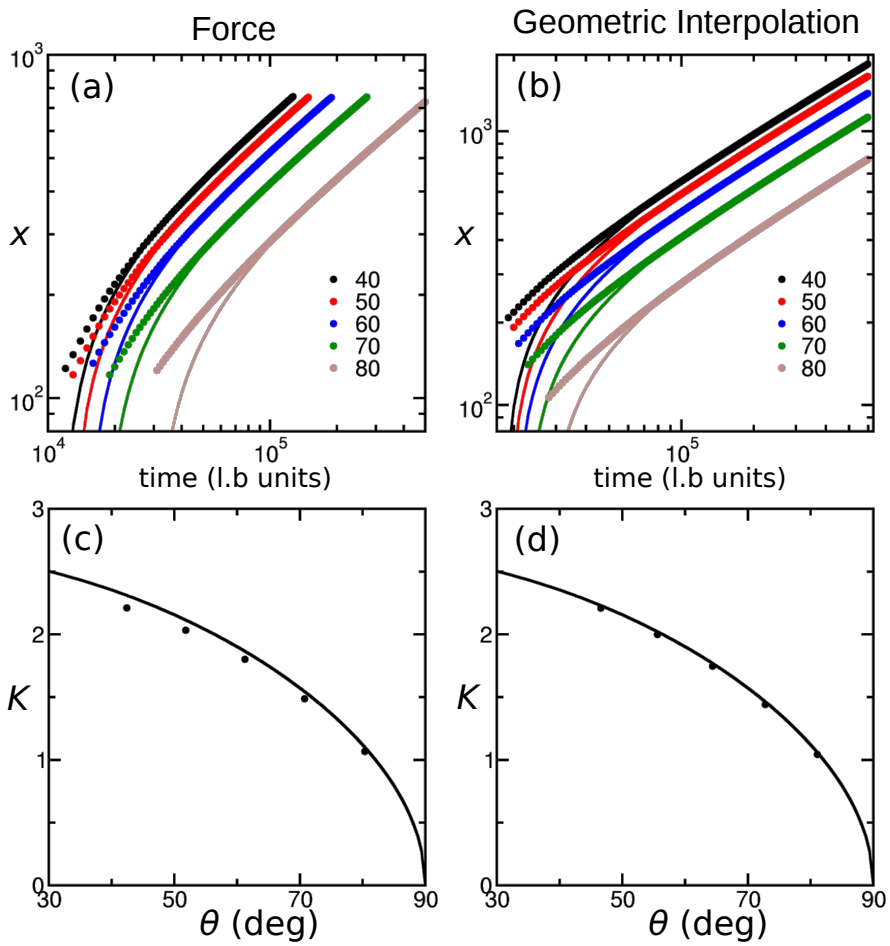

Figure 41: Capillary filling: (a,b) Length of the liquid column vs simulation time for contact angles $\theta = 40°, 50°, 60°, 70°$ and $80°$. Dots represent numerical measure of position of front of liquid column, while continuous lines represents the Eqn.4.11 for the fitted values of K and t_0 within the analysis window (last 10% of the simulation time). (c,d) Pre-factor K for the Lucas-Washburn law. Dots represent fits to the numerical results, the continuous line is the model prediction (Eqn. Washburn (4.12)). Left panels (b,d) are obtained employing the *force* method, while right panels (c,e) employ the *geometric interpolation* method.

In Fig. 41 (a,b) we report the time evolution of the front of the liquid column for contact angles varied in the range of $[30°, 80°]$, comparing the *force* and *geometric interpolation* methods. The initial stage of the invasion is not well described by Wahsburn law [26]. As shown in Fig. 40 (b), during the filling process the dynamic angle varies over time, and approaches the equilibrium value only asymptotically. Consequently, Washburn law, Eqn. 4.11 describes accurately only the asymptotic regime, while for the initial and transient regimes inertia and viscous bending should also be considered.

As in this specific test our main interest is comparing the accuracy of the *force* and *geometric*

interpolation methods, we analyse the last 10% of the simulation time, where the variation of dynamic angles are below one degree, and we can assume Eqn. 4.11 to be sufficiently accurate. To eliminate systematic sources of errors, we compute the average dynamic angle $< \theta >$ within the analysis window, and replace with it the angle θ in Eqn. (4.12). Furthermore, we perform a parametric fit of the numerical data within the analysis window with Eqn. (4.11), and compute the time constant t_0 and the pre-factor K. After placing the value of t_0 and K, we plot Eq.(4.11) represented by continuous lines together with numerical data shown by dots in Fig. 41 (a,b). Both the curves overlap with each other especially towards the end of the simulation time, where the effect of dynamic contact angle and inertial forces become negligible.

In Fig.41(c,d) we compare the values of K to the model (Eq.(4.12)). The data for the *force* method show small deviations between predicted and measured values of the prefactor. The deviations increase proportionally with the magnitude of the forcing term, which increases as θ decreases. This suggests that the discrepancy is related to spurious velocities near the walls, due the force term in the *force* method. In contrast, we observe no deviations for the *geometric interpolation*.

4.5 Self-propelled slugs

In this section we focus on a ternary-specific benchmark, consisting in a self-propelled train of drops (bi-slug) in a 2D channel. In experiments, a bi-slug with three finite contact angles can not self-propel, unless the Girifalco-Good relation, Eqn. (4.2), is broken. This may be done by introducing a step or gradient of wettability on the channel surfaces[29, 45]. Alternatively, at least one liquid phase must be completely wetting. This last condition was exploited by Bico and Queré to study experimentally in detail self propelled bi-slugs [9, 10]. Taking advantage of the *geometric interpolation* method, we can numerically introduce arbitrary contact angles in the system providing a controlled mechanism for self-propulsion.

The simulation geometry, sketched in Fig. 42 (a), consists of a periodic channel of height $H = 39$ l.u. It contains a train of drops having equal volumes. For simplicity, we assume the length $L_1 = L_2$ of each liquid drop, approximated by the length of the equivalent rectangle having the same area and height H. The total length of the periodic channel is adjusted in each simulations to allow the presence of at least 200 lattice units of gas at the two sides of the bi-slug.

4.5.1 Bi-slug dynamics

In long trains of drops the driving force is almost completely dissipated in the liquid bulk. Consequently the velocity is small and the contact angles remain close to the equilibrium value. According to the convention for contact angles employed in this work, the surface tension unbalance is expressed by

$$\Delta\gamma = \gamma_{23}\cos\theta_{23} - \gamma_{13}\cos\theta_{31} + \gamma_{12}\cos\theta_{21}, \tag{4.13}$$

and the driving force is

$$F^{\text{cap}} = 2\Delta\gamma, \tag{4.14}$$

Assuming a Poiseuille flow profile in the bi-slug, and liquids with equal viscosity, the viscous force is

$$F^{\text{visc}} = -\frac{12\rho_l\nu L\dot{x}}{H}, \tag{4.15}$$

where $\dot{x}$ is the mean fluid velocity, associated to the velocity of the center of mass of the bi-slug.

In the limit of long trains ($L = L_1 + L_2 >> H$) the viscous bending can be neglected, and the equation of motion for the center of mass is [26, 29]

$$\rho_l LH\ddot{x} = F^{\text{cap}} + F^{\text{visc}}. \tag{4.16}$$

By introducing Eqns. (4.14) and (4.15) into Eqn. (4.16), we obtain

$$\ddot{x} + \frac{12\nu}{H^2}\dot{x} - \frac{2\Delta\gamma}{\rho_l LH} = 0. \tag{4.17}$$

Integrating once with time and imposing $\dot{x}(0) = 0$, we obtain an exponential relaxation of the bi-slug velocity to the steady velocity v_∞

$$\dot{x}(t) = v_\infty(1 - e^{\frac{-t}{\tau_{\text{rel}}}}), \tag{4.18}$$

where the steady velocity is

$$v_\infty = \frac{H\Delta\gamma}{6\rho_l\nu L} \tag{4.19}$$

and the relaxation time is

$$\tau_{\rm rel} = \frac{H^2}{12\nu}. \tag{4.20}$$

Integrating Eqn. (4.18) once again with time we obtain the displacement of the center of mass with respect to its initial position $x(0)$

$$x(t) = x(0) + \tau_{\rm rel} v_\infty (e^{\frac{-t}{\tau_{\rm rel}}} + \frac{t}{\tau_{\rm rel}} - 1). \tag{4.21}$$

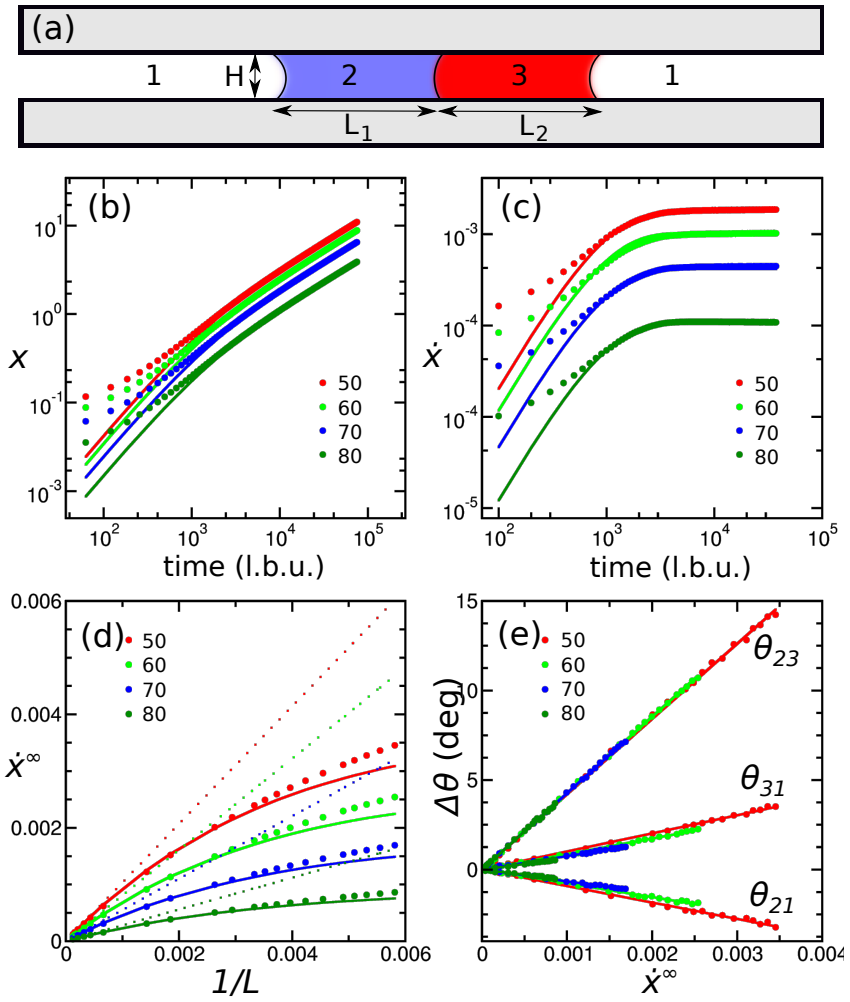

Figure 42: Self- propeled bi-slugs: (a) Sketch of the simulation setup. The other panels report data for bi-slugs defined by the first parameter set in table 1. We set $\beta = 0.5$ and contact angles θ_{23}=θ_{21}=θ_{31} $= 50°, 60°, 70°, 80°$. (b,c) Transient regime in the motion of the bi-slugs of length $L = 1500$l.u., showing (b) the position of centre of mass, where dots represent numerical measurement, while continuous lines represents the Eq. (4.21) and (c) the velocity of the center of mass, where dots represent numerical results, and continuous lines represents the Eq. (4.18) (d) The measured steady velocity $\dot{x}_\infty$ as function of $1/L$. (e) The dynamic contact angles for the three interfaces as function of $\dot{x}_\infty$.

In the simulation we initialise the bi-slug as two rectangular liquid drops in the beginning of the channel. Typically, during the first 10^3 steps of the simulation, the liquid interfaces quickly deform to approach the contact angle of the steady moving bi-slug, and initiate the self-propulsion mechanism. In Fig. 42 we compare the trajectory (panel (b)) and velocity (panel (c)) of a long train of drops ($L = 1500$l.u.), with Eqns. (4.21) and (4.18), for contact angles θ_{23}=θ_{21}=θ_{31} varied in the range $[50°, 80°]$. Eqns. (4.18) and (4.21) capture accurately the bi-slug dynamics after the first 10^3 time steps, for this reason, the initial part ($t < 10^3$) of the Fig. 42 (b,c) is not overlaping with the numerical results. A close inspection of panel (c) shows that after 10^4 time steps the bi-slug speed has fully reached the steady value v_∞.

In Fig. 42 (d) we report the steady velocity $\dot{x}_\infty$ of the bi-slug as function of L^{-1} for the same combinations of contact angles. We observe that $\dot{x}_\infty \simeq v_\infty$ (dotted lines) in the limit of long bi-slugs, while, as the bi-slugs shorten, $\dot{x}_\infty$levels off, implying the importance of additional channels for energy dissipation. To assess whether in our numerical model the additional dissipation originates predominantly from the viscous bending of the fluid interfaces, we measure dynamic angles for all the fluid interfaces, fitting the fluid interfacial profiles with circles [60]. By fitting the interface in the central region of the channel to a circle, as sketched below. We define the dynamic contact angle (θ, macroscopic) which is the angle of intersection this circle makes with the wall. Equilibrium contact angle is represented by θ_e (microscopic). In Fig.42(e) we report the contact angle difference $\Delta\theta = \theta(\dot{x}_\infty) - \theta(0)$, and observe a linear dependence with the bi-slug speed $\dot{x}_\infty$.

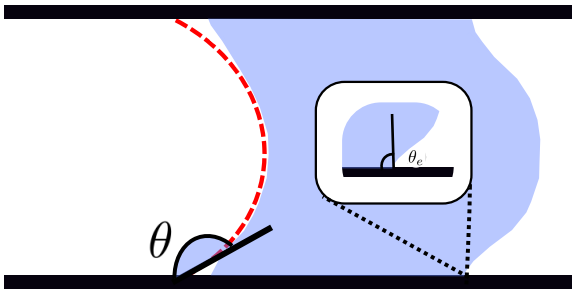

Sketch of fitting the fluid interfacial profiles with circle

Motivated by this observation, we perform linear fits and introduce the correction $\Delta\theta$ in the evaluation surface tension unbalance $\Delta\theta$, Eqn. (4.13). The corrected model is depicted by solid lines in Fig. 42 (d), and shows excellent agreement with the measured values of $\dot{x}_\infty$.

4.5.2 Contact line slip

We now further employ the numerical experiment of self-propelled bi-slugs to quantify the slip properties of our ternary model. While a similar analysis could be carried out also for the capillary filling, the bi-slug geometry has the advantage that trains of drops approach a steady motion with constant velocity, which can be measure more accurately. Furthermore, by tuning the length of the bi-slugs it is possible to vary accurately the velocity in a wide range.

As shown by Briant [13, 14], in multiphase Lattice Boltzmann models, the main slip mechanism relies on evaporation-condensation of the liquid interface, while in multicomponent models the contact line advances in virtue of the diffusion of the phase field [48, 60]. When coupling multiphase and multicomponent models, both evaporation/condensation and diffusion mechanisms occur at the liquid-gas interface. In contrast, at the liquid-liquid interface, only the diffusion mechanism is important, as the density ρ does not vary.

Following Cox's analysis [22, 23], the viscous bending of a fluid interface is described by

$$g(\theta, \lambda) - g(\theta_w, \lambda) = \mathrm{Ca} \ln(L_c/L_s), \tag{4.22}$$

where θ is a dynamic contact angle measured at a macroscopic distance from the surface, and θ_w is the equilibrium contact angle at the solid boundaries. The Capillary number $\mathrm{Ca} = \mu \dot{x}_\infty / \gamma$ represents the non-dimensional velocity of the interface, where the viscosity $\mu = \mu_{\mathrm{adv}}$ is referred to the invading fluid. In our simulation we identify the macroscopic distance L_c with the channel height H, and interpret the microscopic length L_s as an estimate for the slip length. The parameter $\lambda = \mu_{\mathrm{adv}}/\mu_{\mathrm{rec}}$ describes the ratio between the dynamic viscosity of the invading μ_{adv} and resisting μ_{res} fluids.

For liquid with equal density we have $\lambda = \nu_{\mathrm{adv}}/\nu_{\mathrm{rec}}$. Specifically, for the bi-slug simulations $\lambda = 1$ at the liquid-liquid interface, $\lambda \simeq 10^3$ for a liquid displacing the gas phase and $\lambda \simeq 10^{-3}$ for the gas displacing a liquid phase. The function $g(\theta, \lambda) = \int_0^\theta 1/f(\phi, \lambda) d\phi$ is a known function

of θ and λ, given in Refs. [22] and [23]:

$$f(\theta) = \frac{2\sin\theta\{\lambda^2(\theta^2 - \sin^2\theta) + 2\lambda[\theta(\pi-\theta) + \sin^2\theta] + [(\pi-\theta)^2 - \sin^2\theta]\}}{\lambda(\theta^2 - \sin^2\theta)[(\pi-\theta) + \sin\theta\cos\theta] + [(\pi-\theta)^2 - \sin^2\theta](\theta - \sin\theta\cos\theta)}. \quad (4.23)$$

To systematically explore the slip properties, we perform simulations for two sets of contact angles. In the first set we fix $\theta_{23} = 60^\circ$ and vary systematically $\theta_{21} = \theta_{31}$ in the range $[50^\circ, 120^\circ]$. In the second set we fix $\theta_{21} = \theta_{31} = 90^\circ$ and vary systematically θ_{23} in the range $[30^\circ, 150^\circ]$. The first set allows us to extract information for the liquid-gas interfaces, while the second set for the liquid-liquid interface.

For each combination of contact angles we simulate the motion of bi-slugs for a wide range of lengths and speeds. Furthermore we compute the capillary length Ca of the advancing fluid (which can be either a liquid or the gas phase, depending the interface considered), and evaluate the Cox function $g(\theta)$ in Eqn. (4.22) for the appropriate value of viscosity contrast λ. Due to the limited variation of the dynamic contact angles (in a range of a few degrees) for simplicity we perform a linear regression to evaluate the slope $m = \partial g(\theta)/\partial \mathrm{Ca} = \ln(L_c/L_s)$. Finally, introducing the geometric parameter $L_c = H = 39$, we estimate the slip length as $L_s = L_c \exp(-m)$.

In Fig. 43, we compare L_s for the three interfaces, as function of the equilibrium contact angle. More specifically, for our geometry we obtain θ_{21} (receding), θ_{31} (advancing) and θ_{23} (advancing for $\theta_{23} < 90^\circ$ and receding for $\theta_{23} > 90^\circ$). The slip length for the liquid-liquid interface shows a minimum for $\theta_{23} = 90^\circ$ (the data point not present, because for this combination of angles we have no net driving force $\Delta\gamma = 0$) and increases symmetrically for larger and smaller angles. In contrast the slip length for the liquid-gas interfaces shows a monotonic decrease as the equilibrium contact angle increases. For the last available data point, at $\theta = 120^\circ$, L_s is similar for all three interfaces, while for smaller angles L_s is significantly larger for the liquid-gas interfaces.

These results show that the slip properties in the system strongly depend on the nature of the fluid-fluid interface. In our tests the liquid-gas interfaces present a larger slip length (up to a factor 4) compared to the liquid-liquid interface, likely due to the combined effect of two distinct

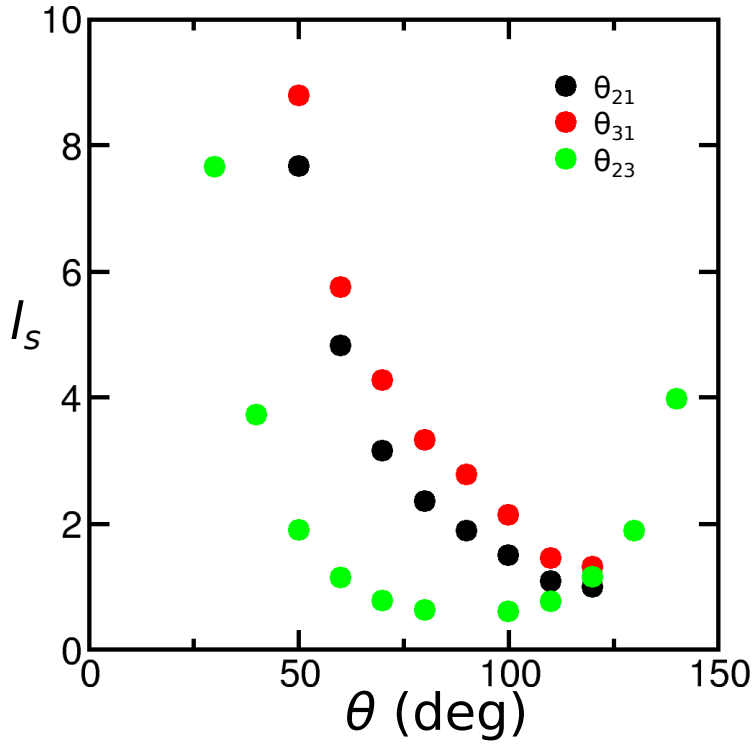

Figure 43: Estimated slip length vs. equilibrium contact angle for the liquid-liquid and the liquid-gas interfaces.

mechanisms operating on the density ρ and the field ϕ.

4.6 Conclusion

We have compared three methods for wetting of solid boundaries. Of the two geometric methods, geometric interpolation is significantly more accurate. The force method provides an useful alternative to geometric methods, as it does not require us to detect the fluid interface a priori, and automatically satisfies the Girifalco-Good relation, Eqn.(4.2). The benchmark on the dynamics of capillary filling shows that the force method is slightly less accurate than the geometric methods which we expect that the deviations are related to additional spurious velocities generated by the forcing terms. At the same time no spurious velocities are observed in the geometric methods. Furthermore the ternary specific benchmark using motion of self-propelled bi-slugs and its analytic modelling are performed. This shows the level-off of the velocity experimentally observed for shorter bi-slugs is captured in our simulations. Finally we have shown that coupling multiphase and multicomponent models leads to significant differences in the slip properties of liquid-liquid and liquid-gas interfaces.

Chapter 5

Background and simulation setup for immiscible droplet collisions

Having developed and thoroughly analysed the properties of our free energy lattice Boltzmann model, we then performed numerical experiments of collisions between two immiscible droplets surrounded by gas phase. For this study we will make use of the improved ternary free energy model (section.3.10) which allows better stability and more flexibility in the choice of the free energy parameters. In this chapter we discuss the fundamental background to droplet collision, simulation setup and relevant concepts which are needed to discuss collision result in chapter 6 and 7.

5.1 Motivation

The dynamic of droplet collision has received significant attention across different fields, ranging from natural phenomena to industrial processes. The early study of bouncing phenomena dates back to Lord Rayleigh, who observed that tiny droplets of rain bounce after contact with a pool of water rather than dive straight into it [99]. One of the most relevant industrial applications is spray drying, where by spraying solutions or slurries into hot, turbulent air in a spray-drying tower, particulate products are made. During the spray drying process droplets can collide with each other. These collision and their outcomes can have a significant effect on the process operation and on the powder properties, such as the size distribution and morphology. Understanding, and

predicting the outcome, of droplet collisions of identical and non-identical droplets is, therefore, of great interest in this area [31]. Another application where understanding droplet collisions is critical is in Ink-jet printing, as the coalescence of droplets impinging on paper affects the quality of ink-jet printing [106].

The droplet collision process is one of the most challenging topics in fluid dynamics and in the past few decades, extensive research has been conducted to understand the physics that determines the outcome of droplet collisions [86]. For a long time, it is the focus of a number of experimental [5],[97],[88] and analytical studies [103]. A significant amount of experimental work has been carried out to study collision dynamics of both miscible as well as immiscible liquids. For example a comparative study of collision outcomes between binary diesel droplets and collision of ethanol droplet with diesel droplet was studied by Rong-Horng Chen in 2007[18]. In 2005, an experimental study of collision between water and ethanol, because of the large surface tension difference was conducted by Gao [33] and between water and diesel oil by Chen [19], where they demonstrated the role of impact parameter (the vertical center to center distance between droplets) on the collision outcome. In 2010, C.Planchette shows the experimental investigations on droplet collisions using aqueous glycerol solutions and silicon oils. In his work, a new unstable mechanism called $crossing\ separation$ replacing reflexive separation was identified [94]. Since theoretical models are challenging and often rely on dramatic approximations [103] numerical simulations have gained significant attention to learn more about collision dynamics [78],[122] [90]. The advantage of numerical simulations is that they allow a great degree of freedom in the choice of initial boundary conditions as well as provide substantial information on the flow field, energy balance during the collision process.

The motivation to study the full wetting states of immiscible droplets comes from industrial applications. The encapsulation of water droplets by n-hexadecane can induce micro-explosions which enhance the effective burning rate in combustion engines [132]. The fundamental research on the combustion of water-oil emulsions was conducted by Ivanov and Nefedov in 1965, where he described the spontaneous microexplosion of suspended water/residual-oil emulsions during combustion process [47]. The microexplosion occurrence was responsible for the observed faster burning rate, better combustion characteristics and decreased emissions of smoke. Microexplosion was also observed by Lasheras et al. (1979) [63], Wang and Law (1985)[131], and Wang and

Chen (1996) [133] in their free-droplet experiments. A study focused to investigate the complex *encapsulation* morphology is performed by many researchers. In 2004, Wang and Lin performed an experimental study on combustion characteristics of freely falling immiscible droplets of water and hexadecane [132]. In this study, during the free fall of water and hexadecane droplets, two mode of merging were identified: adhesive or insertive mode. The insertive mode represent the collision outcome when one droplet is completely encapsulated by another droplet. *Insertion* and *encapsulation* are synonyms by convention. We adopt the term *encapsulation* in this study to indicate the same outcome when discussing our numerical results. The insertive outcome of collision were the dominating one in the experimental study by Wang and Lin when performed at high temperatures unless the water contact is really high as compared to n-hexadecane. The *insertive* and *adhesive* merging of the water and hexadecane droplets of identical and non-identical sizes shows that, as the droplet size for the pure fuels increases there is an increase in the ignition delay inside the combustion engine. Also the delay in the ignition for merged droplets were much longer as compare to the pure hexadecane for the same droplet size and it is shorter than that of the merged droplet for the same water content.

In 2018, M.Wöhrwag and co-authors have shown the lattice Boltzmann method using Carnahan-Starling equation of state is able to capture both adhesive and insertive/encapsulation collision outcomes [141]. They compared the numerical study with experimental result by Wang and Lin [132] for two collision scenarios. In their numerical study, they demonstrated that impact speed is critical for triggering encapsulation from the adhesive state at the parity of other parameters, and they described the general behavior of drop collisions.

In this research, we undertake a collision study using an improved version of the existing model which is more stable. This allows us to investigate the transition boundary between collision outcomes for a wider range of parameters such as surface tension combinations, impact speed, droplet size and viscosity. In this research, we illustrate how an additional control parameter, the surface tension ratio between two liquid gas interfaces, together with the spreading coefficient, affects the interfacial thermodynamics for encapsulation outcome.

5.2 Background of droplet collisions

The collision between two droplets is a complex phenomenon as it involves many different parameters. For example the colliding droplets can be made of different material (immiscible or miscible) and/or have different size, viscosity, surface tension properties. Additionally, the liquids involved can be complex, and the rheological properties can makes the system significantly more difficult to analyse. In systems far from thermodynamic equilibrium, as in diesel combustion chambers, the Marangoni effect, i.e. the difference of surface tension along the droplet surface, the evaporation and burning of the droplets, will also have a major influence on the collision dynamics and the overall collision process.

Depending on the range of physical parameters mentioned above, different collision outcomes can occur. The most studied case in literature involves collision of identical fluid droplets (droplets made of the same liquid). In this case typically four type of collision outcomes are identified [97],[74]. These are *Coalescence*, *Bouncing*, *Near head-on separation*, *Off-centre separation* and *Spatter*, and are usually reported as a function of Impact parameter (b: rescaled vertical center to center distance between droplets) and Weber number (We: Relative importance of the droplet's inertia compared to the surface tension). The typical outcome diagram is similar to the one reported below (Fig.44):

This diagram can be qualitatively explained by considering the roles of surface tension and inertia. In the relative lower range of We number (region I,II,III), the outcome of the collision is a non-monotonic shift from coalescence-bouncing-coalescence. In region I of coalescence, when the droplets approach each other with very small inertia the gas phase between the droplets is hardly able to resists the approaching droplets and the coalescence occurs. This happens as long as the distance between the colliding surfaces gets so small that the force of attraction between the molecules of the two droplets, i.e. the Van der Waals force, becomes dominant. In numerical methods, especially the diffuse interface methods [83],[46],[74], it is very challenging to simulate this region of droplet coalescence. This is because when the droplets are close enough, they "feel" each other due to their diffuse interface shapes which is much larger than the order of magnitude of the van der Waals forces $(10nm)$.

By increasing the inertia (higher We) we encounter region II, where the gas phase is trapped

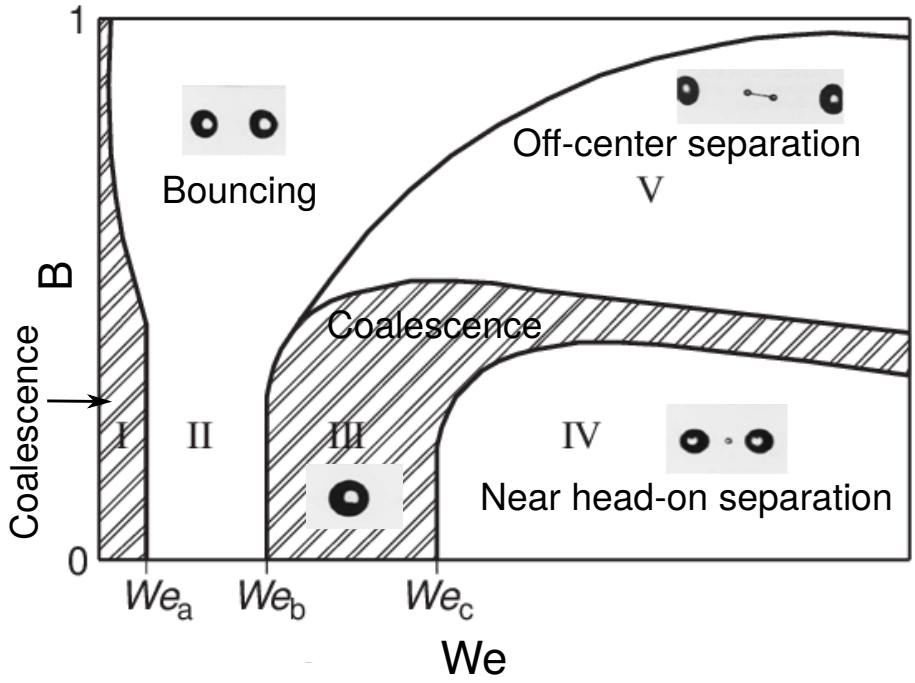

Figure 44: Collision phase diagram for identical fluid droplets [49], [104]

between the droplets and a high pressure builds up. The kinetic energy is temporally stored in the deformed surfaces, and returned to the droplets before coalescence can occur, forcing the droplets back and bounce away. On further increasing the We number, the droplets deform more substantially and the pressure in the liquids near the centre of the gas layer becomes higher and pushes the gas away from the centre. When a significant amount of the gas is drained the droplets are able to coalescence again.

In region IV, near head-on collision and at relatively higher We number the colliding droplets oscillate along the colliding axis. In this regime surface tension forces are not able to balance the inertial forces, so the coalesced droplet breaks up into smaller droplets. At relatively high inertia and high impact parameter in region V, separation can happen without oscillations as significant portions of the droplets only weakly interact with each other. The colliding droplets form a small coalesced portion which elongates into a thin thread before falling apart due to the inertia and centrifugal force.

Most previous studies focused on detecting and modeling the boundary between different regions in Fig.44 in the Weber number - Impact parameter phase space. For example, in 1990, based on the in-viscid assumption Ashgriz and Poo developed correlations for the boundary curves III-

IV and III-V [5]. In 1992 Jiang et al takes into account the viscous effect and purposed a the boundary curve for the region III-IV [49]. More recently (2016), Sommerfeld et al.[118] developed a composite universal model which is an extension and combination of the model of Ashgriz and Poo [5] and the model of Jiang et al.[49]. Study conducted by Qian and Law in 1997 shows that, for head-on collision in region III and IV, the dependency of critical Weber number is linear with respect to the Ohnesorge number.

Through the numerical studies the transition curve curves between coalescence and separation were inspected. Using Volume of Fluid (VOF) method, Rieber and Frohn. [102] presented numerical results in good agreement with experimental results from Ashgriz and Poo[5]. Using same VOF method, Saroka et al in 2012 found that for head-on collision the boundary between region III-IV depends on Reynolds number and the dependence decreases with increasing Reynolds number [107].

In the majority of previous works, the collision between droplets of the same liquids (hence same surface tension of each droplet) is the most studied. In contrast, the case of collision between immiscible droplets (of different liquids) gained much lower attention. The most relevant difference is that two immiscible liquids cannot coalesce, but can be observed in two metastable morphologies, namely adhesive and encapsulated. Bouncing is also a possible outcome, but it will likely occurs as a separation between adhesive droplets rather than break-up of a single distorted droplet.

Previously, collision studies were conducted as a function of Weber number and impact parameter. However, differing Oh can have a major effect on the collision result. In our analysis, we investigate the role of Oh in the dynamics of immiscible droplet collision, along with We and Impact parameter. In this study we have performed both $2D$ and $3D$ simulations. While $3D$ simulation results offer the possibility of quantitative comparison with experiments, systematic variations of system parameters in $3D$ is numerically too costly. Consequently, we complement our study with $2D$ simulations, which are helpful in identifying qualitative trends. The main difference between $2D$ and $3D$ is related to the surface-to-volume ratio. Typically, for small impact velocity and poorly adhesive droplets , the deformations during the collisions are small, and minimally alter the surface to volume ratio. In this regime we observe a good qualitative agreement between $2D$ and $3D$ simulations, and even quantitative in some observables. Conversely, in presence of strong

deformations, either because of larger impact velocity or because the configuration of global energy minimum is very different from the shape of two droplets just before the impact, the collision dynamics is can be significantly altered, leading to both quantitative and qualitative differences between $2D$ and $3D$ systems. In chapter 6, both $2D$ and $3D$ results will be discussed in the same context, and the main similarities and differences will be highlighted and discussed case by case.

5.3 Simulation setup

In all our simulation we set up a density ratio between the liquid droplets and gas phase of the order 10^3 (gas $(\rho_1) = 0.001$, $droplet_1(\rho_2)$= $droplet_2(\rho_3) = 1$). The simulation setup is sketched in Fig.45. The system consists of two immiscible droplets: $droplet_1$ and $droplet_2$ surrounded by gas. The droplets are initialized with sharp interface smoothed eight times with a numerical averaging procedure. This procedure approximates the typical concentration profiles at equilibrium, which because of the stiffness of the density gradient do not follow an analytic shape. As consequence of the large density ratio, droplets are initially subjected to strong oscillations of the concentration and density profiles, in the form of density waves propagating towards the droplet center. To ensure the stability of the algorithm we pre-equilibrate droplets of given size in separate simulations domains large twice the droplet diameter. The pre-equilibration lasts a sufficient number of time steps until the density oscillations decay as effect of viscous damping. The viscosity is also artificially increased during the equilibration to speed up the damping. The duration of the equilibration varying for droplet size and also whether the domain is two-dimensional $(2D)$ or three-dimensional $(3D)$. A detailed analysis of droplet equilibration before impact is reported in the below section 5.4. Once droplets a pre-equilibrated, the concentrations are patched into the simulation domain for the collision experiments, typically 5 diameters apart from each other. The typical domain size is 1600×1200 in $2D$ and $700 \times 320 \times 320$ lattice units in $3D$ for head on collision between identical droplets. While the main part of our investigation focuses on head-on collisions, we consider also off center collisions.

In the simulation setup shown in Fig.45, B is the vertical centre to centre distance between the two

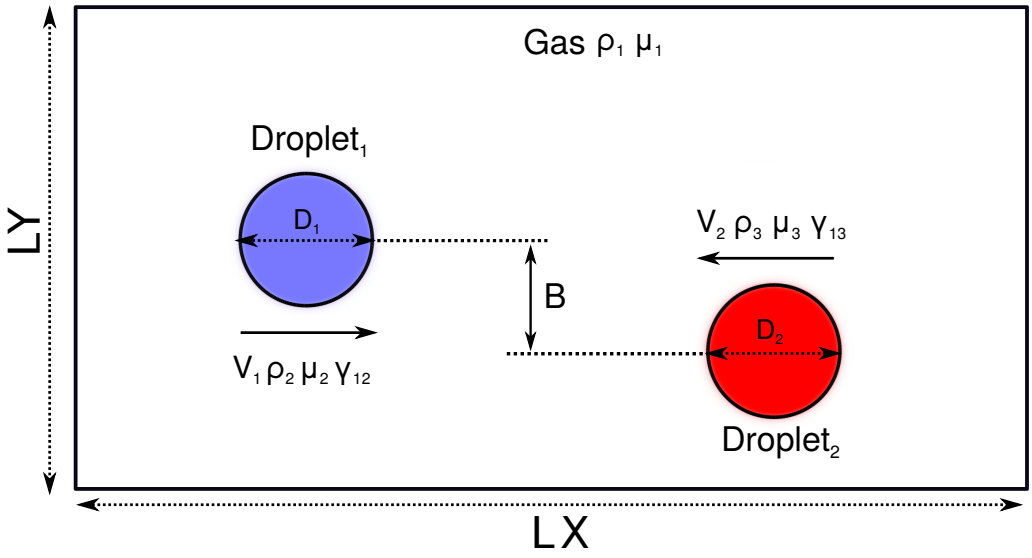

Figure 45: Setup of droplet collision, where the size of the domain is $1600 \times 1200 \times 1$ in $2D$ and $700 \times 320 \times 320$ in $3D$. The size of the droplet D=180 $l.u$ both in $2D$ and $3D$

droplets and is related to impact parameter χ as below:

$$\chi = \frac{2B}{D_1 + D_2} \tag{5.1}$$

where χ has a value between 1 and 0, where 1 shows collision when droplets just touches each other (grazing collision) and 0 represents a head-on collision. When the droplet are of equal size ($D_1 = D_2 = D$), the impact parameter has the form shown below:

$$\chi = \frac{B}{D} \tag{5.2}$$

In our preliminary benchmarks we have investigated the viscous drag exerted by the gas phase (at rest) on a moving drop, obtaining that for a typical initial velocity of centre of mass ($V_{com} = 0.0488 l.u$) during the fight time to reach the center of the domain (where the collision occurs) the reduction is less than 4%. More detailed analysis on the free flight of the droplet is shown in section 5.5. Although the difference is small, to improve the consistency in the estimate of Weber numbers (We) we measured the velocity of the center of mass at the time when velocity is assigned to the droplets *(t=0)*. Importantly, this model is not able to reproduce the formation of the gas layer when droplets are colliding, due to the diffuse nature of the liquid-gas interface. Therefore we are not able to observe an equivalent of region II of bouncing for droplets of the same liquid. Instead,

when analysing the collision mechanism, we observe a minimal dependence of the results while varying the gas density, as long as the ratio remains approximately of order $\sim 10^3$. Therefore in this work we assume the surrounding gas has a negligible effect on the collision dynamics, and will be neglected in the remaining of our analysis.

5.4 Droplet Equilibration

In drop collision study, before the droplets start approaching each other, we pre-equilibrate each droplet. This is done in a separate simulations domains which double in size as compared to the droplet diameter as shown in Fig.46.

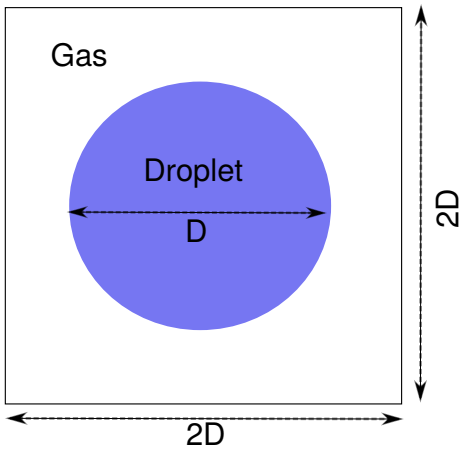

Figure 46: Set-up of equilibration of droplet before collision

In the plot shown in Fig.47, we show the evolution of the kinetic energy corresponds to different size of the droplet ranging from $R = 90 - 200$ lattice units $(l.u)$ during equilibration. It is observed, a large number of oscillations occur at the start which decay after certain time and stabilises to minimum value of kinetic energy. The duration of the oscillation depends on the size of the droplet. For example the droplets of smaller size reaches to its stable configuration much earlier as compared to larger droplets. The comparison of equillibation time in $2D$ w.r.t $3D$ setup at $R = 90$ l.u is shown in Fig.48. In $3D$, the droplet experience less oscillations and rest to its stable state earlier as compare to $2D$ setup.

Therefore, for the drop collision study, before the two droplets starts approaching each other, they are equilibrated until the surface deformation or interface fluctuations are damped and the drops are in a rest state. The equilibration time depends on the size of the droplet and whether the

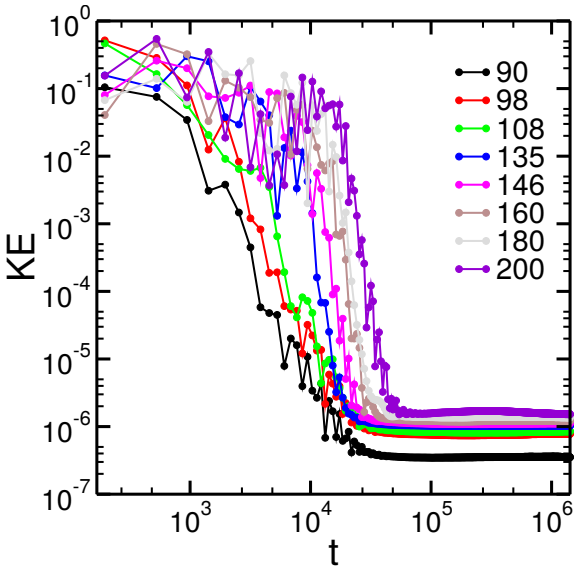

Figure 47: Time evolution of kinetic energy (KE) during equillibation of droplet at different droplet size in $2D$

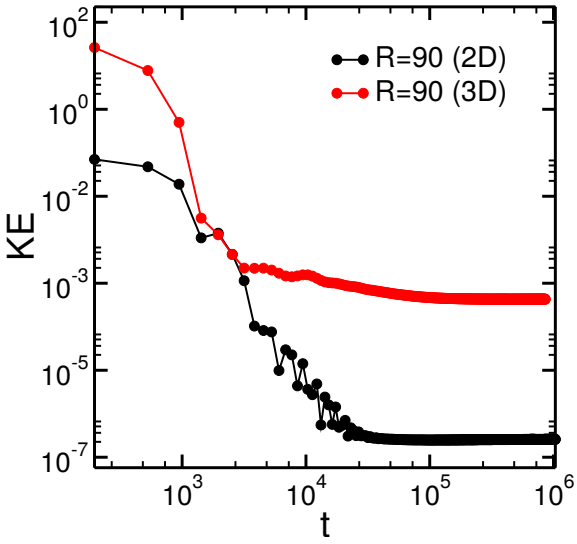

Figure 48: Time evolution of kinetic energy (KE) during equillibation of droplet in $2D$ vs $3D$

system is two dimensional $(2D)$ or three dimensional $(3D)$. The variation in the equilibration time between $2D$ and $3D$ droplets comes from the difference in surface to volume ratio between the two. After equilibration, a certain velocity is applied to the drops so that they start approaching each other.

5.5 Droplet Free-flight

Our high density ternary free energy model has a feature of the diffuse interface. Due to a large density contrast ($\sim 10^3$) between liquid and gas phase, it is considered that the surrounding gas phase have negligible effect on the collision dynamic. To dominate this fact, we have investigated the viscous drag exerted by the gas phase (at rest) on a moving droplet. In Fig.49, we show the evolution of velocity of center of mass (V_{com}). The left half of the plot shows the V_{com} during equilibration and as expected is represented by zero value.

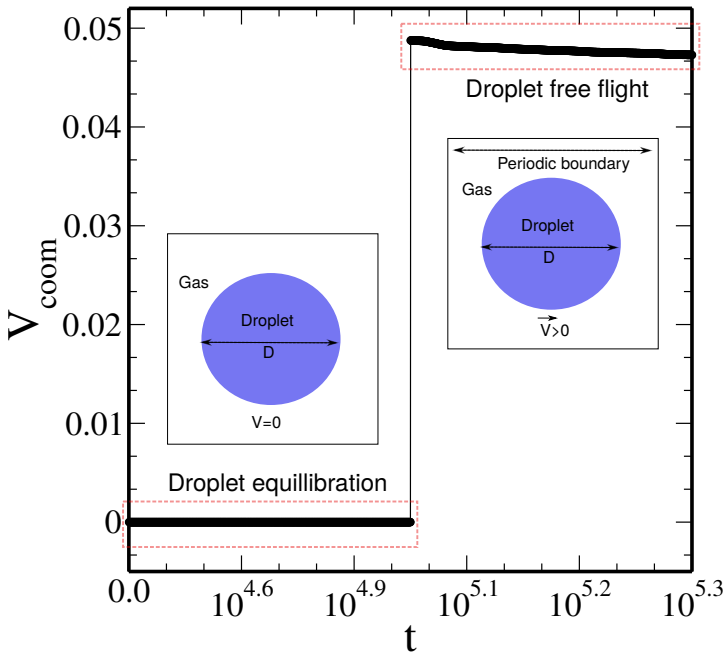

Figure 49: Time evolution of velocity of centre of mass (V_{COM}) during equillibation and free flight of droplet

After 10^5 time steps at the end of equilibration, a velocity of centre of mass V_{com} = 0.0488 l.u is provided to the droplet surrounded by gas phase which is in rest. In the right half of the plot, the V_{com} is shown during the free flight of the droplet. The magnified portion of the free flight region is shown in Fig.50. It is observed that during the fight time there is reduction in the velocity of centre of mass which is less than 4%. To be consistent in term of measurement of the dimensionless number (We), we use the velocity of the center of mass at the time when velocity is provided to the droplets ($t = 10^5$ in this case). Due to the small reduction in velocity and large density contrast in the two phases, we neglect the effect of the surrounding gas in the our analysis during collision dynamics.

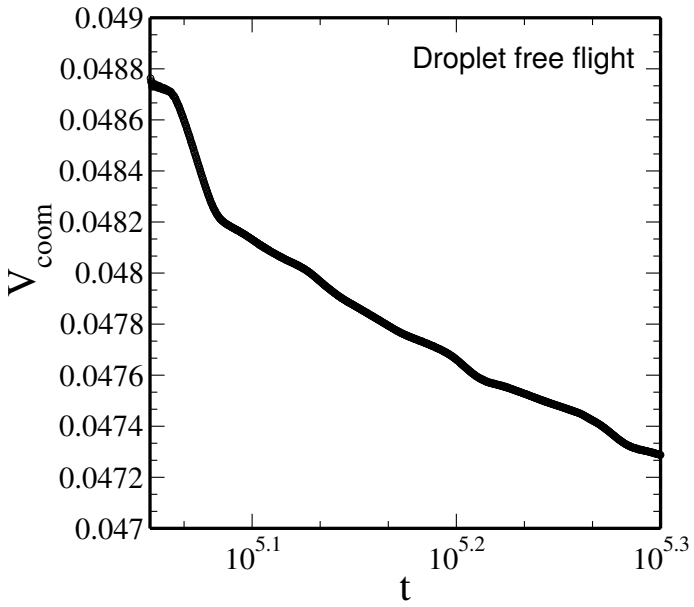

Figure 50: Time evolution of velocity of centre of mass (V_{COM}) during free flight of droplet.

5.6 Collision parameters and Energy measurement

The collisions of two droplets are characterised by a number of physical parameters, such as the density (ρ) and viscosity (μ) of both the liquid droplets and the surrounding gas, and geometrical parameters, such as the droplet diameter (D), impact velocity (V) and centre to centre distance (B) as shown in the previous section 5.3. The relative importance of these parameters are expressed by non-dimensional groups, Weber number (We), Ohnesorge number (Oh) and the impact parameter (χ). At parity surface tension combination, droplet size and density, the Weber number represents the re-scaled impact speed and the Ohnesorge number represents the re-scaled liquid viscosity. The impact parameter χ, represents the the scaled center to center distance between droplets. Note that fluid properties are labelled according to the fluid ordering in the free energy parameters, where index 1 is related to the gas and indices 2 and 3 to the liquids. However the two drops are labelled 1 and 2, so properties labelled as 2 refer to $droplet_1$ while properties labelled as 3 refer to $droplet_2$, unless otherwise stated. From the physical parameters specific to above collision setup, we can construct below form of relevant non-dimensional groups to rationalise the results of droplet collision.

$$\mathsf{We}_1 = \frac{\rho_2 \mathsf{D}_1 \Delta \mathsf{V}^2}{\gamma_{12}}, \quad \mathsf{We}_2 = \frac{\rho_3 \mathsf{D}_2 \Delta \mathsf{V}^2}{\gamma_{13}} \tag{5.3}$$

We_1 and We_2 are the Weber number of $droplet_1$ and $droplet_2$ respectively. In above equation, D_1=2R_1, D_2=2R_2 and $\Delta V = V_1 - V_2$. Similarly the Oh corresponds to each droplet is written below:

$$\mathsf{Oh}_1 = \frac{\mu_2}{\sqrt{\rho_2 \gamma_{12} \mathsf{D}_1}}, \quad \mathsf{Oh}_2 = \frac{\mu_3}{\sqrt{\rho_3 \gamma_{13} \mathsf{D}_2}} \tag{5.4}$$

In chapter 6 and 7, in order to discuss results of collision between non-identical droplets and to account for the combined effect of two droplets we employ average of the above dimensionless numbers, such that:

$$\mathsf{We}_{\mathsf{av}} = \frac{\rho_{\mathsf{av}} \mathsf{D}_{\mathsf{av}} \Delta \mathsf{V}^2}{\gamma_{\mathsf{av}}}, \quad \mathsf{Oh}_{\mathsf{av}} = \frac{\mu_{\mathsf{av}}}{\sqrt{\rho_{\mathsf{av}} \gamma_{\mathsf{av}} \mathsf{D}_{\mathsf{av}}}} \tag{5.5}$$

where ρ_{av}, μ_{av} and γ_{av} are the average density, viscosity and surface tension of the two droplets. The average diameter is computed by accounting for the fixed average mass of the collision system such that: $D_{av} = 2R_{av} = 2\sqrt{\frac{M_{av}}{\pi \rho_{av}}}$ in $2D$ and $2\sqrt[3]{\frac{3M_{av}}{4\pi \rho_{av}}}$ in $3D$.

In our simulations, the natural Lattice Boltzmann simulation time (t) is rescaled by the capillary-inertial time scale (T) as shown by Eq.(5.6). The rescaled time τ remain constant when comparing the results of identical droplets, but τ is of significance importance when comparing the collision results from different surface tension combination or droplet size.

$$\tau = \frac{t}{T}, \quad where \quad T = \sqrt{\rho R^3 / \gamma} \tag{5.6}$$

In order to estimate the energy balance during collision, we measure the three components of energy: *Kinetic energy*, *Free energy* and *Energy dissipation* as below.

Kinetic Energy (KE): The total kinetic energy during collision is measured by summation of the kinetic energy corresponding to each droplet as shown below:

$$KE_{total} = KE_1 + KE_2 = \frac{1}{2} m_1 v_1^2 + \frac{1}{2} m_2 v_2^2 \tag{5.7}$$

where KE_1 is the kinetic energy of $droplet_1$ and KE_2 is the kinetic energy of $droplet_2$. In our simulation results, the kinetic energy evolution is normalised by the initial kinetic energy (KE_0), that is kinetic energy before droplets start approaching each other ($t = 0$).

Free Energy (FE): Total free energy during the collision of droplet is computed from the integral of free energy density (bulk (Eq.(3.51)) + inerfacial (Eq.(3.61))) over the system domain.

$$F = \int \left[F^{in}_{Bulk} + F^{out}_{Bulk} + F^{gas}_{Bulk} + f_{Inter}\right] dV \tag{5.8}$$

During collision, the evolution of free energy is generally normalised by the free energy (FE_0) of the droplets at non-deformed state (that is configuration before collision). The free energy of the non deformed state can also be estimated analytically as below:

$$FE_0 = FE_{01} + FE_{02} \tag{5.9}$$

$$FE_0 = A_1\gamma_{12} + A_2\gamma_{13} \tag{5.10}$$

where, A_1 = $2\pi R_1$ in $2D$ and $4\pi R_1^2$ in $3D$, similarly A_2 = $2\pi R_2$ in $2D$ and $4\pi R_2^2$ in $3D$.

Energy dissipation: During collision, viscous dissipation of energy occurs. This dissipation is computed by integrating the viscous dissipation function over space and time as defined by Eq.(2.54) in the theoretical background.

5.7 Conclusion

In this chapter we highlighted the motivation behind the study of droplet collision. We also discussed the fundamental background to collision phenomenon. The simulation setup and relevant test specific to collision problem is explained in this chapter. All the concepts and discussion here are applicable to the below two chapter on immiscible droplet collision.

Chapter 6

Immiscible droplet collisions: adhesion - bouncing transition

In this chapter we perform a systematic numerical study to investigate the collision between two immiscible droplets. We focus on the collision dynamics for systems dominated by the transition between *bouncing* and *adhesion* outcomes. We developed a minimum model for identical droplet collision, which is able to reproduce the essential feature of the transition between adhesion and bouncing. In our analysis we will trace the evolution of the energy balance during the collision process, systematically varying physical parameters such as droplet size, viscosity, surface tension, impact speed and impact parameter.

6.1 Characterisation of the range of adhesion energies

In collision between two immiscible droplets, one of the key quantity is the adhesion energy related to the creation of the liquid-liquid interface. In general the adhesion energy can be controlled by setting the three surface tensions. In our free energy model these depend in general on six parameters, but for our purpose it is convenient to vary only the parameter controlling the bulk free energy of the gas phase (λ_1). A convenient control parameter is the non-dimensional spreading parameter of the gas phase $S_1 = 1 - (\gamma_{12} - \gamma_{13})/\gamma_{23}$. To investigate the regime at the transition between bouncing and adhesion, the S_1 needs to be slightly negative. In this case at equilibrium the to droplets will be found in the adhesive state, separated by a small portion of

liquid-liquid interface. In this regime the Neumann angle of the gas phase $\theta_1 \sim 0°$ (Eq.2.25) is defined and can be employed as equivalent control parameter. More negative values of S_1, correspondingly larger values of θ_1, describe states with larger portion of liquid-liquid interface and correspondingly larger adhesion energy, making more likely the adhesive state as collision outcome. If $S_1 > 0$ the thermodynamically stable state will instead involve a gas layer in between the droplets, corresponding to vanishing adhesion energy. In this case the droplets will bounce away for any combination of the other parameters and impact speed. The variation of S_1 and θ_1 as a function of bulk free energy parameter (λ_1) are depicted in Fig. (51) and Fig.(52) respectively.

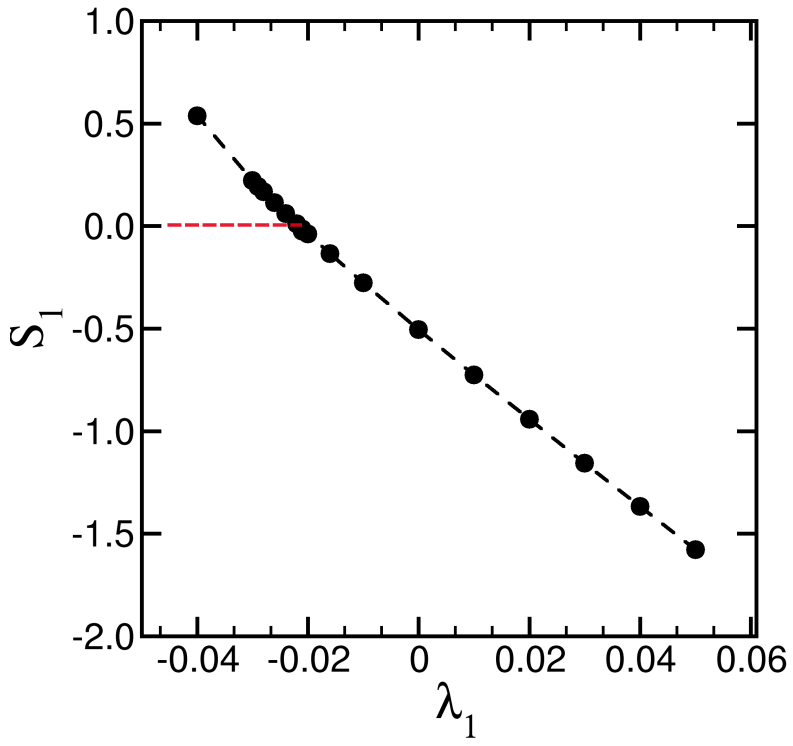

Figure 51: Variation of spreading parameter (S_1) of the gas phase vs bulk free energy parameter λ_1

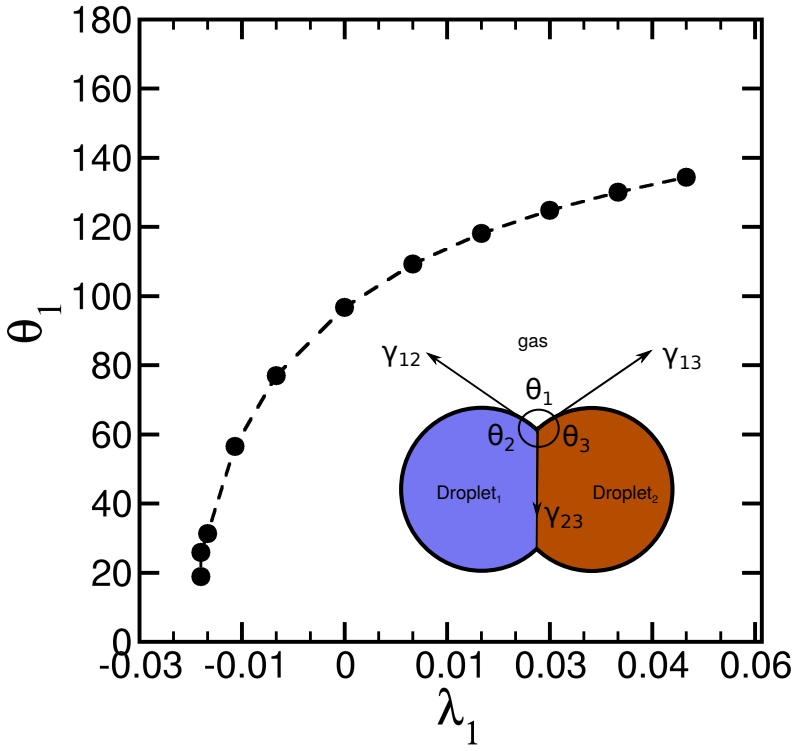

Figure 52: Variation of Neumann angles (θ_1) of the gas phase vs bulk free energy parameter λ_1

6.2 Head-on collision of identical droplets

We start our numerical investigation considering the simpler case of head-on collisions of two-dimensional ($2D$) identical droplets, in terms of the surface tension $\gamma_{12} = \gamma_{13} = \gamma$, diameter $D_1 = D_2 = D$, density $\rho_2 = \rho_3 = \rho$ and viscosity $\mu_2 = \mu_3 = \mu$. We also impose the same magnitude of impact speed $|V_1| = |V_2| = V$, with opposite sign so the total momentum is zero. Depending on the collision parameters and using the $2D$ simulation setup shown in Fig. 45, three typical collision outcomes are identified. These outcomes are: *Adhesion, Bouncing and Delayed Adhesion*. To elucidate the qualitative features of different outcomes we report in the following a set of simulation results obtained by initializing the colliding droplets at a different impact speed (V) and keeping the rest of the parameters constant ($\gamma = 0.007 l.u, D = 180 l.u, \mu = 0.2037 l.u, \rho = 0.001 l.u$) such that $\theta_1 \sim 0°$ and $\mathrm{Oh} = 0.181$. Besides the visualization of the evolution of droplet shapes through a sequence of simulation snapshots as shown in Fig.53, a useful quantity to trace the droplet evolution is given by the velocity of the center of mass. These outcomes are discussed below:

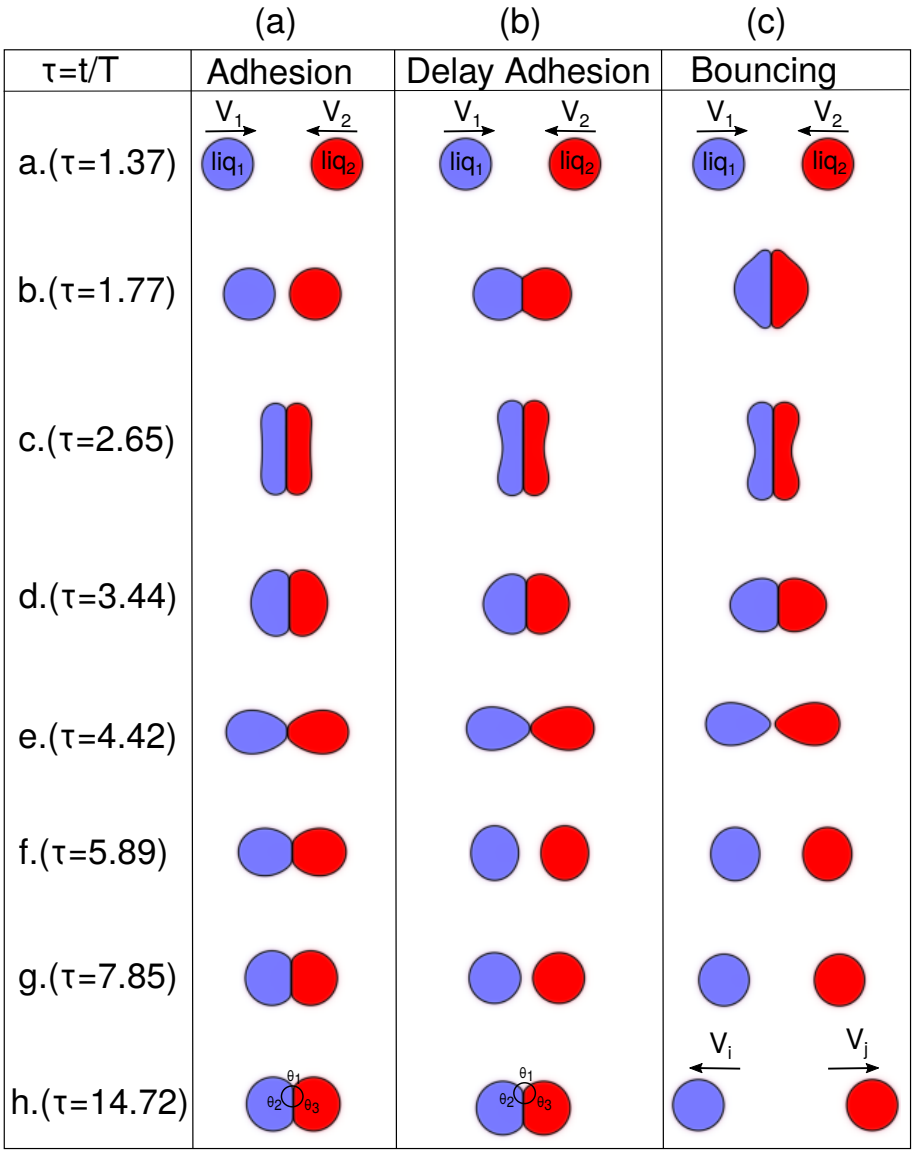

Figure 53: Sequence of steps during collision in two dimensional ($2D$) at $\theta_1 \sim 0^\circ$ Oh $= 0.181$ (a) Adhesion at We $= 41$ (b) Delay Adhesion at We $= 50$ (c) Bouncing at We $= 64$.

1. *Adhesion (A)*: A typical Adhesion outcome is depicted in Fig.54, showing the evolution of velocity of centre of mass V_{com} of the two droplets during the collision at a relatively low We $= 41$. The corresponding sequence of snapshots is depicted in Fig.53(a). During the Impact, the deformation of both droplets happens (here symmetric as the the droplets have identical properties). The deformation squeezes the droplets along the collision direction, while the liquid is pushed in the orthogonal direction (radial direction in 3D), reaching a maximum extension in the case analyzed at $\tau = 2.65$. After experiencing the maximum shape deformation along the direction perpendicular to the collision axis, the surface ten-

sions forces revert the motion and both droplets regain the a circular shape as visualized approximately at $\tau = 3.44$. Once the circular shape is attained, the residual momentum pushes the droplets further apart, until reaching a maximum extensions along the collision axis approximately at $\tau = 4.42$. Here the two droplets are still connected by a portion of interface, carrying a residual adhesion energy, sufficient to revert the motion once again. Therefore the two droplets remain attached, and the compound oscillates until droplets rest in their final equilibrium state. Interestingly, despite the large deformation, the amplitude of the oscillations quickly approach the typical exponential decay of a damped harmonic oscillator. The final equilibrium configuration is eventually determined by relative strength of surface tensions, or equivalently by the Neumann angles. The (approximate) equilibrium morphology is depicted in the last simulation snapshot ($\tau = 14.72$).

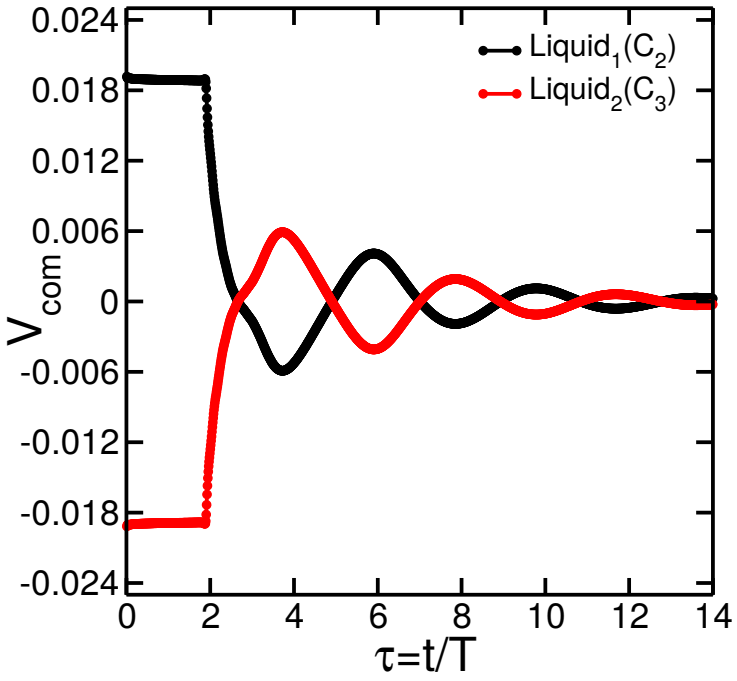

Figure 54: Time evolution of velocity of centre of mass (V_{com}) during the a collision with adhesion outcome ($\theta_1 \sim 0°$, Oh $= 0.181$, We $= 41$)

2. *Bouncing (B)*: A typical bouncing outcome is reported in Fig.55 obtained at larger We $=$ 64. A sequence of snapshots of the collision mechanism that results in *Bouncing* outcome is reported in Fig.53(c). Due to a higher impact speed available during the collision the compression of the droplets during the first impact is larger as compared to *Adhesion* in Fig.53(a). Also in this case, after reverting the motion the momentum acquired by the

centres of mass of the two droplets is sufficient to overcome the residual adhesion energy and separate the two droplets. This mechanism is depicted in Fig.55, showing the evolution of the velocity of the centres of mass of the two droplets. After the two droplets separate, the move apart at (approximately) constant velocity, as dictated by the momentum conservation. Note that after separation both droplets still oscillate individually, although this motion is not captured by time evolution of the velocities of the centers of mass. The droplets keep moving away until reaching the domain boundaries.

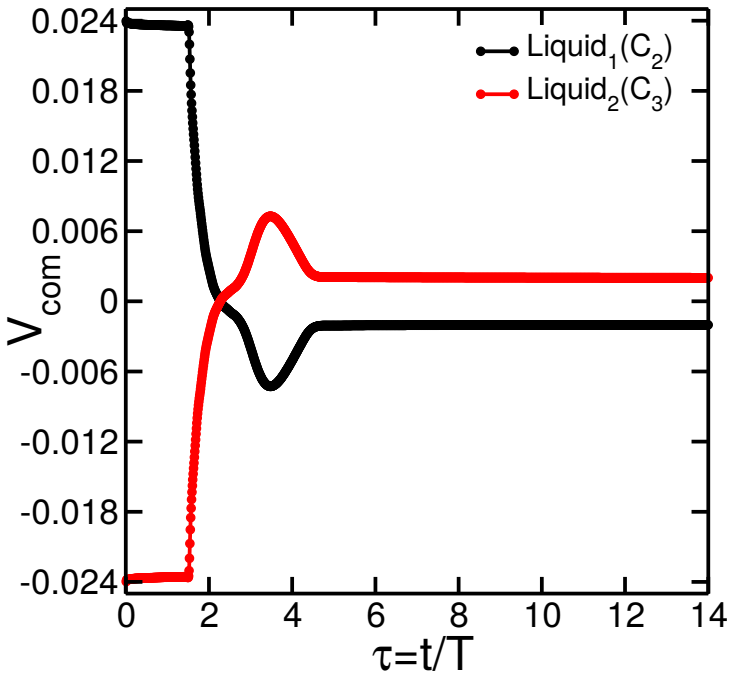

Figure 55: Time evolution of velocity of centre of mass (V_{com}) during the Bouncing outcome ($\theta_1 \sim 0°$, Oh $= 0.181$, We $= 64$)

3. *Delayed Adhesion (DA)*: Interestingly, at intermediate We $= 50$ between adhesion and bouncing a mixed dynamics is observed, which first leads to bouncing, subsequently followed by adhesion. A sequence of snapshots representing a typical DA outcome is shown in Fig.53(b). Qualitatively the initial collision dynamics is similar to *Bouncing* (Fig.53(c)), except that the residual momentum of the center of mass of each droplet inverts the sign right after the separation, bringing the droplets slowly back together. This mechanism is clarified in the time evolution of V_{COM} reported in Fig.56. To understand how this is possible, we need to consider the energy stored in the droplet deformation and converted back into kinetic energy. This energy is not entirely conveyed into the individual momentum of

each droplet, as a fraction is also conveyed into individual deformations of each droplet. This occurs also for bouncing droplets, but in the present case the energy stored in the oscillations dominates over the one stored in the velocity of the center of mass. Consequently the droplet splitting is triggered by the individual oscillations rather than the motion of the centers of mass. Indeed by the time the droplets are split, the motion of the centers of mass was already inverted. Next, the droplets slowly approach until a new collision event, in which the kinetic energy involved is small enough to lead to adhesion.

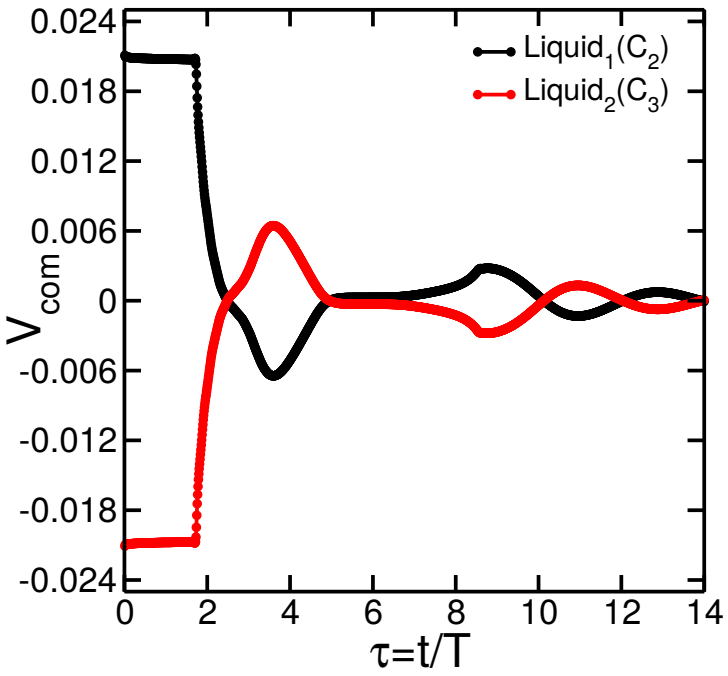

Figure 56: Time evolution of velocity of centre of mass (V_{com}) during the Delayed Adhesion outcome ($\theta_1 \sim 0°$, Oh $= 0.181$, We $= 50$)

6.3 Analysis of Bouncing dynamics for identical droplets (2D and 3D)

In this section emphasis is given on a more systematic analysis of the dynamics of the collision mechanism for leading to bouncing droplets. Specifically, we investigate the energy balance within the collision mechanism, and how this is affected at varying of physical parameters, which determine the speed and individual oscillations of droplets after bouncing. In general the total energy of the systems is divided into kinetic energy, and potential energy. During the collision energy is

also dissipated by the viscous flow as discussed in section 5.6.

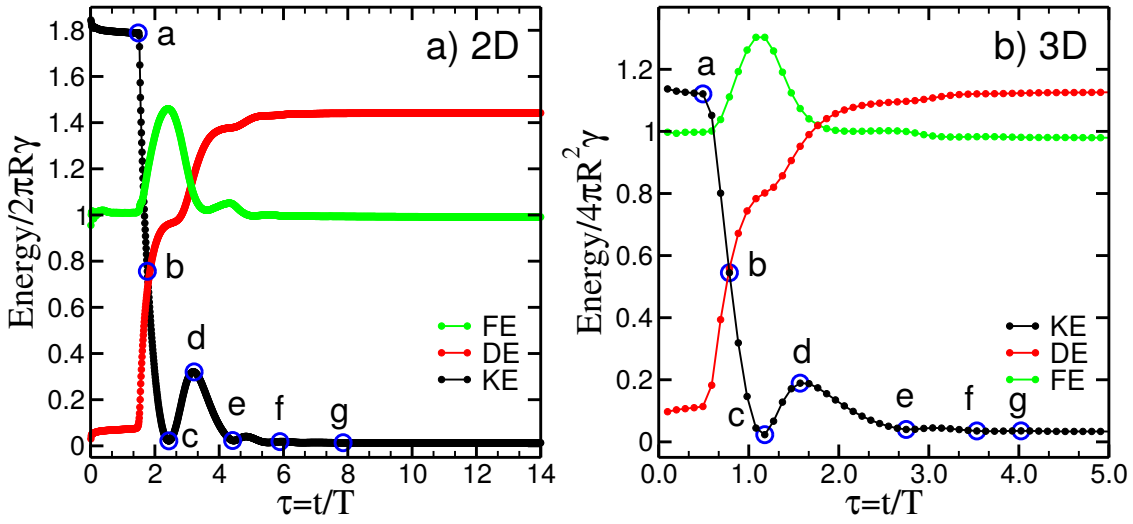

Figure 57: Time evolution of kinetic energy (KE), Free energy (FE) and Energy dissipation (DE) at We $= 64$, Oh $= 0.181$ and $\theta_1 \sim 0°$ (a) $2D$ results and (b) $3D$ results.

Fig.57 reports an example of time evolution of the kinetic energy (Black curve), Free energy (Green curve) and integral of energy dissipation (red curve) for $2D$ (panel a) and $3D$ (panel b) simulations respectively. The energy is normalized by the total free energy of the initial configuration, corresponding to the surface energy of two independent droplets of different liquids with identical surface tension. As expected, at the contact between the colliding droplets, a rapid decrease in kinetic energy is observed ($\tau = 1.48 - 2.44$ in $2D$ and $\tau = 0.6 - 1.3$ in $3D$), corresponding to a quick rise in the free energy, as the droplets are increasingly deformed and increase their surface length ($2D$) and area ($3D$). The evolution of the sum of free and kinetic energy corresponds with good approximation to the integral of total dissipation, which is represented by red curve. The calculation is started when the droplets are assigned the velocity, corresponding to a small amount of kinetic energy which is dissipated. The main dissipation step is related to the first impact of the droplets. Additional energy is dissipated in the following, related to the shape oscillations of the individual droplets. A detailed comparison between $2D$ ad $3D$ cases (the parameters are set such as We is the same in both cases) shows the same qualitative evolution, except the $3D$ case evolves faster in the inertial-capillary time-scale.

To gain further insight from numerical experiments, we have collected in Figure 58 snapshots of the colliding droplets both for $2D$ and $3D$. The blue and red colors indicate the two different liquids, while the color (normalized) intensity is proportional to the kinetic energy (panel a) and

the dissipation function (panel b). Letters indicate the points along the time evolution in Fig.57. Remarkably 2D and 3D show a striking similarity in both the densities of kinetic energy and energy dissipation, which will be exploited to complement our analysis of the role of constitutive parameters.

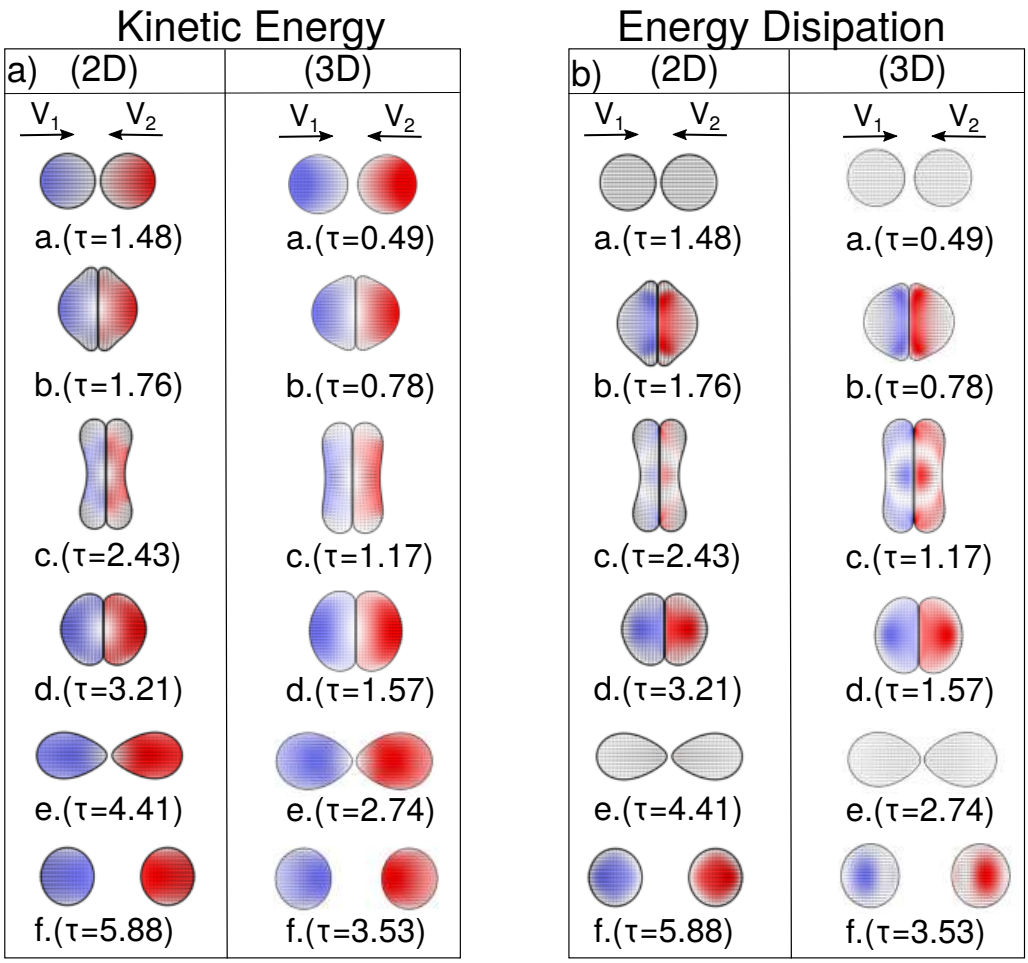

Figure 58: Sequence of collision steps showing the intensity of a) Kinetic energy and b) Energy dissipation at We $= 64$, Oh $= 0.181$ and $\theta_1 \sim 0°$

6.3.1 Role Impact speed

In this and following sections we will consider only simulations leading to Bouncing outcomes, and start our investigation exploring the role of the impact speed on the energy balance, and specifically how this affects the velocity of droplets after collisions. To this aim, five set of simulations in 2D and 4 sets in 3D are performed. We consider two identical droplets each time colliding at a different rescaled impact speed represented by Weber number (We). All the remaining parameters such as viscosity surface tension are not varied across simulations. Specifically, we choose a the

following free energy parameters $\lambda_1 = \kappa_1 = -0.02, \lambda_2 = \kappa_2 = \lambda_3 = \kappa_3 = 0.05$ giving $\theta_1 \sim 0°$. This corresponds to a system with approximately vanishing adhesion energy, which will ensure Bouncing occurs for a wide range of impact speed. The viscosity in both liquids is also fixed, leading to an Ohnesorge number $\mathsf{Oh} = 0.181$ also fixed for both droplets. The detailed analysis of the set of simulations is reported in Fig.59, which shows for both $2D$ and $3D$ cases the time evolution of kinetic energy, free energy and energy dissipation.

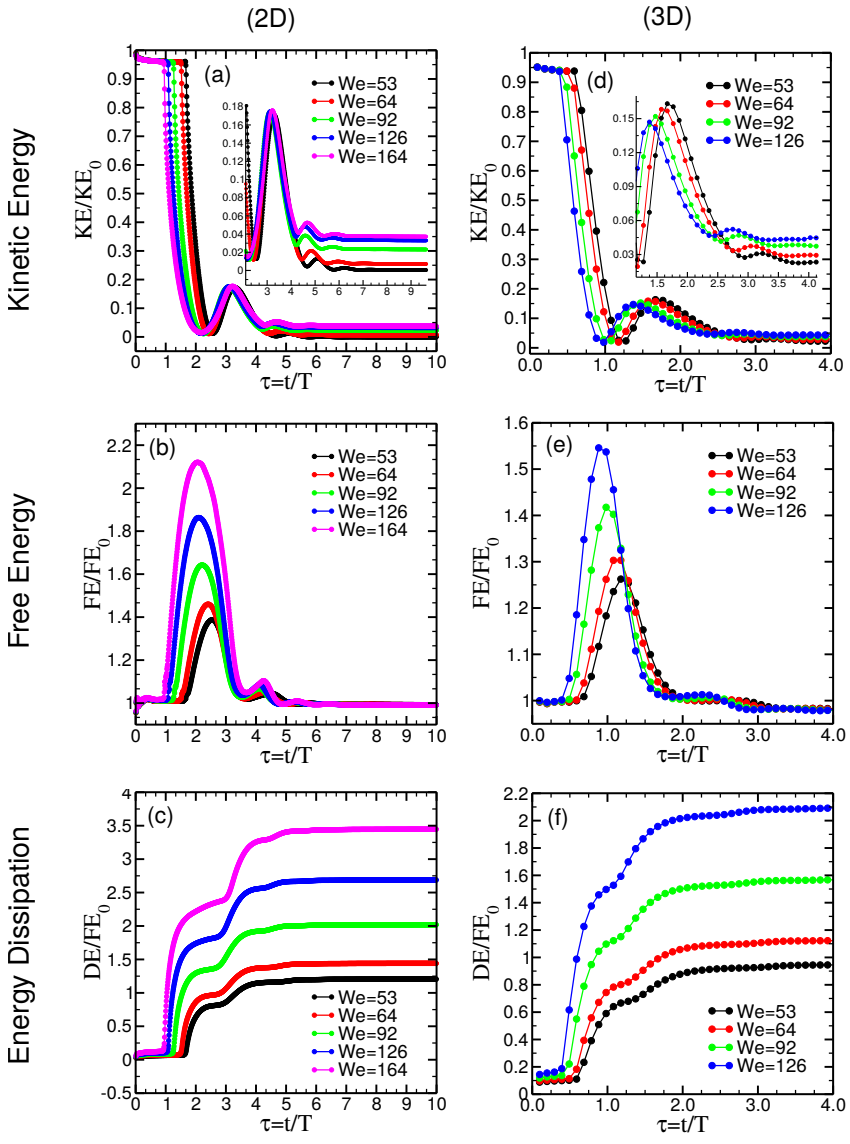

Figure 59: Evolution of energy balance during bouncing droplets at different We and fixed $\mathsf{Oh} = 0.181$ and $\theta_1 \sim 0°$ (a.d) $2D$, $3D$ evolution of Kinetic energy (b,e) $2D$, $3D$ evolution of free energy (c,f) $2D$, $3D$ energy dissipation.

The kinetic energy is normalised by the kinetic energy in the initial configuration, while the free and dissipated energy are normalised by the free energy of the initial configuration of the sys-

tem (two separated droplets at rest). As the simulation time starts once the velocity is assigned, droplets with larger We cover the separation distance in shorter time and collide earlier, as shown by the sudden droplet of kinetic energy in Fig.59(a,d). All plots shows a consistent picture that the larger the impact speed (We) the larger is the droplet deformation during impact, which reflects in the larger first peak of the free energy shown in Fig.59(b,e). The second (much smaller) peak in the free energy corresponds to the droplet elongation along the collision axis, leading to droplet separation in all cases due to the nearly vanishing adhesion energy. The remaining energy oscillations, quickly damped, describe the individual shape oscillations of both droplets when moving apart. Because the system is symmetric, each droplet accounts for exactly half of the system energy along the curve, the oscillations being synchronised. Interestingly, no matter how large is the initial kinetic energy, it is dissipated nearly completely within the first and second deformation, as can be observed in the evolution of the dissipated energy in Fig.59(c,f). Nevertheless, the amount of kinetic energy left in the droplets after bouncing remains larger for colliding droplets with larger impact speed, as expected. To quantify the the dissipation occurring in the whole collision process, we have computed the restitution coefficient, defined as the ratio between final and initial kinetic energy. The restitution coefficient is reported in Fig 60 for both $2D$ and $3D$ systems.

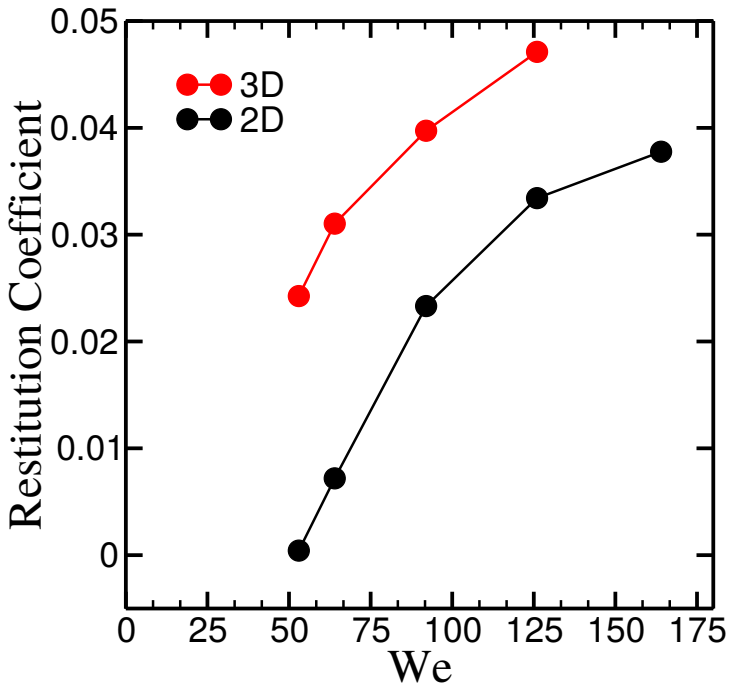

Figure 60: Restitution Coefficient's variation with droplet We and at fixed Oh $= 0.181$ and $\theta_1 \sim 0^\circ$

Here the final kinetic energy is taken in the dips of the individual droplet oscillations, as it represents the component of energy stored in the motion of the center of mass. The restitution coefficient is reported in Fig 60 for both $2D$ and $3D$ systems. It varies in both cases in the range $0-0.05$, which is a typical for strongly inelastic collisions, as expected. In general, in the $3D$ case the restitution coefficient is larger than in $2D$, which can be explained by the smaller deformation occurring in $3D$ due to the different surface to volume ratio. As the We declines, both curves rapidly decay and appear to vanish at a finite We. This imply that a residual adhesion energy is acting in the system, likely due to the diffuse nature of the liquid interfaces in the model.

6.3.2 Role of viscosity

Next, we have investigated the role of liquid viscosity for the same system tested previously and fixed impact speed ($\mathsf{We} = 53$). The summary of the analysis of the set of these simulations is shown in Fig.61. We observed that after the collision (at same impact speed) the residual kinetic energy of the droplets decreases for more viscous droplets (higher Oh) as depicted in Fig.61(a,d). Consistently the amplitude of the free energy peak at the first impact and subsequent oscillations also decreases as Oh decreases represented by Fig.61(b,e). As liquid viscosity is proportional to the dissipation rate, we observe that the integral of the dissipation function increases as Oh increases as shown in Fig.61(d,f). From these data we have computed the relation between Oh and restitution coefficient, displayed in Fig.62. As expected the restitution coefficient is reduced as Oh increases. At larger values of Oh the restitution coefficient vanishes, in correspondence to the transition from bouncing to adhesion. In the left panel of Fig.62, we represent the same data as function of the inverse of the Ohnesorge number $\Delta(\mathsf{Oh}^{-1}) = \mathsf{Oh}^{-1} - \mathsf{Oh}_0^{-1}$ where the shift Oh_0^{-1} is estimated through a linear fit of the smallest values of the restitution coefficient. Interestingly we observe the same linear dependence with $\Delta(\mathsf{Oh}^{-1})$ both from 2D and 3D data, followed by a level-off.

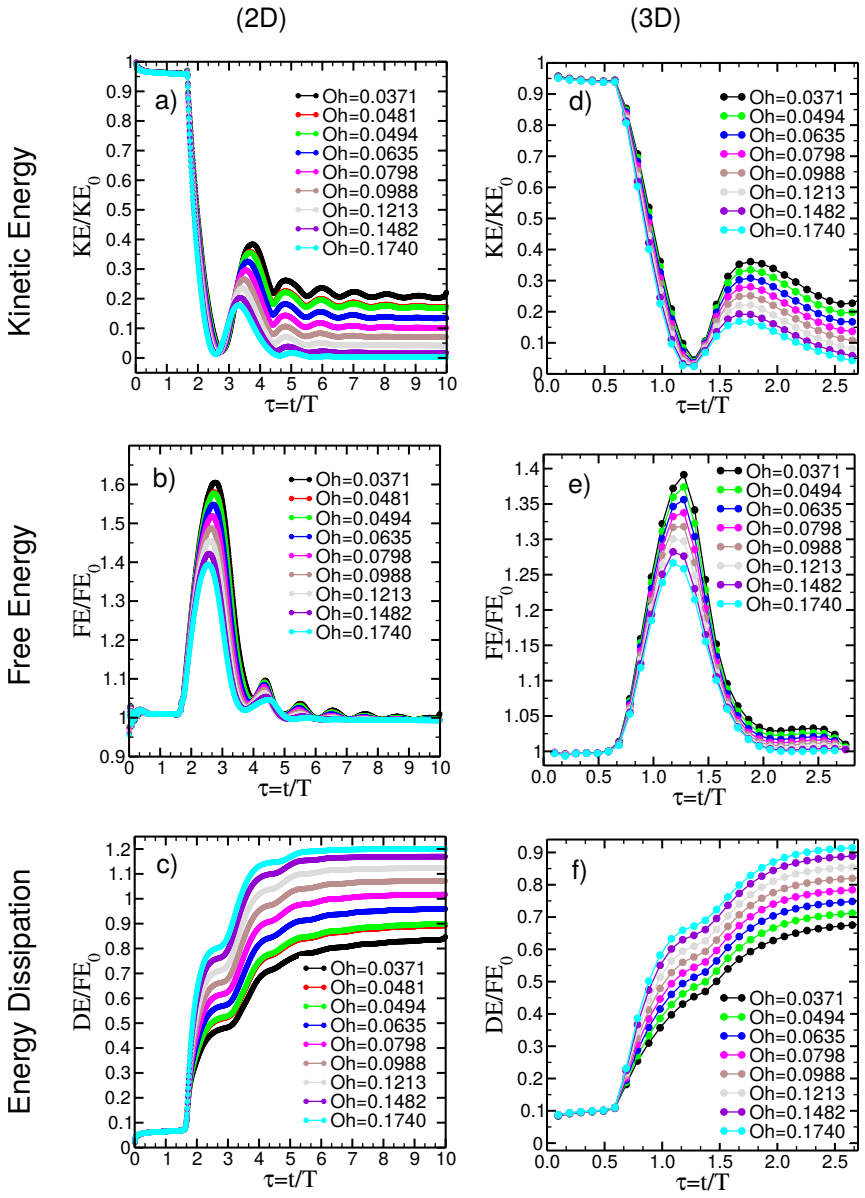

Figure 61: Energy evolution w.r.t time for bouncing droplets at different Oh and at fixed We $= 53$, $\theta_1 \sim 0^\circ$ (a,d) $2D$ and $3D$ evolution of Kinetic energy (b,e) $2D$ and $3D$ evolution of free energy (c,f) $2D$ and $3D$ energy dissipation

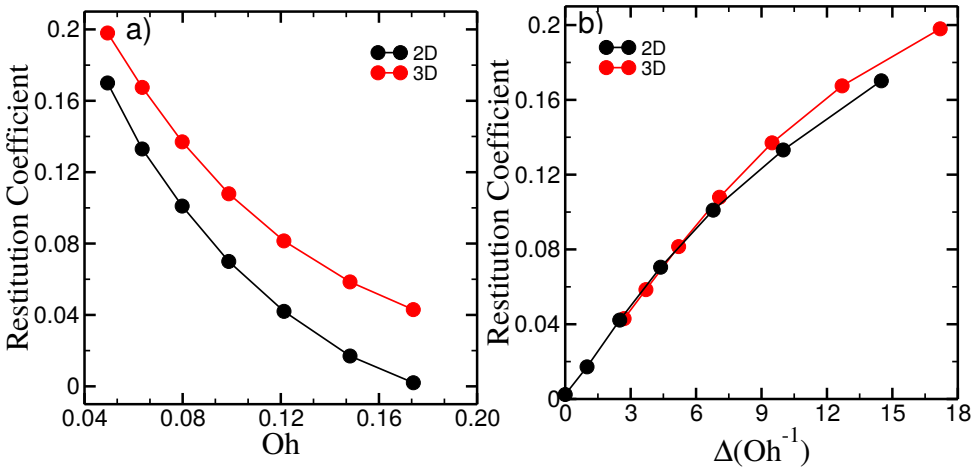

Figure 62: Restitution Coefficient at different Oh and at fixed We $= 53$, $\theta_1 \sim 0°$

6.3.3 Role of surface tension

In this section we focus on the relative strength of surface tensions, which plays a key role in collisions of immiscible droplets as it tunes the adhesion strength. While in our analysis so far we have set Neumann angles $\theta_1 \sim 0°$, corresponding to nearly vanishing adhesion energies, we now extend our simulations increasing θ_1 and therefore the adhesion energies. Note that because surface tensions vary, the impact speed and viscosity also varied in order to maintain We $= 53$ and Oh $= 0.048$ constant. The simulations results are reported in Fig.63 where now all the free energy of isolated droplets (employed as rescaling factor) varies with the surface tension and therefore with θ_1. For simplicity the kinetic energy is rescaled by the kinetic energy before the impact. The evolution of the free energy shows now a dip in correspondence of the initial contact between colliding droplets, corresponding in the gain of adhesion energy in the compound formation. Immediately after, however the droplets are squeezed and deformed as observed in the previous cases. The relative amplitude of the corresponding energy peak is smaller as θ_1 increases, while in contrast the amplitude of the second peak, corresponding to stretching along the collision axis, increases as θ_1 increases, associated to a larger deformation, likely related to the increased energy cost to splitting the droplets (Fig.63(b,e)).

In contrast as shown in Fig.63(a,d), the evolution of the kinetic energy during in the droplet at the impact and the rise of the first peak does not vary significantly as θ_1 is varied. However the residual kinetic energy stored in the individual droplets after separation decreases significantly as θ_1 increases, since a larger amount of energy is required to overcome the adhesion energy

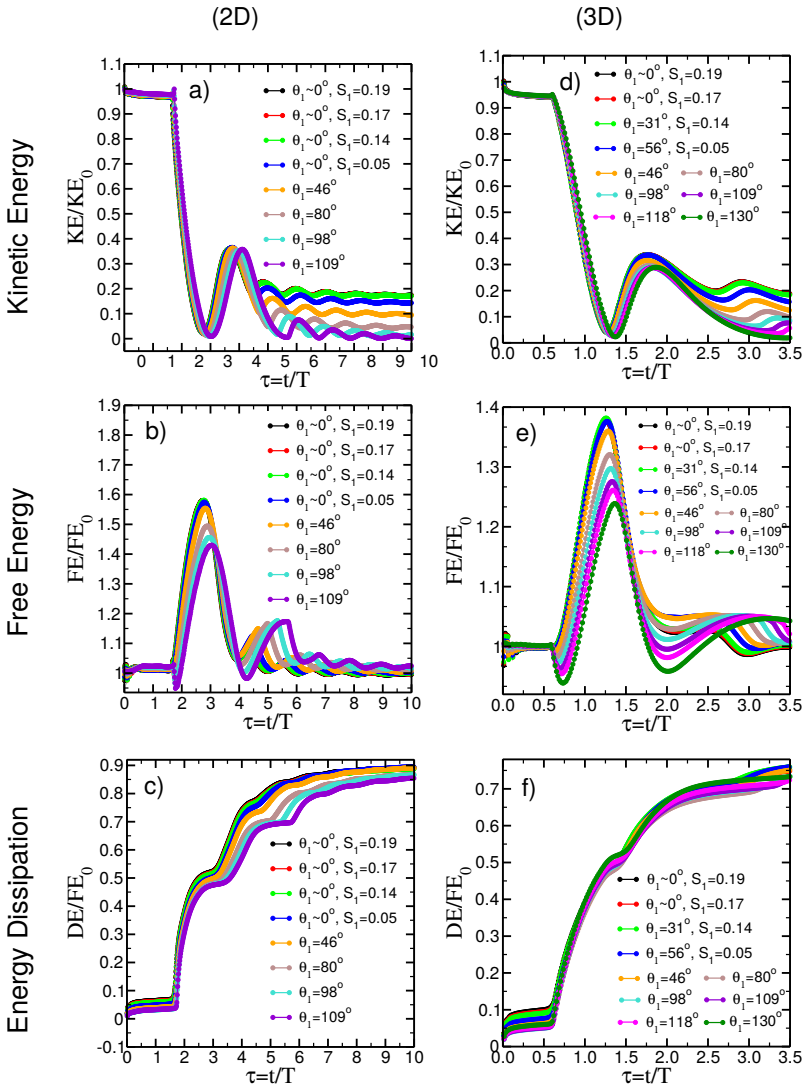

Figure 63: Energy evolution w.r.t time for bouncing droplets at different surface tension combination (θ_1/S_1) and fixed We and Oh $(53, 0.048)$ (a,d) $2D$ and $3D$ evolution of Kinetic energy (b,e) $2D$ and $3D$ evolution of free energy (c,f) $2D$ and $3D$ energy dissipation

established at the contact,and separate the droplets. Inspecting the evolution of the dissipated energy rescaled by the energy of the individual droplets, we observe that despite the evolution is different, the relative amount of dissipated energy is very close, with slightly larger dissipation occurring for smaller values of θ_1 (Fig.63(c,f)). We illustrates the restitution coefficient evaluated as function of θ_1 in Fig. 64, which decreases as θ_1 increases, consistently to the additional energy required to overcome adhesion. The same data is represented in panel b as function of $\Delta(\theta_1^{-1})$. The data suggest the crossover between two regimes, both in the 2D and 3D case, being the 3D more marked.

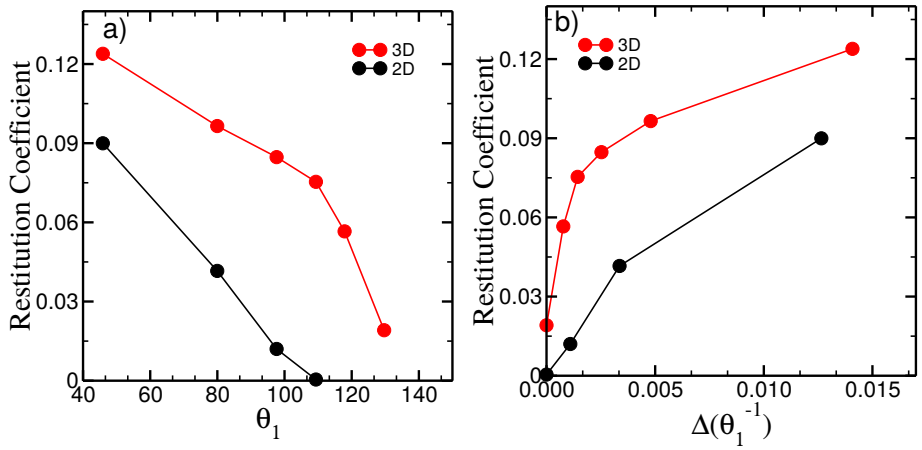

Figure 64: Restitution coefficient at different surface tension combination represented by Neumann angle (θ_1) (We $= 53$,Oh $= 0.048$)

6.4 Additional insight on energy re-partition

As we have observed in the previous analysis, the collision mechanism reshuffles the the available energy between kinetic and potential form, while is dissipated by the viscous flow. However the kinetic energy itself can be split in the component contributing to the linear momentum of individual droplets and their surface oscillations. In the head-on setup, the total momentum is zero, as we assign velocities equal in magnitude and opposite in the sign to the colliding droplets. As momentum is conserved, whenever adhesion outcome is observed, the compound has zero momentum and the only form of kinetic energy is contributes to shape oscillations damped by viscous dissipation. When bouncing is observed, instead, the kinetic energy transferred to each individual droplet presents a linear component contributing the the droplet momentum and a component linked to the shape oscillations that is also dissipated by the internal viscous flow. We are now seeking to understand how the collision mechanism determines how the available kinetic energy is split in the linear and oscillatory components. To this aim we perform a more detailed analysis of the numerical simulations, by defining characteristic moments during collision and trace their properties for simulations with varying spreading parameter. These moments are highlighted in Fig.65 ($\theta_1 = 0°$) and corresponding to

- $Before\ Impact$: non deformed droplet before collision
- $Maximum\ Deformation$: deformation in y direction after first impact
- $Oscillation_1$: first oscillation after separation

- $Oscillation_2$: second oscillation after separation
- $Oscillation_n$: n^{th} oscillation after separation

Panel b shows a magnification of the oscillation region after bouncing, highlighting the energy minima corresponding to the energy stored in the linear momentum and the oscillation peaks. In Fig.66 we report the variation of kinetic energy of the linear momentum rescaled by the kinetic energy before impact and the kinetic energy stored in the first oscillation after separation (defined as the energy in the third peak less the value of the troughs), also rescaled by the kinetic before impact. Interestingly both in the $2D$ and $3D$ case we observe a crossover approximately at $S_1 = -0.2$ in 2D and $S_1 = -0.7$ in $3D$. This shows that by tuning the adhesion energy is possible to control the velocity of bouncing droplets after collision, channelling the residual kinetic energy into shape oscillations rather than into linear momentum.

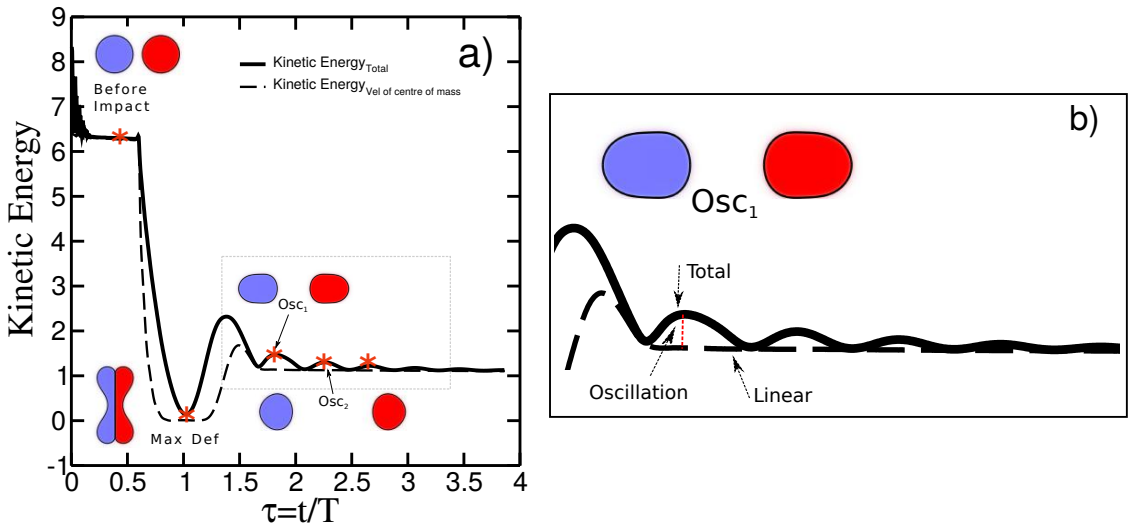

Figure 65: a) Critical stages during collision of bouncing droplets, b) magnification of components of Kinetic energy

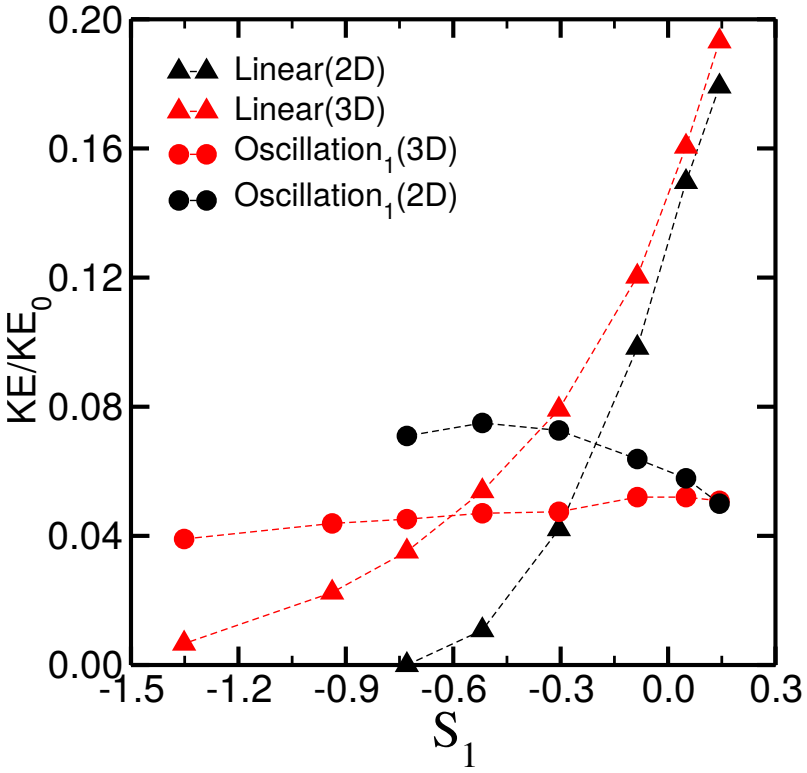

Figure 66: Variation of kinetic energy rescaled by kinetic energy before impact with respect to surface tension combination (S_1) (*Black points:* $2D$ *results, Red points,* $3D$ *results.*)

6.5 Phase diagram of head-on droplet collision

In the previous sections we have listed the main collision outcomes observed in our simulations and analysed the detailed mechanism of head-on collisions between equal immiscible droplets, leading to bouncing. In the section we report the phase diagram of head-on droplet collision as a function of rescaled impact speed (We) and viscosity (Oh) at fixed droplet size and surface tension combination. To this aim we have extended the range of dimensionless numbers We and Oh, and two additional collision outcomes: *Bouncing with fragmentation* $(B-WF)$ and *Adhesion with fragmentation* $(A-WF)$ specific of $2D$ system are observed in our simulations. For these two outcomes, the visualization of the evolution of droplet shapes through a sequence of simulation snapshots as shown in Fig.67 and are discussed below:

1. *Bouncing with fragmentation* $(B-WF)$: At significantly larger We $= 208$, the collision mechanism becomes more complex. A typical sequence of snapshots of Bouncing with fragmentation is shown in Fig.67(a). In this case the impact speed involved is related to a larger squeezing of the droplets during the impact, whose morphology resembles the one of

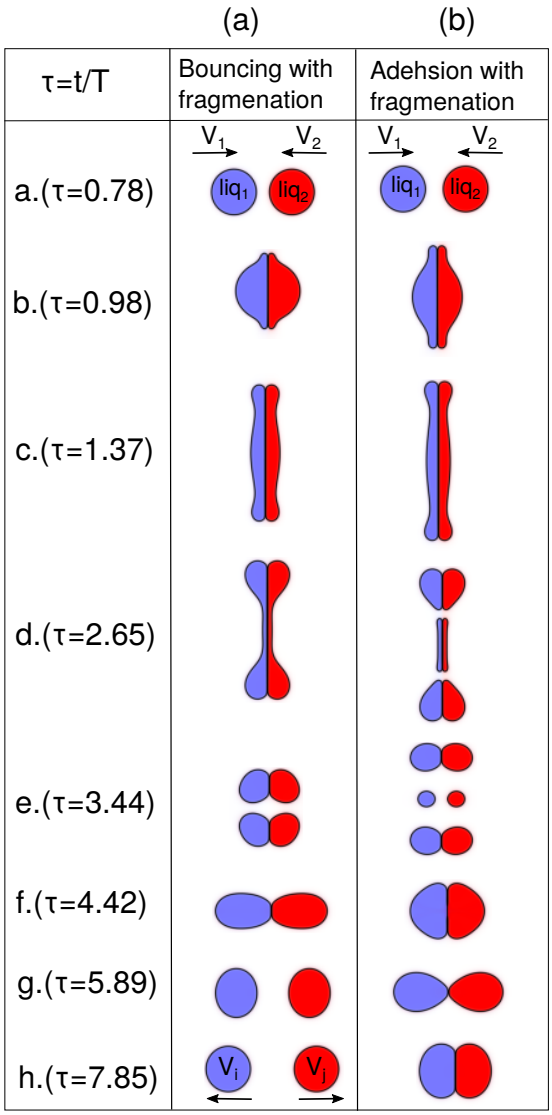

Figure 67: Sequence of steps during collision in two dimensional ($2D$) at $\theta_1 \sim 0^\circ$ Oh $= 0.181$ (a) Bouncing with fragmentation at We $= 208$ (b) Adhesion with fragmentation at We $= 256$.

the parallel liquid layers. Clearly, for such large deformation the way liquid is distributed significantly differ between $2D$ and $3D$ cases. At the maximum deformation the droplet recoiling starts from the outer portion, which bulges while withdrawing additional liquid from the central region. Eventually the thin liquid layers break in the middle, as observed also in collisions between droplets for the same liquid, creating two equal compounds symmetrically placed respect to the collision axis. The equivalent morphology in $3D$ would be represented by two connected annular rings. While in $3D$ the recoiling process is mainly driven by the surface tension, here it is driven by the residual momentum in the orthogonal direction, which builds up with a similar mechanism to the Delayed adhesion. Once

the two symmetric compounds touch again, they form a single compound, further stretched along the collision axis. This eventually triggers the droplet detachment as in the standard bouncing scenario.

Fig.68 reports the time evolution of the component of V_{com} in the collision direction. Compared to the previous cases, we observe that the velocity changes sign shortly after the impact, but it remains small for a certain time interval. This slow increase corresponds to the orthogonal extension of the compound forming the liquid layers. Then the velocity increases more rapidly, as the outer recoiling is triggered peaking at the intermediate breaking. A nearly discontinuous velocity increase is recorded as the two compounds coalesce, and the sudden release of deformation energy is converted into kinetic energy. The remaining part of the curve follows the characteristic decrease of the bouncing scenario, until the droplets separate and maintain the residual momentum.

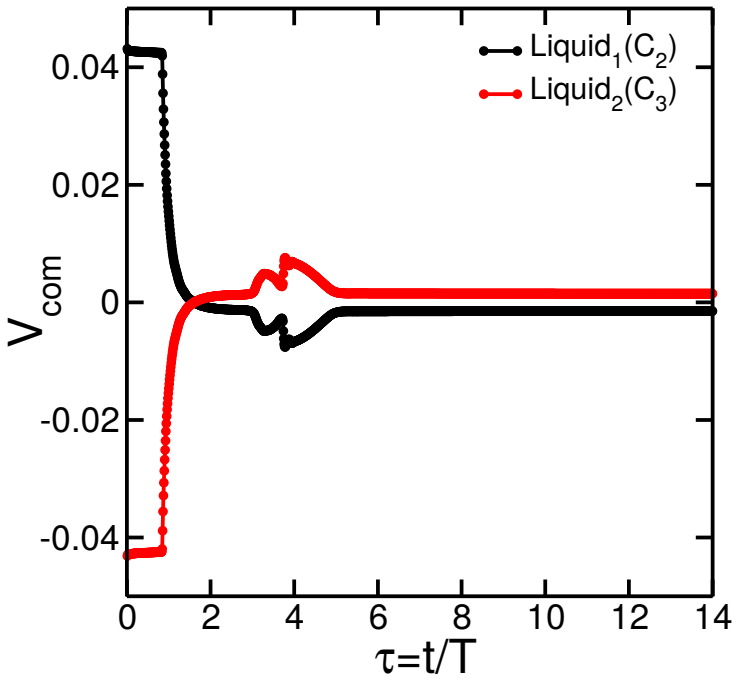

Figure 68: Time evolution of velocity of centre of mass (V_{com}) during the Bouncing with fragmentation process ($\theta_1 \sim 0°$, $\mathsf{Oh} = 0.181$, $\mathsf{We} = 208$)

2. *Adhesion with fragmentation ($A - WF$)*: While it would be expected that upon further increasing $\mathsf{We} = 256$, the bouncing mechanism if further strengthened, the opposite is observed in our simulation, as Adhesion is observed again. To understand how this is possible we can inspect the snapshot sequence reported in Fig.67(b). Here the evolution is similar

to the previous case of Bouncing with fragmentation, except the the liquid layers formed during the impact are further extended. The recoiling then begins in a similar way, but in now the liquid layers do not break in the middle, but rather pinches off in proximity of the outer bulges. This mechanism resembles the recoiling dynamics of liquid filaments [134]. Because of the symmetric pich-off, we have the formation of three compound droplets at an earlier stage, consisting of two larger compounds at the extremities and a smaller one in the middle. The middle compounds has itself the morphology of a filament, quickly recoiling and splitting in two smaller droplets as in the bouncing case. The two outer compounds instead have a smaller momentum in the vertical direction, while most of the energy stored in the deformation triggers larger oscillations of the compounds. Eventually the two compounds and the two inner droplets merge into a single compound, but this time a larger amount of energy were dissipated, since larger oscillations were triggered. Consequently the residual kinetic energy is insufficient to trigger the droplet splitting and the final outcome is adhesion rather than bouncing. Fig.69 reports the evolution of V_{com}, which initially follows the same pattern of $A - WF$.

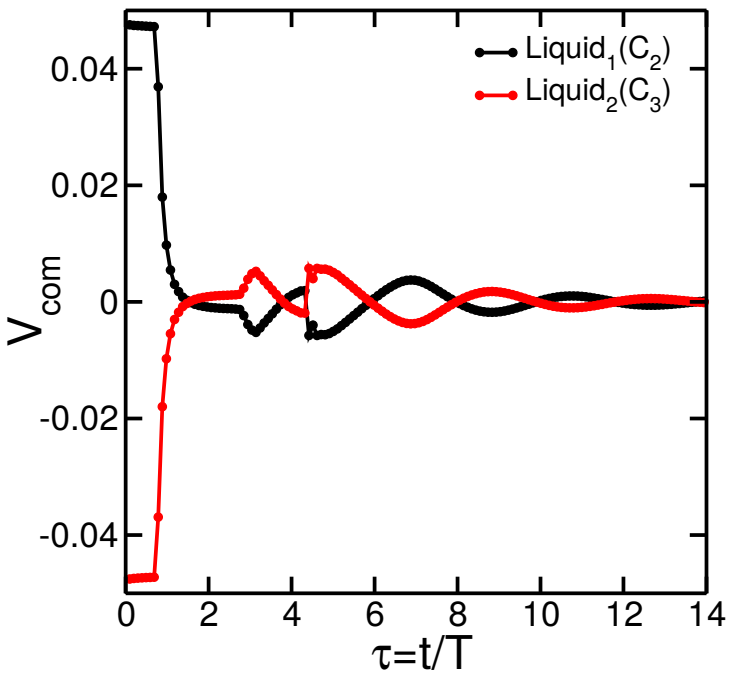

Figure 69: Time evolution of velocity of centre of mass (V_{com}) during the adhesion with fragmentation process ($\theta_1 \sim 0°$, Oh $= 0.181$, We $= 256$)

In this case, however, in correspondence of the pinch-off, the velocity changes sign again,

as more kinetic energy is channelled to the compound oscillations. Eventually the energy release at the coalescence appears as sudden jump swapping the signs once more, but insufficient to trigger the separation, leading o adhesion outcome. In Fig.70 we compare the kinetic energy of the two outcomes showing fragmentation. The kinetic energy is normalised by the free energy of the droplets in the non deformed state. The left panel shows that in the red curve (adhesion with fragmentation) the droplets collide with larger kinetic energy, but during the impact which is highlighted in the panel b of Fig.70, because of the multiple fragmentation, a larger amount of kinetic energy is dissipated compared to the black curve (bouncing with fragmentation). So that with the fragmentation residual kinetic energy is not sufficient to induce bouncing after the fragments have merged.

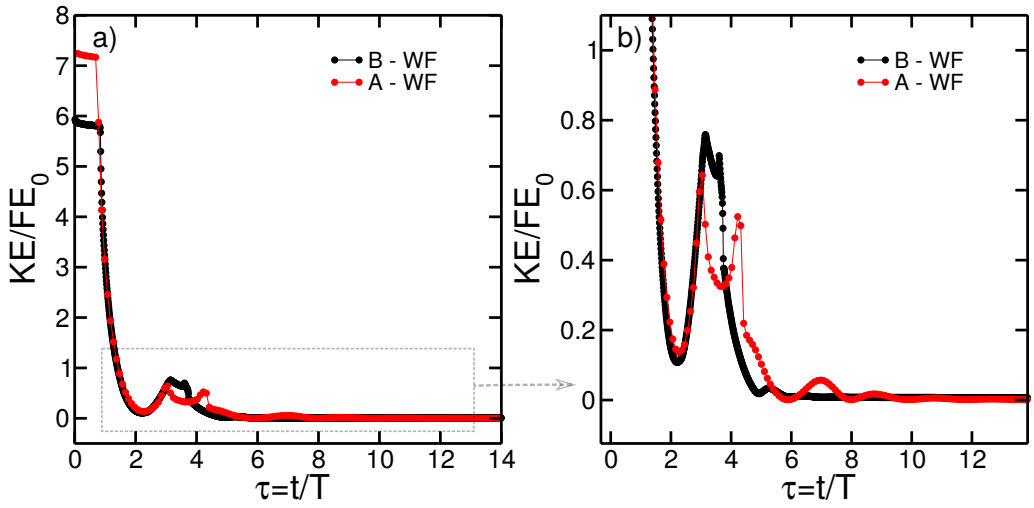

Figure 70: Time evolution of kinetic energy (KE) rescaled by free energy (FE_0) of the droplets in the non-deformed state. *Black curve*: Bouncing with fragmentation ($B-WF$), Red curve: Adhesion with fragmentation ($A-WF$) ($\theta_1 \sim 0°$, $\mathsf{Oh} = 0.181$, $\mathsf{We} = 208$)

6.5.1 Phase diagram for 2D collision

After identifying two more possible collision outcomes (with fragmentation) in our simulations, We then performed systematic simulations of $2D$ head-on collisions of immiscible identical droplets, for fixed adhesion energy ($\theta_1 = 98°$) in the parameter space of the non dimensional numbers Weber (We) and Ohnesorge (Oh). Results are summarised in Fig. 71, where points represent simulation data with different outcomes, highlighted by shaded regions. Transition lines between regions are guidelines for the eyes. Simulations for $\mathsf{Oh} < 0.03$ were unstable as the required viscosity of droplets was too low to be handled in the current collision setup.

The region of large (Oh) and small (We) is dominated by $Adhesion(A)$ (black points) outcome, while moving to smaller (Oh) and larger (We) $Bouncing(B)$ (red points) outcomes appear. In between Bouncing and Adhesion, we observed a narrow region of $DelayedAdhesion(DA)$ (green points). As commented in the previous section, Delayed Adhesion is not just a resolution artefact, as these outcomes were confirmed by a numerical resolution test, increasing the droplet size at parity of interface width. Interestingly, the occurrence of Delayed Adhesion is not limited by specific values of We or Oh, but is observed throughout the whole transition line. The outcome delayed adhesion was also observed by L.Brown and I.Karlin in their droplet collision simulation by a multi-speed lattice Boltzmann method (Shan and Chen) of binary liquids [73]. Further decreasing (Oh) and increasing (We) observe fragmentation during collision. For $(\mathrm{Oh}) < 0.11$ we observe a thin region of Adhesion with fragmentation $(A - WF)$ (blue points), followed by a region where different alternating outcomes (Bouncing, Bouncing with fragmentation, Adhesion with fragmentation) appear alternatively.

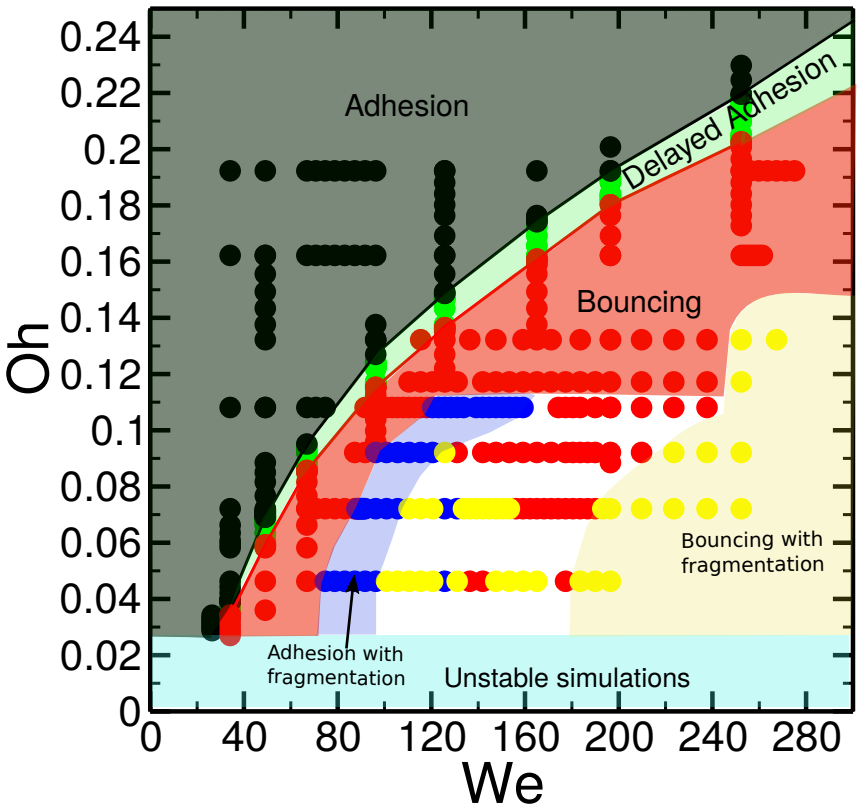

Figure 71: Phase diagram for head-on collision of identical droplets at Neumann angles $\theta_1 = 98°$

This phenomenon is likely linked to the oscillation pattern developing at the extremities of the liquid layers, and presents striking similarities with a similar phenomenon observed in contacting

filaments [134], despite these data however represent a $2D$ system. In the region with largest (We) Bouncing with fragmentation is the only observed outcome, indicating that the kinetic energy available at the impact is sufficiently large to overcome all dissipation occurring, also in presence of fragmentation.

6.5.2 Transition from *Adhesion* to *Bouncing* ($2D$ vs $3D$)

In the previous section having verified that the presence of the (DA) collision regime is not a finite size artefact, and considering the possibility that this is related to the low dimensionality $(2D)$ of the system. Therefore, in this section we performed the calculation for the computationally more expensive full $3D$ case and show the comparison of $2D$ and $3D$ results. A comparative study between $2D$ and $3D$ simulations of transition line is shown in Fig.72. The $3D$ simulations are performed for $\theta_1 = 98°$ and compared with $2D$ results. All the physical parameters are same as in both dimensions. In Fig.72(a) results from $2D$ simulation is shown and Fig. 72(b) corresponds to the $3D$ results. It is clear form Fig.72(a,b) that the results from both the dimensions follows the same path, not only qualitatively, but also quantitatively. Furthermore, the DA region in the parameter space is observed in the $3D$ case as well, confirming that this phenomenon is not an artefact related to the system dimensionality.

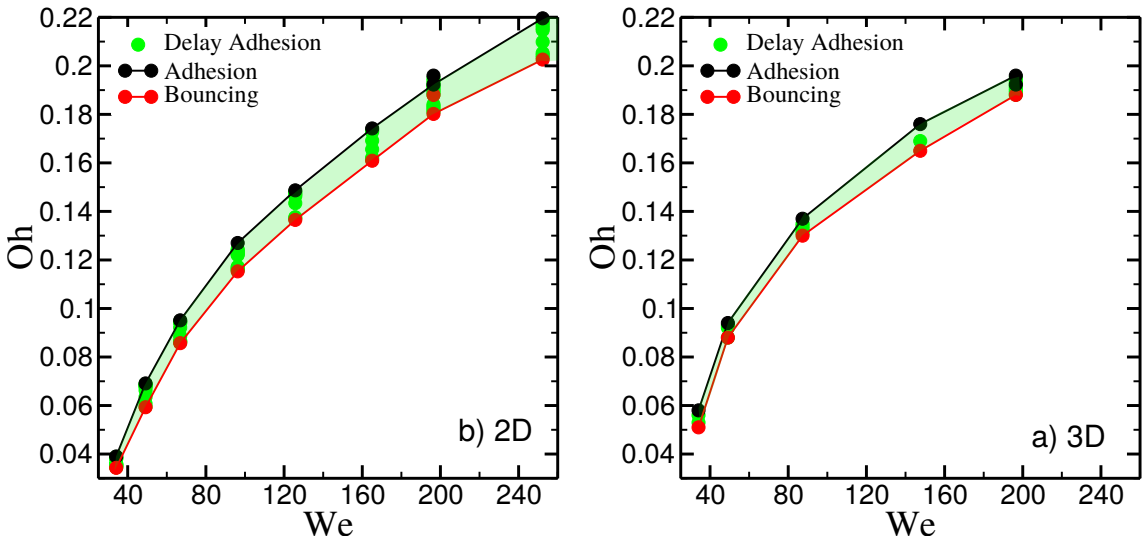

Figure 72: Transition curve from Adhesion to Bouncing in $2D$ vs $3D$ at Neumann angle $\theta_1 = 98°$

6.5.3 Transition from *Adhesion* to *Bouncing* as a function of surface tension

After detecting the transition from *Adhesion* to *Bouncing* for a fixed combination of surface tension. In this section, the impact of changing the combination of surface tension (still keeping it identical in both the droplets) on the transition line is investigated. As we addressed that both $2D$ and $3D$ results of transition curve follows the same path, here we perform the computationally less expensive $2D$ simulations to detect the role of surface tension which is cast in the form of Neumann angle (θ_1). In Fig.73, a summary of $2D$ simulation results is shown. The transition line is detected for two more sets of Neumann angle (θ_1) of the gas phase which are $\theta_1 \sim 0°$, $\theta_1 = 46°$. As expected, with the increase in the value of θ_1 (more adhesion energy) the transition curve shifts to lower Oh (or equivalently larger We), implying that additional kinetic energy is required for the droplets to bounce away which we also demonstrated in the energy analysis of bouncing droplets in section.6.3.3.

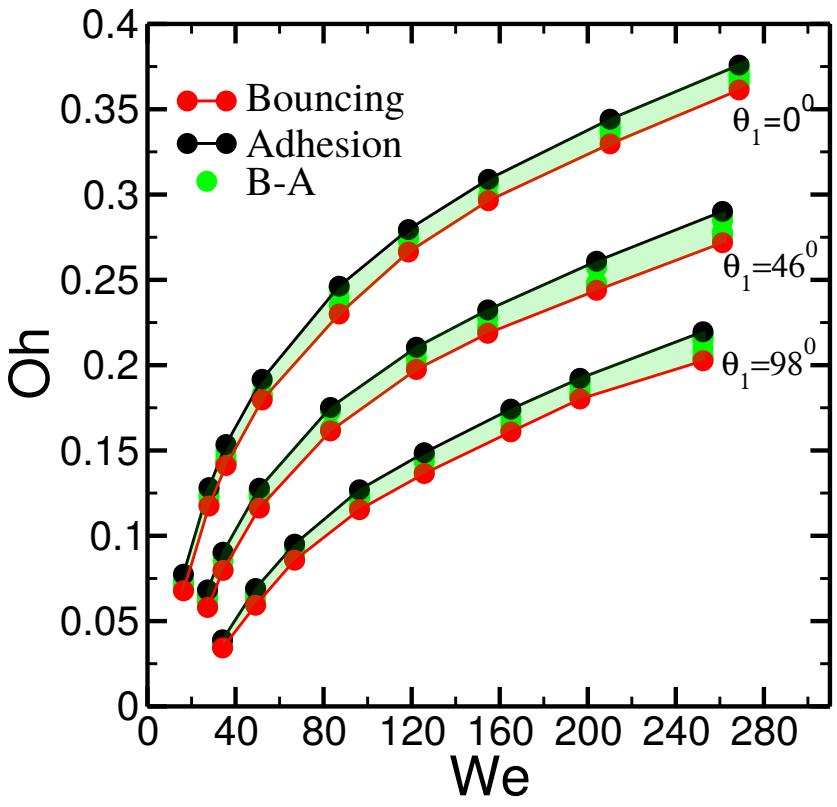

Figure 73: Transition curve from Adhesion to Bouncing as a function of surface tension (θ_1) which are $\theta_1 = 98°$, $\theta_1 = 46°$ and $\theta_1 \sim 0°$

6.6 Minimal model for transition region

We now attempt building a minimal $2D$ model reproducing the essential features of the transition between adhesion and bouncing. In the following we assume the droplets to be two-dimensional and constrained to a rectangular shape, parameterised by the center to center distance during a head-on collision. They provided with the exact same kinetic energy of the instant before the collision, and the collision process is modelled as the evolution of the deformation (compression and stretching) during which the kinetic energy is dissipated by the internal fluid flow while temporarily converted in potential energy. Furthermore we assume that if the droplet extends along the collision axis up to a certain threshold value, a break up mechanism will take place leading to separation (bouncing outcome), while if the threshold value is not achieved, the compound droplets will oscillate dissipating the whole kinetic energy. Since the model uses a single coordinate, it captures only the fundamental oscillation mode, while higher modes are suppressed.

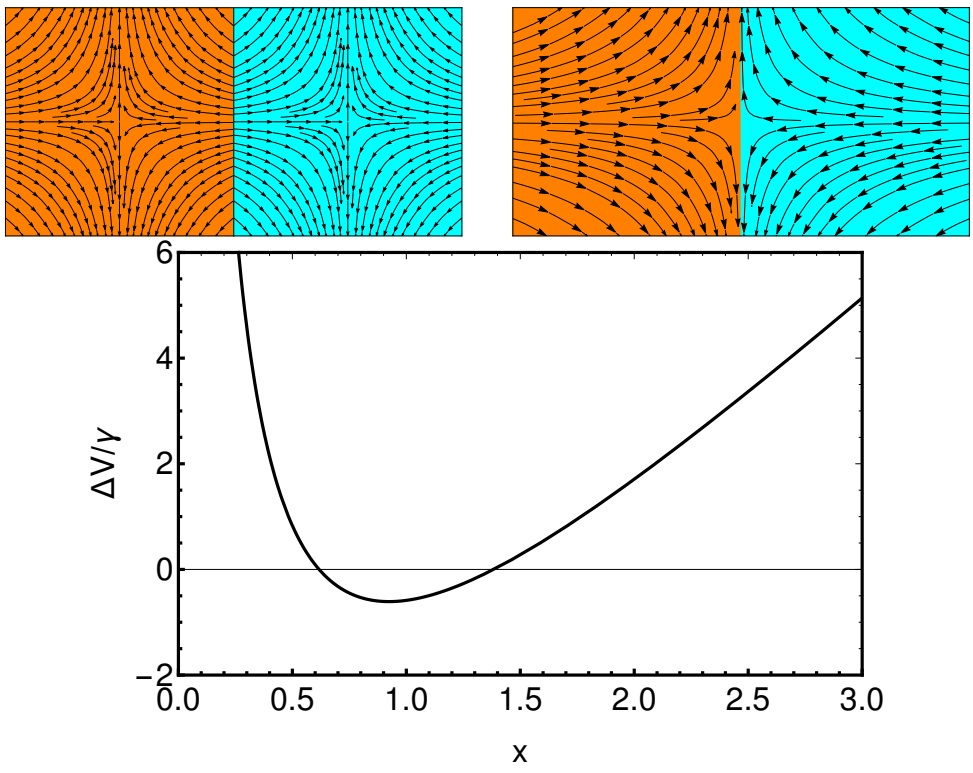

Figure 74: Top left: two square droplets brought in contact, with the flow field in the frame of reference of the centre of mass of each drop. Top right: two square droplets brought in contact, with the flow field in the frame of reference of the common centre of mass. Bottom: Normalised potential energy of two rectangular droplets sharing one side, as function of the distance between centres of mass, for $\theta = 90°$. the energy of two isolated droplets at equilibrium is subtracted.

6.6.1 Surface energy

To model the two droplets in the compound state, let us consider two rectangles with representing droplets of liquids indexed as 2 and 3, embedded in a gas phase denoted by index 1, as depicted in Fig.74. The surface energy of the liquid-liquid interface, represented by the shared side of the rectangle, is given by $\gamma_{ll} = 2\gamma\cos(\theta_1/2)$, where θ_1 represents the Neumann angle for the gas phase when two liquid droplets form a compound. Denoted by X the distance between centres of mass, and by A the conserved area of each drop, the excess of interfacial energy of the compound system (compared to two isolated droplets) is

$$\Delta V = \gamma\left(4X + \frac{2A(1+\cos(\theta/2))}{X}\right) - 8\gamma\sqrt{A} \tag{6.1}$$

where we have the expressed the vertical side of the rectangle as $Y = A/X$.

6.6.2 Kinetic energy

To model the liquid flow within each droplet during collision we assume a potential flow of the form

$$\phi = \frac{\dot{\epsilon}}{2}\left(x^2 - y^2\right) \tag{6.2}$$

where $\dot{\epsilon} = \dot{X}/X$ is the rate of strain during the deformation and x and y are the spatial coordinates in the frame of reference of the centre of mass of the drop. The velocity field is then given by $\mathbf{v} = \nabla\phi$ with components $v_x = \partial_x\phi = x$ and $v_y = \partial_y\phi = -y$. The kinetic energy associated to the flow in one droplet of density ρ is then expressed by the integral of $\rho|\nabla\phi|^2/2$ over the rectangular domain $\Omega = [-X/2, X/2] \times [-Y/2, Y/2]$

$$T^{\text{flow}} = \frac{\rho}{2}\int_\Omega |\nabla\phi|^2 dxdy = \frac{\rho\dot{\epsilon}^2}{2}\int_\Omega (x^2+y^2)dxdy \tag{6.3}$$

leading to the expression

$$T^{\text{flow}} = \frac{\rho\dot{\epsilon}^2}{24}XY(X^2+Y^2) = \frac{A\rho\dot{\epsilon}^2}{24}(X^2+Y^2) \tag{6.4}$$

where in the second expression we have used $A = XY$. During the collision, the kinetic energy associated to the linear momentum is given by

$$T^{\text{linear}} = \frac{\rho A}{2} v_x^2 = \frac{\rho A \dot{\epsilon}^2}{8} X^2 \tag{6.5}$$

where the second equality is obtained considering that the velocity of centre of mass is half the compression velocity $v_x = \dot{X}/2$ and substituting $v_x^2 = \dot{\epsilon}^2 X^2/4$. Combining both terms and counting two symmetric droplets we finally obtain

$$T = 2(T^{\text{flow}} + T^{\text{linear}}) = \frac{A\rho}{12} \dot{X}^2 \left(4 + \frac{A^2}{X^4}\right) \tag{6.6}$$

Where in the last step we have used the conservation of droplet area $Y = A/X$ and replaced $\dot{\epsilon} = \dot{X}/X$. Note that the same expression could have been obtained integrating the potential flow over the area of the compound drop, as the kinetic energy associated to the shared center of mass is zero by definition. Figure.75 depicts 4 stages of potential flow pattern in the compound droplets during collision, two in compression and two during stretching.

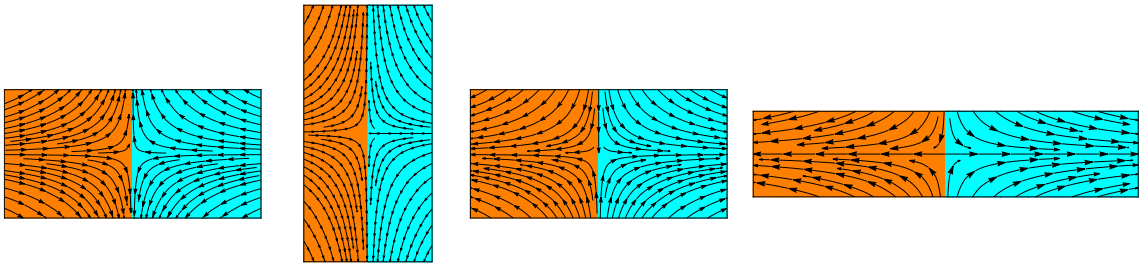

Figure 75: Sequence of droplet deformations during collision, with stream lines of potential flow: 1) First contact, droplets not deformed 2) droplet compressed 3) droplet stretched along collision axis (initial configuration recovered) 4) droplet further stretched

6.6.3 Dissipation function

For a hyperbolic flow field, we evaluate the dissipated power one droplets as

$$\begin{aligned} P^{\text{diss}} &= \mu \int_\Omega |\nabla \otimes \mathbf{v}|^2 dxdy \\ &= \mu \int_\Omega ((\partial_x v_x)^2 + (\partial_y v_y)^2) dxdy \\ &= \mu \int_\Omega \left((\partial_{xx}\phi)^2 + (\partial_{yy}\phi)^2\right) dxdy \\ &= 2\mu A \dot{\epsilon}^2. \end{aligned} \tag{6.7}$$

The corresponding Rayleigh dissipation function is for une droplet is therefore

$$R^{\text{diss}} = P^{\text{diss}}/v_x = \frac{4\mu A}{X^2}\dot{X} \tag{6.8}$$

where we have used the fact that $v_x = \dot{X}/2$ in each drop. The total Rayleigh dissipation force in both droplets is therefore

$$R^{\text{diss tot}} = \frac{8\mu A}{X^2}\dot{X} \tag{6.9}$$

6.6.4 Equations of motion

The Lagrangian function for the system is given by $\mathcal{L} = T - V$

$$\mathcal{L} = \frac{A\rho}{12}\dot{X}^2\left(4 + \frac{A^2}{X^4}\right) - \gamma\left(4X + \frac{2A(1+\cos(\theta/2))}{X}\right) + 8\gamma\sqrt{A} \tag{6.10}$$

from which the non-conservative equations of motion are obtained

$$\left(\frac{\partial \mathcal{L}}{\partial X}\right) - \frac{d}{dt}\left(\frac{\partial \mathcal{L}}{\partial \dot{X}}\right) = R^{\text{diss}}. \tag{6.11}$$

where in the right-hand side we have introduced the Rayleigh dissipation force. Eqn. 6.11 leads to

$$\gamma\left(\frac{2+2\cos(\theta/2)}{X^2} - 4\right) - \frac{8\mu\dot{X}}{X^2} + \frac{\rho\dot{X}^2}{3X^5} - \frac{\rho}{6}\left(4 + \frac{1}{X^4}\right)\ddot{X} = 0 \tag{6.12}$$

The expression in non-dimensional units is readily obtained by setting $\rho = 1$, $\gamma = 1$ and $A = L^2 = 4R^2 = 1$, where we have employed the droplet radius $R = L/2$ as length scale. In these

units the liquid viscosity is proportional to the Ohnesorge number $\mathsf{Oh} = \mu/\sqrt{\rho\gamma R} = \sqrt{2}\mu$. The other nondimensional group is the Weber number $\mathsf{We} = \rho(\Delta v)^2 L/\gamma = 2\dot{X}^2|_{X=1}$, where the relative velocity $\Delta v = \dot{X}$ is measured at the impact, determined by the initial condition $X = 1$. Replacing these definitions we can rewrite the equations of motion as

$$\frac{2+2\cos(\theta/2)}{X^2} - 4 - \mathsf{Oh}\frac{8\dot{X}}{\sqrt{2}X^2} + \frac{\dot{X}^2}{3X^5} - \frac{1}{6}\left(4+\frac{1}{X^4}\right)\ddot{X} = 0 \tag{6.13}$$

6.6.5 Numerical Integration of equations of motion

Figure 76 shows a typical trajectory computed by numerically integrating of the equations of motion, superimposed to a contour plot of the energy landscape as function of the coordinates X and $\dot{X}$. Where X represent the separation between droplet centres of mass and $\dot{X}$ is twice the velocity of the centre of mass of each drop in the reference of the global centre of mass. The droplet is initially compressed ($X < 0$) and subsequently stretched ($X > 0$) until reaching a maximum separation $X \simeq 2.9$, before spiraling towards the minimum of potential energy. As this model does not account for an implicit criterion for droplet separation, we introduce a threshold value to discriminate whether the collision leads to adhesion or bouncing of the two droplets. In the current analysis the threshold value is estimated to be a linear function of the angle $X_{\text{threshold}}(\theta) = 1 + \alpha\theta$, where the slope α can be employed as a fitting parameter. In the following we employ $\alpha = 0.02$.

To capture the transition between bouncing and adhesion in the We - Oh parameter space, we initialise the system at $X = X_{\text{threshold}}$ for various Oh and integrate the equations of motion backward in time. From the numerical solution we detect the velocity $v_{in} = \dot{X}/2$ when the orbit hits the condition $X = 1$ for the first time, and compute the corresponding $\mathsf{We} = v_{in}^2$. The transition lines displayed in Fig. 77 qualitatively capture the adhesion/bouncing transition in the phase diagram for droplet collision obtained from lattice Boltzmann simulations.

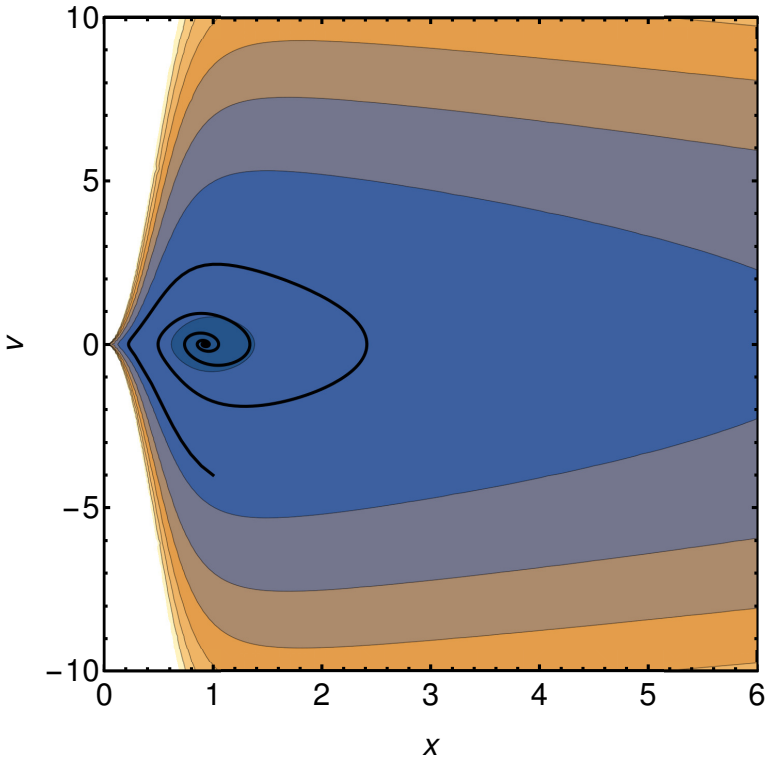

Figure 76: Energy landscape of the minimal collision model. Abscissas represent the separation X between droplet centres of mass, while ordinate the rate of variation $\dot{X} = 2v_x$, corresponding to two times the velocity of the centre of mass of each drop, in the reference of the global centre of mass. Superimposed is a typical trajectory produced by the numerical integration of the equations of motion for Oh $= 0.2$ with initial conditions $X_0 = 1$ and $\dot{X}_0 = -4$, corresponding to We $= 32$.

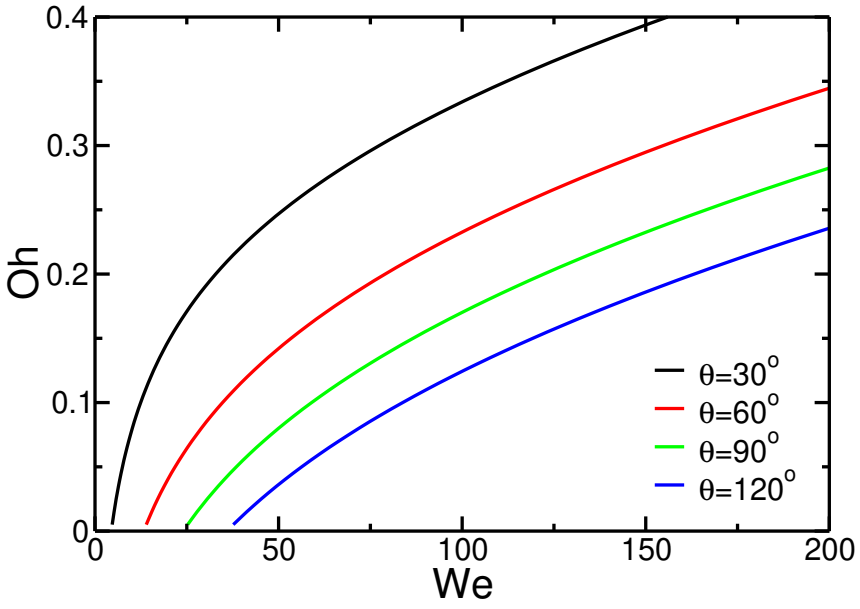

Figure 77: Transition lines between bouncing (bottom region) and adhesion (top region) in the We - Oh parameter space for $\theta = 30°, 60°, 90°$ and $120°$.

6.6.6 Re-partition of the free energy at breakup

Once the breakup occurs, we are now interested in estimating which fraction of the excess energy will contribute to the linear momentum of the droplets, and which fraction will excite free surface oscillations. By definition, if the breakup occurs exactly on the transition line, the linear momentum of each droplet individually is zero as the kinetic energy is also zero, so all the excess energy will drive surface oscillations. On the other hand, if the breakup occurs with some residual kinetic energy, the linear component in each drop $T^{\text{linear}}_{\text{break}} = 2T^{\text{linear}}$ is now conserved, due to the conservation of the momentum, while the excess of free energy is added to the non vanishing flow component of kinetic energy $T^{\text{flow}}_{\text{break}} = T^{\text{flow}} + \Delta V$. Introducing Eqns. 6.1, 6.4 and 6.5 we obtain the following expressions:

$$T^{\text{linear}}_{\text{break}} = 2\left(\frac{\dot{X}}{2}\right)^2 = \frac{\dot{X}^2}{2} \tag{6.14}$$

$$T^{\text{flow}}_{\text{break}} = \frac{\dot{X}^2}{6}\left(1 + \frac{1}{X^4}\right) + \frac{2}{X} + 4X + \frac{2\cos(\theta/2)}{X} - 8 \tag{6.15}$$

Equating the two terms $T^{\text{linear}}_{\text{break}} = T^{\text{flow}}_{\text{break}}$ leads to a relation in the phase space for the condition where the excess free energy at breakup is equally split between linear motion and surface oscillations

$$\dot{X}^2 = 12\frac{(1+\cos(\theta/2))\,X^3 - 4X^4 + 2X^5}{3X^4 - 1} \tag{6.16}$$

If the breakup occurs of any combination of X and $\dot{X}$ at the right of the transition line reported in Fig. 78, the kinetic energy of the internal flow is larger than the kinetic energy of the centre of mass. The transition line hits the axis $\dot{X} = 0$ when both $T^{\text{linear}}_{\text{break}} = 0$ and $T^{\text{flow}}_{\text{break}} = 0$. Breakup cannot occur at the left of this point, as the compound droplet has lower energy of two separated droplets. In real systems with large number of degrees of freedom one cannot exclude the presence of exotic configurations leading to breakup, but such cases cannot be predicted with the current model. In Fig. 79 we compare the transition line of the model with the numerical results for $\theta_1 = 98°$, where the breakup length has been employed as fitting parameter. Remarkably, despite the crude approximations, the model is able to reproduce both qualitatively and quantitatively the numerical results.

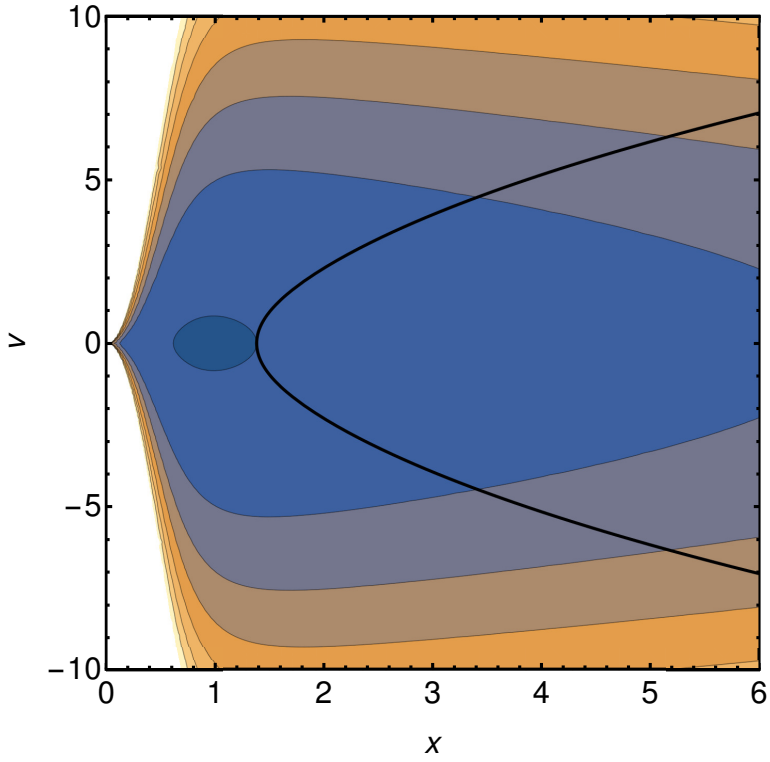

Figure 78: Energy landscape with superposed the transition boundary for equal splitting the excess of free energy. droplets where the kinetic energy of the internal flow is larger than the kinetic energy of the centre of mass are found in the right region.

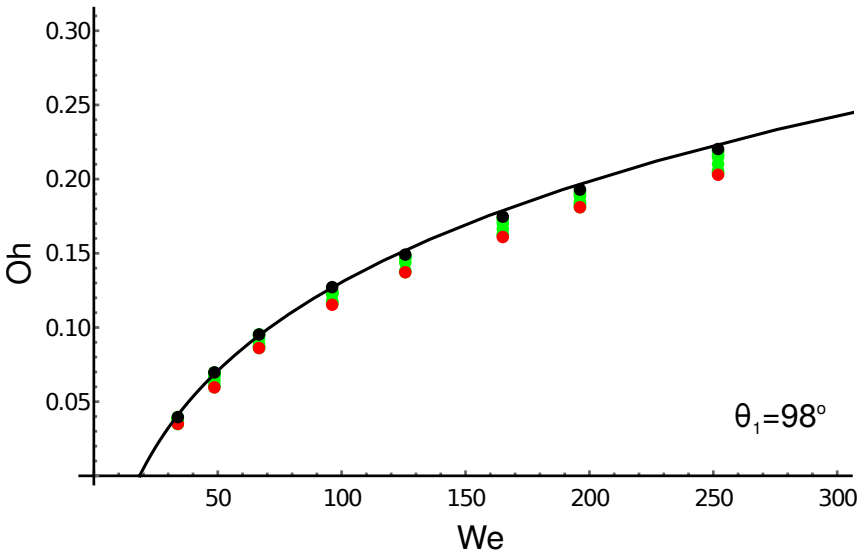

Figure 79: Comparison of the transition lines between *Adhesion*(top region) and *Bouncing*(bottom region) in the We − Oh parameter space for $\theta_1 = 98°$ *Solid line:* minimum model prediction *Points:* simulation data (Black:adhesion, Red: bouncing, green: delayed adhesion)

6.7 Head-on collision of droplets of different size

After analysing the collision dynamics of identical droplets and detecting the corresponding transition line from *Adhesion* to *Bouncing* outcome, in this section, we will relax the strong condition of droplets with identical properties. We explore how the relative size of colliding droplets affects the impact outcome. As previously, the collision study at size contrast is conducted at head-on collision setup as shown in Fig.45. In this analysis the two droplets have size ratio (R_2/R_1) is varied in the range $1.0 - 1.5$. Being all remaining properties equal, we assume that by swapping the droplets these data will represent also size ratios below unity. In this study we are seeking to explore the Bouncing to Adhesion transition as function of impact velocity and size ratio. All the simulations are performed at fixed surface tension combination $\theta_1 \sim 0^\circ$ and fixed average $\mathsf{Oh}_{\mathsf{av}} = 0.181$. The second condition is used to tune the liquid viscosities accordingly as the relative droplet size is varied. In order to keep the net momentum of the system to zero value, we also adjust the impact speed of each droplet such that:

$$m_1 V_1 = -m_2 V_2 \tag{6.17}$$

In 2D $m_1 = \rho_1 \pi R_1^2$ and $m_2 = \rho_2 \pi R_2^2$. As the density of the two droplets is equal ($\rho_2 = \rho_3$), the above equation determine the relative magnitude of impact velocities:

$$V_2 = -\frac{R_1^2}{R_2^2} V_1 \tag{6.18}$$

and therefore the velocity terms entering the Weber numbers is :

$$\Delta V = V_1 - V_2 = V_1 \left(\frac{R_1^2}{R_2^2} + 1 \right) \tag{6.19}$$

Fig.80 reports the summary of the 2D results as a function of the average $\mathsf{We}_{\mathsf{av}}$ number (Eq.(5.5)) and size ratio between the two droplets R_1/R_2. As for the case of equal size droplets, the transition region between bouncing and adhesion involves a narrow region of delayed adhesion, for all tested size ratios. Interestingly, the larger the size ratio, the larger the Weber number at which the transition is observed, with the adhesion outcome favoured. It has been observed that at the

parity of R_1/R_2 and by increasing the $\mathsf{We}_{\mathsf{av}}$ we see the transition from *Adhesion* to *Bouncing*. The same is observed at the parity of $\mathsf{We}_{\mathsf{av}}$ and decreasing the size ratio in the phase diagram. The equal size droplets ($\frac{R_1}{R_2} = 1$), the bouncing happens at much lower impact speed ($\mathsf{We}_{\mathsf{av}}$), but as the size contrast increases the two droplets must collide at larger impact speed in order to bounce away. This phase diagram, which is produced at relatively bigger in size of the droplets as compared to previously shown results of identical droplets (Fig.73), still it shows a significant region of *Delayed adhesion* (DA) region.

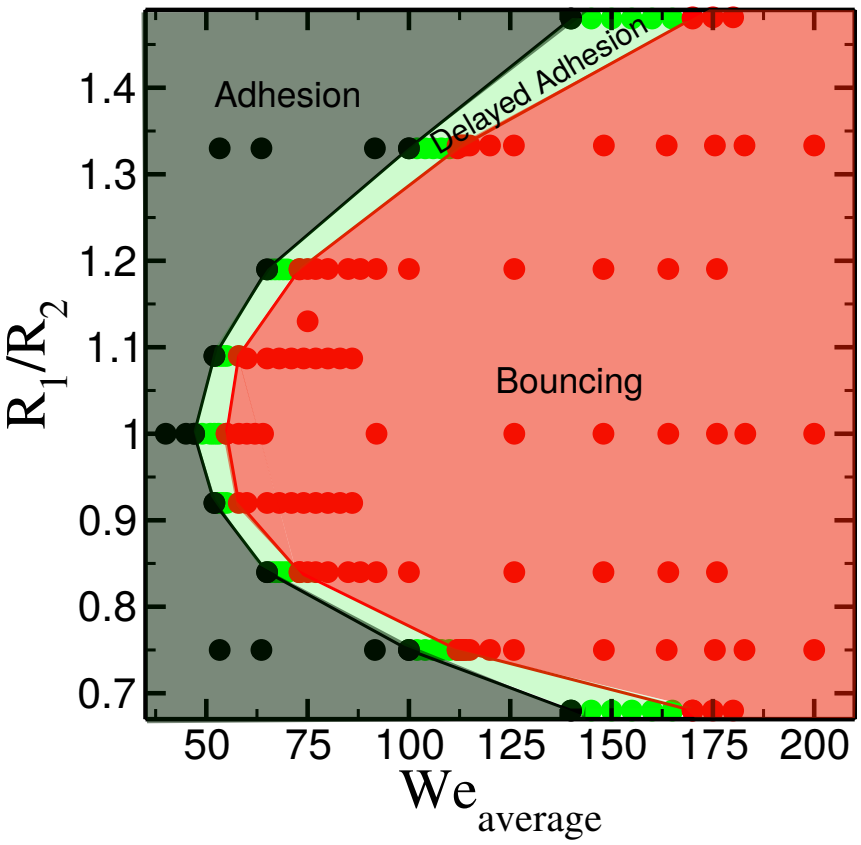

Figure 80: Phase diagram between the average Weber number ($\mathsf{We}_{\mathsf{av}}$) and size ratio between the two droplets ($\frac{R_1}{R_2}$) at $\theta_1 \sim 0°$

6.7.1 Inspection of bouncing dynamics of droplets with different size

In this section we will investigate how the size contrast between the two droplets effects the bouncing dynamics. For this, we perform a comparative study between two cases: a) droplets with non-identical size ($R_1/R_2 = 0.75, R_1 = 135, R_2 = 180$) b) droplets with identical size ($R_1/R_2 = 1.00, R_1 = R_2 = 158$). These two sets are selected such that the average mass ($M_{av} = 78427l.u$), $\mathsf{We} = 148$, $\theta_1 \sim 0°$ and $\mathsf{Oh}_{\mathsf{av}} = 0.181$ are fixed. In Fig.81(a.b), a comparison

of sequence of collision steps corresponds to $R_1/R_2 = 0.75$ and 1.0 is shown respectively.

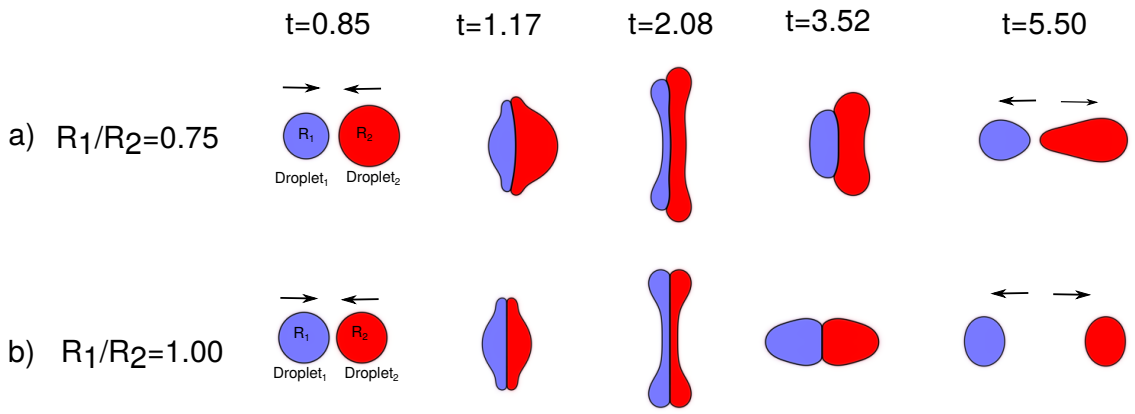

Figure 81: Sequence of snapshots during the collision at different size contrast a) $\frac{R_1}{R_2} = 0.75$ ($R_1 = 135$,$R_2 = 180$) b) $\frac{R_1}{R_2} = 1.00$ ($R_1 = R_2 = 158$). The other parameters are fixed: $M_{av} = 78427 l.u$, We $= 148$, $\mathrm{Oh_{av}} = 0.181$ and $\theta_1 \sim 0^\circ$

A comparison of the evolution of energy balance corresponds to these two sets are shown in Fig.82. The *black curve* represents the data corresponds to size contrast and *red curve* shows the set of data when the size of the droplets is same. In Fig.82(a), It is observed that after the first impact, the kinetic energy drops rapidly for both the cases. The kinetic energy corresponds to identical size droplets relaxes to its minimum (zero value) immediately as compared to the non-identical size droplets. This is explained with the evolution of free energy shown in Fig.82(b) , where the peak of total free energy during maximum deformation is significantly larger for non-identical droplets and the deformation is spread over longer duration. Consequently, in Fig.82(c), it is shown that for both identical and non-identical droplet size majority of the energy is dissipated in the first step. For identical size droplet collision (red curve), the droplets relaxes quickly after dissipating all the energy in the proceeding steps. However at size contrast (black curve), after the first impact, when droplets are detached from each other, they experience more shape deformation, hence dissipate slightly higher energy duration bouncing.

After collision, when the droplets are separated from each other (bouncing away), the energy transferred to each individual droplet plays an important role. Therefore it is worth to have a look at the individual droplet's kinetic energy. In Fig.83, we show the evolution of kinetic energy corresponds to $droplet_1$ and $droplet_2$. As expected, when there is not size contrast, the contribution by each droplets is 50% of the total kinetic energy represented by red curve in Fig.83(a,b).

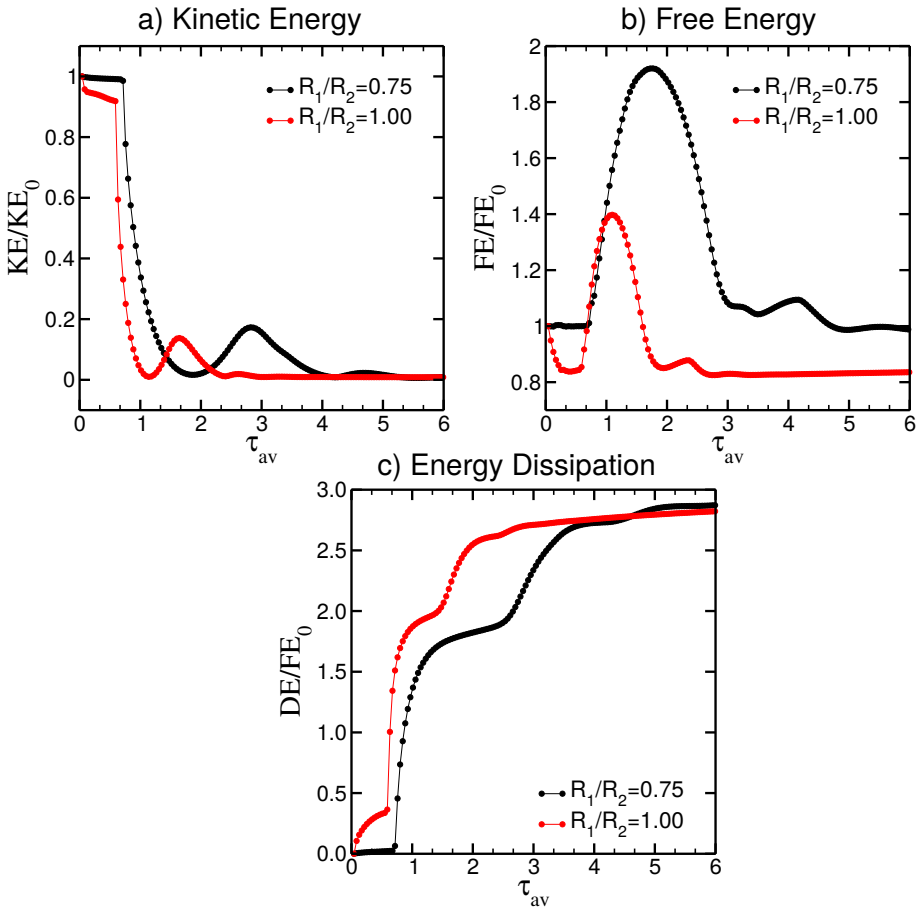

Figure 82: Comparison of the evolution of a) Kinetic energy b) Free energy c) Energy dissipation *black curve:* $\frac{R_1}{R_2} = 0.75$ ($R_1 = 135$, $R_2 = 180$), *red curve:* $\frac{R_1}{R_2} = 1.00$ ($R_1 = R_2 = 158$). The other parameters are fixed: $M_{av} = 78427l.u$, $\mathrm{We} = 148$, $\mathrm{Oh_{av}} = 0.181$ and $\theta_1 \sim 0°$.

On the other hand, at size contrast, the two droplets contribute differently in the total kinetic energy. As shown by the *black curves* in Fig.83(a,b), the $droplet_1$ which is smaller in size carried more kinetic energy before impact as compared to the $droplet_1$ (bigger in size). After the impact, $droplet_2$ experience larger shape deformation represented by the oscillations in kinetic energy plot Fig.83(b) at approximately $\tau = 3 - 5$. However, both droplets relaxes to its minimum zero value after dissipating all the kinetic energy.

The kinetic energy transferred to each individual droplet presents a linear component contributing the individual droplet's momentum (same for equal size droplets). We further investigate the bouncing mechanism at size constant and how during bouncing the residual linear component of kinetic energy is split between the droplets. To this aim we perform a more detailed analysis of the numerical simulations. In addition to simulation at $\mathrm{We_{av}} = 148$, we perform five more sets ranging from $\mathrm{We_{av}} = 126$ to 200 and compare the residual linear component of kinetic energy

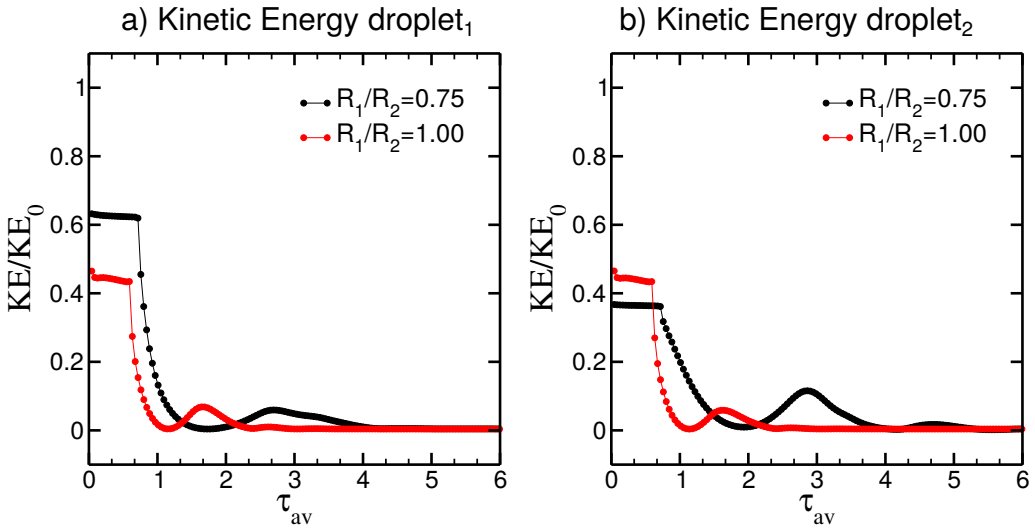

Figure 83: Comparison of the evolution of a) Kinetic energy of $droplet_1$ b) Kinetic energy of $droplet_2$. *black curve:* $\frac{R_1}{R_2} = 0.75$ ($R_1 = 135$, $R_2 = 180$), *red curve:* $\frac{R_1}{R_2} = 1.00$ ($R_1 = R_2 = 158$). The other parameters are fixed: $M_{av} = 78427l.u$, $\mathsf{We} = 148$, $\mathsf{Oh_{av}} = 0.181$ and $\theta_1 \sim 0°$

with the case of no size contrast. In Fig.84(a), the total linear component of kinetic energy is plotted as a function of $\mathsf{We_{av}}$. The curve is re-scaled by the linear component of kinetic energy before impact. As expected, the droplets impacting at higher $\mathsf{We_{av}}$ carry larger linear component of kinetic energy when they start bouncing away. However, it is observed that when the droplets starts bouncing away, the total linear kinetic energy carried by system with identical droplet size is larger as compared to the non-identical case. On the other hand, if we have a look at kinetic energy carried by the individual droplet in Fig.84(b). The *red curve* at size ratio one shows the contribution by each droplet and is same for both. This act as a reference curve understand the split between two droplets at non identical size. The solid *black curve* represent the linear kinetic energy contribution by smaller size droplet ($droplet_1 = 135l.u$) and it has more energy as compared to the *red curve* at ($droplet_1 = droplet_2 = 159l.u$). On the other hand the dashed *black curve* shows the kinetic energy associated with bigger size droplet ($droplet_2 = 180l.u$) and smaller than the equal size case.

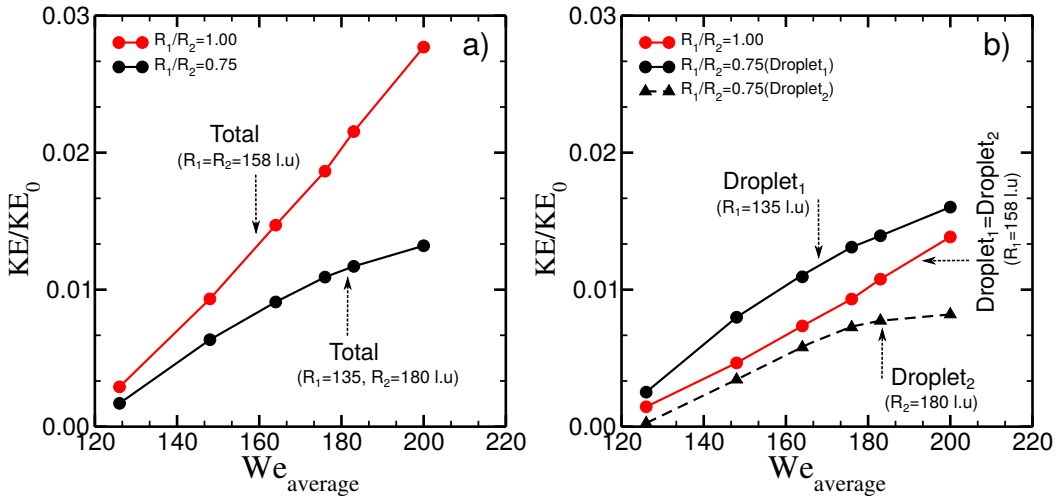

Figure 84: Variation of linear component of kinetic energy rescaled by linear kinetic energy before impact with respect to We_{av} a) Total (*red curve:* identical size *black curve:* non-identical size) b) split between $droplet_1$ and $droplet_2$ (*red curve:* identical size $droplet_1$=$droplet_2$ *solid black curve:* smaller droplet $droplet_1$,*dashed black curve:* bigger droplet $droplet_2$).The other parameters are fixed: $M_{av} = 78427l.u$, We = 148, $Oh_{av} = 0.181$ and $\theta_1 \sim 0°$

6.8 Head-on collision at non-identical viscosity of droplets

After investigating the collision between droplets at non identical size, in this section we relax the condition of equal viscosity of the droplets and explore how the relative viscosity of the colliding droplets affects the impact outcome. This collision study at viscosity contrast is conducted at head-on collision setup as shown in Fig.45. In this study we are aim to investigate the transition between Bouncing to Adhesion outcome as a function of average impact velocity (We_{av}) and average viscosity (Oh_{av}) between the droplets. The viscosity of the droplets is varied such that the ratio between two is always fixed ($\frac{\mu_2}{\mu_3} = 1.97$). All the simulations are performed at fixed surface tension combination $\theta_1 \sim 0°$ and $D = 180l.u$.

The summary of 2D results at viscosity contrast as a function of We_{av} and Oh_{av} is shown in Fig.85(a). From the simulation results, it is observed that, in the same parameter space, the transition curve with and without viscosity contrast behave similar. For the comparison, in Fig.85(b) we show the transition curve at no viscosity contrast ($\frac{\mu_2}{\mu_3} = 1.0$) but same rest of the collision parameters. It is noted that there is a larger width opening of the *Delayed Adhesion* (DA) region when collision occurs at a viscosity constant as compared to no viscosity ratio between the droplets.

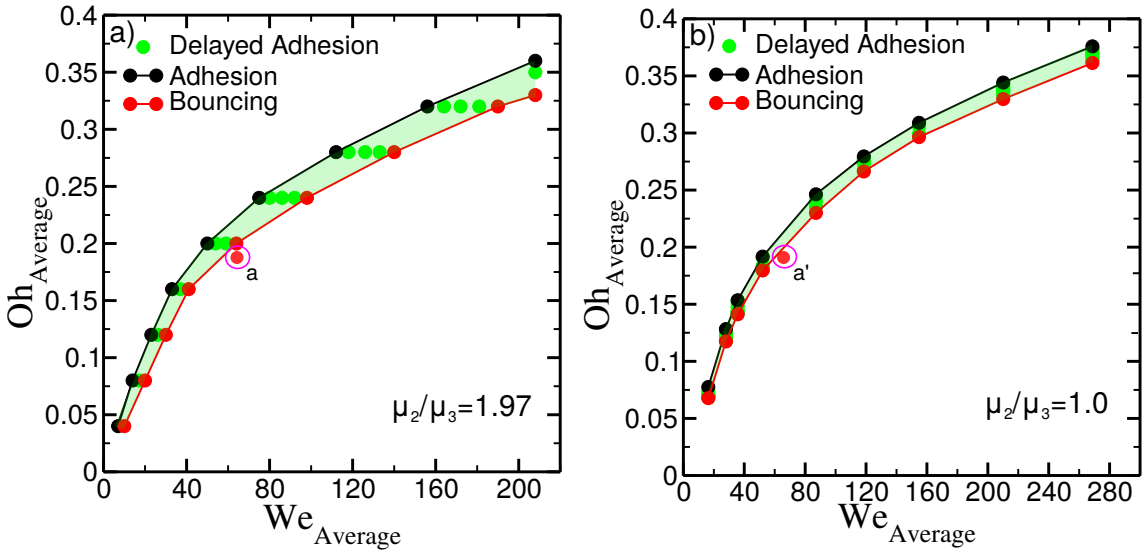

Figure 85: Transition curve from *Adhesion* to *Bouncing* with viscosity contrast at $\theta_1 \sim 0°$, $D = 180$

6.8.1 Inspection of bouncing dynamics of droplets with different viscosity

To gain more insight on how the viscosity contrast affects the bouncing dynamics, four sets of simulations are analysed in this section. These four sets are performed at different viscosity ratios ($\mu_2/\mu 3$=1.00, 1.55, 1.97 and 3.41). The average viscosity ($\mu_{\mathsf{av}} = 0.181$) is kept constant in these four sets. The other collision parameters are also fixed such as: impact velocity ($\mathsf{We}_{\mathsf{av}} = 64$), droplet size ($D = 180$) and surface tension combination $\theta_1 \sim 0°$. The sequence of collision steps corresponds to these four viscosity ratios is shown in the Fig.86. The snapshot at μ_2/μ_3=1.97 and 1.00 corresponds to point a and a' circled in Fig.85(a,b) respectively.

In Fig.87, we show the comparison of the evolution of energy budget corresponds to each case. In Fig.87(a), we show the kinetic energy rescaled by the initial kinetic energy of the droplets. The snapshots shown above are taken at the points circled ($a - f$) in kinetic energy plot. It has been observed that, at the same impact speed, for all the sets the kinetic energy decreases rapidly after the impact. However, the total kinetic energy left after the collision decreases as the viscosity contrast increases. This decrease in kinetic energy is accompanied by an increase in the energy stored in the surface deformation as shown in the free energy plot in Fig.87(b). The evolution of free energy and energy dissipation is normalized by the free energy of droplets in the non-deformed state. The energy dissipation comparison shown in Fig.87(c) depicts that as the viscosity contrast increase the total energy dissipation during bouncing decreases.

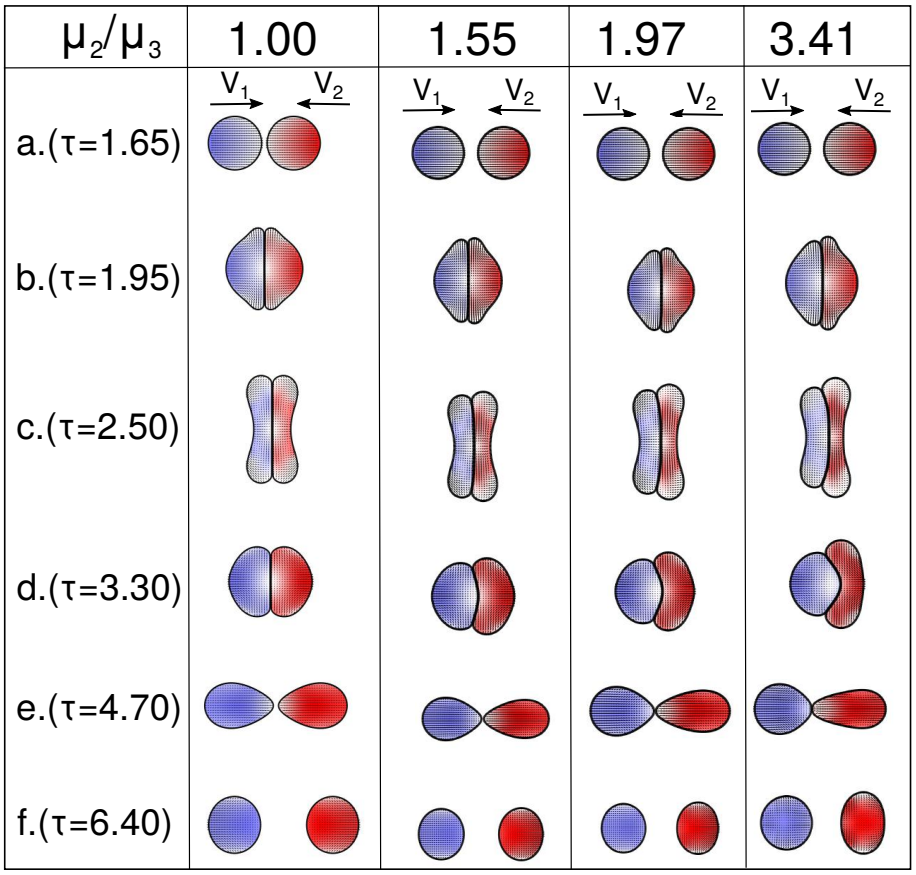

Figure 86: Sequence of snapshots during the collision process and its comparison at different viscosity contrast ($Oh_{av} = 0.181$, $We = 64$, $D = 180$, $\theta_1 \sim 0°$). The color in the snapshots corresponds to the intensity of kinetic energy.

To further understand the bouncing dynamics at viscosity contrast, we analyse the partition of kinetic energy into the linear motion of individual droplets and their surface oscillations. To do so, we choose point circled f in Fig.87(a) which corresponds to first oscillation after separation ($Oscillation_1$). In Fig.88, we report the variation of kinetic energy of the linear momentum and the kinetic energy stored in the first oscillation after separation as a function of viscosity contrast. Both are rescaled by the linear kinetic energy before impact. In Fig.88(a) represents the linear and oscillating potion of kinetic energy for the whole system. The *black curve* shows the linear component and *red curve* represent the surface oscillations. It is observed that as the viscosity contrast increases, the total kinetic energy into the linear motion of the droplets decreases and is accompanied by large surface oscillations. Also, we observe that there is a crossover approximately at $\frac{\mu_2}{\mu_3} = 1.5$. This shows that, by tuning the viscosity contrast between the droplets, it is possible to channel the residual velocity of the droplets into surface deformation rather than linear motion. Fig.88(b,c) shows the linear and oscillating potion of kinetic energy for $droplet_1$ (more

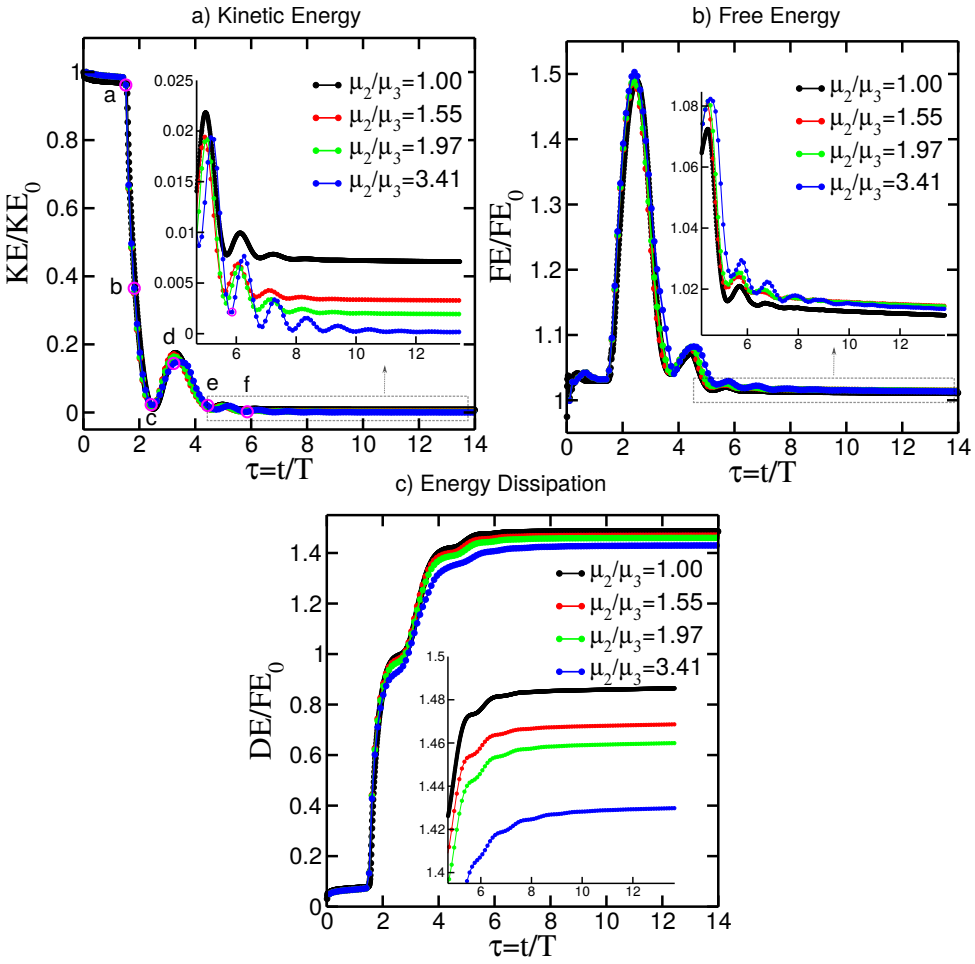

Figure 87: Evolution of the total kinetic energy for bouncing droplets at different viscosity contrast ($\mathsf{Oh}_{\mathsf{av}} = 0.181$, $\mathsf{We} = 64$, $D = 180$, $\theta_1 \sim 0°$)

viscous) and $droplet_2$ (less viscous). In both the panel b and c the linear component is same and nearly half of the total. The is because the droplets collide at same impact speed in order to keep the net momenta to zero value. However the surface oscillations experienced by the two droplets are different. The $droplet_1$ (more viscous) the surface oscillation decease as the viscosity contrast increase and $droplet_2$ (less viscous) experience more surface oscillation. As the viscosity contrast increase the magnitude of these oscillations starts to level-off.

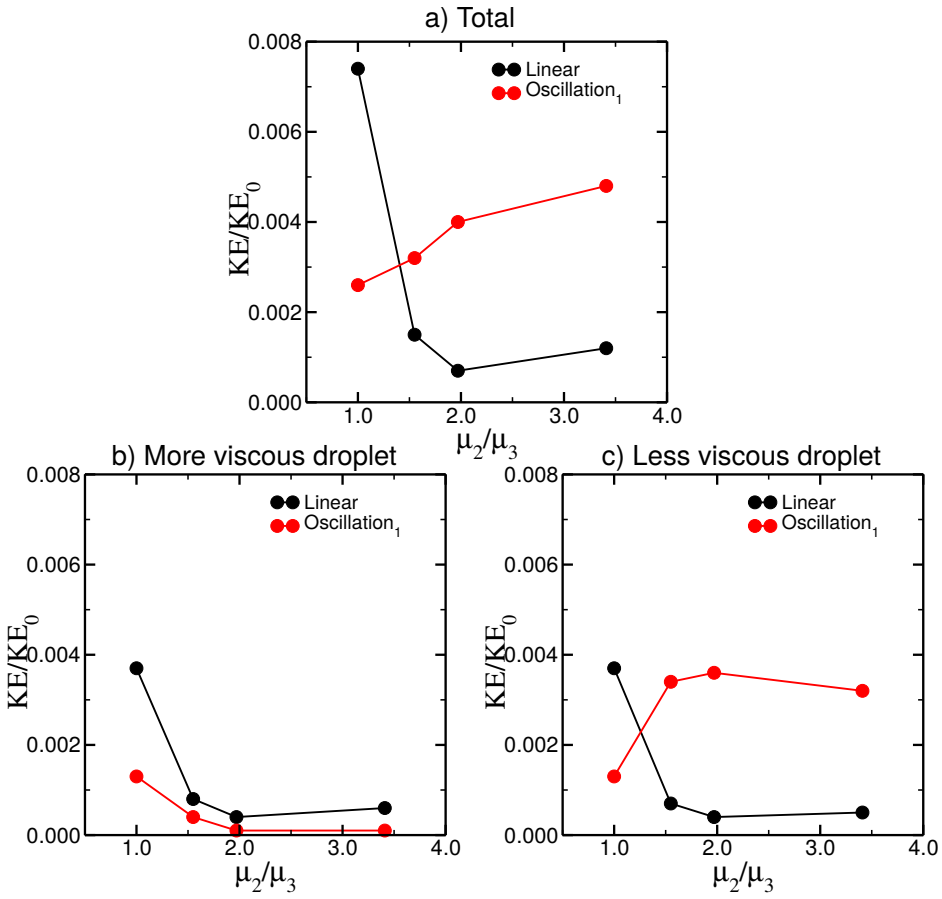

Figure 88: Variation of linear and oscillation components of kinetic energy rescaled by kinetic energy before impact as a function of viscosity contrast a) Total b) $Droplet_1$ (more viscous) b) $Droplet_2$ (less viscous) (*red*:oscillation,*black*:linear) ($\mathsf{Oh_{av}} = 0.181$, $\mathsf{We} = 64$, $D = 180$, $\theta_1 \sim 0^\circ$)

6.9 Off-centre droplet collision of 2D identical droplets

In the previous sections, we studied the collision between the immiscible droplets (identical and non-identical) at head-on collision setup ($\chi = 0$ in Fig.45). In this section, a comprehensive 2D numerical investigation of the collision dynamics at off-centre is discussed. Collision between droplets which occur off-centre ($\chi > 0$) are more complex in nature and are closer to realistic collision scenarios. Generally, one of the following can occur when the two droplets collide at off-center: the droplets remain permanently in adhesion state, they can be temperately coupled and, at a later point, split into two or more droplets, they may lead to fragmentation upon contact. The fragmentation collision happens at high impact speed where the surface tension forces are only of secondary significance and the collision mechanism is driven by inertia. The Relative importance of surface tension and inertia is represented by We number which is one of the control parameters

in off-centre droplet collision. The other control variable is impact parameter (χ). Depending on these two control parameters, different collision outcomes can occur [5] [88] [139].

6.9.1 Outcomes of Off-centre droplet collision

We stared our numerical investigation of off-centre droplet collision using the simulation setup shown in Fig.45 in $2D$. The domain size for this study is 1700×1000. Similar to head-on collision, the two liquid droplets are considered to be identical in terms of the surface tension $\gamma_{12} = \gamma_{13} = \gamma$, diameter $D_1 = D_2 = D$, density $\rho_1 = \rho_2 = \rho$, impact speed $|V_1| = |V_2| = V$ and viscosity $\mu_1 = \mu_2 = \mu$. In general, the outcome of the collision can be different depending on these physical parameters cast into We and χ. A few examples of typical collision outcomes at off-centre setup is discussed below using Fig.89 to Fig.94. For few cases, we show a comparison of sequence of collision steps from our simulation along with: a) experimental results by N.Ashgris and J.Y.Poo, which was conducted for binary collision between water droplets for equal size [5]. b) $3D$ numerical study by Yu Pan and Kazuhiko Suga using level set method [90]. Despite our simulations are carried only in 2D, the comparison with experiments shows striking similarities. It is worth reminding however that the comparison remains only qualitative due to the fundamental difference in mass and energy repartition between $2D$ and $3D$ systems.

1. *Adhesion*: A typical collision sequence from our simulation which leads to *Adhesion* outcome is shown in Fig.89(b), This simulation is performed at off-centre setup such that the impact parameter ($\chi = 0.22$) and impact speed (We=43) is relatively low. It is observed that after the impact, the droplets experience shape deformation as well as rotation along the collision axis. Based on the selected collision parameters, the droplets do not have sufficient energy to detach from each other. After dissipating all the energy in deformation and rotation droplets slowly relaxes to the adhesive morphology. In Fig.89(a), we show a sequence of steps from the experimental study by N.Ashgris and J.Y.Poo [5] at possible collision parameter close to our simulation results. In 1990, N.Ashgris and J.Y.Poo conducted a comprehensive experimental examination of the binary collision dynamics of water droplets for various size ratios. For comparison, we illustrate the collision dynamics for water droplets of equal size. In Ashgris and Poo's experimental investigation, one of the water streams was colored to illustrate the extent of mass transfer during collision.

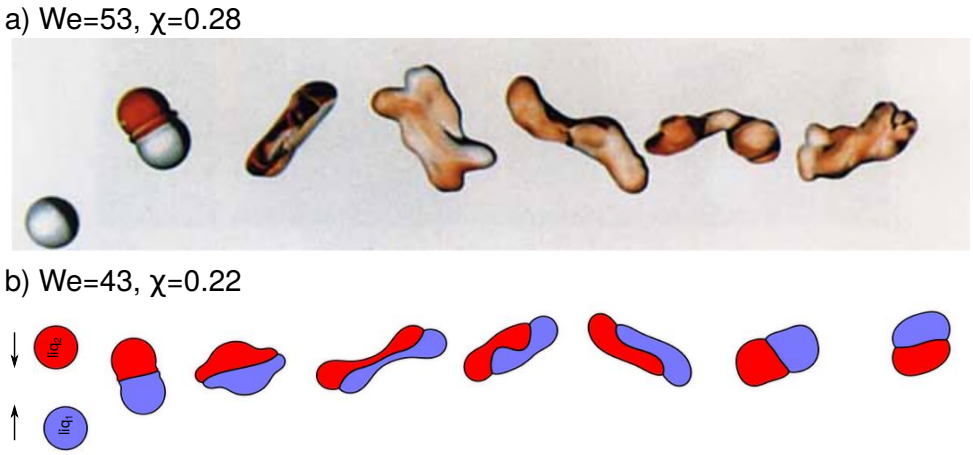

Figure 89: Off-centre Adhesion a) experimental result of binary collision between water droplets for equal size by N.Ashgris and J.Y.Poo [5] b) our $2D$ simulations results (corresponds to point a in Fig.95.

2. *Delayed Adhesion*: Similar to head-on collision, a intermediate step $DelayedAdhesion$ is captured at off centre as well. Here the droplets separate briefly, but then interact again and rest in adhesive state as shown in Fig.90. Our $2D$ results are represented in Fig.90 are performed at $\mathsf{WE} = 50$ and nearly head-on collision such that ($\chi = 0.08$). This set of simulation corresponds to point b in Fig.95 (lower impact parameter range).

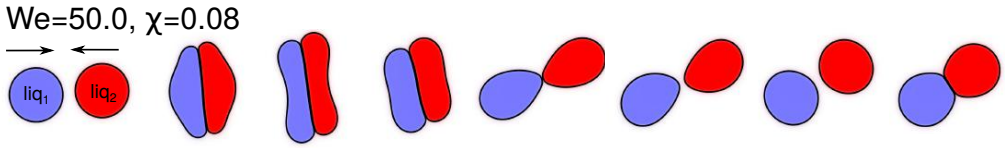

Figure 90: $2D$ simulations results of Off-centre Delayed Adhesion (corresponds to point b in Fig.95)

3. *Separation without fragmentation:* During off-centre collision, the colliding droplets can simply get separated after the impact. Depending on the range of χ and We number, the separation can also leads to fragmentation leaving one or more satellite droplets behind. In Fig.91, near head-on collision setup ($\chi = 0.1$) and $\mathsf{We} = 70$, separation of droplets without any fermentation is shown.

   In Fig.92(a,b), a qualitative comparison of collision steps between the experimental study by N.Ashgris and J.Y.Poo [5] and our 2D results is shown respectively. It is observed that the qualitative features of the separation process is similar in both the studies. However in

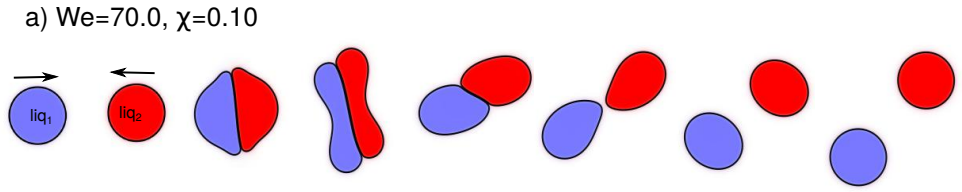

Figure 91: $2D$ simulations results at We $= 70$ and near head-on setup ($\chi = 0.1$) (corresponds to point c in Fig.95)

our simulations, this feature is observed at relatively lower We and high χ value.

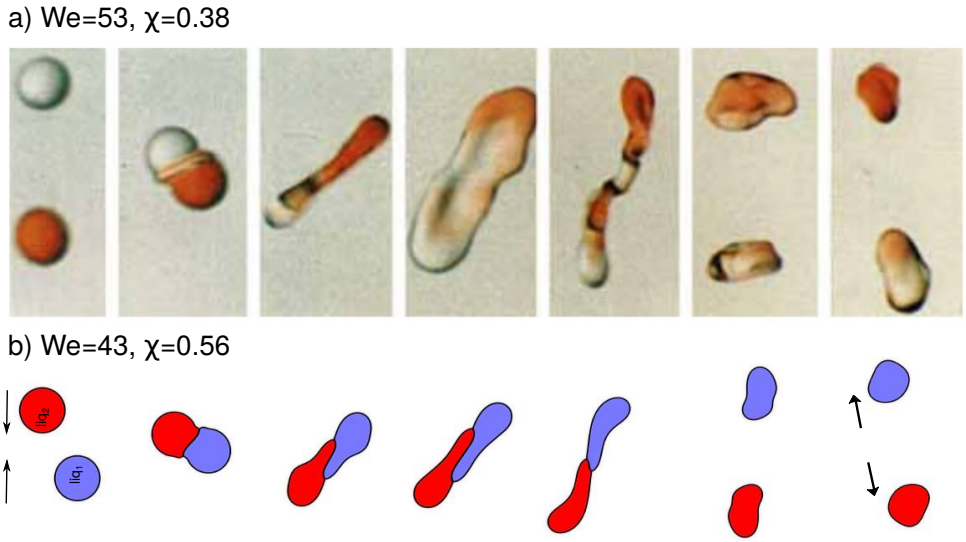

Figure 92: Off-centre Bouncing a) experimental result of binary collision between water droplets for equal size by N.Ashgris and J.Y.Poo [5] b) our $2D$ simulations results (corresponds to point d in Fig.95)

4. *Separation with fragmentation:* The colliding droplets at off-centre can also experience fragmentation leaving more than one satellite droplet behind. This behaviour is shown in Fig.93 and Fig.94. When collision occur at high impact speed, inertial forces dominate over the surface tension and the droplets experience large deformation which can lead to fragmentation. In Fig.93, an example of off-centre separation which leaves one satellite droplet behind is shown in comparison with experimental results by N.Ashgris and J.Y.Poo (Fig.93(a)[5] and $3D$ simulation results by Yu Pan and Kazuhiko Suga (Fig.93(b)) [90]. It is observed that, at almost same impact speed (We $\approx$ 80) in all three cases, the same qualitative collision behaviour is observed at significantly different impact parameters.

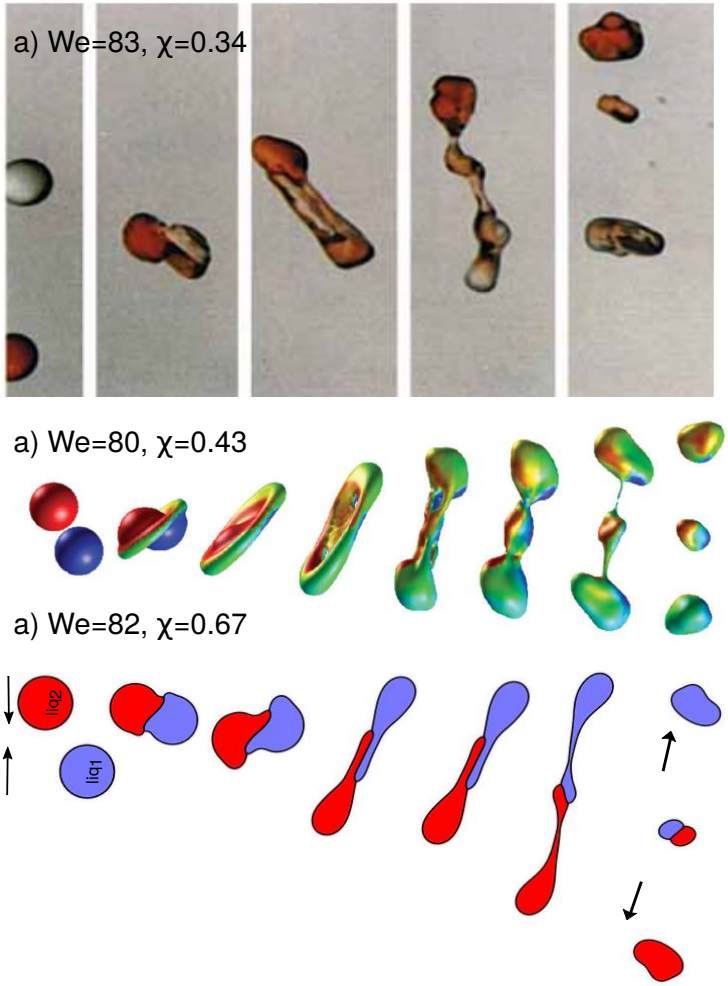

Figure 93: Off-centre separation leaving one-satellite droplet a) experimental result of binary collision between water droplets for equal size by N.Ashgris and J.Y.Poo [5] b) $3D$ simulation results of collision between equal size water droplets in air at high density ratios (above 500) by Yu Pan and Kazuhiko Suga [90] c) our $2D$ simulations results (corresponds to point f in Fig.95)

In Fig.94(a,b), we show a qualitative comparison of separation when two satellite droplets are generated after collision. Both the sequence are shown at nearly same impact speed (We $\approx$ 80), however it is observed that the similar dynamics in our simulations is captured at relatively higher impact parameter (χ). Also in our simulation, the two satellite droplets are generated after collision starts moving in the direction perpendicular to the collision axis.

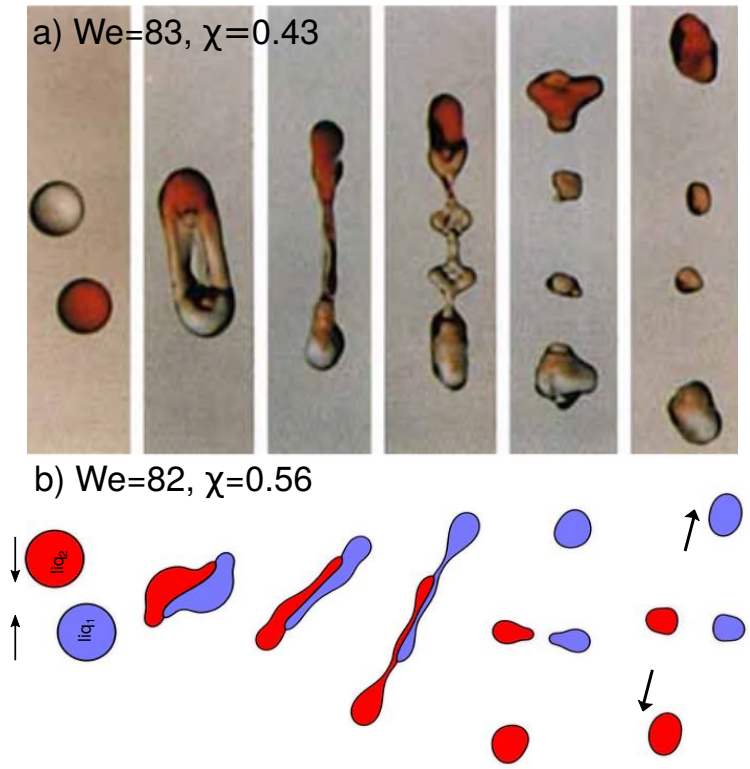

Figure 94: Off-centre separation leaving two-satellite droplet a) experimental result of binary collision between water droplets for equal size by N.Ashgris and J.Y.Poo [5] b) our $2D$ simulations results (corresponds to point e in Fig.95)

6.9.2 Phase diagram at off-centre collision

After identifying the possible scenarios of collision outcomes at off-centre setup , we then performed systematic simulations of 2D off-centre collisions of immiscible identical droplets, in the parameter space of the non dimensional numbers Weber (We) and Impact parameter (χ). Depending on these two control parameters, the summary of 2D simulation results is shown in Fig.95. All points in the phase diagram represents the 2D simulation, where the *black points:* corresponds to adhesion outcome, *red points:* separation (with and without fragmentation) and *green points:* represent delayed adhesion outcome. In the parameter space of (We) and χ, the outcomes of collision in the phase diagram is broadly divided into three three regions. These regions are: *Adhesion*, *near head-on separation*, *off-centre separation*. The Weber number (We) is varied in the range of 5¡We¡110 and impact parameter (χ) from 0 to 1 at a fixed $D = 180$ l.u, $\theta \sim 0°$ and $\mathrm{Oh} = 0.181$

In Fig.95, it is observed for the whole range of impact parameter (χ) and the region of small impact speed ($\mathrm{We} \leq 20$) collision results are dominated by *Adhesion* outcome (black points). As

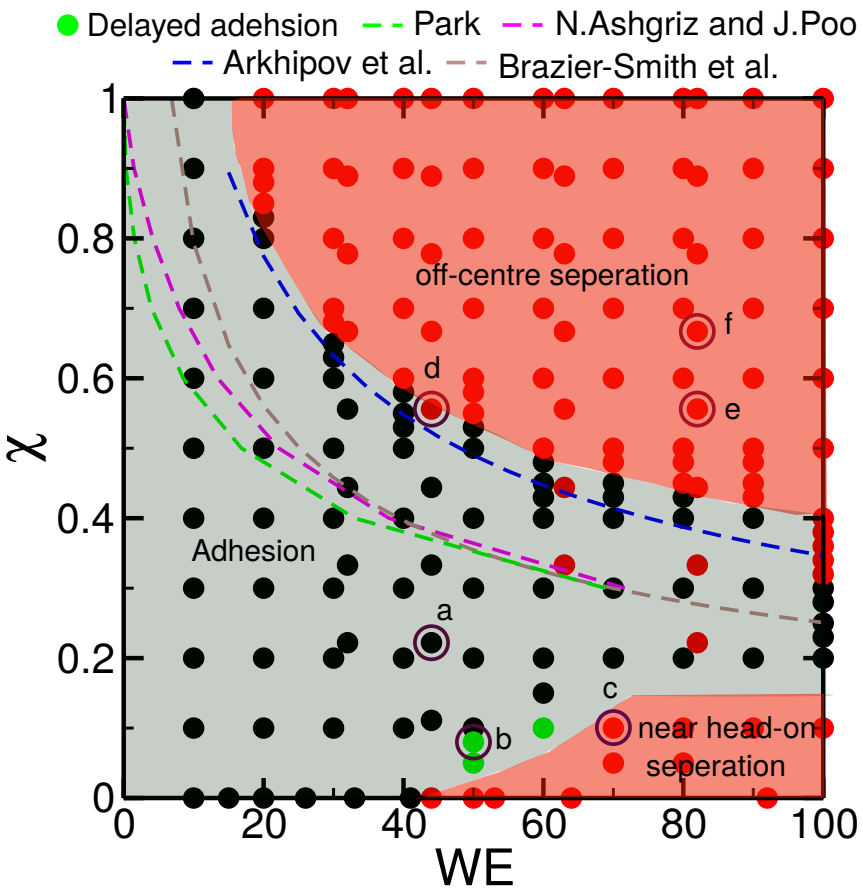

Figure 95: Phase diagram for off-centre droplet collision as a function of We and χ, and at fixed $D = 180$ l.u, $\theta \sim 0^{\circ}$ and Oh $= 0.181$. Dashed lines represents data predicted from theoretical models for miscible droplets of equal size.

the impact speed is increased, the *Adhesion* region starts to become narrow. At high Weber number (We > 20) and impact parameter ($\chi > 0.5$), the region is dominated by *separation* outcome after collision. As small region of *separation* called *near head-on separation* is identified in the narrow range of Weber number and Impact parameter (We > 40 and $\chi < 0.15$). The *delayed adhesion* outcome is captured mostly near the head-on collision setup. The points marked $a - f$ in he phase diagram corresponds to the set of simulations for which the sequence of collision snapshot shown in above figures. The dashed lines represents the boundary between *Adhesion* and *off-centre separation* region predicted by theoretical models. Four separate theoretical models which predicted the *off-centre separation* boundary are reported: Ashgriz and Poo (pink line) [5], Park (green line)[91], Brazier-Smith et al (brown line) [12] and Arkhipov et al (blue line) [4].

In 1970, Park derived the analytical model which predicts the *off-centre separation* boundary for identical droplets. This was done by balancing the surface tension in the region of contact and the

angular momentum. The model has the following form as a function of We and Impact parameter χ [91]:

$$\chi = \left(\frac{12}{\pi}\right)^{1/2} \left[\frac{(\Delta^2 - \Delta + 1)^{1/2}}{\Delta \mathsf{We}^{1/2}}\right] \left[\frac{(1+\Delta^5)(\Delta^2 - \Delta + 1)}{5\Delta^3} + \frac{(1+\Delta)}{2}\right] \left[4 - \left(\chi(1+\Delta) - \frac{(1-\Delta)}{\chi}\right)^2\right]^{1/4} \tag{6.20}$$

where, Δ is droplet size ratio (D_1/D_2).

In 1972, further improvement was done in the Park's model by Brazier-Smith et al. He proposed that the separation of the droplets will occur if the rotational energy would dominate the surface energy needed to reform the two droplets from the Adhesive state.The following relationship was formed on the basis of this criterion [12]:

$$\chi = \left(\frac{24}{5\mathsf{We}}\right)^{1/2} \frac{(1+\Delta^3)^{11/6}}{(1+\Delta)\Delta^{5/2}} \left[1 + \Delta^2 - (1+\Delta^3)^{2/3}\right]^{1/2} \tag{6.21}$$

By equating the first variation of the potential energy of the system to zero in a coordinate system rotating with constant angular velocity, Arkhipov et al.(1983) used the principle of minimum-potential-energy difference to compute the boundary of *off-centre collision*. The following relationship has been developed for the boundary between *Separation at off-centre* and Adhesion [4]:

$$\chi = \frac{1}{\Delta^3}\left(\frac{6(1+\Delta^3)}{\mathsf{We}}\right)^{1/2} \tag{6.22}$$

The above three models for stretching separation are based on a comparison between the rotational energy and some effective surface energy. They all assume that the separation is induced by angular momentum. However after a careful look at the experimental findings by N.Ashgriz and J.Y.Poo in 1989, clearly shows that *off-centre separation* happens much earlier than any substantial rotation growth. Due to the inclination of the droplets to travel down their initial trajectory, the separation takes place. The model proposed by N.Ashgriz and J.Y.Poo [5] has the following

form:

$$\mathsf{We} = \frac{4(1+\Delta^3)^2\left[3(1\Delta)(1-\chi)(\Delta^3\phi_s+\phi_l)\right]^{1/2}}{\Delta^2\left[(1+\Delta^3)-(1-\chi^2)(\phi_s+\Delta^3\phi_l)\right]} \tag{6.23}$$

where, ϕ_s and ϕ_l is defined as below:

$$\phi_s = 1-\frac{1}{4\Delta^3}(2\Delta-\tau)^2(\Delta+\tau) \quad h > \frac{1}{2}D_1 \tag{6.24}$$

$$\phi_s = \frac{\tau^2}{4\Delta^3}(3\Delta-\tau) \quad h < \frac{1}{2}D_1 \tag{6.25}$$

$$\phi_l = 1-\frac{1}{4\Delta^3}(2\Delta-\tau)^2(1+\tau) \quad h > \frac{1}{2}D_2 \tag{6.26}$$

$$\phi_l = \frac{\tau^2}{4}(3-\tau) \quad h < \frac{1}{2}D_2 \tag{6.27}$$

where $\tau = (1-\chi)(1+\Delta)$ and $h = \frac{1}{2}(D_1+D_2)(1-\chi)$.

Overall, there is a significant difference between the three theories for different size ratios. The variation comes from the fact that every model is build on certain criteria and assumption. These four predictions are plotted in Fig.95 for equal size ratios. The comparison with the numerical results with different models shows that the model presented by Arkhipov et al. (1983) [4] can adequately predict the boundary of *off-centre separation* closer our numerical data.

6.10 Conclusion

We identified five collision outcomes called *Adhesion*, *Bouncing*, *Delayed Adhesion* ($2D$ and$3D$) and *Adhesion with fragmentation*, *Bouncing with fragmentation* ($2D$). A systemic study of bouncing outcome (2D and 3D) for head-on collision setup for identical droplets as a function of Impact speed, viscosity and surface tension combination shows that no matter how large is the initial kinetic energy, it is dissipated nearly completely within the first and second deformation. The remaining kinetic energy in the bouncing droplets further contribute to the surface oscillations and linear momentum of the droplets. We observed that as viscosity increases, the amplitude of surface oscillations decreases. A minimum model in 2D is able to reproduce the essential feature of the transition between adhesion and bouncing for identical droplets. The investigation of collision between droplets with non-identical size and viscosity shows that the during bouncing the total linear momentum carrier by identical droplets is always larger and as the viscosity contrast between the droplets increases, the linear component of the kinetic energy carried by droplets increases which is accompanied by increase in the oscillating component. Our numerical results for the transition between adhesion and off-centre separation region is close to the model purposed by Arkhipov et al.(1983).

Chapter 7

Immiscible drop collisions: adhesion-encapsulation transition

In this chapter we perform a systematic numerical study to investigate the collision between two immiscible droplets, with one of the liquid close to spreading over the other liquid. In this case we explore the possibility that the kinetic energy available during the impact can be sufficient to trigger droplet encapsulation. The study therefore focus on detecting the transition between *adhesion* and *encapsulation* at varying of physical parameters such as Impact speed, surface tension, size and viscosity of the droplets. The results are compared to the evolution of the energy balance during the collision process as a function of above parameters.

7.1 Characterisation of free energy parameters for encapsulation

In general, during the collision of immiscible droplets, one of the key quantity is the surface tension combination between the three interfaces ($liquid_1$/gas, $liquid_2$/gas and $liquid_1$/$liquid_2$). In our ternary model, based on the six free energy parameters ($\lambda_1, \lambda_2, \lambda_3, \kappa_1, \kappa_2, \kappa_3$), we can achieve a large range of surface tension combinations. In the interest of this study which is focused on *Adhesion* and *Encapsulation* outcome, it is convenient expressing the surface tension combination in terms of Neumann angle or spreading parameter of one of the two liquids, similarly to the previous chapter on bouncing, where we parameterized the surface tension combinations in terms of the Neumann angle and spreading parameter of the gas phase. In the partial wetting states, three

finite Neumann angles are formed as shown in Fig.5, however in the full wetting state (Fig.7), the Neumann angle does not exists and it is more convenient employing the spreading parameter. Full wetting states will lead to encapsulation independently from the collision parameters, as this represents the global energy minimum. Therefore in our analysis we focus on partial wetting systems, to investigate the key role of collision dynamics.

Encapsulation of one droplet by another becomes possible whenever the spreading parameter of one of the two liquids (liquid 2 in our convention) vanishes, and correspondingly vanishes the Neumann angle of the same liquids. Therefore, to investigate the role of the collision dynamics the parameters of the free energy model needs to be tuned in the region of slightly negative spreading parameters S_2 and correspondingly small Neumann angles θ_2. In order to tune accurately these parameters we have performed a systematic surface tension analysis for fixed values of $\lambda_1 = \kappa_1 = 0.05$ (related to the gas phase) and varying λ_2, λ_3 and κ_2, κ_3 as summarised in Table.3. The choice of the fixed values $\lambda_1 = \kappa_1 = 0.05$ has been made comparing the range of surface tensions of different sets of values, and selecting the combination optimising the requirement of widest range and better stability.

λ_1	λ_2	λ_3	κ_1	κ_2	κ_3
0.05	X	Y	0.05	X	Y

Table 3: Parameter subspace to simulate full wetting scenario.

For the a range of λ_2 and λ_3 keeping the rest of the parameters as indicated in the above table, we perform Laplace tests in 2D using simulation setup in Fig.27 and compute the surface tensions corresponds to each interface. The summary of Laplace test results is plotted in a 2D space (X=λ_2 and Y=λ_3) in Fig.96. The first row of panels depicts the surface tension between $droplet_1/gas$ (γ_{12}), $droplet_2/gas$ (γ_{13}) and $droplet_1/droplet_2$ (γ_{23}) respectively. As expected, the surface tension γ_{12} in Fig.96(a) mainly depend on the variation of $X = \lambda_2$ and the surface tension γ_{13} is a function of $Y = \lambda_3$ in Fig.96(b). However, the $droplet_1/droplet_2$ surface tension (γ_{23}) shows a diagonal variation representing the dependency on both λ_2 and λ_3 in Fig.96(c).

The second row in Fig.96 reports the *Deformation Coefficient* representing the quality of interface measured at the interface between $droplet_1/gas$,$droplet_2/gas$ and $droplet_1/droplet_2$ respectively. In the last row of the color plots, the ratio of surface tensions γ_{12}/γ_{13} in Fig.96(g) is shown. The ratio of surface tensions between the $droplet_1/droplet_2$ and the interface between

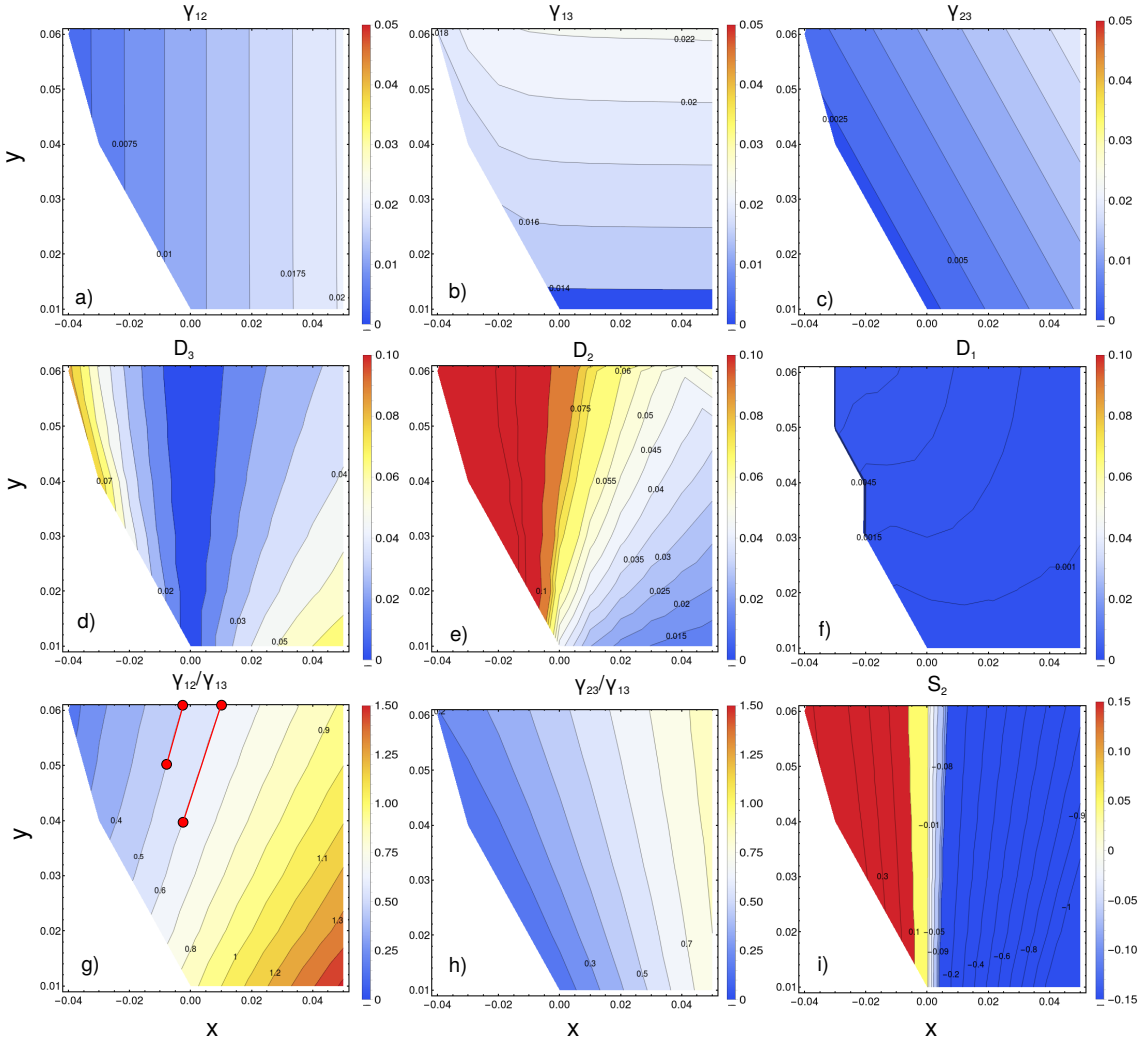

Figure 96: Colour maps of relevant quantities as function of the coordinate $X = \lambda_2$ and $Y = \lambda_3$ Upper row (a,b,c): surface tensions (γ_{12}, γ_{13} and γ_{23}); Middle row (d,e,f): Deformation coefficient (D_3, D_2 and D_1); Lower row (g,h): surface tension ratio (γ_{12}/γ_{13}, γ_{23}/γ_{13}) (i) spreading parameter of $liquid_1$ (S_2)

.

the gas and $droplet_2$ (γ_{23}/γ_{13}) is shown in Fig.96(h). At last in Fig.96(i), we plot the rescaled spreading parameter (S_2) of $droplet_1$ as shown by Eq.7.1. It is worth to remind that notation 1 corresponds to gas phase, 2 for $droplet_1$ and 3 represents $droplet_2$. Hence, spreading parameter of $droplet_1$ is S_2.

$$S_2 = 1 - \frac{\gamma_{12}}{\gamma_{13}} - \frac{\gamma_{23}}{\gamma_{13}} \tag{7.1}$$

In the above expression we have highlighted that the rescaled spreading parameter depends on both the ratios γ_{12}/γ_{13} and γ_{23}/γ_{13}, so that different combinations of surface tensions can lead to the same value of the spreading parameter. Therefore the spreading parameter alone is not sufficient to describe the interfacial thermodynamics.

In our investigation we have chosen the to fix the ratio γ_{12}/γ_{13} as additional control parameter to inspect. Specifically, inspecting Fig.96(i) we observe that S_2 varies horizontally in the parameter space, while inspecting Fig.96(g) we observe that the ratio γ_{12}/γ_{13} is approximately constant along diagonal lines in the same parameter space. Therefore we produced two sequences of S_2 obtained by varying the parameters along the two lines depicted in Fig.96(g) representing γ_{12}/γ_{13}=0.5 and γ_{12}/γ_{13}=0.6. Fitting points at the extrema of the parameter range we obtain the following relations:

$$\frac{\gamma_{12}}{\gamma_{13}} = 0.5, \quad \lambda_3 = 1.43\lambda_2 + 0.067 \tag{7.2}$$

$$\frac{\gamma_{12}}{\gamma_{13}} = 0.6, \quad \lambda_3 = 1.67\lambda_2 + 0.043 \tag{7.3}$$

Comparing the percentage variation in the ratio γ_{12}/γ_{13} from the source data and the fit we obtain a variation less than 1%, which is smaller than the accuracy of surface tension estimate. Fig.97 depicts the effect on the Geometry of Neumann angles of choosing different ratios, at parity of spreading parameters. Specifically we observe that the larger ratio γ_{12}/γ_{13}=0.6 corresponds to a reduced Neumann angle θ_3 of the second droplet, which might favor the encapsulation mechanism triggered by the collision.

7.2 Simulation of head-on collisions of equal size droplets (2D)

We start our numerical investigation considering the simpler case of head-on collisions of equal size droplets. The impact speed and viscosity of the droplets is also considered to be constant in the initial study. After gaining insight into the simpler cases, in the later sections we investigate the collision dynamics at non identical size and viscosity between the two droplets. This study is performed in two-dimensional (2D) space. Even if there is a significant difference between 2D

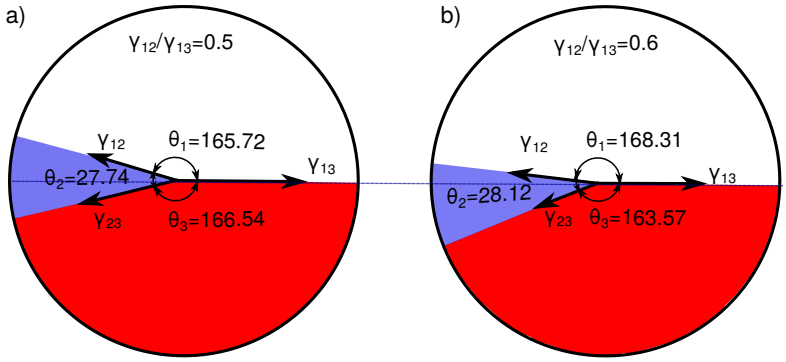

Figure 97: Representation of three Neumann angles at $S_2 = -0.30$ and surface tension ratio a) $\gamma_{12}/\gamma_{13} = 0.5$ b) $\gamma_{12}/\gamma_{13} = 0.6$

and 3D (surface to volume ratio), this study allows a qualitative understanding of the mechanism leading to *encapsulated* morphology.

7.2.1 Simulation setup for head-on collision

The simulation setup for this study is same as shown in Fig.45 at head-on collision setup (B=0). For this study, all the physical parameters are same as motioned in the section.(5.3), except the domain size which is: $1000 \times 800 \times 1$. The two droplets have non-identical surface tension, however, the rest of parameters are considered to be identical, such that the droplets size ($D_1 = D_2$), viscosity ($\mu_2 = \mu_3$), density ($\rho_2 = \rho_3$) and impact speed ($|V_1| = |V_2|$).

7.2.2 Outcomes of head-on collisions of equal size droplets

We start our numerical investigation of drop collision using the 2D simulation setup shown in Fig.45 for identical droplet size, viscosity and density. We also impose the equal magnitude of impact speed with opposite sign so the total momentum is zero. In the range of explored collision parameters, three typical collision outcomes are identified. These outcomes are: *Adhesion*, *Encapsulation* and *Temporary Encapsulation*. To elucidate the qualitative features of these outcomes we report in the following a set of simulation results obtained by initializing the colliding droplets at a different impact speed and keeping the rest of the parameters constant ($\gamma_{12} = 0.01184, \gamma_{13} = 0.01958, \gamma_{23} = 0.00818$, $D_1 = D_2 = 180$, $\mu_2 = \mu_3 = 0.1667$ and $\rho_2 = \rho_3 = 0.001$, all in lattice units). The surface tension ratio γ_{12}/γ_{13} =0.6 and the spreading parameters (S_2) of the *outer droplet* ($droplet_1$) is -0.02255. The corresponding Neumann angles are $\theta_1 = 170.01°$,$\theta_2 = 24.53°$ and $\theta_3 = 165.46°$. For convenience, we will refer $droplet_1$ as

"outer droplet" and $droplet_2$ as *"inner droplet"* during the discussion. Besides the visualization of the evolution of drop shapes through a sequence of simulation snapshots as shown in Fig.98, a useful quantity to understand the typical behaviour of each outcome is the profile of phase field ($\phi = C_2 - C_3$) which comes from the contribution of $droplet_1$ and $droplet_2$. As the surface tension of the droplets is non identical, the Oh of $droplet_1$ and $droplet_2$ is 0.114 and 0.089 $l.u$ respectively with $\mathrm{Oh_{av}} = 0.101$ $l.u$. The observed collision outcomes are described below:

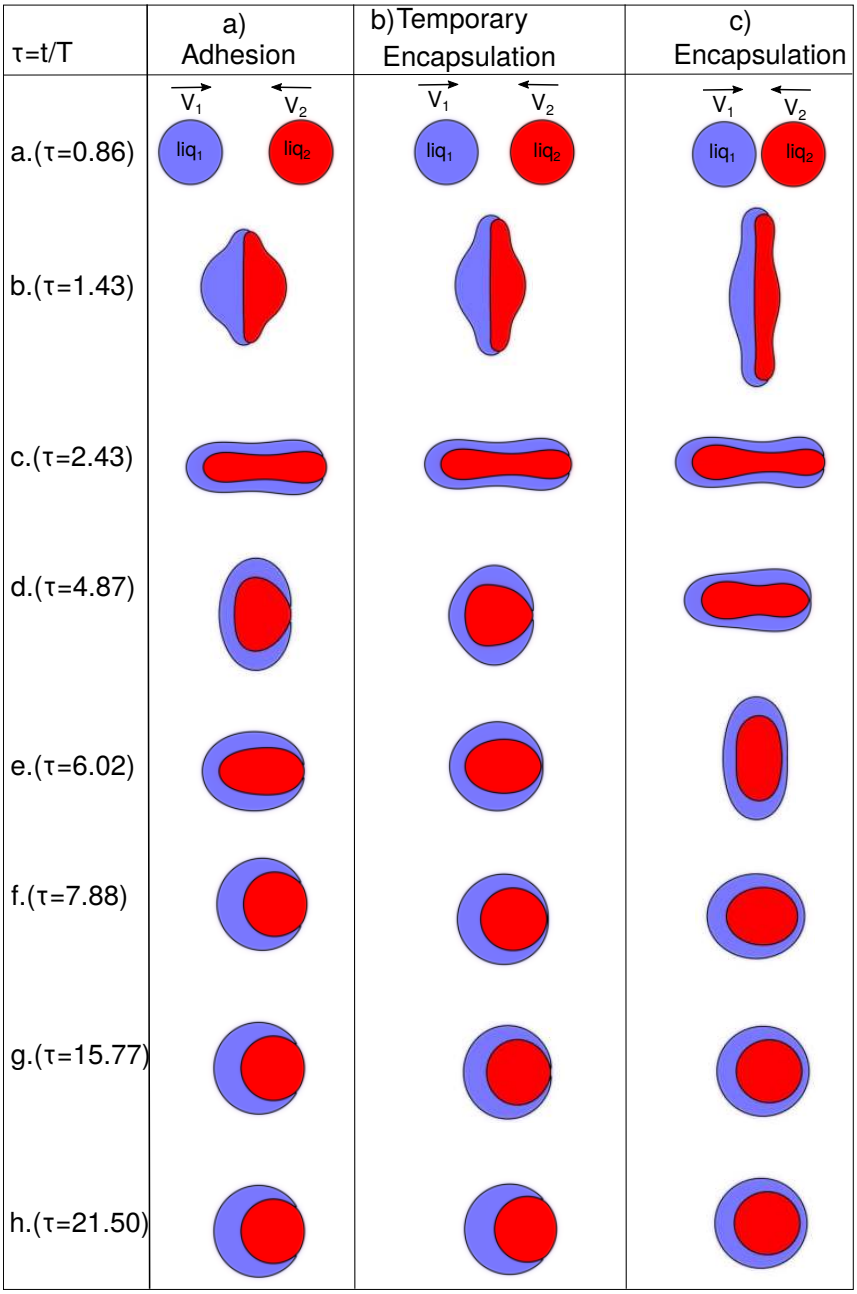

Figure 98: Sequence of steps during collision when outcome is (a) Adhesion at $\mathrm{We_{av}}$=59.78 (b) Temporary Encapsulation at $\mathrm{We_{av}}$=72.34 (c) Encapsulation at $\mathrm{We_{av}}$=98.82. The other parameters such as $\theta_1 = 170.01°$,$\theta_2 = 24.53°$ and $\theta_3 = 165.46°$ ($S_2 = -0.02255$), $\mathrm{Oh_{av}} = 0.101$ are fixed.

1. *Adhesion (A)*: A typical sequence of steps during *Adhesion* outcome is shown in Fig.98(a). It is observed that, just after the impact the droplets deform in the direction perpendicular to collision axis and try to form a bell like structure at $\tau = 1.43$. Based on the set spreading parameter of the $droplet_1$, the blue colored droplet start encapsulating the $droplet_2$ (red color) as shown at time $\tau = 2.43$. During the collision the two droplets also experience the surface oscillations in both x and y direction ($\tau = 2.43 - 6.02$). After the surface deformations, the droplets relaxes to its equilibrium configuration by forming a single compound like shape ($\tau = 7.88 - 21.50$).

   To understand the collision better and classify the outcome in the correct category, in Fig.99, we plot the 1D profile of phase field (ϕ) along the length (LX) of the domain. The profile of ϕ is shown at three time steps from above sequence of steps ($\tau = 0.86, 7.88, 21.50$). The phase field ϕ describes the system state by determining the existence of two liquid components ($droplet_1$,$droplet_2$). When $\phi > 0$, the contribution of $droplet_1$ dominate over $droplet_2$, on the other when $\phi < 0$, the $droplet_2$ contribute more. In the plot, the black curve corresponds to ϕ just before the impact ($\tau = 0.86$). As expected, before impact, ϕ is always positive (existence of $droplet_1$) in the first half of the domain (LX $<$ 500 l.u) and it is negative (existence of $droplet_2$) in the second half of the domain (LX $>$ 500 l.u).

   Even after the impact, at $\tau = 7.88$ *(red curve)* and $\tau = 21.50$ *(green curve)*, there is no existence $droplet_1$ ($\phi > 0$) in the second half of the domain (LX $>$ 500 l.u). Overall, It is observed from the plot that during the *Adhesion* process there is no occurrence of $droplet_1$ in the second half of the domain, which should depict the encapsulation of $droplet_2$ by $droplet_1$

2. *Encapsulation (E)*: In Fig.98(c), we show the sequence of steps for a typical collision phenomenon when the outcome is *Encapsulation*. Just after the impact at $\tau = 1.43$, a large vertical elongation followed by horizontal deformation ($\tau = 2.43$) in the shape of the droplets is observed. At $\tau = 4.87$, the outer droplet (blue) completely encapsulate the inner droplet (red). After this point, droplets remain in the *encapsulated* morphology and experience surface oscillations in both directions ($\tau = 4.87 - 21.50$). Similar to above outcome, the profile of phase field ϕ for the *encapsulation* outcome is shown in Fig.100. It is demonstrated that after the impact which happens at the middle of the simulation domain,

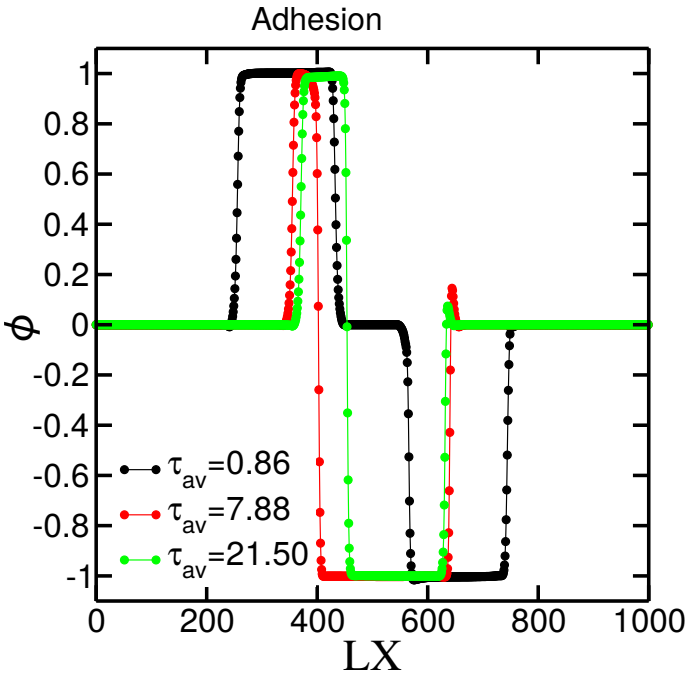

Figure 99: The 1D profile of phase field ϕ along the length LX of the domain when outcome is *Adhesion* ($\theta_1 = 170.01°$,$\theta_2 = 24.53°$ and $\theta_3 = 165.46°$ ($S_2 = -0.02255$), We_{av}=59.78 and $oh_{av} = 0.101$)

at $\tau = 7.88$, there exists a positive ϕ in the second half of the domain (highlighted in a dashed box). The droplets remain in this state which is its the equilibrium configuration (green curve at $\tau = 21.50$). This implies that $droplet_1$ completely encapsulate $droplet_2$.

3. *Temporary Encapsulation (TE)*: During *TE*, a mixed dynamics is observed, which first leads to encapsulation, subsequently followed by adhesion. The sequence of collision steps for *Temporary Encapsulation* is shown in Fig.98(b). Qualitatively, the initial dynamics of *Adhesion* and *Temporary Encapsulation* are similar. The difference is that after the initial impact, shape deformation in both the directions, the $droplet_1$(blue) encapsulate the $droplet_2$ (red) at time step $\tau = 6.02$. However, the droplets do not rest in this encapsulated state and at $\tau = 15.77$, the inner droplet starts to relax to their equilibrium state (single compound) which is determined by forming a three finite Neumann angles. The 1D profile of phase field (ϕ) for *Temporary Encapsulation (TE)* collision process is shown in the Fig.101. It is clear from the plot that, at $\tau = 7.88$ (red curve), the $droplet_1$ ($\phi > 0$) appears on the second half of the domain (highlighted in a dashed box) representing encapsulation of the inner droplet by outer one. However the appearance of $\phi > 0$ in the second half of the domain is not fully developed and as shown at time step $\tau = 21.50$ (green curve), the

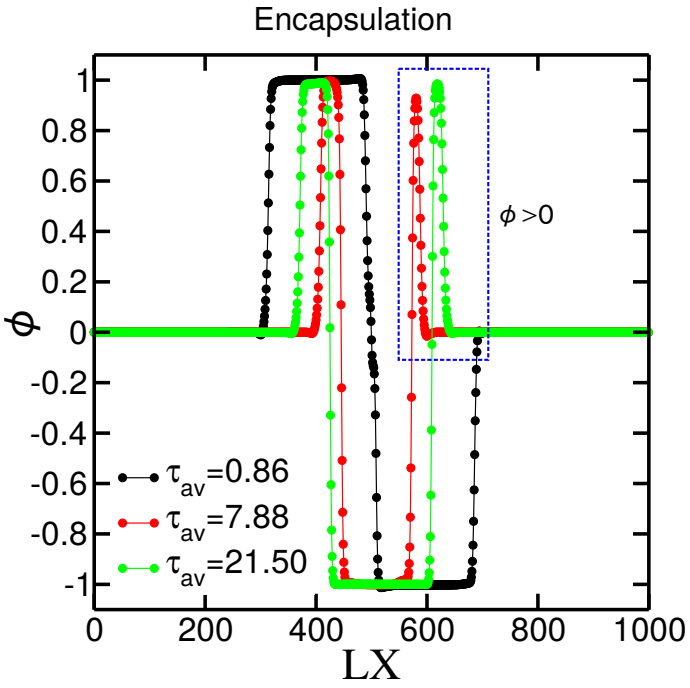

Figure 100: The 1D profile of phase field ϕ along the length LX of the domain when outcome is *Encapsulation* ($\theta_1 = 170.01°$,$\theta_2 = 24.53°$ and $\theta_3 = 165.46°$ ($S_2 = -0.02255$), We_{av}=98.82 and $oh_{av} = 0.101$)

positive ϕ disappears again. At this stage droplets form a single compound which represents its equilibrium state.

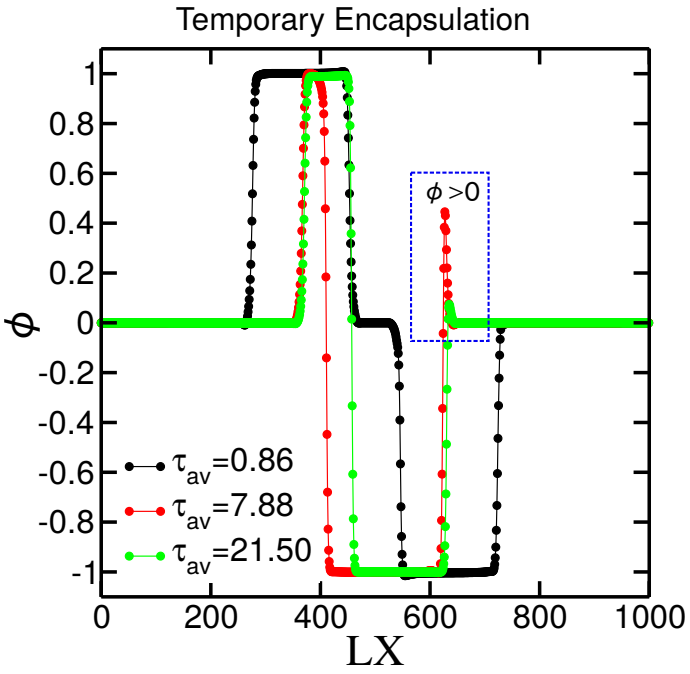

Figure 101: The 1D profile of phase field ϕ along the length LX of the domain when outcome is *Temporary Encapsulation* ($\theta_1 = 170.01°$,$\theta_2 = 24.53°$ and $\theta_3 = 165.46°$ ($S_2 = -0.02255$), We_{av}=72.34 and $oh_{av} = 0.101$)

The temporary encapsulation shows a striking similarity to the delayed adhesion outcome observed in the previous chapter. However while in the previous case the phenomenon is robust enough to have a physical origin, in this present case we need to consider that the system drifts in the long run to the global minimum given by the adhesion state. This occurs because the diffuse nature of the interface does not allow a clear phase separation and the absence of interfacial forces do not allow the formation of a stable thin film. Consequently all encapsulation mythologies are driven to a transition to adhesion states in the long run. In this specific case the transition occurs quickly and is observable within the simulation time. We believe that the temporary encapsulation is mostly related to the relative size of the diffuse interface compared to the thickness of the outer layer. We envisage that higher resolution simulations would allow to better discriminate the region of parameters where temporary encapsulation have a more robust physical origin.

7.3 Transition from Adhesion to Encapsulation for head-on collisions between identical droplet (2D)

After listing the main collision outcomes observed in our simulations at head-on collision set-up, we then performed systematic simulations of $2D$ collisions of immiscible droplets in the parameter space of spreading parameter (S_2) and average Weber number ($\mathsf{We_{av}}$) which correspond to rescaled surface tension combination and impact velocity respectively. We aim to investigate the transition between adhesion and encapsulation outcome with the possibility that the impact speed ($\mathsf{We_{av}}$) available during the collision can be sufficient to trigger droplet encapsulation. The study is performed at fixed $\mathsf{Oh_{av}} = 0.101$ and surface tension ratio $\gamma_{12}/\gamma_{13} = 0.60$ as a additional control parameter. The impact speed of both droplets is kept same with opposite sign to keep the net momentum of the system to zero value. The results from this study are summarised in Fig.102, where points represent simulation data with different outcomes, highlighted by shaded regions.

It has been observed that, at a fixed S_2, by increasing We_{av} the transition from "Adhesion" (black points) to "Encapsulation" (red points) occurs. The same transition is found at constant We_{av} and by increasing spreading parameter S_2 (negative to positive value). The intermediate outcome

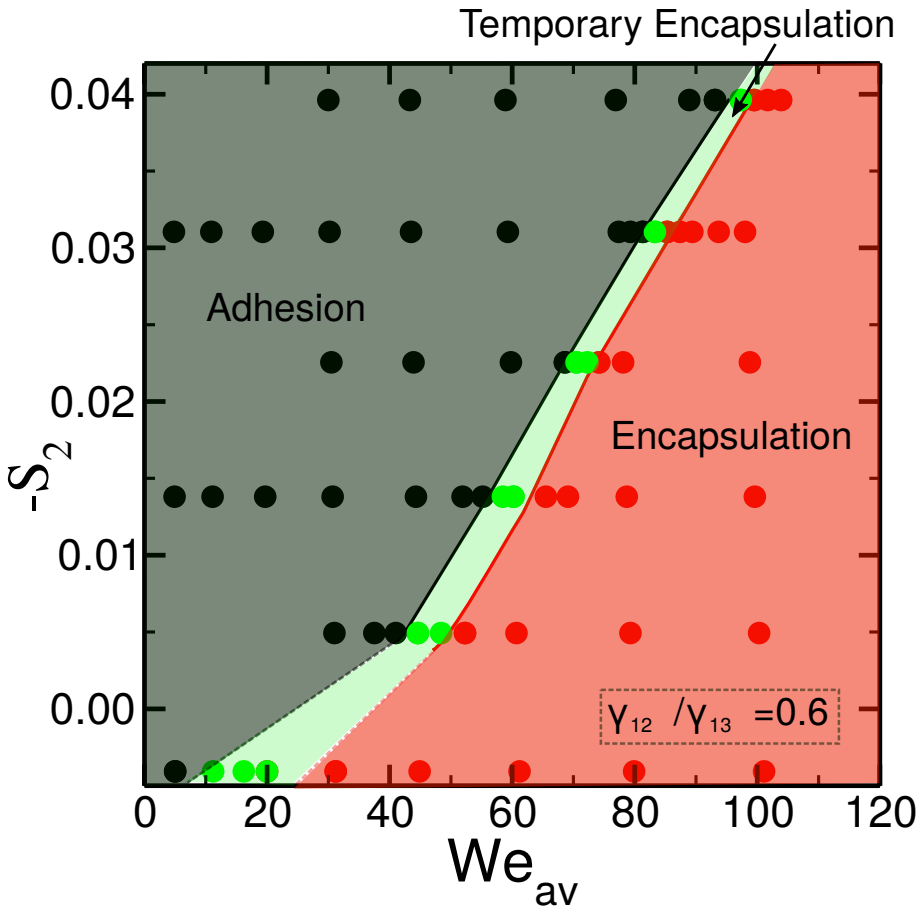

Figure 102: Transition curve from *Adhesion* to *Encapsulation* as a function of spreading parameter (S_2) of $droplet_1$ and average Weber number ($\mathrm{We_{av}}$) between two droplets at fixed $\mathrm{Oh_{av}} = 0.101$ and γ_{12}/γ_{13}=0.60

"Temporary Encapsulation" (green points) appears as a slice along the full transition line, with a width opening as We_{av} decreased and S_2 increases. As S_2 become more negative, the region of *adhesion* expands. In this region, for *Encapsulation* to occur, larger impact speed (larger We_{av}) needs to be provided to the droplets in order to cross the surface energy barrier. On the other hand at $S_2 > 0$, where spontaneous encapsulation of liquid occurs, one should expect only *encapsulation* outcome. But we observe a small region of *adhesion*, which is vanishing towards the origin of the axis. This is most likely related to small inaccuracies in the measurement of surface tensions, combined to the finite size of the diffuse interface, resulting in a spreading parameter slightly larger than our estimate from the measure of the surface tensions.

As mentioned above, the same value of spreading parameter (S_2) can be obtained for different ratios of surface tensions between liquid/gas interfaces $(\gamma_{12}/\gamma_{13})$. To assess the role of this ratio on the collision outcome, we performed another set of simulations fixing γ_{12}/γ_{13}=0.50. The free

energy parameters for this set of simulations have been obtained fitting the data in Fig.96(g) for the diagonal line corresponding to γ_{12}/γ_{13}=0.50. Our results for the 0.5 ratio in the parameter space of S_2 and $\mathrm{We_{av}}$ are shown in Fig.103.

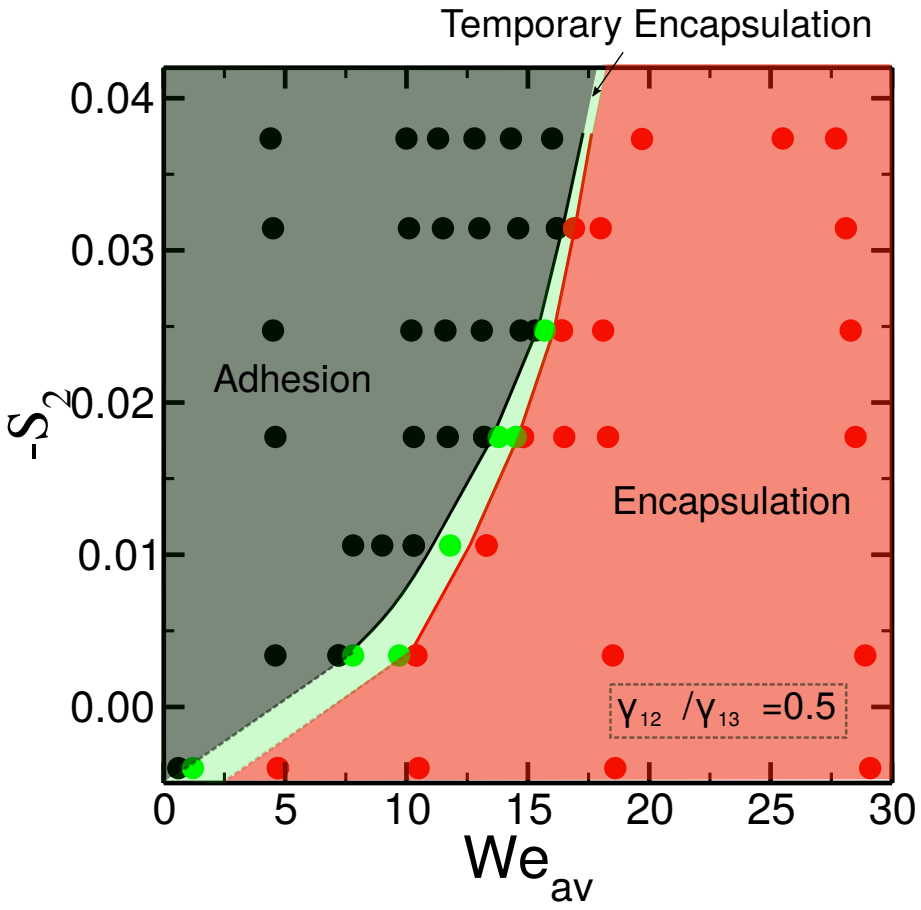

Figure 103: Transition curve from *Adhesion* to *Encapsulation* as a function of spreading parameter (S_2) of $droplet_1$ and average Weber number between the two droplets We_{av} at fixed γ_{12}/γ_{13}=0.50

Overall, a similar trend in the transition curve is observed on qualitative level. In Fig.104, where we show the transition curves at γ_{12}/γ_{13}=0.50 and 0.60 together. We observe that with decreasing the value of surface tension ratio $(\gamma_{12}/\gamma_{13})$ from 0.6 to 0.5, the transition curve shifts to lower We_{av}. This imply that at lower surface tension ratio, *encapsulation* occurs at relatively lower impact speed as compared to the case when the ratio of the surface tensions is higher (γ_{12}/γ_{13}=0.6). The geometry of three Neumann angles made at triple point at same spreading parameter ($S_2 = -0.03$) in Fig.96(a,b) helps to understand the shift in the transition line at two surface tension ratios (γ_{12}/γ_{13}=0.50 and 0.6). The wider encapsulation regime observed for γ_{12}/γ_{13}=0.50 is related to the smaller Neumann angle of the encapsulated phase (θ_2).

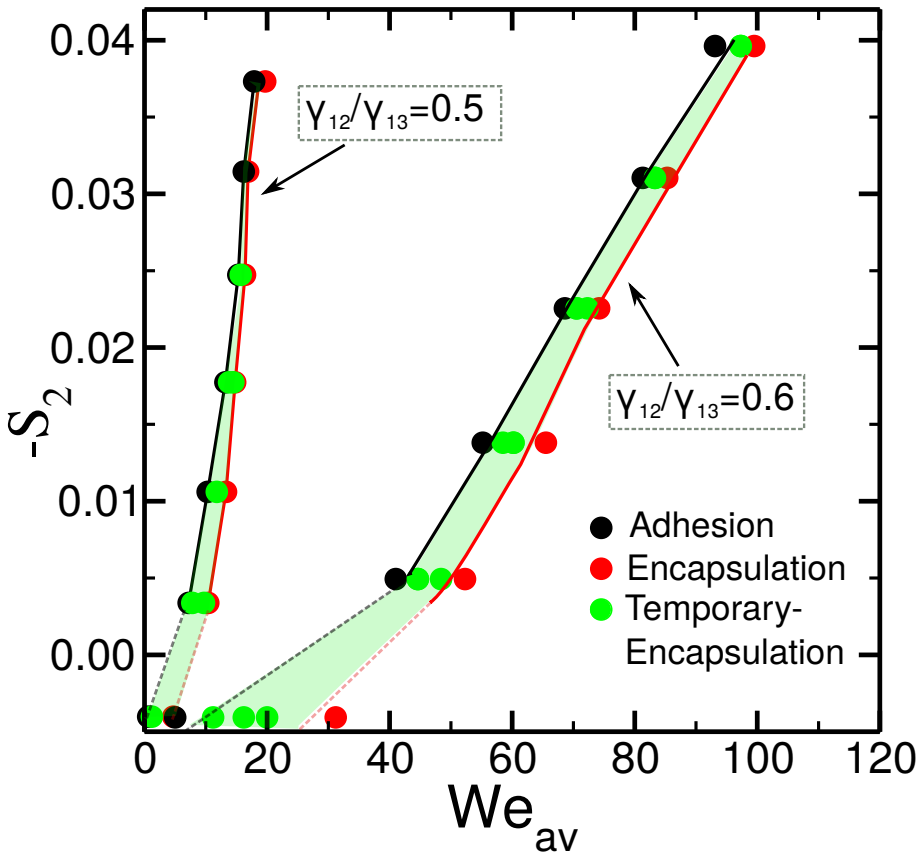

Figure 104: Comparison of the transition curve from Adhesion to Encapsulation at γ_{12}/γ_{13}=0.5 vs γ_{12}/γ_{13}=0.6

7.4 Analysis of collision dynamics for head-on collision between identical droplets (2D)

After having a qualitative analysis of the transition line between *Adhesion* and *Encapsulation* along with its shift with respect to the surface tension ratio, in this section we investigate the energy balance within the collision mechanism, to gain insight on how the collision mechanism is affected by the impact speed and spreading parameter. To do so, from Fig.105 we consider two case and 5 set of simulations in each case. The cases are:

- Fixed $S_2 = -0.01381$ and varying We_{av} (sets circled 1 to 5 in Fig.105)
- Fixed $We_{av} = 60$ and varying S_2 (sets circled 1' to 5' in Fig.105).

The green point labeled 3 which corresponds to *Temporary Encapsulation* is common in both the cases. The point 1, 2, 1', 2' represents to *Adhesion* and 4, 5, 4', 5' represents *Encapsulation* outcome.

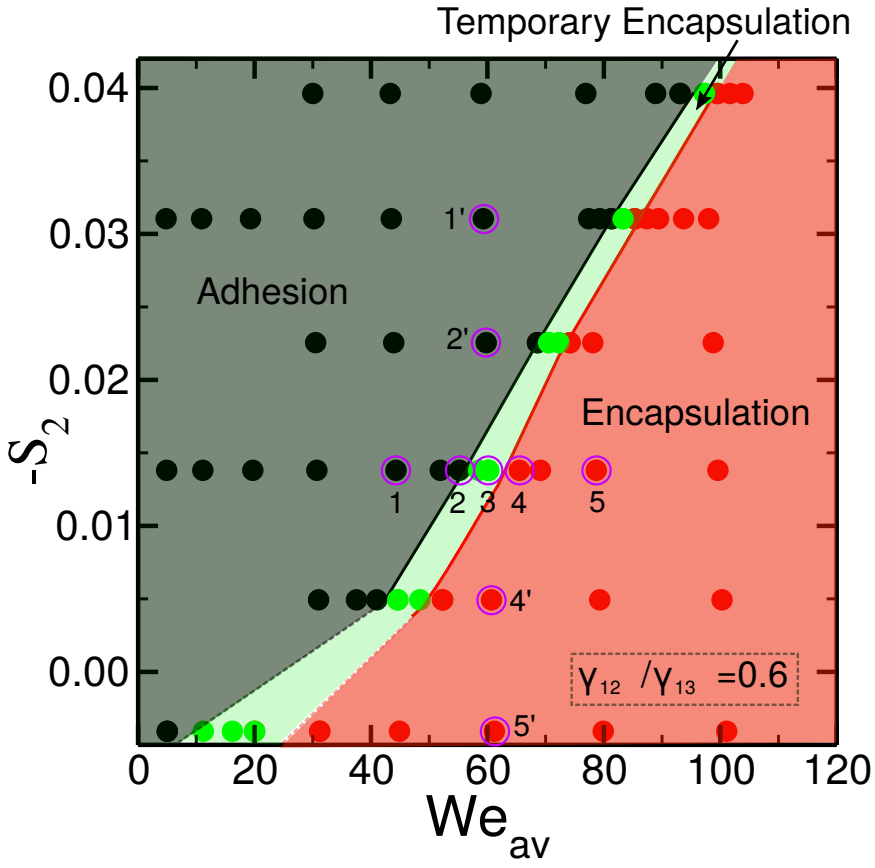

Figure 105: Representation of two cases for the parameter study at γ_{12}/γ_{13}=0.60. $Case_1$: sets marked 1 to 5 at fixed S_2= -0.01381 and different We_{av}. $Case_2$: sets marked 1' to 5' at fixed We_{av}=60 and different S_2.

7.4.1 Role of Impact speed

To investigate the role of Impact speed, consider the $case_1$ first. Here at constant spreading parameter S_2= -0.01381 ($\theta_1 = 172.22°$,$\theta_2 = 19.30°$ and $\theta_3 = 168.48°$), 5 set of simulations are performed at different impact speed (the same in both droplets) represented by We_{av} ranging from 44.3 to 78.7. The rest of the parameters (μ, ρ, D) are fixed and also identical in both droplets. In Fig.106, the snapshot of sequence of collision steps corresponds to all five sets is shown.

In Fig.107, the evolution of the three components of energy which are: *Kinetic, free and energy dissipation* during the collision process is plotted. The kinetic energy curve is normalised by the initial assignied kinetic energy of the droplets, while the free and dissipated energy are normalised by the free energy of the initial configuration of the system (two separated drops at rest). In Fig.107(a), the magnified region of the plot during the initial collision dynamics is shown. It is observed that once the velocity is assigned to the droplets and they start approaching each other,

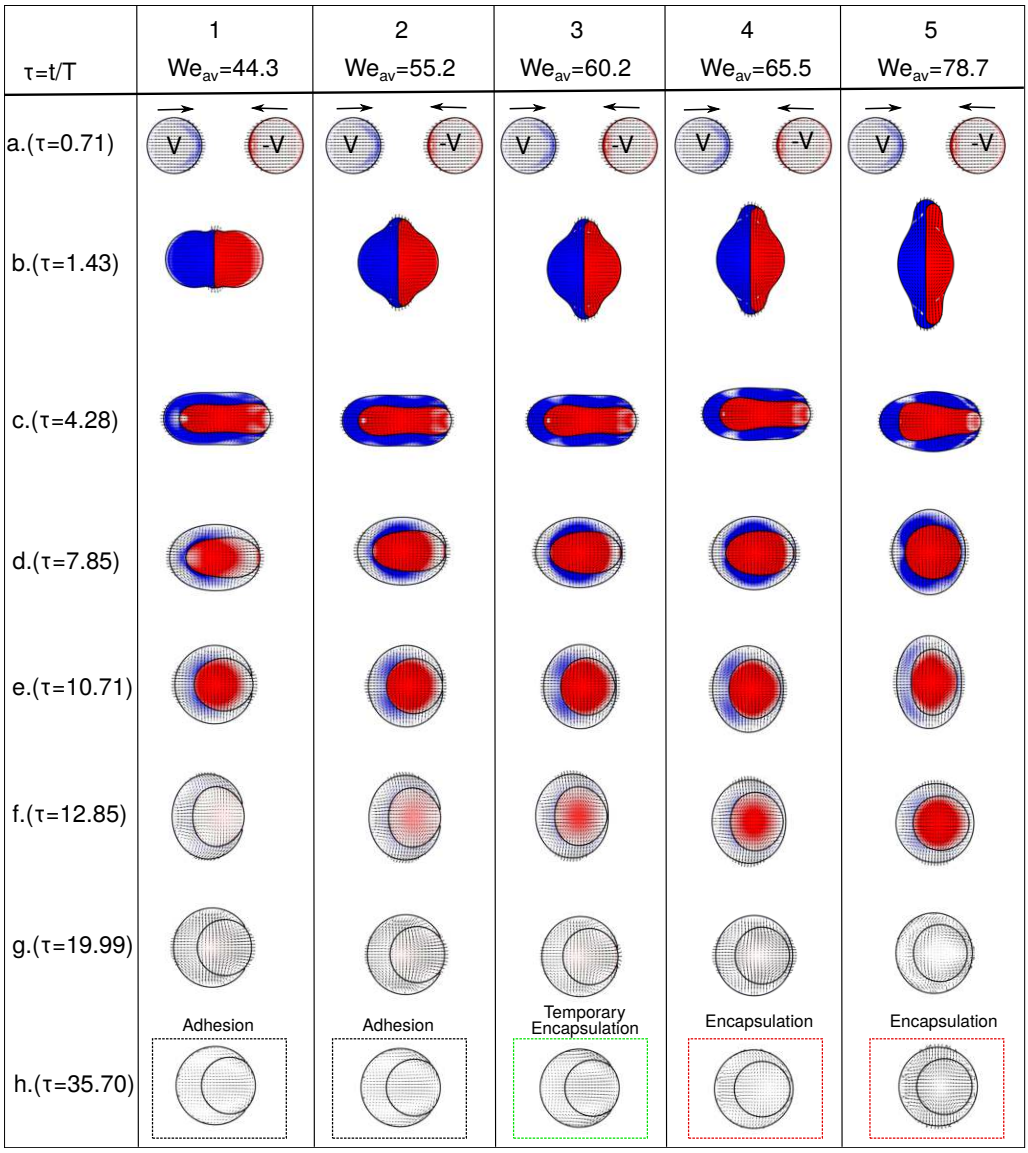

Figure 106: Sequence of steps during collision when outcome is: (1) Adhesion (2) Adhesion (3) Temporary Encapsulation (4) Encapsulation (5) Encapsulation ($S_2 = 0.01381(\theta_1 = 172.22°$,$\theta_2 = 19.30°$ and $\theta_3 = 168.48°)$)

the droplets with smaller We$_{av}$ cover separation distance in longer time as compared to the one at higher We$_{av}$. The droplets at higher We$_{av}$ collide earlier which is represented by the instantaneous drop of kinetic energy. Equivalently at this point, the larger first peak of the free energy is observed for droplets impacting at higher We$_{av}$ as shown in Fig.107(b). This implies that larger surface deformations are experienced by droplets impacting at higher We$_{av}$ as compared to lower ones. The rest of the peaks in kinetic and free energy are much smaller in magnitude and are due to the drop elongation along the collision axis. For all the We$_{av}$, the vanishing kinetic energy after collision represents the double emulsion (compound) like morphology of the final shape of the

droplets. The We $=$ 60.2 act as minimum rescaled impact speed which is required to overcome the encapsulation barrier for this particular surface tension combination. Below We $=$ 60.2 , the droplets always end up in adhesive state.

In Fig.107(c), the evolution of energy dissipation is shown. It is observed that at all impact speeds, the majority of energy dissipation happens within the first and second deformation. Also, as we move from *Adhesion* to *Encapsulation* outcome the energy dissipated during the correspondingly collision process increase significantly. At the points marked $a - h$ in the dissipation plot, the corresponding snapshot of collision steps showing the intensity of energy dissipation is shown in the Fig.106 for all the five sets of simulations.

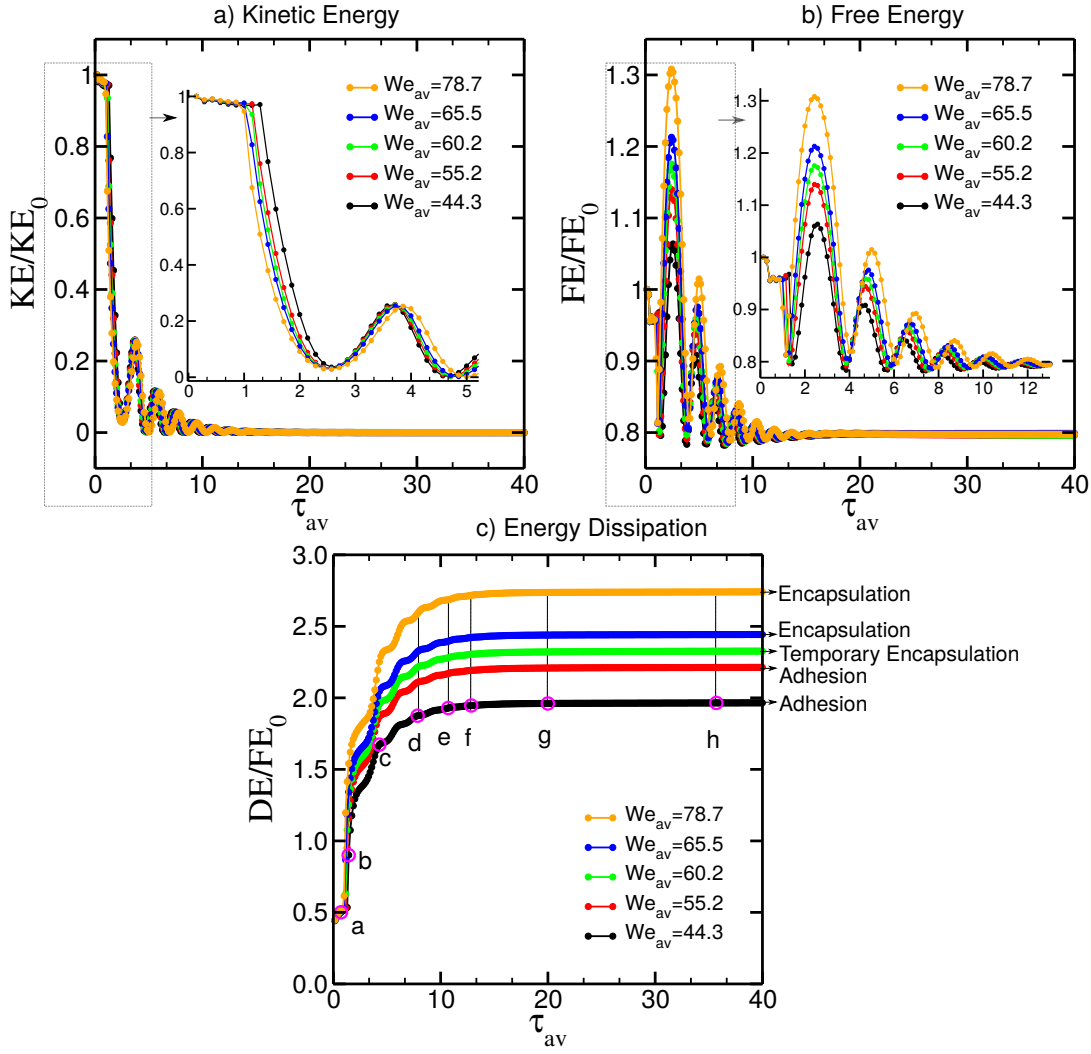

Figure 107: Energy evolution at different Impact speed (We_{av}) (a) Kinetic energy (b) free energy (c) energy dissipation. ($S_2 = 0.01381(\theta_1 = 172.22°$,$\theta_2 = 19.30°$ and $\theta_3 = 168.48°)$)

7.4.2 Role of surface tension

Next we investigate the role of surface tension combination cast into spreading parameter. To do so we consider $case_2$ of Fig. 105. Here five set of simulations marked (1',2',3,4',5') are performed at different spreading parameter ranging from -0.3104 to $+0.004$ and fixed $\mathrm{We_{av}} = 60$. As the viscosity, size of the droplets is still fixed, in order to keep the We_{av} constant, the impact speed is adjusted according in these five sets of simulations. In Fig.108, the snapshot of sequence of collision steps corresponds to all five sets is shown.

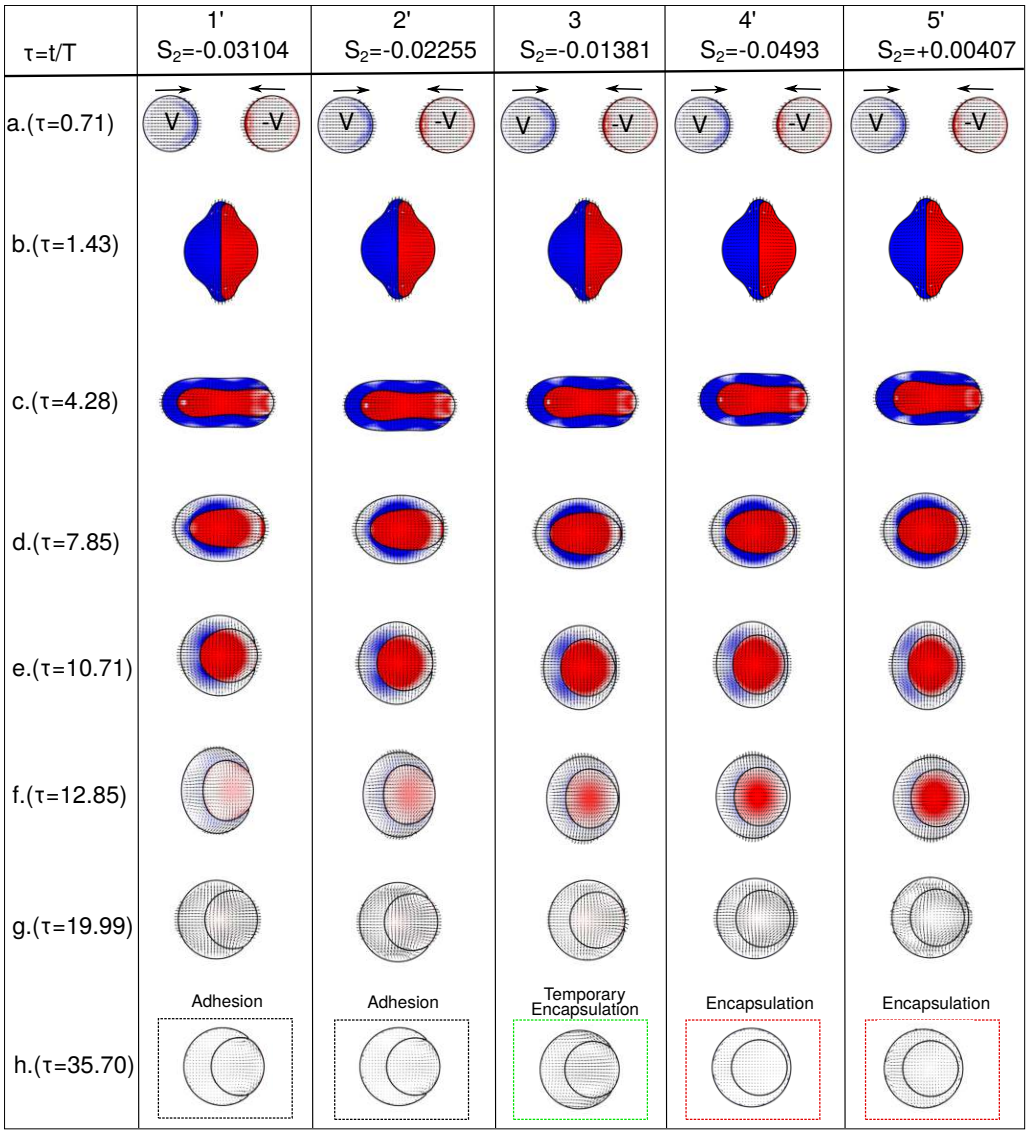

Figure 108: Sequence of steps during collision when outcome is: (1') Adhesion (2') Adhesion (3) Temporary Encapsulation (4') Encapsulation (5') Encapsulation ($We_{av} = 60$)

The evolution of three energy component for each outcome is shown in Fig.109. Similar to above

section, the kinetic energy is normalised by the kinetic energy in the initial state, free and dissipated energy are normalised by the free energy of two separated drops at rest. As all the simulation sets are performed at same $We_{av} = 60$, in Fig.109(a) the kinetic energy curves for all the spreading parameter are almost overlapping. In Fig.109(b), for all the spreading parameters, the first peak in the free energy which comes from the effect to impact rate is not significantly different. However the rest of the peaks representing the surface deformation and the remaining free energy at the end of collision process vary based on the collision outcome. The free energy stores in the interfaces decreases as the spreading parameter increases, means moving from *Adhesion* to *Encapsulation* outcome. Similarly in Fig.109(c), the evolution of energy dissipation shows that as the spreading

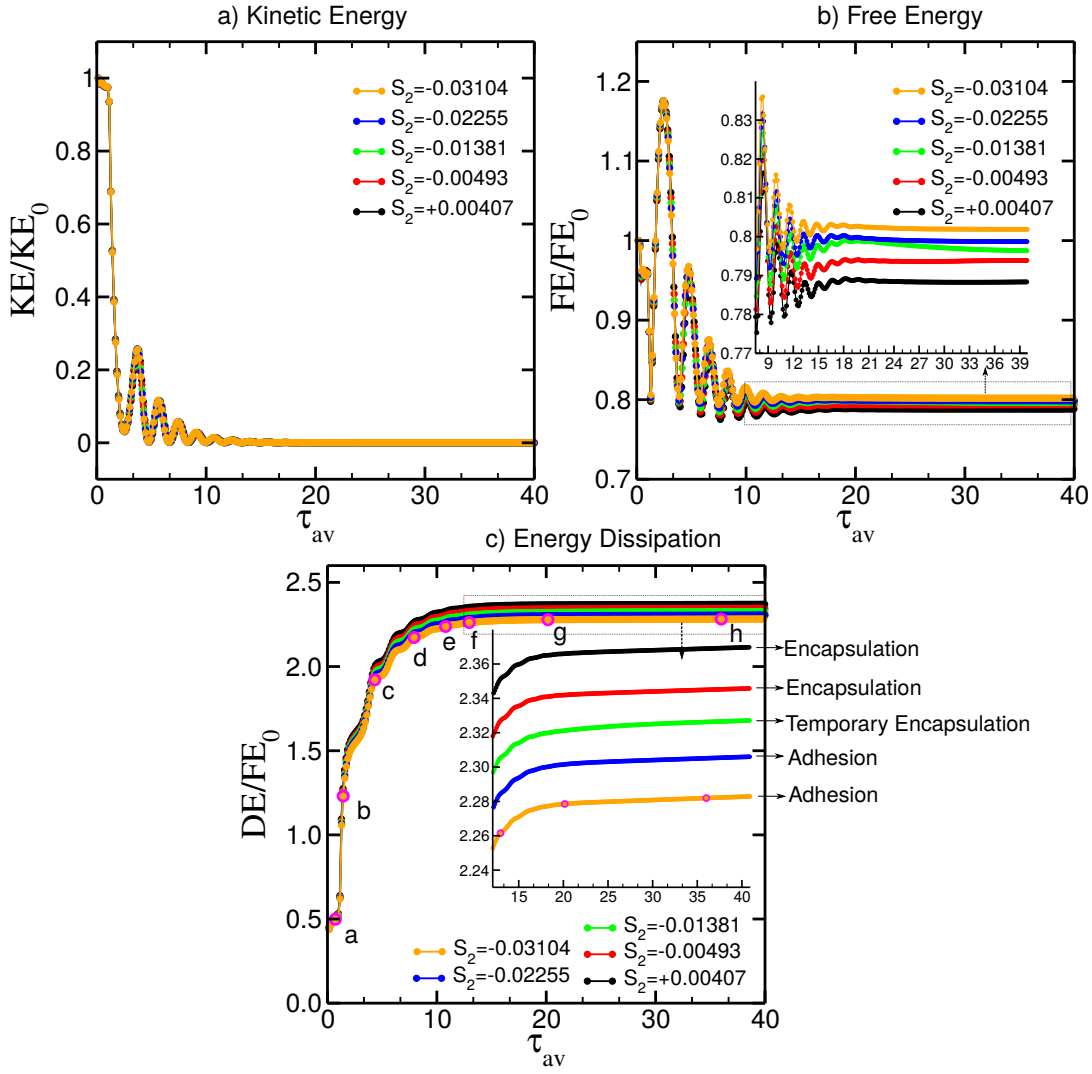

Figure 109: Energy evolution at different spreading parameter(S_2)(a) Kinetic energy (b) free energy (c) energy dissipation.($We_{av} = 60$)

parameter increases the energy dissipation increases. Also, this means in *Encapsulation* mytholo-

gies, the energy is dissipated more as compared to *Adhesion*. The points marked $a - h$ in the dissipation plot, the corresponding snapshot of collision steps are shown in the Fig.(108) for all five sets of simulations.

7.5 Transition from *Adhesion* to *Encapsulation* at varying droplet size

Along with the non-identical surface tension of the droplets, in this section we relax the condition of identical droplet size and study its affect on the collision dynamics. The collision study at size contrast is conducted at head-on collision setup (B=0) as shown in Fig.45. The size of the two droplets is varied systematically such that the total mass is always fixed in all the simulations. The size ratio (R_2/R_1) between the inner and outer droplet is varied in the range from $0.6 - 1.67$. We vary the the impact speed of each droplet in order to keep the net momentum of the system to zero value. All the simulations are performed at fixed surface tension combination such that the Neumann angles $\theta_1 = 167.11°$,$\theta_2 = 25.23°$, $\theta_3 = 167.66°$ and spreading coefficient of the $droplet_1$ (outer droplet) is $S_2 = -0.02473$ at $\gamma_{12}/\gamma_{13} = 0.5$. The viscosity of the two droplets is kept to a constant value $\mu_2 = \mu_3 = 0.1667$ l.u. As the size ratio (R_2/R_1) varies from $0.6 - 1.67$, the Oh of $Droplet_1$ increases in the range from 0.084 to 0.109 and the Oh corresponds to $Droplet_2$ decreases from 0.019 to 0.015. Consequently, the average Ohnesorge number $\mathsf{Oh}_{\mathsf{av}}$ of both droplets increases in the range from 0.052 to 0.062 with the increase in size ratio.

The summary of 2D simulations results as a function of size ratio (R_2/R_1) and impact speed ($\mathsf{We}_{\mathsf{av}}$) is shown in the Fig.110. It is observed that when the size of the inner droplet (R_2) is significantly larger than the outer droplet size (R_1), the outcome of the collision is dominated by *Adhesion*. A larger impact energy (We_{av}) needs to be provided to the system for *Encapsulation* to occur. Also, after a significant size contrast R_2/R_1 (>1.18), a very thin slice of *Temporary Encapsulation* is captured along the transition line. Interestingly, by reducing the size contrast below 0.8 (i.e. the inner droplet becoming smaller) we observe encapsulation through the full range of Weber numbers. This suggests that the required energy to overcome the encapsulation barrier is already provided by the rearrangement of the two separated drops driven towards the adhesive state.

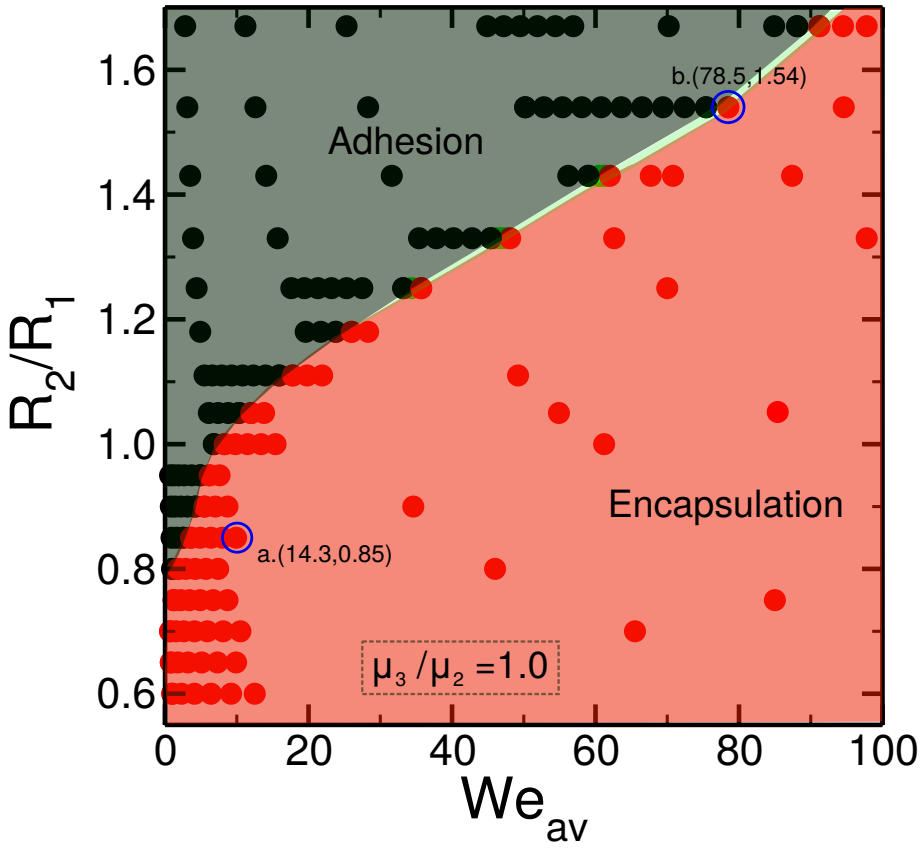

Figure 110: Transition curve from *Adhesion* to *Encapsulation* as a function of size ratio between inner and outer droplet (R_2/R_1) and average Weber number We_{av} ($\theta_1 = 167.11°$,$\theta_2 = 25.23°$, $\theta_3 = 167.66°$,($S_2 = -0.02473$), γ_{12}/γ_{13}=0.50 and $\mu_2/\mu_3 = 1$) (The evolution of drop shapes for blue circled simulation points are shown below in Fig.111, while in the Appendix B.3 we show more sequence of simulation snapshots for completeness.)

7.5.1 Encapsulation dynamics at size contrast

In the previous section after having identified the transition between *Adhesion* to *Encapsulation* for head-on collisions of non-identical droplets size. In this section we focus on a comparative analysis of the dynamics of encapsulation morphology at size contrast between the two droplets. To do so, we analyse two set of simulations (point a,b circled in Fig.110). Both of the points belong to encapsulation outcome but are the example of two extreme cases within the parameter space of impact speed and size contrast ($We_{av}, R_2/R_1$).

The sequence of collision steps corresponds to these two *encapsulation* outcomes are shown in the Fig.111. It is seen from the sequence of steps that when the inner droplet is significantly bigger in size as compare to the outer droplet ($R_2/R_1 = 1.54$), a large surface deformation (which also comes from the larger impact speed) is experienced during collision. The outer droplet (blue)

at negative spreading parameter, but sufficiently high impact speed completely encapsulate the inner droplet making a thin outer layer. The color map in the figure corresponds to the energy dissipation during collision in each droplet. On the other hand when the inner droplet is relatively smaller than the outer droplet ($R_2/R_1 = 0.85$), even a small amount of inertia (kinetic energy) is able to break the encapsulation barrier and push the inner droplet (red) completely inside the outer droplet (blue).

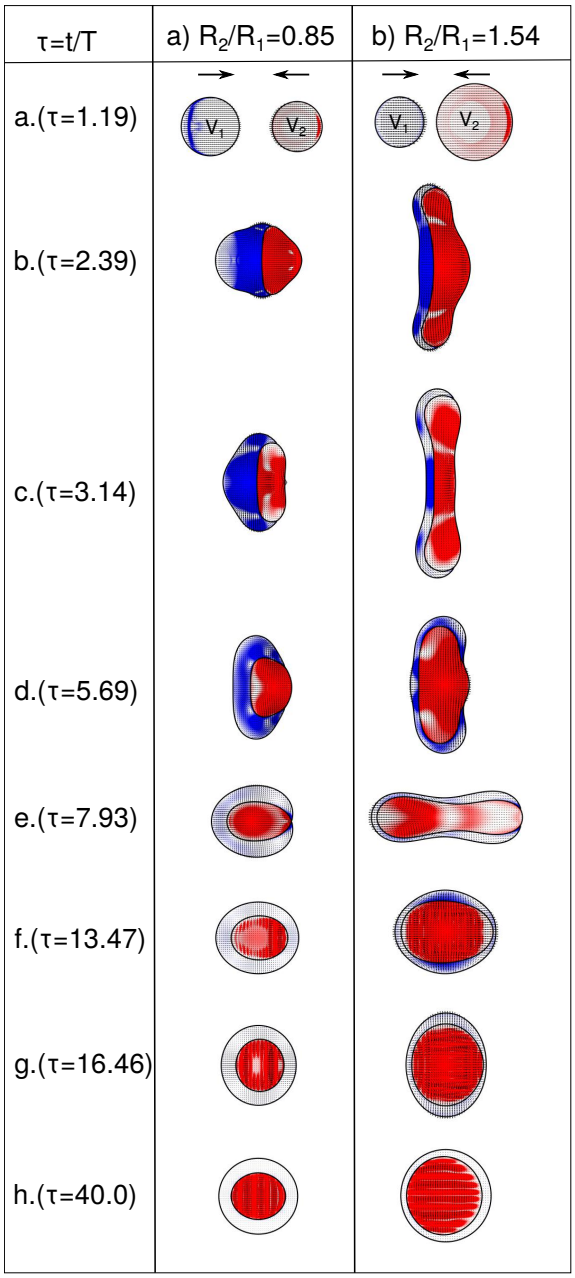

Figure 111: Sequence of steps during collision when outcome is encapsulation (a) R_2/R_1=0.85, $We_{av} = 14.3$ (b) R_2/R_1=1.54, $We_{av} = 78.5$ ($\theta_1 = 167.11°$,$\theta_2 = 25.23°$, $\theta_3 = 167.66°$,$S_2 = -0.02473$, γ_{12}/γ_{13}=0.50 and $\mu_3/\mu_2 = 1$)

Next, we analyse the energy balance corresponds to these two *Encapsulation* outcomes as shown in Fig.112. The kinetic energy is rescaled by the initial kinetic energy, the evolution of free energy and energy dissipation is rescaled by the free energy of the droplets in non-deformed state. It is observed from Fig.112(a) that, among the two sets the droplets at R_2/R_1=0.85, travel longer before the impact because of the small impact speed provided in the beginning. However, after the impact for both the sets, the kinetic energy decreases sharply. There is significant oscillations experienced by the droplets when the inner droplet is of larger size (R_2/R_1=1.54) represented by the black curve, these oscillations last longer during the collision process and then damped to zero value as the droplets rest into their equilibrium shape. On the other hand the red curve which represents the case when inner droplet is of smaller size than outer (R_2/R_1=0.85), after impact the droplets experience less oscillations and very quickly relax to its equilibrium state.

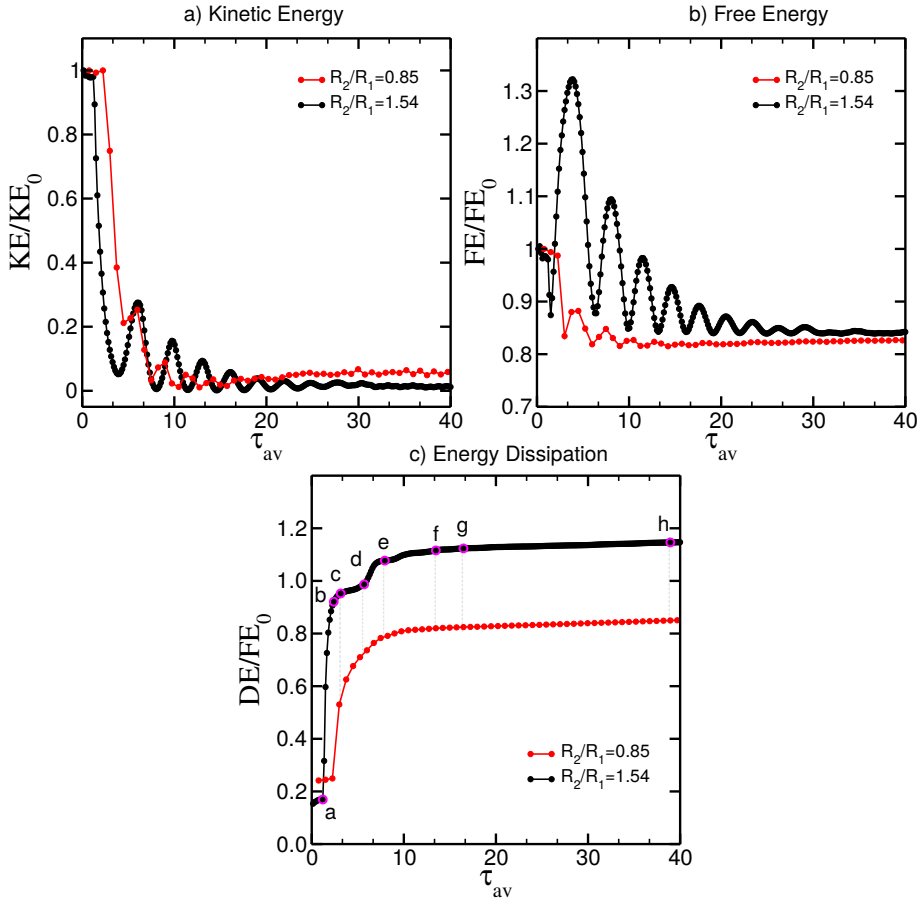

Figure 112: Energy evolution during encapsulation at size contrast (a) Kinetic energy (b) free energy (c) energy dissipation. *black curve:* R_2/R_1=1.54, $\mathrm{We_{av}} = 78.5$ *red curve:* R_2/R_1=0.85, $\mathrm{We_{av}} = 14.3$ ($S_2 = -0.031$ at γ_{12}/γ_{13}=0.50, $\mu_3/\mu_2 = 1$)

Fig.112(b), the comparison of free energy evolution is shown. The opposite trend in the evolution

of free energy is observed in between the two cases. At R_2/R_1=1.54, the free energy increases sharply after the first impact showing large elongation in the shape of the droplets. It reaches its first peak quickly and the the magnitude of the rest of the peaks decrease as the it relaxes to its minimum value representing the equilibrium configuration of the droplets. On the other hand at R_2/R_1=0.85, the free energy of the system decreases just after the impact, and immediately relaxes to its minimum value. During the *encapsulation* process, more energy is being dissipated when the inner droplet is bigger in size as compared to outer droplet, as depicted in the Fig.112(c). The point marked $a - h$ corresponds to the snapshot shown in the above sequence of steps in Fig.111.

7.6 Transition from *Adhesion* to *Encapsulation* at non-identical droplet viscosity

After having investigating the transition between *Adhesion* to *Encapsulation* for head-on collisions of identical and non-identical droplets size, in this section, we investigate the combined role of viscosity contrast between the two droplets. In addition to the above section, where the size of the two droplets differs such that the size ratio (R_2/R_1) between the two droplets is varied from $0.6 - 1.67$, now we repeat the analysis when the two droplets have different viscosity such that $\mu_2 = 0.1667$ and $\mu_3 = 0.50$ l.u. The viscosity ratio μ_3/μ_2 =3.0 between the $droplet_2$ and $droplet_1$. As the viscosity of the $droplet_2$ (μ_3) is increase to 0.5 as compared to the previous section, overall the the Oh corresponds to $Droplet_2$ has increased. Consequently, increases the average Ohnesorge number Oh_{av} of both droplets in the range from 0.143 to 0.158.

In Fig.113, the summary of 2D results which detect the transition line as a function of $\mathsf{We_{av}}$ and R_2/R_1 at viscosity contrast between the droplets is shown. Qualitatively the transition curve behaviour is similar to the one shown at no viscosity contrast in the section above. However, the thin region of *Temporary encapsulation* region does not exists at viscosity contrast along the whole transition line. To clarify the role of viscosity contrast, in Fig.114 we plot the two curves together. It is observed that, when the size of the inner droplet is significantly larger than outer droplet ($R_2/R_1 > 1.3$) and high impact speed ($We_{av} > 50$), the viscosity contrast does not play a significant role. Hence the transition curve behave similar in both cases. However, as the size

ratio start decreasing ($R_2/R_1 < 1.3$), and low impact speed ($\mathrm{We_{av}} < 50$) the region of *Adhesion* outcome starts to grow in the case of viscosity contrast.

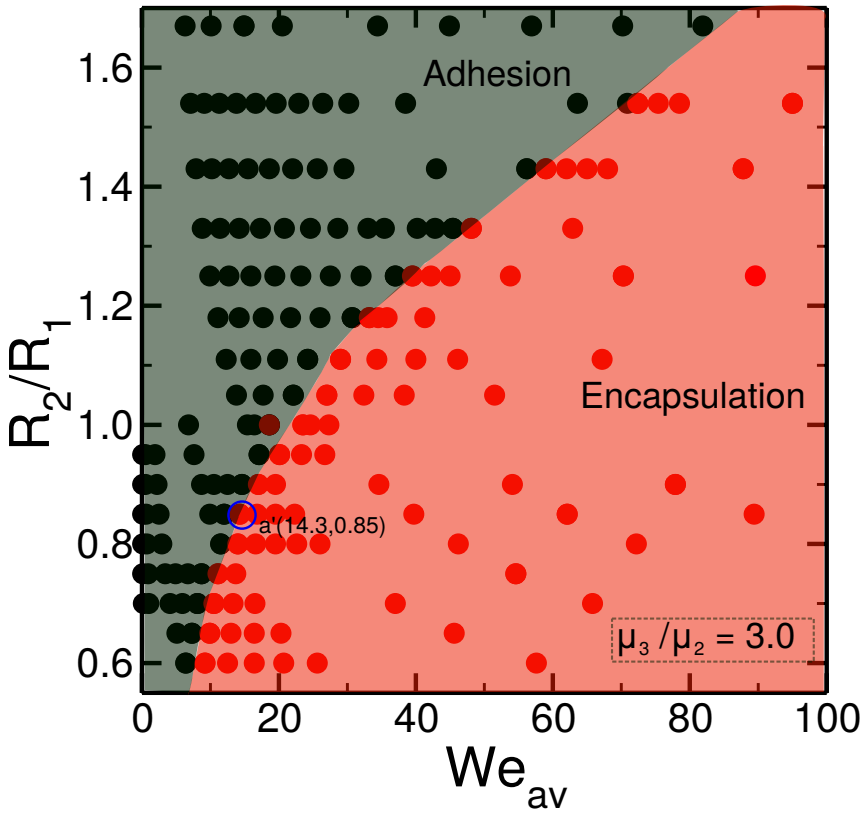

Figure 113: Transition curve from *Adhesion* to *Encapsulation* at viscosity contrast as a function of size ratio between inner and outer droplet (R_2/R_1) and average Weber number $\mathrm{We_{av}}$ ($\theta_1 = 167.11°$,$\theta_2 = 25.23°$, $\theta_3 = 167.66°$,$S_2 = -0.02473$, γ_{12}/γ_{13}=0.50 and $\mu_3/\mu_2 = 3.0$) (The evolution of drop shapes for blue circled simulation point is shown below in Fig.115, while in the Appendix B.4 we show more sequence of simulation snapshots for completeness.)

This is represented by the shift in the transition curve toward higher $\mathrm{We_{av}}$ at viscosity contrast. This suggests that when the collision happens between the droplets of different size and viscosity the system require more kinetic energy (inertia) for encapsulation to occur. As the average viscosity/$\mathrm{Oh_{av}}$ is increased with the increase in the viscosity contrast, more dissipation occurs during collision at viscosity contrast. Hence *adhesion* outcome detected in the whole parameter space which was not the case when the droplets were of identical viscosity.

In Fig.115, a comparison of sequence of steps during *Encapsulation* process with and without viscosity contrast is shown. The rest of the parameters corresponds to these two sets are fixed such as size ratio (R_2/R_1=0.85), $We_{av} = 14.3$, $S_2 = -0.031$ and γ_{12}/γ_{13}=0.50. The sequence of collision steps shown in Fig.115 (a,b) corresponds to point marked a in Fig.110 and a' in Fig.113.

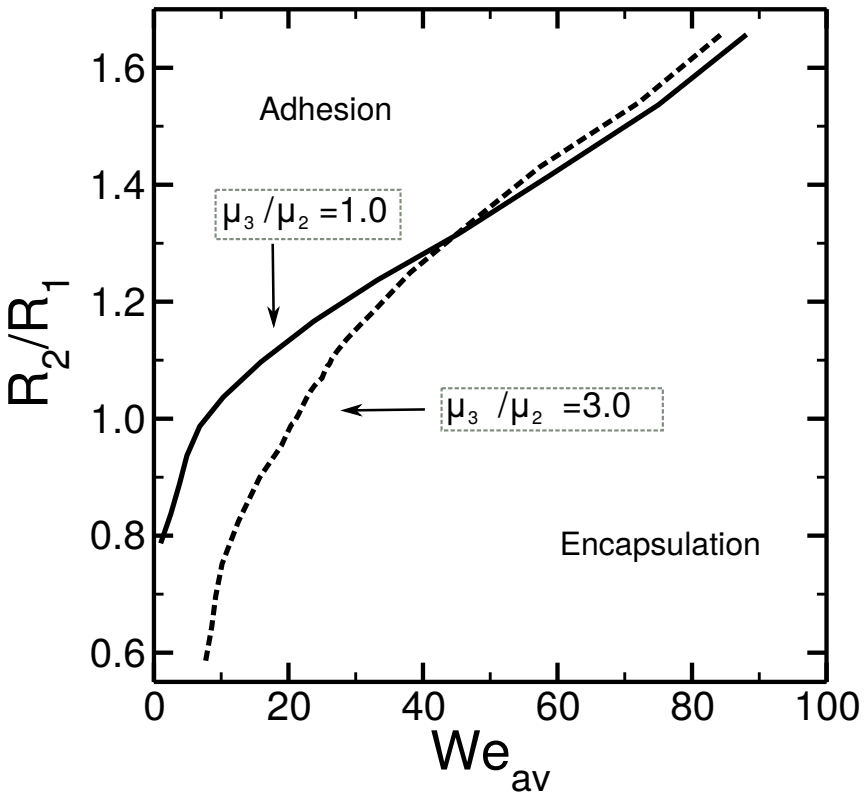

Figure 114: Comparison of the transition curve from *Adhesion* to *Encapsulation* at viscosity contrast ($\mu_3/\mu_2 = 3.0$) vs no viscosity contrast ($\mu_3/\mu_2 = 1$) between droplets ($\theta_1 = 167.11°$,$\theta_2 = 25.23°$, $\theta_3 = 167.66°$,$S_2 = -0.02473$, γ_{12}/γ_{13}=0.50)

It is observed that, at same We_{av}, S_2, R_2/R_1 the initial collision dynamics is qualitatively similar. However, the droplets without viscosity contrast rest deep inside the outer droplet as compared to the case when droplets have different viscosity ($\tau = 40.0$ in Fig.115). At viscosity contrast, the inner droplet rest near the interface. This arises from the of the fact that as we increase the viscosity of the $droplet_2$, keeping viscosity of $droplet_1$ same as previous case, we increase the average viscosity of the system. More viscous dissipation occurs and droplets rest in a state close to transition from encapsulation to adhesive outcome.

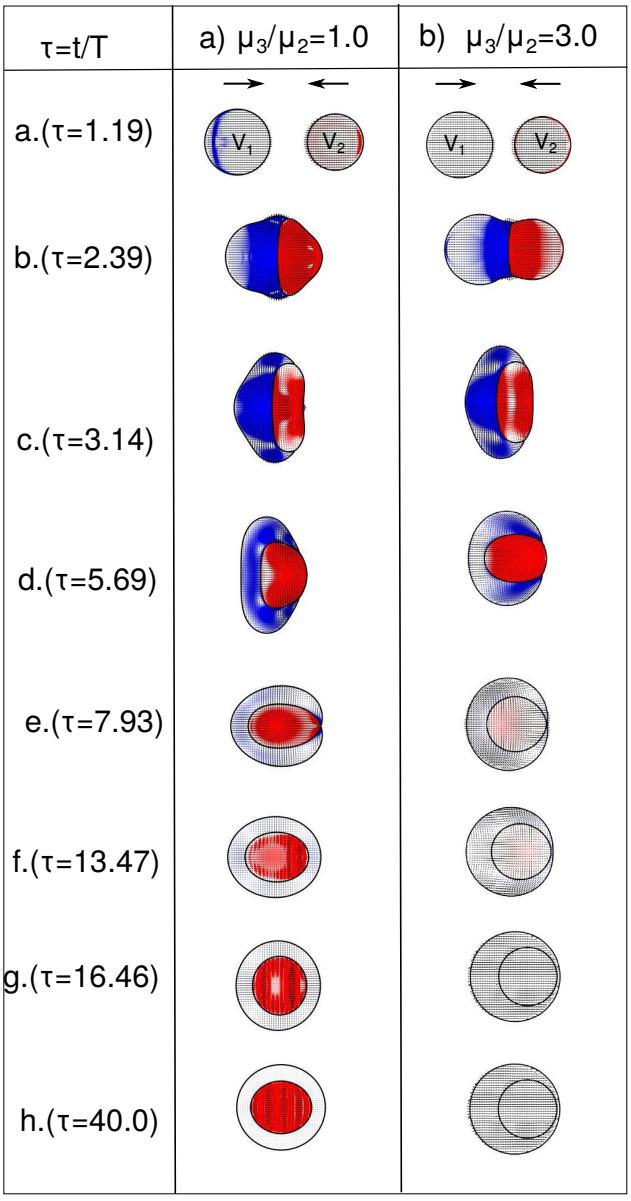

Figure 115: Sequence of steps during collision when outcome is encapsulation (a) $\mu_3/\mu_2 = 1$ (b) $\mu_3/\mu_2 = 3.0$ ($We_{av} = 14.3$, R_2/R_1=0.85,$\theta_1 = 167.11°$,$\theta_2 = 25.23°$, $\theta_3 = 167.66°$,$S_2 = -0.02473$, γ_{12}/γ_{13}=0.50)

7.7 Transition from Adhesion to Encapsulation at non-identical droplet size and viscosity

In the previous section, we observed that as the average viscosity/$\mathsf{Oh_{av}}$ is increased with the increase in the viscosity contrast between $droplet_2$ and $droplet_1$, more dissipation occurs during collision. Now in order to investigate how the collision dynamics is affected by viscosity contrast keeping the average viscosity always fixed. To do so we selected three scenarios of viscosity such that:

Droplets viscosity	$\boldsymbol{\mu_3/\mu_2}$	$\boldsymbol{\mu_{av}}$	$\boldsymbol{\mu_2}$	$\boldsymbol{\mu_3}$
Equal	1	0.333	0.333	0.3333
$Droplet_1$ **more viscous**	0.3	0.333	0.5	0.1667
$Droplet_2$ **more viscous**	3	0.333	0.1667	0.5

Table 4: Summary of viscosity contrast.

In this study we are aim to investigate the transition between encapsulation and adhesion outcome as a function of size (R_2/R_1) and viscosity (μ_3/μ_2) contrast at a fixed $\mathsf{We_{av}}$=25 and $\mathsf{Oh_{av}}$ =0.21. In Fig.116(a), summary of simulation results is shown. It is observed that, when inner droplet ($droplet_2$) is bigger in size as compared to outer droplet ($droplet_1$) ($R_2/R_1 \geq 1$), adhesion outcome occurs at all three viscosity contrast. However for size ratio $R_2/R_1 < 1$, (approximately) a diagonal trend in the transition from adhesion to encapsulation outcome is observed as a function of viscosity contrast. In Fig.116(b), we show a comparison of encapsulation morphology at three viscosity ratios. At the same size ratio, if the viscosity of the outer droplet is larger than the inner droplet more dissipation occurs and the equilibrium state of the droplets is closer to the transition between encapsulation and adhesive morphology. On the other hand, if the inner droplet is more viscous (at the same average viscosity), the inner droplets rest in a deep encapsulated state far from the interface. Overall, at a same size ratio, surface tension combination and impact speed, by tuning the viscosity contrast between the colliding droplets, we can trigger the encapsulation outcome of collision.

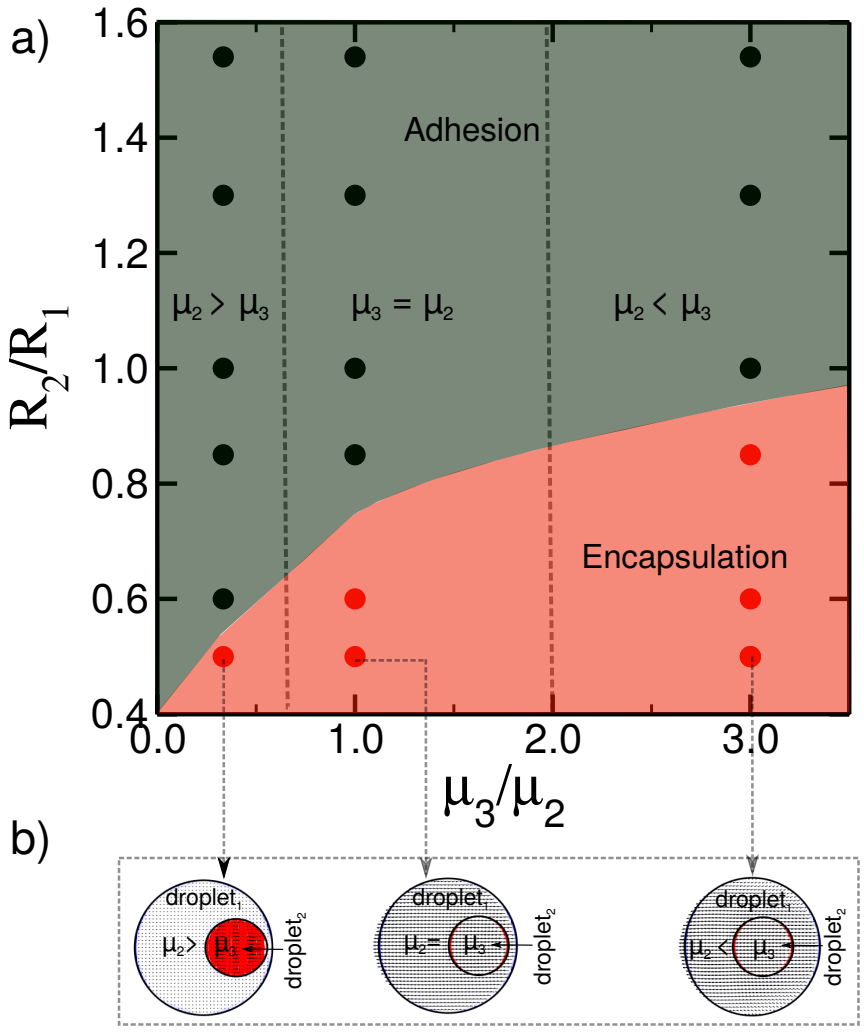

Figure 116: a) Transition curve from *Adhesion* to *Encapsulation* at (R_2/R_1) and viscosity (μ_3/μ_2) contrast b) representation of encapsulation morphology of the droplets at R_2/R_1=0.5 and three ratios of viscosity contrast. (We_{av}=25, Oh_{av}=0.21, $\theta_1 = 167.11°$,$\theta_2 = 25.23°$, $\theta_3 = 167.66°$,$S_2 = -0.02473$, γ_{12}/γ_{13}=0.50

7.8 Conclusion

Three collision outcomes *Adhesion*, *Temporary Encapsulation* and *Encapsulation* occurs in our simulations and has a significant dependency on the physical parameters. We believe that the *temporary encapsulation* is related to the relative scale of the diffuse interface compared to the thickness of the exterior liquid layer. As the spreading parameter become more negatives, a larger impact speed is required for *Encapsulation* to occur. The surface tension ratio between two liquid/gas interfaces play a significant role in the shift of transition curve. As the ratio of surface tension between $droplet_1$/gas and $droplet_2$/gas reduces, the transition curve shifts to a low We_{av} region. There is a significant different in the way the energy is dissipated among each outcome

and as a function of spreading parameter and Impact speed. When the inner droplet is relatively smaller than the outer droplet, only a minimum amount of energy is required for encapsulation to occur. This energy is already provided by the surface tension combination of the two separated droplets. When the size of inner droplet is significantly smaller than outer droplet, the transition from adhesion to encapsulation outcome occurs when the inner droplet become more viscous (at the same average viscosity).

Chapter 8

Conclusion and Future Work

In this thesis, numerical simulations of ternary fluid systems (liquid-liquid-gas), such as, water-oil emulsions in the air or slippery liquid-infused surfaces are reported. To this scope the algorithm developed in the research group also incorporating specifically tuned wetting boundary schemes. The research discussed here was divided broadly into two parts. In the first part, the thermodynamic consistency of the model was verified by simulating the thermodynamic quantities such as Laplace's law and the liquid-gas density profile. As the model does not allow an analytic link between free energy parameters and surface tension between interfaces, an extensive work has been done to understand the free energy parameters. We provide guidelines to select these parameters for obtaining a wide range of surface tension combinations.

We report the details of our implementation of three different approaches to model the wetting boundaries in ternary fluid systems. We have compared these three methods for wetting of solid boundaries, namely *force*, *geometric extrapolation* and *geometric interpolation*. Of the two geometric methods, *geometric interpolation* is significantly more accurate. The *force* method provides an useful alternative to geometric methods, as it does not require us to detect the fluid interface a priori, and automatically satisfies the Girifalco-Good relation (Eq.4.2). From our analysis, the gemetric methods should be generally preferred due to the strong reduction of spurious currents. However methods are to difficult handle in presence of complex surface topographies. Furthermore we have studied the motion of self-propelled bi-slugs forming three finite and unbalanced contact angles showing that coupling multiphase and multicomponent models leads to significant

differences in the slip properties of liquid-liquid and liquid-gas interfaces.

In the second part of the research, we performed numerical investigation of the collisions between two immiscible droplets surrounded by gas phase. The emphasis is given on the collision dynamics for systems dominated by the transition between bouncing and adhesion outcomes. Beside bouncing and adhesion, an intermediate outcome was clearly identified in our simulations. We captured the existence of *delayed adhesion* outcome in both $2D$ as well as $3D$ simulations. A systemic parameter study ($2D$ and $3D$) for head-on collision setup for identical droplets shows that the initial kinetic energy is dissipated nearly completely within the first and second deformation. The kinetic energy left in the droplets after separation is contributing to the linear momentum of individual droplets and their surface oscillation. while the relative contribution of these two components is determined by the combination of collision parameters, and specifically by the adhesion energy between droplets. Furthermore, we propose a minimal model in $2D$ able to reproduce the essential feature of the transition between *adhesion* and *bouncing* for identical droplets. Extending our investigation to collisions between droplets with non-identical size we found that the during bouncing the average linear momentum carried away by both droplet together is larger for identical droplets case compared to droplets with different size but equal total mass. However, between the non-identical droplets, the smaller droplet contribute more to the average moment as compared to the bigger droplet. As the viscosity contrast between the droplets increases, the linear component of the kinetic energy carried by droplets increases which is accompanied by increase in the oscillating component. However, the more viscous droplet experience less surface oscillation than the droplets which is less viscous. At last, the drop collision study at off-centre collision shows that despite the remarkable differences in the system our numerical results for the transition between adhesion and off-centre collision region is close to the model purposed by Arkhipov et al.(1983) [4].

Finally, we perform a systematic $2D$ numerical study to investigate the collision between two immiscible droplets, with one of the liquid close to spreading over the other liquid. In this scenario, the kinetic energy available during the impact could be sufficient to induce the encapsulation of the droplet. Therefore we systematically investigated the transition between adhesion and encapsulation. We observed that, at parity of spreading parameter as the surface tension ratio between the $droplet_1/gas$ and $droplet_2/gas$ reduces, the encapsulation occurs at much lower impact ve-

locity. The collision dynamics near the transition line between *adhesion* and *encapsulation* shows that at high impact speed the droplets experience more shape deformation and contribute to more energy dissipation. Finally, we show that if the size of the outer droplet is smaller than inner, the droplets experience a larger shape deformation and dissipate more energy as compared to the case when outer droplet is larger in size than inner droplet. We can trigger the encapsulation outcome by tuning the viscosity contrast between the colliding droplets at same size ratio and impact speed.

8.1 Discussion for future work

The field of entropic lattice Boltzmann system simulation is very broad and relatively new. As a result, there is still scope for in-depth research and growth. The first path for future studies will be to optimise stability of our existing thermodynamically consistent approach to simulate problem at very higher We and Re such as high speed sprays for $2D$ and $3D$ setup. Though drop collision study for which typical We and Re values are $\sim 10^2$ and $\sim 10^3$ respectively. However for the larger range further development/improvement are required. Another aspect of using multiphase lattice Boltzmann approach which has always gained attention is the resolution of interfaces. In fact, as the LB multi-phase methods are based on the diffuse interface method, in models, the fluid-fluid interface is constructed by certain grid nodes. While changes have been made to multi-phase methods that have shortened the width of the interface, there is still a limit of a few lattice points. Any type of grid refining around the interface will be one way to further minimise the fluid fluid interface width. In terms fluid-fluid interface, we observed in our model that there is significant differences in the slip properties of liquid-liquid and liquid-gas interfaces. However more detailed analysis of the slip properties of the system will be the subject of a future investigation. Also the simulation of problem such as drop impact on liquid pool using wetting boundary condition is next future step. In Fig.117, we show a preliminary $2D$ tests of drop impact on thin oil layer. The droplet impacting at different speed, viscosity and on different oil thickness is the area of interest.

In drop collision we detected the *delayed adhesion* phenomenon, and our analysis suggests that this outcome is a physical and not model artefact. however a detailed analysis is required to understand it better. The two-dimensional simulations of drop collision at off-centre gives the qualitative

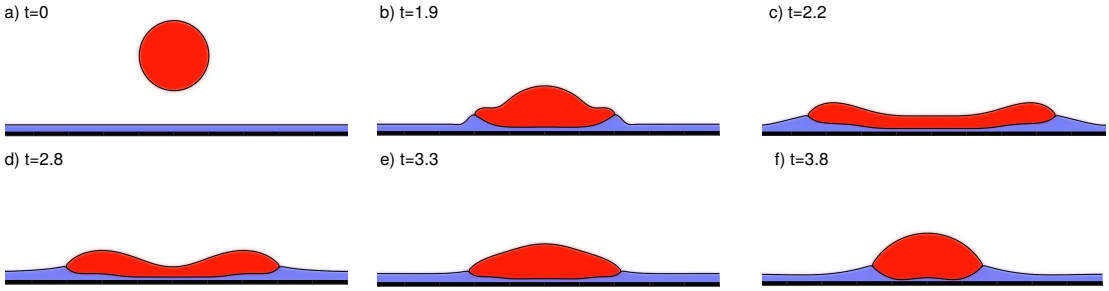

Figure 117: Sequence of steps for simulation of drop impact on thin oil film

picture when compared with the experimental results and theoretical models. However, a systemic three-dimensional simulations is the next future step for better comparison of the results. In drop collision study focused on *adhesion* and *encapsulation* outcome. To the best of our knowledge, there are very limited numerical works for these systems, and this study represents a first attempt to perform a more systematic analysis. One of the major challenges encountered is related to the relative scales between the thickness of the encapsulating layer and the diffuse interface in the model, which is unphysically large in our simulations. Additionally, free energy parameters for nearly vanishing spreading parameters turn to be rather unstable when setting lower viscosities, which represent a limiting constrain the the range of parameters that could be explored in the current study. This study has been limited at some point by the emerging of the Covid19 pandemic and by a simultaneous IT disruption lasting several months, which prevented to complete some of the simulations originally planned. Despite that, we were able to gather a number of qualitative results that can shed light on parameter ranges not easy to access or control experimentally. Our hope is that this study can stimulate further research and improvement of numerical and experimental works in this field.

Appendix A

Surface Tension database: High density ternary free energy model

In this ternary high density ratio lattice Boltzmann model, the free energy is expressed by:

$$\begin{aligned} f &= \frac{\lambda_1}{2}(\Psi_{\text{eos}}(\rho) - \Psi_0) + \frac{\lambda_2}{2}C_2^2(1-C_2)^2 + \frac{\lambda_3}{2}C_3^2(1-C_3)^2 \\ &+ \frac{\kappa_1}{2}(\nabla\rho)^2 + \frac{\kappa_2}{2}(\nabla C_2)^2 + \frac{\kappa_3}{2}(\nabla C_3)^2. \end{aligned} \tag{A.1}$$

The six parameters $\boldsymbol{\lambda} = (\lambda_1, \lambda_2, \lambda_3)$ and $\boldsymbol{\kappa} = (\kappa_1, \kappa_2, \kappa_3)$ allow to tune combinations of surface tensions. To facilitate the choice of suitable parameter sets to simulate different combinations of fluids of interest, we have performed a systematic investigation to quantify the shape of the difuse interface properties, and the related combinations of surface tensions. In all tests we set $T_{red} = 0.61$, which leads to an effective density ratio $\rho_l/\rho_g \simeq 10^3$. To reduce the extension of the six-dimensional parameter space, we have identified eight two-dimensional subspaces. The criterion for the choice of the subspaces is to facilitate simulations of systems with similar surface tensions (within a subspace), and capture the effect of systematic variations of the surface tension in the fluid response. Consequently, the same parameter sets might be included in different subspaces, but will differ in the local variation of some parameters.

Using simulation setup in section.(3.9.4), and as discussed in the main text of section.(3.9.4), each

Subspace is described by two coordinates, X and Y and is mapped by a $20 \times 20 = 400$ points grid, where each point represents a given parameter set. For each parameter set we have performed three independent measures (drop/bubble test) of the surface tensions (one for each interface). Our analysis of each subspace is summarised in a figure reporting 2D maps of the measured surface tensions (first row), the Neumann angles θ_i (second row), the spreading coefficients S_i (third row) and the Deformation factors D_i (fourth row), respectively defined by Eq.(2.25) to Eq.(3.49). A high order polynomials (Eq.3.50), is extracted for each set after fitting the surface tension values. This is a quick way to determine the necessary parameter set and the corresponding combination of surface tensions. Similar to the analysis of subspace 4 (section.3.9.4), all the remaining sets which are summarised in table.5 are discussed below.

Subspace	$\boldsymbol{\lambda_1}$	$\boldsymbol{\lambda_2}$	$\boldsymbol{\lambda_3}$	$\boldsymbol{\kappa_1}$	$\boldsymbol{\kappa_2}$	$\boldsymbol{\kappa_3}$
1	Y	X	X	0.01	X	X
2	Y	X	X	0.01	$0.5X$	$0.5X$
3	Y	X	0.5	0.01	X	0.5
4	0.01	X	Y	0.01	X	Y
5	0.5	X	Y	0.01	X	Y
6	1.0	X	Y	0.01	X	Y
7	Y	X	0.5	0.01	$2X - 0.5$	$1 - X$
8	0.1	X	1.0	0.01	Y	$1 + X - Y$

Table 5: Summary of surface tension tests.

We also show the fitting parameters for the high order polynomial corresponds to each phase in each subspace.

$$\gamma = A(x) + B(x)y + C(x)y^2 \tag{A.2}$$

$$A(x) = a_1 + a_2x + a_3x^2 + ...$$
$$B(x) = b_1 + b_2x + b_3x^2 + ...$$
$$C(x) = c_1 + c_2x + c_3x^2 + ...$$

A.1 Maps: Bubble tests for Surface tensions

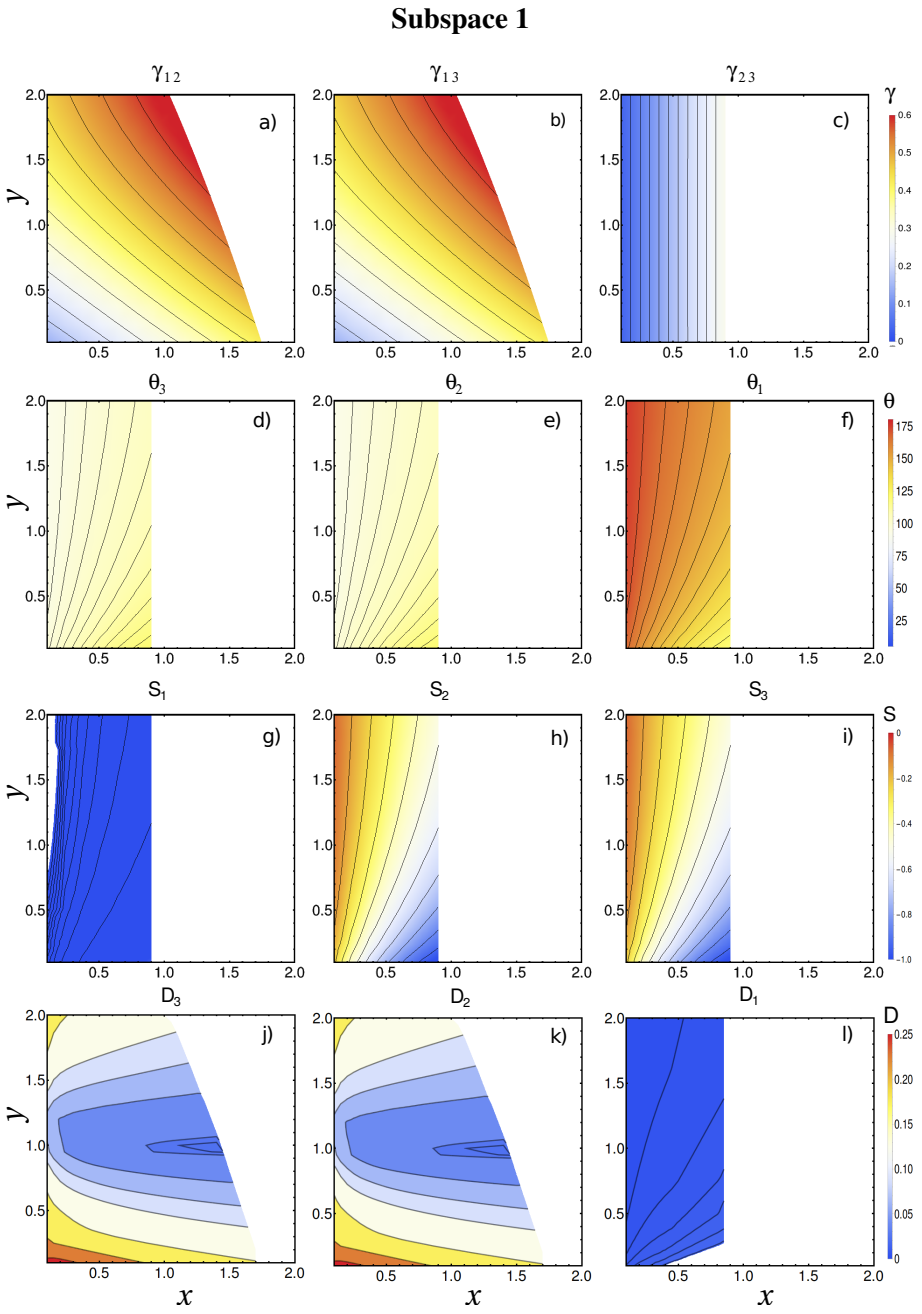

Subset coordinates

Subspace	$\boldsymbol{\lambda}_1$	$\boldsymbol{\lambda}_2$	$\boldsymbol{\lambda}_3$	$\boldsymbol{\kappa}_1$	$\boldsymbol{\kappa}_2$	$\boldsymbol{\kappa}_3$
1	Y	X	X	0.01	X	X

Fitting coefficients

1* $\gamma_{12} = \gamma_{13}$			
	a	b	c
1	0.09668041266042737	0.2837496899035988	−0.05512689060902226
2	0.1887008554437671	−0.0517341619888367	0.02364378174833557
3	−0.009911634325995271	0.01887959182850299	−0.008592943188584739

1* γ_{23}			
	a	b	c
1	0.00012196129808580297	−0.00011866854356189962	−0.00013007818378063803
2	0.32103226178221356	−0.00025878524202585897	0.0017215995185091888
3	−0.002102530555554442	0.004720444252924098	−0.0070237228094129365
4	0	−0.005163887301085149	0.005895379262217849

Subspace 2:

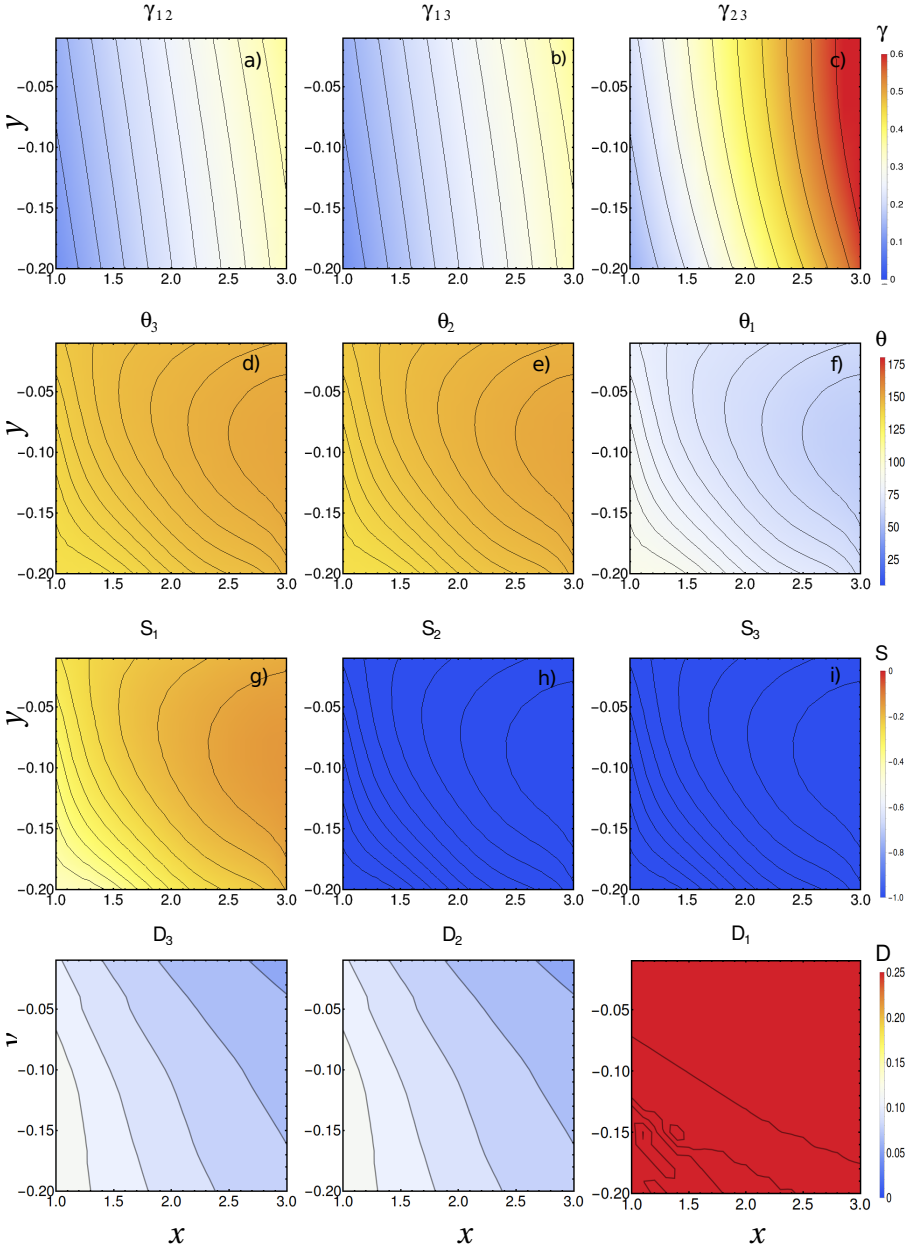
γ12
γ13
γ23
γ
a)
b)
c)
θ3
θ2
θ1
θ
d)
e)
f)
S1
S2
S3
S
g)
h)
i)
D3
D2
D1
D
y
x
−0.05
−0.10
−0.15
−0.20
1.0
1.5
2.0
2.5
3.0

Subset coordinates

Subspace	$\boldsymbol{\lambda}_1$	$\boldsymbol{\lambda}_2$	$\boldsymbol{\lambda}_3$	$\boldsymbol{\kappa}_1$	$\boldsymbol{\kappa}_2$	$\boldsymbol{\kappa}_3$
2	Y	X	X	0.01	$0.5x$	$0.5x$

Fitting coefficients

1* $\gamma_{12} = \gamma_{13}$			
	a	b	c
1	0.020727812062204098	0.16411586559497282	−0.7142882359628013
2	0.11975607304848708	−0.007517426651514831	0.8150849407236493
3	−0.0005973966422455415	0.01570574805056057	−0.27858064652299036
4	0	−0.0018495848008796014	0.03947979646573858

1* γ_{23}			
	a	b	c
1	0.017760279387512425	−0.945113486738741	−9.895007372730758
2	0.20147195241655358	6.096772086939355	42.33801620503938
3	0.0013080405588957475	−9.120922830872901	−60.45639952652519
4	0	6.087103295166769	37.67730365441279
5	0	2.020190743683211	10.894365326975374
6	0	0.3101493332091379	1.1944216926602245
7	0	−0.01564752826013218	0

Subspace 3:

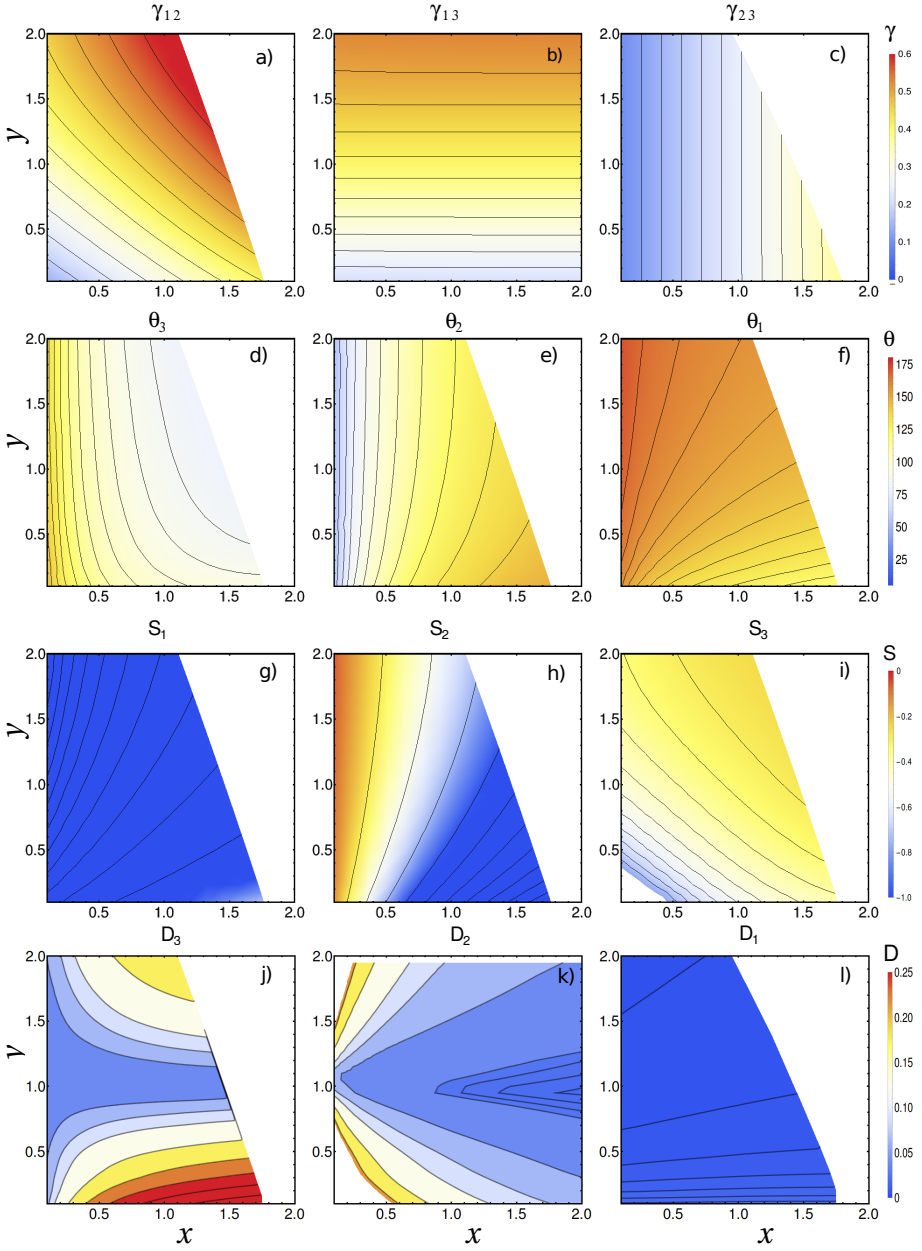

Subset coordinates

Subspace	$\boldsymbol{\lambda}_1$	$\boldsymbol{\lambda}_2$	$\boldsymbol{\lambda}_3$	$\boldsymbol{\kappa}_1$	$\boldsymbol{\kappa}_2$	$\boldsymbol{\kappa}_3$
3	Y	X	0.5	0.01	X	0.5

Fitting coefficients

1* γ_{12}			
	a	b	c
1	0.09582672231293243	0.28505698785588457	−0.055236104664359825
2	0.1942508998489134	−0.06133645405361527	0.02616168467115924
3	−0.01756462693226569	0.032781230361199384	−0.013486787744883856

1* γ_{13}			
	a	b	c
1	0.1841362356926559	0.2721973785704864	−0.050501589361160414
2	0.009476541050595925	−0.01870770626499292	0.009374538610289125
3	−0.005689405225526139	0.011234405081585606	−0.005739090725357518
4	0.0012222791406269302	−0.0024211593770592063	0.0012571397147517452

1* γ_{23}			
	a	b	c
1	0.0805346561807159	0.00026287051008620126	−0.00016462845530654444
2	0.16162702147733815	−0.0007851080434884273	0.0006968953989562777
3	−0.0002827374700916004	0.0013043024303415335	−0.0008346482546355441

Subspace 4:

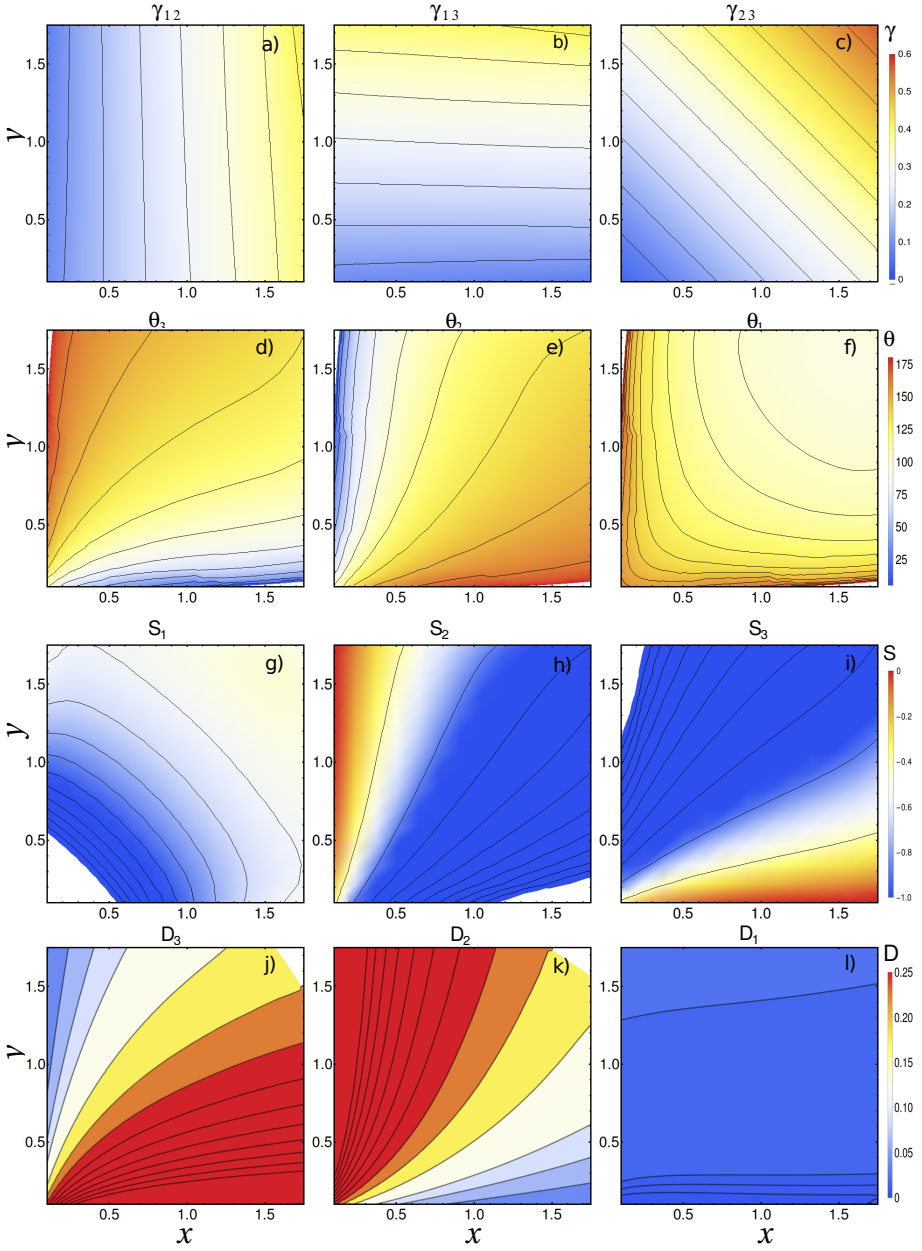

Subset coordinates

Subspace	λ_1	λ_2	λ_3	κ_1	κ_2	κ_3
4	0.01	X	Y	0.01	X	Y

Fitting coefficients

1*γ_{12}			
	a	b	c
1	0.07116425636918997	−0.008054800909232647	−0.008668075470668564
2	0.22641469306366468	−0.006246920681918574	0.07827584764832109
3	−0.06381025382880216	0.04859980966246758	−0.1943880781395426
4	0.021684054453607927	−0.025752475653084424	0.21516135956711802
5	0	0.0010567097596947273	−0.11822361611312888
6	0	0	0.026500508993061538

1*γ_{13}
All Coefficients are same as γ_{12} , we just swap the x and y axis in Eqn.(3.50)

1*γ_{23}			
	a	b	c
1	−0.00007609029551985845	0.1611422524718045	0.0007616812549378891
2	0.16140783688413907	−0.0007641583617704355	0.00002578015767993373
3	0.00028283814677441623	0.00038179157194921784	0.00001801470052202483 2
4	0	−0.00009688163692885255	$-5.592562581362088 * 10^{-}6$

Subspace 5:

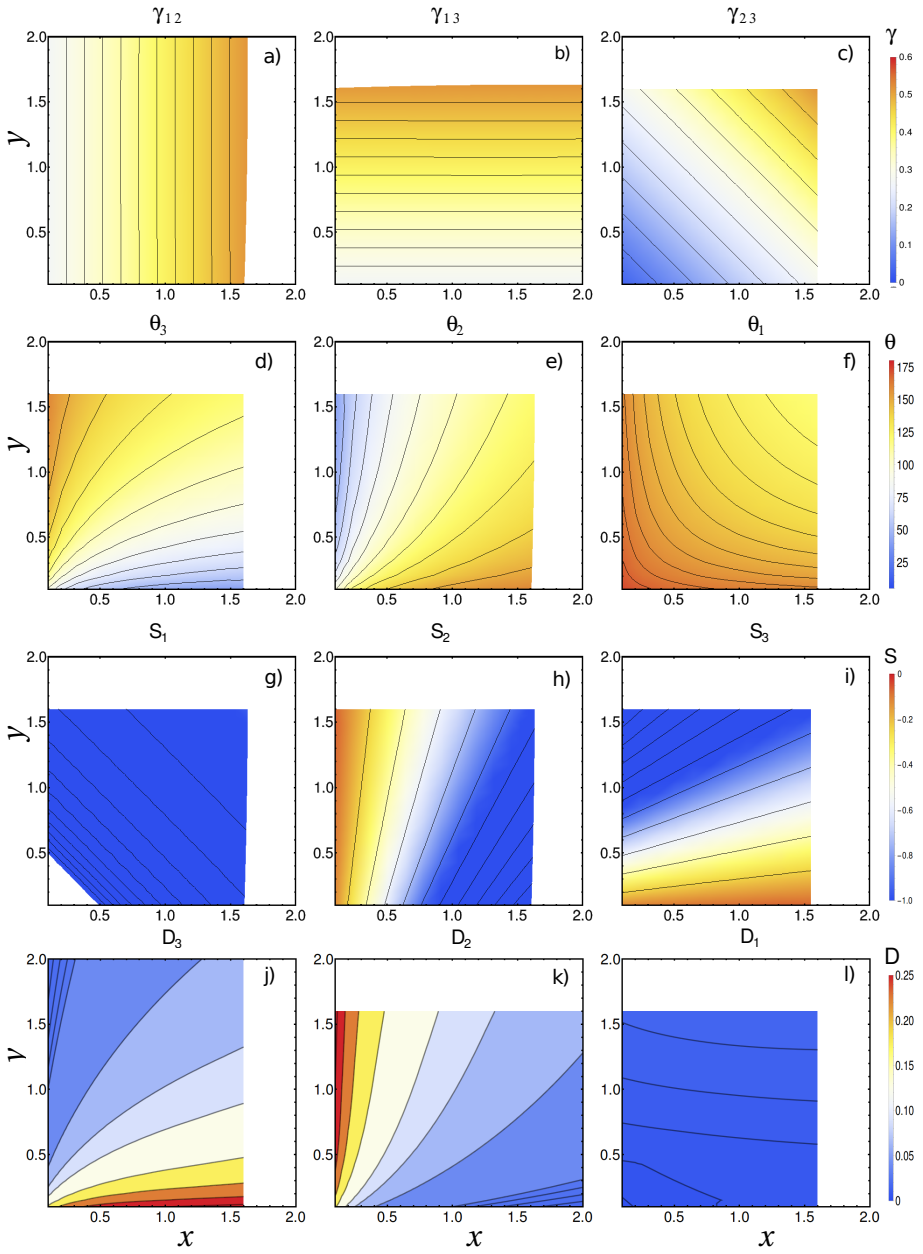

Subset coordinates

Subspace	$\boldsymbol{\lambda}_1$	$\boldsymbol{\lambda}_2$	$\boldsymbol{\lambda}_3$	$\boldsymbol{\kappa}_1$	$\boldsymbol{\kappa}_2$	$\boldsymbol{\kappa}_3$
5	0.6	X	Y	0.01	X	Y

Fitting coefficients

1*γ_{12}			
	a	b	c
1	0.25299225767012545	−0.00018379173499900783	0.000051698723633803804
2	0.16119993658507953	0.0012301330148314813	−0.0005120244319034921
3	−0.00003184213224684729	−0.0003887655821528309	0.00020109491093040914

1*γ_{13}
All Coefficients are same as γ_{12} , we just swap the x and y axis in Eqn.(3.50)

1*γ_{23}			
	a	b	c
1	−0.00007044058056222096	0.1612738826450767	0.00046827872668499845
2	0.161103434403991	0.0002683926997548863	−0.00014298682893786402
3	0.00042120026719995465	0.00009732882664308531	−0.00010134417282735175
4	0	−0.00011455633707692966	0.0000733310714144682

Subspace 6:

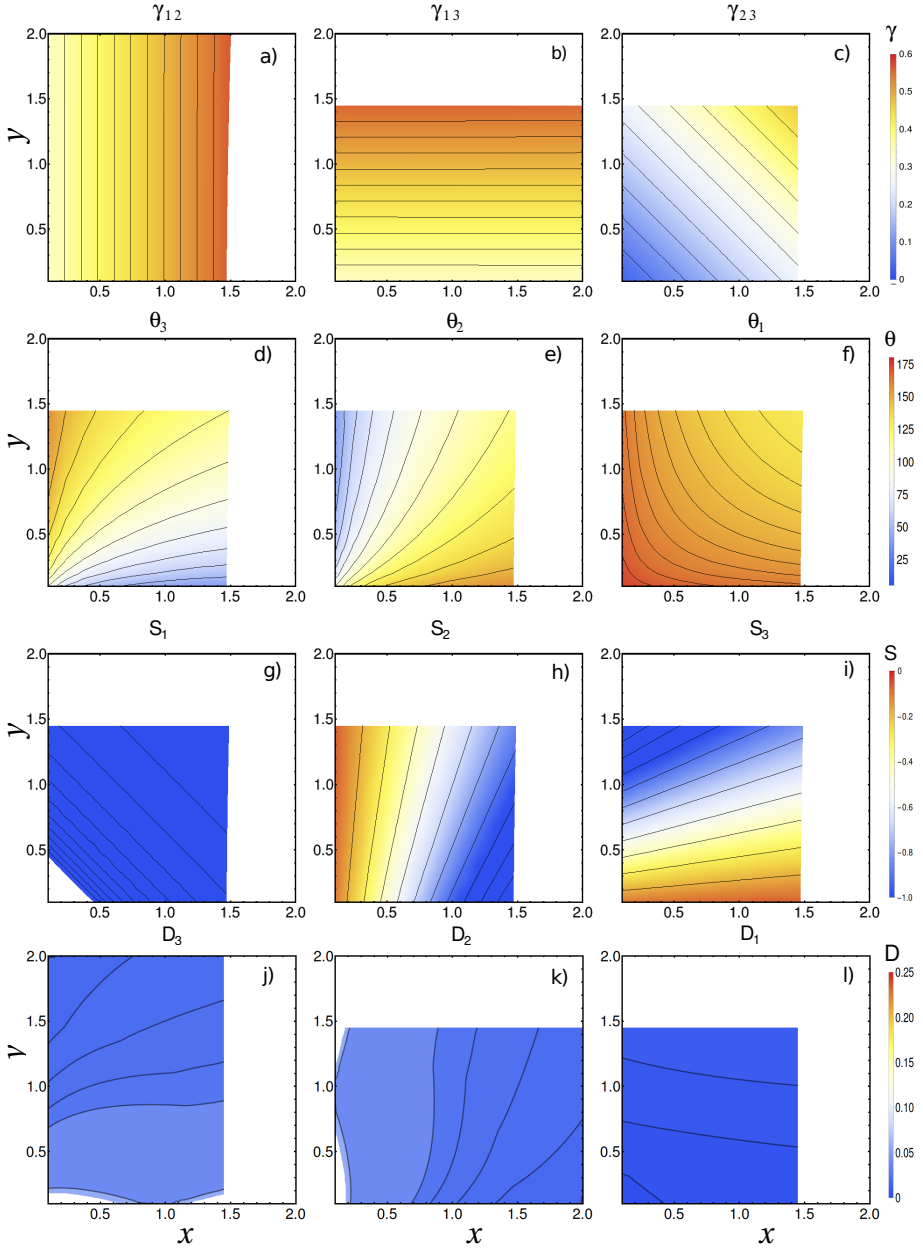

Subset coordinates

Subspace	$\boldsymbol{\lambda}_1$	$\boldsymbol{\lambda}_2$	$\boldsymbol{\lambda}_3$	$\boldsymbol{\kappa}_1$	$\boldsymbol{\kappa}_2$	$\boldsymbol{\kappa}_3$
6	1.0	X	Y	0.01	X	Y

Fitting coefficients

1*γ_{12}			
	a	b	c
1	0.3246567734056512	-0.00021081133855638227	0.00012389882047871643
2	0.16096433423438267	0.000719580138034537	-0.00018594945883418566
3	0.000417762951058353	-0.00035579346560786376	-0.00011065130975874638

1*γ_{13}
All Coefficients are same as γ_{12} , we just swap the x and y axis in Eqn.(3.50)

1*γ_{23}			
	a	b	c
1	-0.00008759487368671038	0.16127819405945612	0.0004360020782471717
2	0.1613196734539803	0.00018779933992801423	-0.00009498193895878964
3	0.0003661270399684589	$9.749190809289126 * 10^{-}6$	-0.00007330488531070058
4	0	-0.00007033895603225673	0.00006069774540076861

Subspace 7:

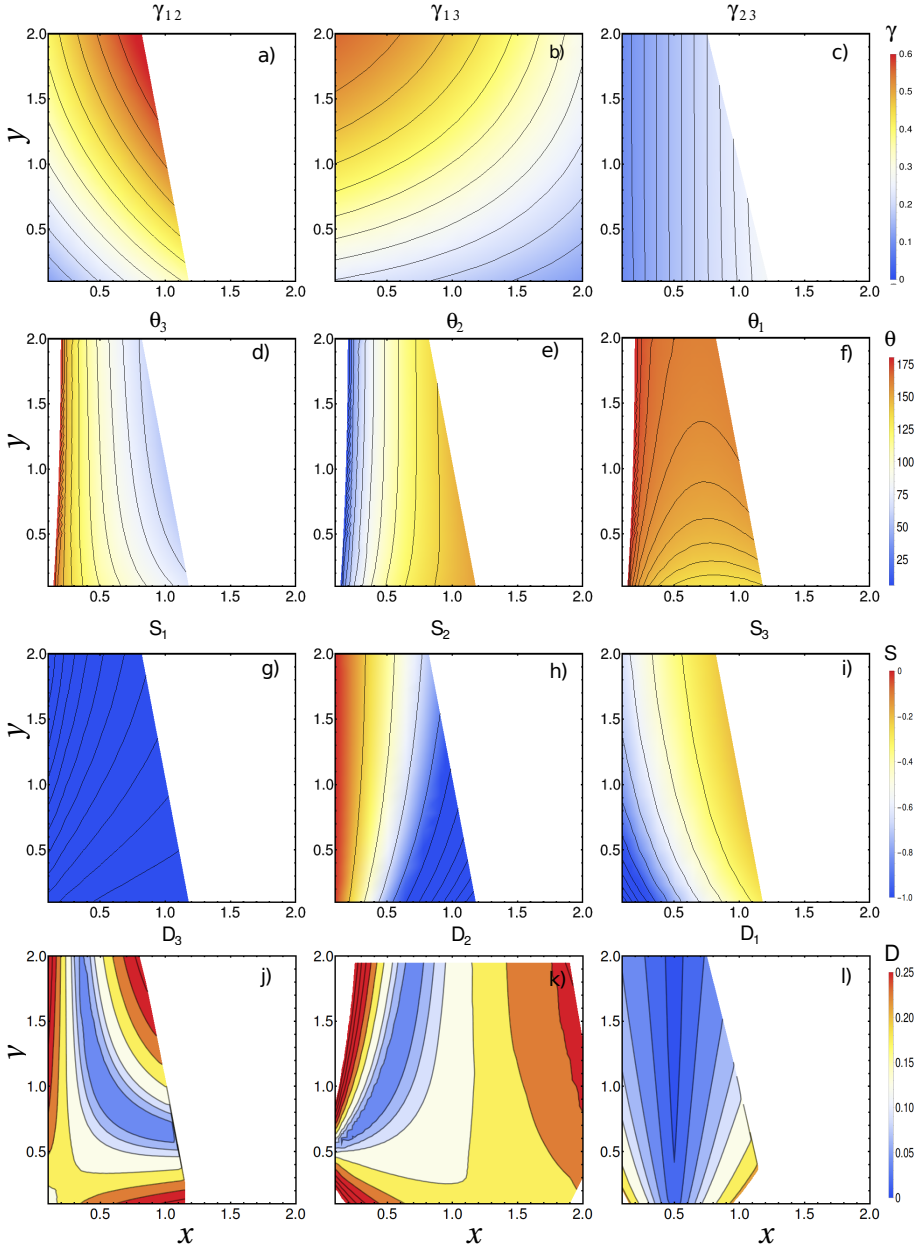

Subset coordinates

Subspace	$\boldsymbol{\lambda}_1$	$\boldsymbol{\lambda}_2$	$\boldsymbol{\lambda}_3$	$\boldsymbol{\kappa}_1$	$\boldsymbol{\kappa}_2$	$\boldsymbol{\kappa}_3$
7	Y	X	0.5	0.01	$2x - 0.5$	$1 - x$

Fitting coefficients

1* γ_{12}			
	a	b	c
1	0.07372066944290014	0.24767682485814288	−0.049633354985338725
2	0.24508043553916561	0.010011810497016584	0.02498082082668315
3	−0.02710224298715041	0.033288870985378284	−0.030701855052926396

1* γ_{13}			
	a	b	c
1	0.2091178129421897	0.29313458494658157	−0.058212411033451913
2	−0.038210323098545745	−0.05012296001685868	0.02265219490438797
3	−0.007649239179563179	−0.01127915905489349	−0.003730754866199104

1* γ_{23}			
	a	b	c
1	0.07241802586902751	0.00828625440470605	0.0025958721740917145
2	0.19286039229453433	−0.03178771991432241	0.009960522443626843
3	0.029962819397260462	$0.03092330815333692 * 10^{-}6$	−0.009638626560087522

Subspace 8:

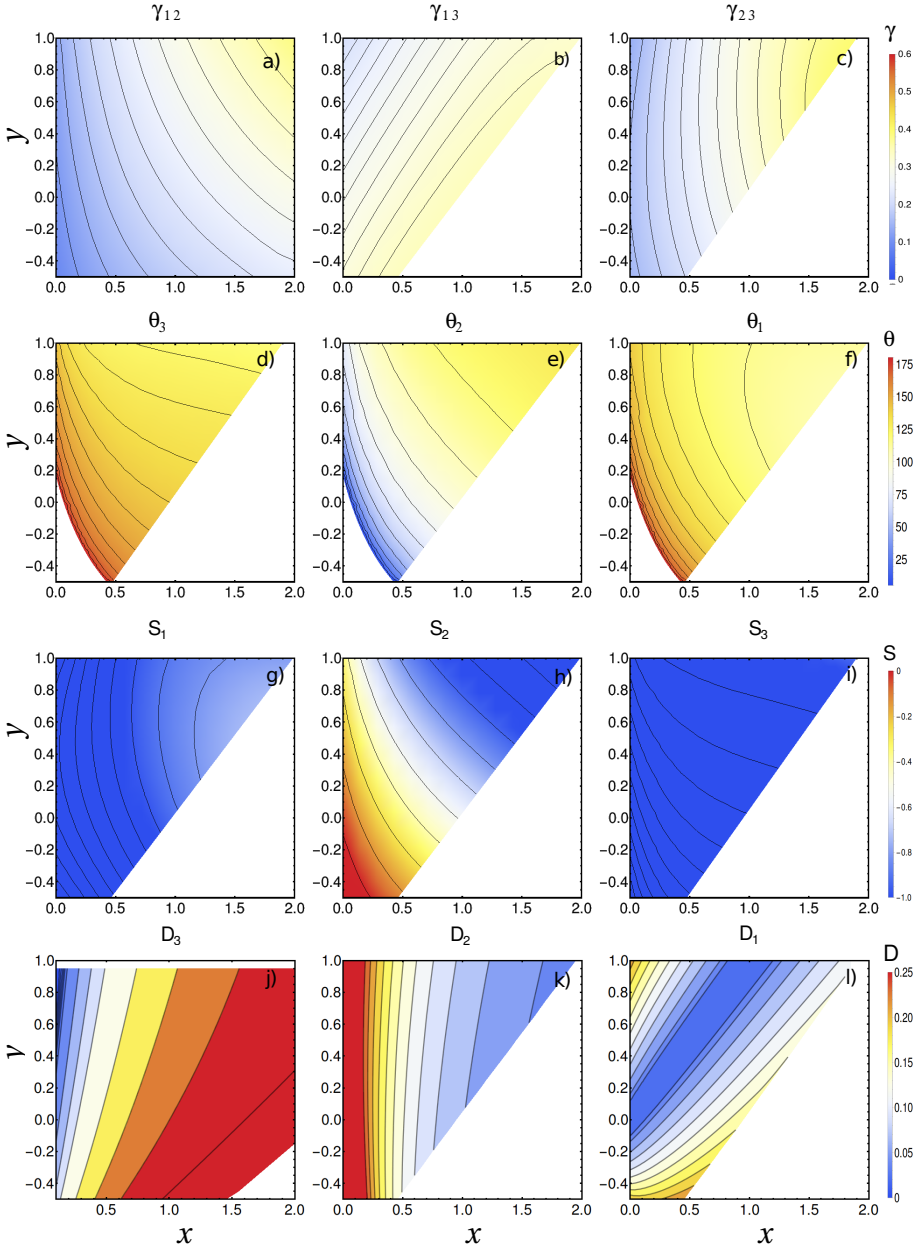

Subset coordinates

Subspace	$\boldsymbol{\lambda}_1$	$\boldsymbol{\lambda}_2$	$\boldsymbol{\lambda}_3$	$\boldsymbol{\kappa}_1$	$\boldsymbol{\kappa}_2$	$\boldsymbol{\kappa}_3$
8	0.1	X	1.0	0.01	Y	$1 + x - y$

Fitting coefficients

1* γ_{12}			
	a	b	c
1	0.104595425374764	0.03273953217093202	−0.008571503989837633
2	0.1909356708499759	0.06868513996661697	0.06764491685477873
3	−0.11042407992665253	−0.02699745695229467	−0.41032834506595134
4	0.04880377488198531	0.0011121630107568984	−0.9977671886754743
5	0.008863265461577424	−0.010049339044360969	−1.322509904304185
6	0	0.02999529627045429	1.045794675071525
7	0	−0.021324672340505012	−0.49995345710672173
8	0	0.004687668782405248	−0.13489338842851933
9	0	0	−0.015842802853142247

1* γ_{13}			
	a	b	c
1	0.2824768057579995	−0.06290918193767604	−0.009822980296540986
2	0.08294910002039922	0.00969540859399386	0.009737763529669964
3	−0.017856294513047617	0.006490470546187193	−0.004976293629430881
4	0	−0.002499016883507906	0

1* γ_{23}			
	a	b	c
1	0.16137055333973369	0.007698237803576588	−0.03220459066702922
2	0.15589560808063258	0.05088808092048638	0.013264922176866017
3	−0.016892705584066938	−0.008769085032880364	−0.0185132241705879

Appendix B

Validation of the model

B.1 Laplace Law validation

We validated "Laplace law" using our ternary free energy lattice Boltzmann model. The simulation setup sketched in Fig.27. We perform the test for three sets of parameter which belong to subspace 1, 2 and 8 (with phase 2 and 3 swapped along in X, Y space). The summary of the parameters in shown in table.6.

Set	**Subspace**	$\boldsymbol{\lambda}_1$	$\boldsymbol{\lambda}_2$	$\boldsymbol{\lambda}_3$	$\boldsymbol{\kappa}_1$	$\boldsymbol{\kappa}_2$	$\boldsymbol{\kappa}_3$
1	1	0.6	1	1	0.01	1	1
2	3	0.6	1.1	0.5	0.01	1.1	0.5
3	8 (swapping phases 2,3)	0.1	1	0.2	0.01	1.6	-0.4

Table 6: Summary of parameter sets to perform Laplace tests.

For each parameter set we have performed three independent measures (drop/bubble test) of Laplace law, which in two dimensional space has a form of Eq.B.1. The simulation setup is shown in Fig.118.

$$p_{in} - p_{out} = \Delta p = \frac{\gamma}{R} \tag{B.1}$$

Where p_{in} is the inside pressure of the droplet, p_{out} is the pressure outside the droplet measured far away from the interface and Δp is the the pressure difference between the inner and outer regions of the droplet, γ is the surface tension and R is the radius of the droplet. For the three set of free

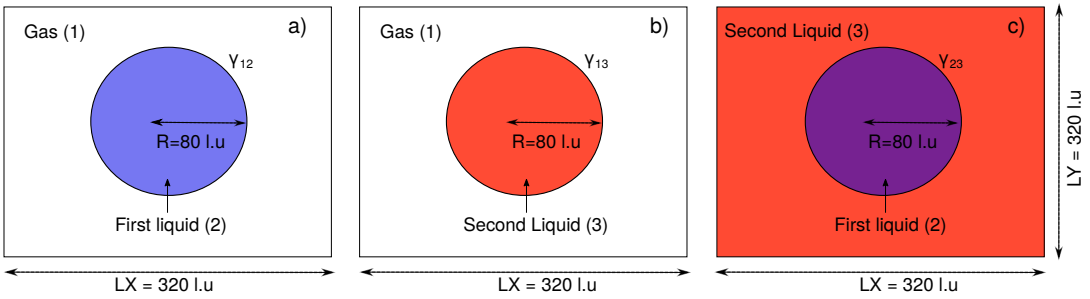

Figure 118: Simulation set up for Laplace test for each interface.

energy parameters shown in table.6, we measure the surface tension of the each interface for a range of droplet size. This is done for each interface such that γ_{12} represents the surface tension between gas and liquid component 1 (Fig.118(a)), γ_{13} shows the surface tension between gas and liquid component 2 (Fig.118(b)) and the surface tension between liquid component 1 and liquid component 2 is denoted by γ_{23} (Fig.118(c)). The results from the Laplace test corresponds to the three three sets of parameters is shown in Fig.119.

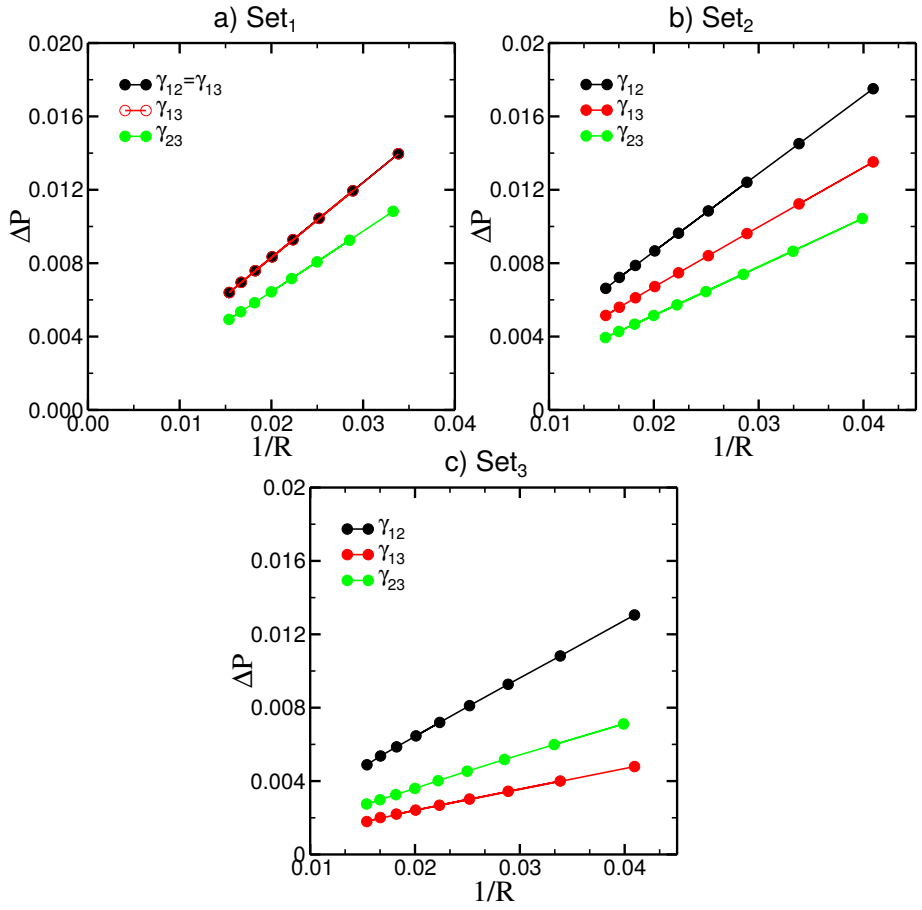

Figure 119: Validation of Laplace law each interface.

B.2 Mass conservation and high density accuracy

First, the capability of the current model to accurately capture the high density contrast between liquid and gas phase is depicted in Fig.(120). It is clear from the Fig.(120) that two immiscible liquid droplets of diameter 180 lattice units (l.u) each surrounded by gas phase in a 2D domain of 1600x1200 l.u, the density corresponds to the gas phase 0.001 and for the liquid phase its 1. The figure shows that the model is able to capture the collision dynamics at the density contrast of the order of 10^3 between liquid and gas phase. For the simulation details, in Fig.(121) conservation of mass and the accuracy to capture the prescribed radius of the liquid droplets during the whole process of collision is reported.

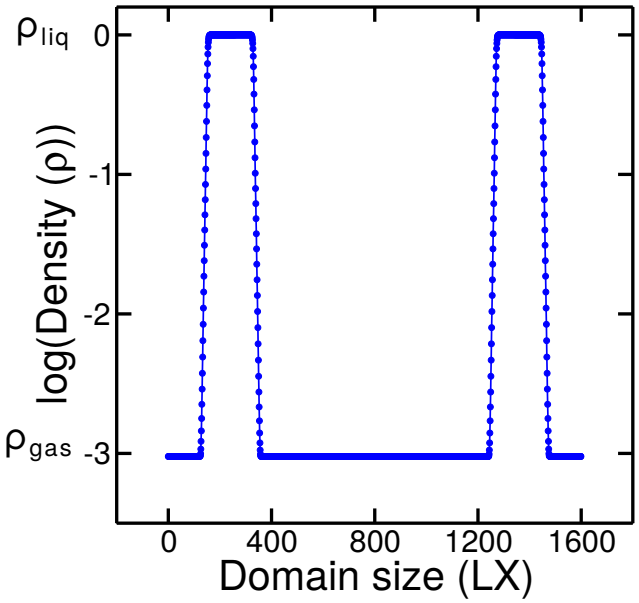

Figure 120: Density ratio of the order of 10^3 in ternary free energy model.

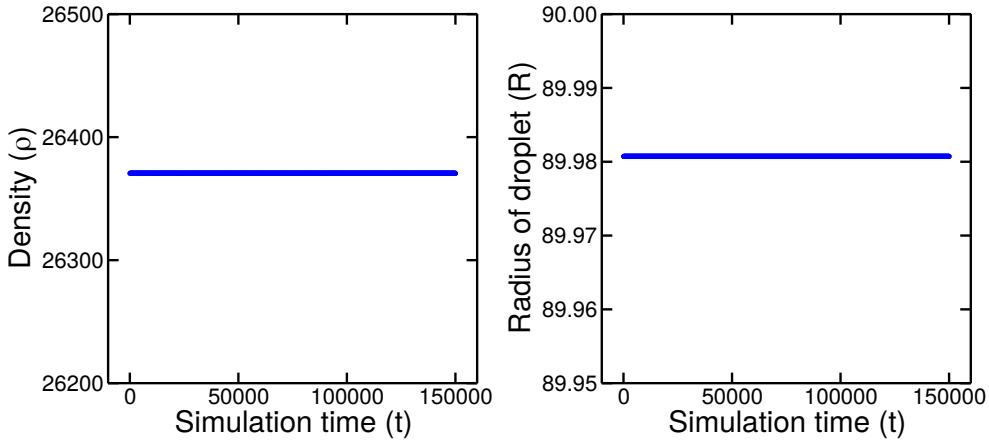

Figure 121: Conservation of density and accuracy to capture the prescribed droplet radius.

B.3 Visualization of the evolution of drop shapes through a sequence of simulation snapshots corresponds to Fig.110

Figure is updated by adding more simulation points to the Encapsulation region. Among newly added simulations, the screenshot of few new points (N_1 - N_4) are shown in Fig.123 below.

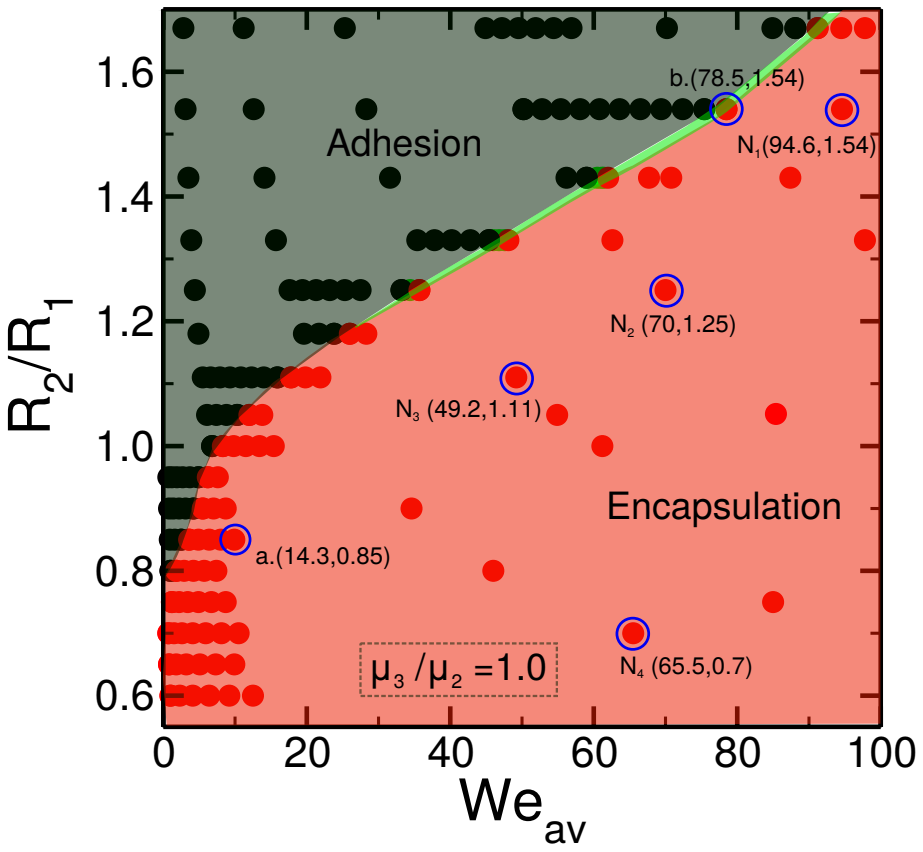

Figure 122: Transition curve from *Adhesion* to *Encapsulation* as a function of size ratio between inner and outer droplet (R_2/R_1) and average Weber number $\mathrm{We_{av}}$ ($\theta_1 = 167.11°$,$\theta_2 = 25.23°$, $\theta_3 = 167.66°$,($S_2 = -0.02473$), γ_{12}/γ_{13}=0.50 and $\mu_2/\mu_3 = 1$)

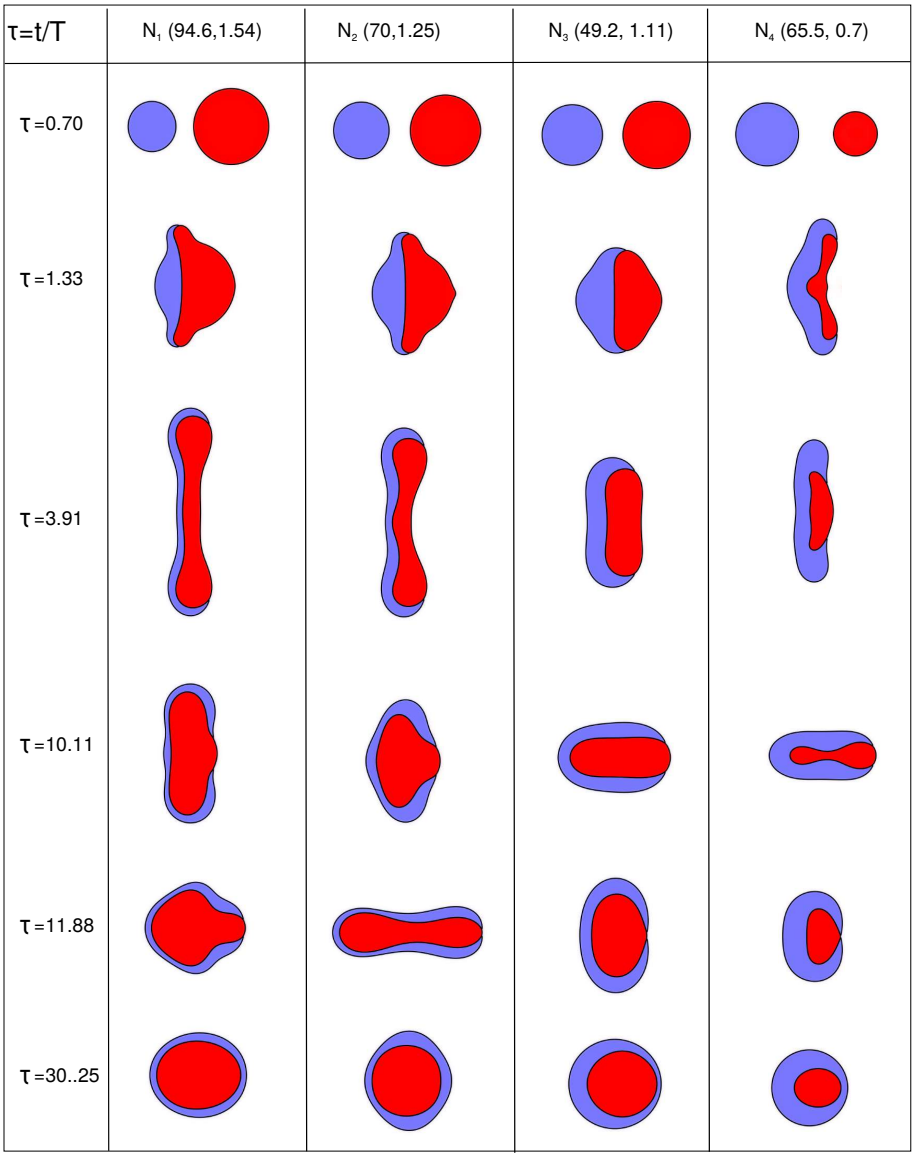

Figure 123: Sequence of steps during collision when outcome is encapsulation

B.4 Visualization of the evolution of drop shapes through a sequence of simulation snapshots corresponds to Fig.113

Figure is updated by adding more simulation points to the Encapsulation region. Among newly added simulations, the screenshot of few new points (N_1 - N_5) are shown in Fig.125 below.

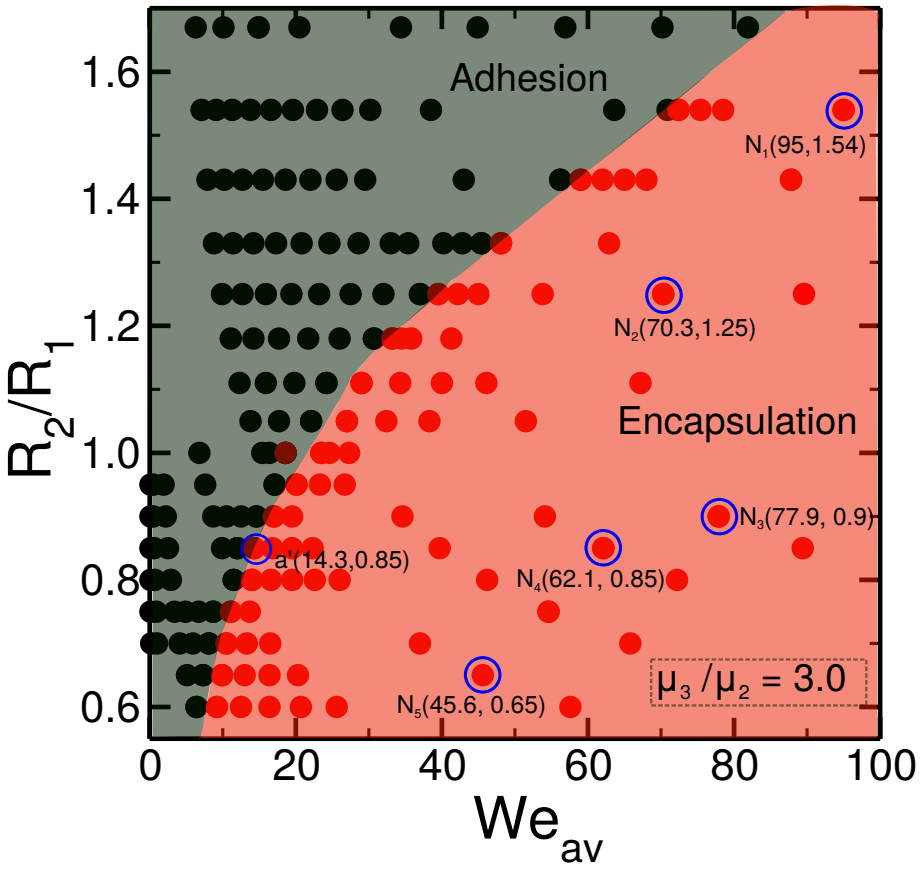

Figure 124: Transition curve from *Adhesion* to *Encapsulation* at viscosity contrast as a function of size ratio between inner and outer droplet (R_2/R_1) and average Weber number We_{av} ($\theta_1 = 167.11°$,$\theta_2 = 25.23°$, $\theta_3 = 167.66°$,$S_2 = -0.02473$, γ_{12}/γ_{13}=0.50 and $\mu_3/\mu_2 = 3.0$)

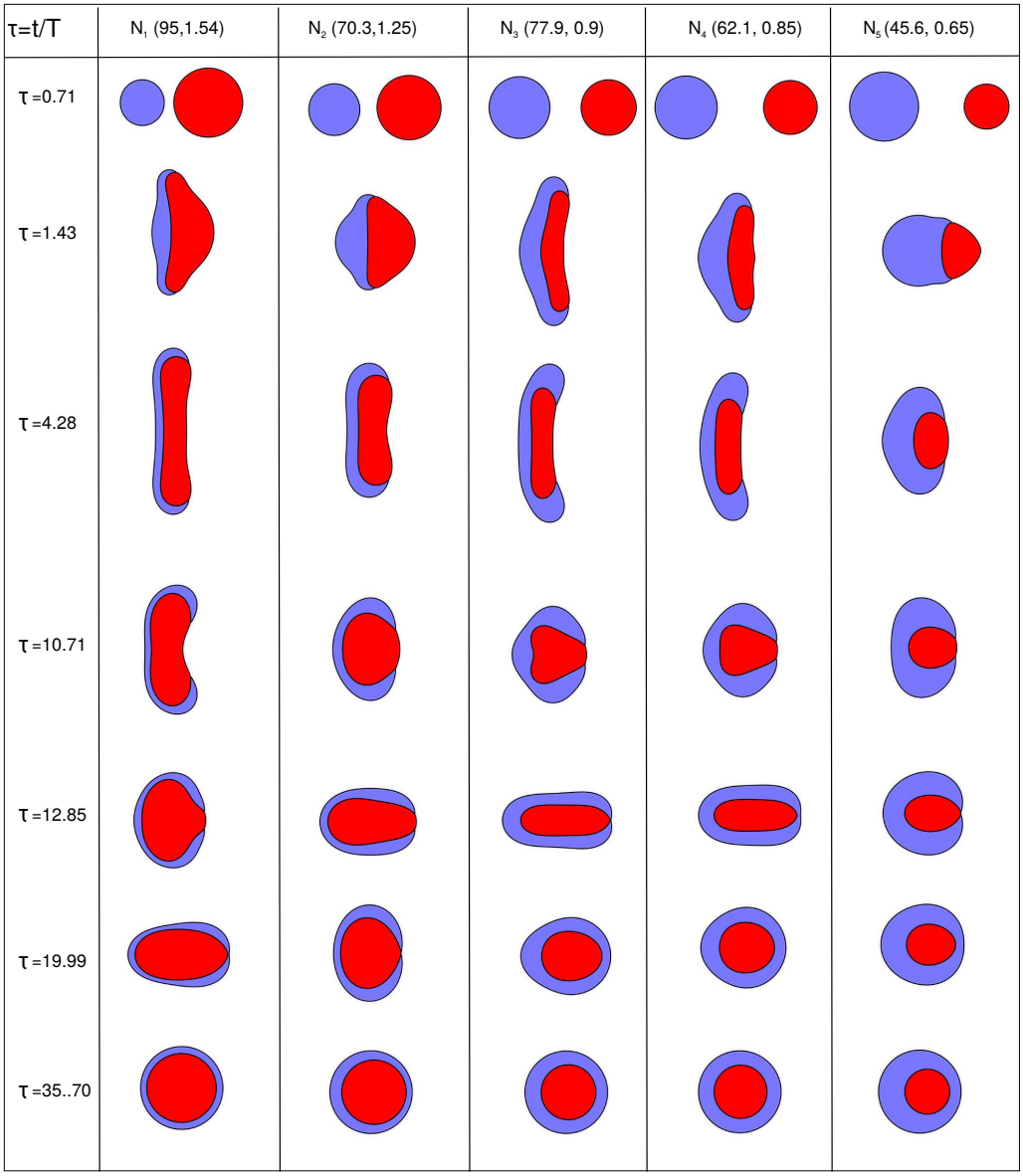

Figure 125: Sequence of steps during collision when outcome is encapsulation

Bibliography

[1] John David Anderson and J Wendt. *Computational fluid dynamics*, volume 206. Springer, 1995.

[2] Santosh Ansumali and Iliya V Karlin. Stabilization of the lattice boltzmann method by the h theorem: A numerical test. *Physical Review E*, 62(6):7999, 2000.

[3] Santosh Ansumali, Iliya V Karlin, and Hans Christian Öttinger. Minimal entropic kinetic models for hydrodynamics. *EPL (Europhysics Letters)*, 63(6):798, 2003.

[4] VA Arkhipov, IM Vasenin, and VF Trofimov. Stability of colliding drops of ideal liquid. *Journal of Applied Mechanics and Technical Physics*, 24(3):371–373, 1983.

[5] N Ashgriz and JY Poo. Coalescence and separation in binary collisions of liquid drops. *Journal of Fluid Mechanics*, 221:183–204, 1990.

[6] Amir Hossein Askari, Mehrzad Shams, and Pierre E Sullivan. Numerical simulation of double emulsion formation in cross-junctional flow-focusing microfluidic device using lattice boltzmann method. *Journal of Dispersion Science and Technology*, 2019.

[7] Neeru Bala, Marianna Pepona, Ilya Karlin, Halim Kusumaatmaja, and Ciro Semprebon. Wetting boundaries for a ternary high-density-ratio lattice boltzmann method. *Physical Review E*, 100(1):013308, 2019.

[8] Cx K Batchelor and GK Batchelor. *An introduction to fluid dynamics*. Cambridge university press, 2000.

[9] J. Bico and D. Quéré. Liquid trains in a tube. *Europhys. Lett.*, 51(5):546–550, 2000.

[10] J. Bico and D. Quéré. Self-propelling slugs. *J. Fluid Mech.*, 467:101–127, 2002.

[11] Daniel Bonn, Jens Eggers, Joseph Indekeu, Jacques Meunier, and Etienne Rolley. Wetting and spreading. *Reviews of modern physics*, 81(2):739, 2009.

[12] PR Brazier-Smith, SG Jennings, and J Latham. The interaction of falling water drops: coalescence. *Proceedings of the Royal Society of London. A. Mathematical and Physical Sciences*, 326(1566):393–408, 1972.

[13] A. J. Briant, a. J. Wagner, and J. M. Yeomans. Lattice Boltzmann simulations of contact line motion. I. Liquid-gas systems. *Phys. Rev. E*, 69(3):031602, mar 2004.

[14] A. J. Briant and J. M. Yeomans. Lattice Boltzmann simulations of contact line motion. II. Binary fluids. *Phys. Rev. E*, 69(3):031603, 2004.

[15] AJ Briant, AJ Wagner, and JM Yeomans. Lattice boltzmann simulations of contact line motion. i. liquid-gas systems. *Physical Review E*, 69(3):031602, 2004.

[16] Andreas Carlson. *Capillarity and dynamic wetting*. PhD thesis, KTH Royal Institute of Technology, 2012.

[17] Liao Changlin-lin, Liao Xin-wei, Zhao Xiao-liang, Lu Ning, Ding Hong-na, Wang Huan, Liu Yong-ge, et al. Study on enhanced oil recovery technology in low permeability heterogeneous reservoir by water-alternate-gas of coflooding. In *SPE Asia Pacific Oil and Gas Conference and Exhibition*. Society of Petroleum Engineers, 2013.

[18] Rong-Horng Chen. Diesel–diesel and diesel–ethanol drop collisions. *Applied Thermal Engineering*, 27(2):604 – 610, 2007.

[19] Rong-Horng Chen and Chiu-Ting Chen. Collision between immiscible drops with large surface tension difference: diesel oil and water. *Experiments in Fluids*, 41(3):453–461, Sep 2006.

[20] SS Chikatamarla, IV Karlin, et al. Entropic lattice boltzmann method for multiphase flows. *Physical review letters*, 114(17):174502, 2015.

[21] PL Chueh and JM Prausnitz. Vapor-liquid equilibria at high pressures. vapor-phase fugacity coefficients in nonpolar and quantum-gas mixtures. *Industrial & Engineering Chemistry Fundamentals*, 6(4):492–498, 1967.

[22] R. G. Cox. The dynamics of the spreading of liquids on a solid surface. Part 1 viscous flow. *J. Fluid Mech.*, 168(-1):195–220, 1986.

[23] R. G. Cox. Inertial and viscous effects on dynamic contact angles. *J. Fluid Mech.*, 357:249–278, feb 1998.

[24] Pierre-Gilles De Gennes, Françoise Brochard-Wyart, and David Quéré. *Capillarity and wetting phenomena: drops, bubbles, pearls, waves*. Springer Science & Business Media, 2013.

[25] Hang Ding and Peter D M Spelt. Wetting condition in diffuse interface simulations of contact line motion. *Phys. Rev. E*, 75(4):1–8, 2007.

[26] F. Diotallevi, L. Biferale, S. Chibbaro, A. Lamura, G. Pontrelli, M. Sbragaglia, S. Succi, and F. Toschi. Capillary filling using lattice Boltzmann equations: The case of multi-phase flows. *Europ. Phys. J: Special Topics*, 166(1):111–116, 2009.

[27] Burkhard Dünweg and Anthony JC Ladd. Lattice boltzmann simulations of soft matter systems. In *Advanced Computer Simulation Approaches for Soft Matter Sciences III*, pages 89–166. Springer, 2009.

[28] Antonin Eddi, Koen G Winkels, and Jacco H Snoeijer. Short time dynamics of viscous drop spreading. *Physics of fluids*, 25(1):013102, 2013.

[29] E. Esmaili, A. Moosavi, and A. Mazloomi. The dynamics of wettability driven droplets in smooth and corrugated microchannels. *J. Stat. Mech.*, 2012(10), 2012.

[30] Joel H Ferziger, Milovan Perić, and Robert L Street. *Computational methods for fluid dynamics*, volume 3. Springer, 2002.

[31] Víctor Francia, Luis Martín, Andrew E. Bayly, and Mark J.H. Simmons. Agglomeration during spray drying: Airborne clusters or breakage at the walls? *Chemical Engineering Science*, 162:284 – 299, 2017.

[32] Daan Frenkel, Berend Smit, and Mark A Ratner. *Understanding molecular simulation: from algorithms to applications*, volume 2. Academic press San Diego, 1996.

[33] T.-C. Gao, R.-H. Chen, J.-Y. Pu, and T.-H. Lin. Collision between an ethanol drop and a water drop. *Experiments in Fluids*, 38(6):731–738, Jun 2005.

[34] Sebastian Geller, Manfred Krafczyk, Jonas Tölke, Stefan Turek, and Jaroslav Hron. Benchmark computations based on lattice-boltzmann, finite element and finite volume methods for laminar flows. *Computers & fluids*, 35(8-9):888–897, 2006.

[35] La Girifalco and Rj Good. A theory for the estimation of surface and interfacial energies. I. Derivation and application to interfacial tension. *J. Phys. Chem.*, 61(13):904–909, jul 1957.

[36] Andrew K Gunstensen, Daniel H Rothman, Stéphane Zaleski, and Gianluigi Zanetti. Lattice boltzmann model of immiscible fluids. *Physical Review A*, 43(8):4320, 1991.

[37] Jan Guzowski, Piotr M Korczyk, Slawomir Jakiela, and Piotr Garstecki. The structure and stability of multiple micro-droplets. *Soft Matter*, 8(27):7269–7278, 2012.

[38] Xiaoyi He, Shiyi Chen, and Raoyang Zhang. A lattice boltzmann scheme for incompressible multiphase flow and its application in simulation of rayleigh–taylor instability. *Journal of computational physics*, 152(2):642–663, 1999.

[39] Xiaoyi He and Gary D Doolen. Thermodynamic foundations of kinetic theory and lattice boltzmann models for multiphase flows. *Journal of Statistical Physics*, 107(1-2):309–328, 2002.

[40] Xiaoyi He, Xiaowen Shan, and Gary D Doolen. Discrete boltzmann equation model for nonideal gases. *Physical Review E*, 57(1):R13, 1998.

[41] TL Hill and J Gillis. An introduction to statistical thermodynamics (courier corporation). 2012.

[42] Cyril W Hirt and Billy D Nichols. Volume of fluid (vof) method for the dynamics of free boundaries. *Journal of computational physics*, 39(1):201–225, 1981.

[43] Mark H Holtz et al. Immiscible water alternating gas (iwag) eor: Current state of the art. In *SPE Improved Oil Recovery Conference*. Society of Petroleum Engineers, 2016.

[44] Haibo Huang, Daniel T. Thorne, Marcel G. Schaap, and Michael C. Sukop. Proposed approximation for contact angles in Shan-and-Chen-type multicomponent multiphase lattice Boltzmann models. *Phys. Rev. E*, 76(6):1–6, 2007.

[45] Jun-Jie Huang, Haibo Huang, and Xinzhu Wang. Numerical study of drop motion on a surface with stepwise wettability gradient and contact angle hysteresis. *Phys. Fluids*, 26(6):062101, jun 2014.

[46] T Inamuro, S Tajima, and F Ogino. Lattice boltzmann simulation of droplet collision dynamics. *International journal of heat and mass transfer*, 47(21):4649–4657, 2004.

[47] VM Ivanov and PI Nefedov. Experimental investigation of the combustion process of natural and emulsified liquid fuels. *NASA Report 65N14944*, 1962.

[48] DAVID JACQMIN. Contact-line dynamics of a diffuse fluid interface. *J. Fluid Mech.*, 402:S0022112099006874, jan 2000.

[49] YJ Jiang, A Umemura, and CK Law. An experimental investigation on the collision behaviour of hydrocarbon droplets. *Journal of Fluid Mechanics*, 234:171–190, 1992.

[50] JF Joanny and Pierre-Gilles De Gennes. A model for contact angle hysteresis. *The journal of chemical physics*, 81(1):552–562, 1984.

[51] Qinjun Kang, Dongxiao Zhang, and Shiyi Chen. Displacement of a three-dimensional immiscible droplet in a duct. *Journal of Fluid Mechanics*, 545:41–66, 2005.

[52] Iliya V Karlin, Santosh Ansumali, Christos E Frouzakis, and Shyam Sunder Chikatamarla. Elements of the lattice boltzmann method i: Linear advection equation. *Commun. Comput. Phys*, 1(4):616–655, 2006.

[53] Iliya V Karlin, Alexander N Gorban, Sauro Succi, and Vinicio Boffi. Maximum entropy principle for lattice kinetic equations. *Physical Review Letters*, 81(1):6, 1998.

[54] Ilya V Karlin, Antonio Ferrante, and Hans Christian Öttinger. Perfect entropy functions of the lattice boltzmann method. *EPL (Europhysics Letters)*, 47(2):182, 1999.

[55] Dirk Kehrwald. Numerical analysis of immiscible lattice bgk. 2002.

[56] Armelle Keiser, Ludovic Keiser, Christophe Clanet, and David Quéré. Drop friction on liquid-infused materials. *Soft Matter*, 13(39):6981–6987, 2017.

[57] Diederick Johannes Korteweg. Sur la forme que prennent les équations du mouvements des fluides si l'on tient compte des forces capillaires causées par des variations de densité considérables mais connues et sur la théorie de la capillarité dans l'hypothèse d'une variation continue de la densité. *Archives Néerlandaises des Sciences exactes et naturelles*, 6:1–24, 1901.

[58] Timm Krüger, Halim Kusumaatmaja, Alexandr Kuzmin, Orest Shardt, Goncalo Silva, and Erlend Magnus Viggen. The lattice boltzmann method. *Springer International Publishing*, 10(978-3):4–15, 2017.

[59] AL Kupershtokh, DA Medvedev, and DI Karpov. On equations of state in a lattice boltzmann method. *Computers & Mathematics with Applications*, 58(5):965–974, 2009.

[60] H. Kusumaatmaja, E. J. Hemingway, and S. M. Fielding. Moving contact line dynamics: from diffuse to sharp interfaces. *J. Fluid Mech.*, 788:209–227, 2016.

[61] Anthony J. C. Ladd. Numerical simulations of particulate suspensions via a discretized Boltzmann equation. Part 2. Numerical results. *J. Fluid Mech.*, 271:285, 1994.

[62] Lev Davidovich Landau and Evgenii Mikhailovich Lifshitz. *Course of theoretical physics*. Elsevier, 2013.

[63] JC Lasheras, AC Fernandez-Pello, and FL Dryer. Initial observations on the free droplet combustion characteristics of water-in-fuel emulsions. *Combustion Science and Technology*, 21(1-2):1–14, 1979.

[64] M Latva-Kokko and Daniel H Rothman. Static contact angle in lattice boltzmann models of immiscible fluids. *Physical Review E*, 72(4):046701, 2005.

[65] Leonid P Lebedev and Michael J Cloud. *Tensor analysis*. World Scientific, 2003.

[66] Hyun Geun Lee and Junseok Kim. Accurate contact angle boundary conditions for the Cahn-Hilliard equations. *Comp. Fluids*, 44(1):178–186, 2011.

[67] Taehun Lee and Ching-Long Lin. A stable discretization of the lattice boltzmann equation for simulation of incompressible two-phase flows at high density ratio. *Journal of Computational Physics*, 206(1):16–47, 2005.

[68] Taehun Lee and Lin Liu. Lattice Boltzmann simulations of micron-scale drop impact on dry surfaces. *J. Comp. Phys.*, 229(20):8045–8063, 2010.

[69] SV Lishchuk, CM Care, and I Halliday. Lattice boltzmann algorithm for surface tension with greatly reduced microcurrents. *Physical review E*, 67(3):036701, 2003.

[70] Haihu Liu, Yaping Ju, Ningning Wang, Guang Xi, and Yonghao Zhang. Lattice Boltzmann modeling of contact angle and its hysteresis in two-phase flow with large viscosity difference. *Phys. Rev. E*, 92(3):1–12, 2015.

[71] Qin Lou, Mo Yang, and Hongtao Xu. Wetting Boundary Condition in an Improved Lattice Boltzmann Method for Nonideal Gases. *Comm. Comp. Phys.*, 23(4):1116–1130, 2018.

[72] Richard Lucas. Ueber das Zeitgesetz des kapillaren Aufstiegs von Flüssigkeiten. *Kolloid-Zeitschrift*, 23(1):15–22, jul 1918.

[73] Daniel Lycett-Brown, Ilya Karlin, and Kai H Luo. Droplet collision simulation by a multi-speed lattice boltzmann method. *Communications in Computational Physics*, 9(5):1219–1234, 2011.

[74] Daniel Lycett-Brown, Kai H Luo, Ronghou Liu, and Pengmei Lv. Binary droplet collision simulations by a multiphase cascaded lattice boltzmann method. *Physics of Fluids*, 26(2):023303, 2014.

[75] Lasse Makkonen. A thermodynamic model of contact angle hysteresis. *The Journal of chemical physics*, 147(6):064703, 2017.

[76] Abraham Marmur. Wetting on hydrophobic rough surfaces: to be heterogeneous or not to be? *Langmuir*, 19(20):8343–8348, 2003.

[77] Nicos S Martys and Hudong Chen. Simulation of multicomponent fluids in complex three-dimensional geometries by the lattice boltzmann method. *Physical review E*, 53(1):743, 1996.

[78] F Mashayek, N Ashgriz, WJ Minkowycz, and B Shotorban. Coalescence collision of liquid drops. *International Journal of Heat and Mass Transfer*, 46(1):77–89, 2003.

[79] Ali Mazloomi, Shyam S Chikatamarla, and Iliya V Karlin. Entropic lattice boltzmann method for multiphase flows: Fluid-solid interfaces. *Physical Review E*, 92(2):023308, 2015.

[80] A. Mazloomi M, S. S. Chikatamarla, and I. V. Karlin. Entropic Lattice Boltzmann Method for Multiphase Flows. *Phys. Rev. Lett.*, 114(17):174502, may 2015.

[81] Ali Mazloomi M., Shyam S Chikatamarla, and Iliya V Karlin. Entropic lattice Boltzmann method for multiphase flows: Fluid-solid interfaces. *Phys. Rev. E*, 92(2):023308, aug 2015.

[82] A. Mazloomi Moqaddam, S. S. Chikatamarla, and I. V. Karlin. Simulation of Droplets Collisions Using Two-Phase Entropic Lattice Boltzmann Method. *J. Stat. Phys.*, 161(6):1420–1433, 2015.

[83] Ali Mazloomi Moqaddam, Shyam S Chikatamarla, and Ilya V Karlin. Simulation of binary droplet collisions with the entropic lattice boltzmann method. *Physics of Fluids*, 28(2):022106, 2016.

[84] A Mazloomi Moqaddam, Shyam S Chikatamarla, and Iliya V Karlin. Simulation of droplets collisions using two-phase entropic lattice boltzmann method. *Journal of statistical physics*, 161(6):1420–1433, 2015.

[85] David W Murphy, Cheng Li, Vincent d'Albignac, David Morra, and Joseph Katz. Splash behaviour and oily marine aerosol production by raindrops impacting oil slicks. *Journal of Fluid Mechanics*, 780:536, 2015.

[86] JJ Nijdam, B Guo, DF Fletcher, and TAG Langrish. Challenges of simulating droplet coalescence within a spray. *Drying Technology*, 22(6):1463–1488, 2004.

[87] R Robert Nourgaliev, Truc-Nam Dinh, Theo G Theofanous, and D Joseph. The lattice boltzmann equation method: theoretical interpretation, numerics and implications. *International Journal of Multiphase Flow*, 29(1):117–169, 2003.

[88] Melissa Orme. Experiments on droplet collisions, bounce, coalescence and disruption. *Progress in Energy and Combustion Science*, 23(1):65–79, 1997.

[89] C Pan, M Hilpert, and CT Miller. Lattice-boltzmann simulation of two-phase flow in porous media. *Water Resources Research*, 40(1), 2004.

[90] Yu Pan and Kazuhiko Suga. Numerical simulation of binary liquid droplet collision. *Physics of Fluids*, 17(8):082105, 2005.

[91] Robert Watson Park. Behavior of water drops colliding in humid nitrogen. *PhDT*, 1970.

[92] Charles S Peskin. The immersed boundary method. *Acta numerica*, 11:479–517, 2002.

[93] E Pierce, FJ Carmona, and A Amirfazli. Understanding of sliding and contact angle results in tilted plate experiments. *Colloids and Surfaces A: Physicochemical and Engineering Aspects*, 323(1-3):73–82, 2008.

[94] C. Planchette, E. Lorenceau, and G. Brenn. Liquid encapsulation by binary collisions of immiscible liquid drops. *Colloids and Surfaces A: Physicochemical and Engineering Aspects*, 365(1):89 – 94, 2010. 4th International Workshop.

[95] Mihail Nicolae Popescu, G Oshanin, S Dietrich, and AM Cazabat. Precursor films in wetting phenomena. *Journal of Physics: Condensed Matter*, 24(24):243102, 2012.

[96] EG Puckett. Level set methods: Evolving interfaces in geometry, fluid mechanics, computer vision, and materials science, 1998.

[97] J Qian and Chung King Law. Regimes of coalescence and separation in droplet collision. *Journal of fluid mechanics*, 331:59–80, 1997.

[98] RS Qin. Mesoscopic interparticle potentials in the lattice boltzmann equation for multiphase fluids. *Physical Review E*, 73(6):066703, 2006.

[99] John William Strutt Baron Rayleigh. *The theory of sound*, volume 2. Macmillan, 1896.

[100] Otto Redlich and Joseph NS Kwong. On the thermodynamics of solutions. v. an equation of state. fugacities of gaseous solutions. *Chemical reviews*, 44(1):233–244, 1949.

[101] Timothy Reis and Timothy Nigel Phillips. Lattice boltzmann model for simulating immiscible two-phase flows. *Journal of Physics A: Mathematical and Theoretical*, 40(14):4033, 2007.

[102] Martin Rieber and Arnold Frohn. A numerical study on the mechanism of splashing. *International Journal of Heat and Fluid Flow*, 20(5):455–461, 1999.

[103] Ilia V Roisman. Inertia dominated drop collisions. ii. an analytical solution of the navier–stokes equations for a spreading viscous film. *Physics of Fluids*, 21(5):052104, 2009.

[104] N Roth, M Rieber, and A Frohn. High energy head-on collision of droplets. In *Fifteenth International Conference on Liquid Atomization and Spray Systems*, 1999.

[105] Daniel H Rothman and Jeffrey M Keller. Immiscible cellular-automaton fluids. *Journal of Statistical Physics*, 52(3-4):1119–1127, 1988.

[106] Kalpana Sarojini KG, Purbarun Dhar, Susy Varughese, and Sarit K Das. Coalescence dynamics of pedot: Pss droplets impacting at offset on substrates for inkjet printing. *Langmuir*, 32(23):5838–5851, 2016.

[107] MD Saroka, N Ashgriz, and M Movassat. Numerical investigation of head-on binary drop collisions in a dynamically inert environment. 2012.

[108] MRLSK Sbragaglia, R Benzi, L Biferale, S Succi, K Sugiyama, and F Toschi. Generalized lattice boltzmann method with multirange pseudopotential. *Physical Review E*, 75(2):026702, 2007.

[109] Ciro Semprebon, Timm Krüger, and Halim Kusumaatmaja. Ternary free-energy lattice boltzmann model with tunable surface tensions and contact angles. *Physical Review E*, 93(3):033305, 2016.

[110] Ciro Semprebon, Timm Krüger, and Halim Kusumaatmaja. Ternary free-energy lattice Boltzmann model with tunable surface tensions and contact angles. *Phys. Rev. E*, 93(3):033305, mar 2016.

[111] Xiaowen Shan and Hudong Chen. Lattice boltzmann model for simulating flows with multiple phases and components. *Physical review E*, 47(3):1815, 1993.

[112] Xiaowen Shan and Hudong Chen. Simulation of nonideal gases and liquid-gas phase transitions by the lattice boltzmann equation. *Physical Review E*, 49(4):2941, 1994.

[113] Theodore Shifrin. Differential geometry: a first course in curves and surfaces. *University of Georgia*, 2015.

[114] J David Smith, Rajeev Dhiman, Sushant Anand, Ernesto Reza-Garduno, Robert E Cohen, Gareth H McKinley, and Kripa K Varanasi. Droplet mobility on lubricant-impregnated surfaces. *Soft Matter*, 9(6):1772–1780, 2013.

[115] Katherine Marie Smyth. *Wetting hysteresis and droplet roll off behavior on superhydrophobic surfaces by Katherine Marie Smyth.* PhD thesis, Massachusetts Institute of Technology, 2010.

[116] Jacco H Snoeijer and Bruno Andreotti. Moving contact lines: scales, regimes, and dynamical transitions. *Annual review of fluid mechanics*, 45, 2013.

[117] JH Snoeijer, J Ziegler, B Andreotti, M Fermigier, and J Eggers. Thick films of viscous fluid coating a plate withdrawn from a liquid reservoir. *Physical review letters*, 100(24):244502, 2008.

[118] Martin Sommerfeld and Matthias Kuschel. Modelling droplet collision outcomes for different substances and viscosities. *Experiments in fluids*, 57(12):187, 2016.

[119] Sauro Succi. *The lattice Boltzmann equation: for fluid dynamics and beyond*. Oxford university press, 2001.

[120] M Sukop. *DT Thorne, Jr. Lattice Boltzmann Modeling Lattice Boltzmann Modeling*. Springer, 2006.

[121] Michael R Swift, WR Osborn, and JM Yeomans. Lattice boltzmann simulation of nonideal fluids. *Physical review letters*, 75(5):830, 1995.

[122] Sébastien Tanguy and Alain Berlemont. Application of a level set method for simulation of droplet collisions. *International journal of multiphase flow*, 31(9):1015–1035, 2005.

[123] LH Tanner. The spreading of silicone oil drops on horizontal surfaces. *Journal of Physics D: Applied Physics*, 12(9):1473, 1979.

[124] Oleg N Tretinnikov and Yoshito Ikada. Dynamic wetting and contact angle hysteresis of polymer surfaces studied with the modified wilhelmy balance method. *Langmuir*, 10(5):1606–1614, 1994.

[125] Grétar Tryggvason, Bernard Bunner, Asghar Esmaeeli, Damir Juric, N Al-Rawahi, W Tauber, J Han, S Nas, and Y-J Jan. A front-tracking method for the computations of multiphase flow. *Journal of computational physics*, 169(2):708–759, 2001.

[126] Mark E Tuckerman and Glenn J Martyna. Understanding modern molecular dynamics: Techniques and applications. *The Journal of Physical Chemistry B*, 104(2):159–178, 2000.

[127] Salih Ozen Unverdi and Grétar Tryggvason. A front-tracking method for viscous, incompressible, multi-fluid flows. 1992.

[128] Johannes Diderik van der Waals. *Thermodynamische theorie der capillariteit in de onderstelling van continue dichtheidsverandering, door JD Van der Waals...* J. Müller, 1893.

[129] AJ Wagner and Qi Li. Investigation of galilean invariance of multi-phase lattice boltzmann methods. *Physica A: Statistical Mechanics and its Applications*, 362(1):105–110, 2006.

[130] C. H. Wang, C. Z. Lin, W. G. Hung, W. C. Huang, and C. K. Law. On the burning characteristics of collision-generated water/hexadecane droplets. *Combust. Sci. Technol.*, 176(1):71–93, 2004.

[131] CH Wang and CK Law. Microexplosion of fuel droplets under high pressure. *Combustion and Flame*, 59(1):53–62, 1985.

[132] CH Wang, CZ Lin, WG Hung, WC Huang, and Chung King Law. On the burning characteristics of collision-generated water/hexadecane droplets. *Combustion science and technology*, 176(1):71–93, 2004.

[133] CH Wang and LH Ni. The feasibility study of water–oil emulsion in diesel engine. *The Chinese Journal of Mechanics*, 12(4):465–474, 1996.

[134] F Wang, FP Contò, N Naz, JR Castrejón-Pita, AA Castrejón-Pita, CG Bailey, W Wang, JJ Feng, and Y Sui. A fate-alternating transitional regime in contracting liquid filaments. *Journal of Fluid Mechanics*, 860:640–653, 2019.

[135] Zhaoyuan Wang, Jianming Yang, Bonguk Koo, and Frederick Stern. A coupled level set and volume-of-fluid method for sharp interface simulation of plunging breaking waves. *International Journal of Multiphase Flow*, 35(3):227–246, 2009.

[136] Edward W. Washburn. The Dynamics of Capillary Flow. *Phys. Rev.*, 17(3):273–283, mar 1921.

[137] Binghai Wen, Bingfang Huang, Zhangrong Qin, Chunlei Wang, and Chaoying Zhang. Contact angle measurement in lattice boltzmann method. *Computers & Mathematics with Applications*, 76(7):1686–1698, 2018.

[138] H. S. Wiklund, S. B. Lindström, and T. Uesaka. Boundary condition considerations in lattice Boltzmann formulations of wetting binary fluids. *Computer Physics Communications*, 182(10):2192–2200, 2011.

[139] Keeney Willis and Melissa Orme. Binary droplet collisions in a vacuum environment: an experimental investigation of the role of viscosity. *Experiments in fluids*, 34(1):28–41, 2003.

[140] HH Winter. Viscous dissipation term in energy equations. *Calculation and Measurement Techniques for Momentum, Energy and Mass Transfer*, 7:27–34, 1987.

[141] Moritz Wöhrwag, Ciro Semprebon, A Mazloomi Moqaddam, Ilya Karlin, and Halim Kusumaatmaja. Ternary free-energy entropic lattice boltzmann model with a high density ratio. *Physical Review Letters*, 120(23):234501, 2018.

[142] Moritz Wöhrwag, Ciro Semprebon, Ali Mazloomi Moqaddam, Ilya Karlin, and Halim Kusumaatmaja. Ternary free-energy entropic lattice Boltzmann model with high density ratio. *Phys. Rev. Lett.*, 120(23):234501, 2018.

[143] M Yoshino and T Inamuro. Lattice boltzmann simulations for flow and heat/mass transfer problems in a three-dimensional porous structure. *International Journal for Numerical Methods in Fluids*, 43(2):183–198, 2003.

[144] Yuan Yu, Haihu Liu, Dong Liang, and Yonghao Zhang. A versatile lattice boltzmann model for immiscible ternary fluid flows. *Physics of Fluids*, 31(1):012108, 2019.

[145] Peng Yuan and Laura Schaefer. Equations of state in a lattice boltzmann model. *Physics of Fluids*, 18(4):042101, 2006.

[146] Chun-Yu Zhang, Hang Ding, Peng Gao, and Yan Ling Wu. Diffuse interface simulation of ternary fluids in contact with solid. *J. Comp. Phys.*, 309:37–51, mar 2016.

[147] Junfeng Zhang and Daniel Y Kwok. Lattice boltzmann study on the contact angle and contact line dynamics of liquid- vapor interfaces. *Langmuir*, 20(19):8137–8141, 2004.

[148] HW Zheng, Chang Shu, and Yong-Tian Chew. A lattice boltzmann model for multiphase flows with large density ratio. *Journal of computational physics*, 218(1):353–371, 2006.